WAVEFORM DELINEATION AND ANALYSIS OF SEISMOCARDIOGRAPHIC SIGNALS

TILENDRA CHOUDHARY

WAVEFORM DELINEATION AND ANALYSIS OF SEISMOCARDIOGRAPHIC SIGNALS

A

Thesis submitted

for the award of the degree of

DOCTOR OF PHILOSOPHY

By

TILENDRA CHOUDHARY

DEPARTMENT OF ELECTRONICS AND ELECTRICAL ENGINEERING

INDIAN INSTITUTE OF TECHNOLOGY GUWAHATI

GUWAHATI - 781 039, ASSAM, INDIA

OCTOBER 2020

Certificate

This is to certify that the thesis entitled "**WAVEFORM DELINEATION AND ANALYSIS OF SEISMOCARDIOGRAPHIC SIGNALS**", submitted by **Tilendra Choudhary** (156102016), a research scholar in the *Department of Electronics and Electrical Engineering, Indian Institute of Technology Guwahati*, for the award of the degree of **Doctor of Philosophy**, is a record of an original research work carried out by him under our supervision and guidance. The thesis has fulfilled all requirements as per the regulations of the institute and in our opinion has reached the standard needed for submission. The results embodied in this thesis have not been submitted to any other University or Institute for the award of any degree or diploma.

Prof. M.K. Bhuyan
Professor
Dept. of Electronics and Electrical Engg.
Indian Institute of Technology Guwahati
Guwahati - 781 039, Assam, India.

Dated:
Guwahati.

Dr. L.N. Sharma
Senior Technical Officer
Dept. of Electronics and Electrical Engg.
Indian Institute of Technology Guwahati
Guwahati - 781 039, Assam, India.

Dated:
Guwahati.

To

The Almighty Lord Krishna

for His blessings

My parents

Mr. Chandra Bhanu Choudhary & Mrs. Meera Choudhary

for their blessings, support and encouragement

&

My other family members

for their love and support

Acknowledgements

I am obliged to GOD for His divine guidance, grace, and blessings. I solely dedicate my thesis to Him. This thesis would not have been possible without the immense help and support of several people in various measures. I would like to convey my acknowledgment to all of them.

First and foremost, I express my deepest and most sincere gratitude to my Ph.D. supervisors, Prof. M.K. Bhuyan and Dr. L.N. Sharma, for their guidance, help, and encouragement throughout my research work. I greatly admire their attitude towards research and enthusiasm for work. It is very difficult to describe my feelings in words to acknowledge my supervisors for their constant motivation, positive thinking, and moral support. Their insightful feedbacks have helped me greatly in improving myself scientifically and personally. It would be completely impossible for me to bring the research as well as the thesis to this form without the immense facilities and freedom of work provided by them in the EMST Laboratory.

I am very much thankful to the members of my doctoral committee, Prof. S. Dandapat, Dr. K. Karthik and Prof. S. R. Ahamed for their support, encouragement, and valuable suggestions on my research work. I also would like to thank all the anonymous reviewers for their useful suggestions about my work. I would like to thank faculty members and the office-staffs of the Department of Electronics and Electrical Engineering, IIT Guwahati, for their help in carrying out this research work. I sincerely thank my M.Tech. supervisor, Dr. M. S. Manikandan. After my post-graduation, it was he who motivated me to join for Ph.D.

I am thankful to my friends of IIT Guwahati for their care, love, support, and assistance during my doctoral studies. I am grateful to the members of the EMST Laboratory for their enormous support and help, who helped me whenever I need them. I would like to thank my senior members of IIT Guwahati, who supported me well in the journey of my Ph.D. Above all, I am deeply grateful to my parents and my other family members, including my sibling, cousins, uncle, aunt, and grandmother. It would not have been possible for me to complete my Ph.D. without their love, support, and sacrifice. I attribute this achievement to them for their constant blessings, support, silent prayers for my success, and making me stand in this position.

Tilendra Choudhary

Abstract

Cardiac disorder is one of the major risk factors for human mortality. Continuous monitoring and assessment of cardiac mechanics are most important to reduce the risk factors of cardiovascular diseases and death rates. Seismocardiogram (SCG) is the manifestation of thoracic vibrations induced by cardiac movements. It is measured non-invasively on the chest-wall. This helps in diagnosing and monitoring cardiac mechanical activities. Proper diagnosis of cardiac pathology using this signal needs precise signal characterization, delineation, and feature extraction. Delineation facilitates the estimation of SCG fiducial points corresponding to cardiac events. In this study, the fiducial points of the SCG signal are estimated, and their applications are investigated. These may be helpful for personalized healthcare, telemonitoring, and wireless body area networks. Delineation of SCG waveform is investigated under the categories of standalone and other cardiac-signal assisted approaches. Two different standalone approaches are developed based on time-frequency analysis of the SCG signal. These methods mainly estimate the prominent peaks of SCG cycles that due to aortic valve opening (AO). The first method is based on data-independent multiscale decomposition. In the second method, data-adaptive variational mode decomposition (VMD) is modified, providing an optimal combination of input parameters (α, K). Results suggest that the modified VMD based method performs better. With the assistance of electrocardiogram (ECG) signal, orthogonal subspace projection-based a new delineation framework is developed. It can efficiently estimate two fiducial points, AO and post-AC peaks from SCG systole and diastole profiles, respectively. To extract more fiducial points, the scalographic-photoplethysmogram (PPG) assisted SCG delineation algorithm is proposed. This algorithm can extract six fiducial parameters, simultaneously. More specifically, three fiducial points are estimated from each of both profiles, and a better characterization of the systole and diastole profiles is made possible with them.

Being a cardiac mechanical signal, the SCG is employed to derive the fundamental heart sounds (HS) and to characterize them as an application. The developed HS extraction method is mainly based on multiscale decomposition and center-of-gravity criterion. Another application is explored, which relates to the extraction of morphological variability in the SCG cycles. These morphological variations can be utilized to analyze the SCG affecting factors, including body movement, posture, and breathing pattern. In this study, the effect of respiratory-effort levels on to the SCG signal is analyzed. Results suggest that the SCG morphology changes with varying lung volume due to various

breathing states, such as breathlessness, normal breathing, and long and labored breathing. A method is deployed, where the morphological changes are quantified by extracted hybrid features, including fiducial and non-fiducial features. The assistance of ECG signals is taken into consideration for this method. Under this method, the SCG signals are classified into different respiratory-effort levels using stacked-autoencoder based classifier. Performance results are also compared with other well-known classifiers. The robustness of the proposed methods is evaluated using SCG signals from publically available database and in-house recordings. For creating an SCG database, a small electronic circuit board is designed, which consists of a 3-D MEMS-based accelerometer, pre-amplifier, and filter. It is interfaced with a standard data acquisition system to record SCG signals.

KEYWORDS: Seismocardiogram, Variational mode decomposition, AO peaks, Delineation, Stacked autoencoder, Scalogram, Cardiac activity

Contents

List of Figures

List of Tables

List of Acronyms and Abbreviations

AO	Aortic Valve Opening
AC	Aortic Valve Closure
ACF	Autocorrelation Feature
AV	Atrioventricular
AUSMC	Airborne Ultrasound Surface Motion Camera
ARS	Angular Rate Sensor
ACoef	Autocorrelation Coefficient
AWGN	Additive White Gaussian Noise
ACC	Accuracy related to detection of fiducial points
Acc	Accuracy related to event classification(or recognition)
AUC	Area Under the ROC Curve
BEnr	Beat Energy
BEnt	Beat Entropy
BSEnt	Beat Spectral Entropy
BSC	Beat Spectral Centroid
CT	Computerized Tomography
CEBS	Combined measurement of ECG, Breathing, and SCG
CWT	Continuous Wavelet Transform
CEEMDAN	Complete Ensemble Empirical Mode Decomposition with Adaptive Noise
CCE	Cardiac Cycle Envelope
CoG	Center of Gravity
DAQ	Data Acquisition
DWT	Discrete Wavelet Transform
DFT	Discrete Fourier Transform

DMK	Dominant Multiscale Kurtosis
DMCF	Dominant Multiscale Central Frequency
DER	Detection Error Rate
DHR	Heart Rate Difference
DBEnr	Beat Energy Difference
DBEnt	Beat Entropy Difference
DEnr	Diastole Energy
DEnt	Diastole Entropy
ECG	Electrocardiogram
ECHO	Echocardiogram
EMD	Electromechanical Delay (QS1)
EMS	Electromechanical Systole (QS2)
EMAC	Electro-Mechano-Acoustic Cardiovascular
EMD	Empirical Mode Decomposition
EEMD	Ensemble Empirical Mode Decomposition
EMw	Electro-Mechanical Window
EWT	Empirical Wavelet Transform
FOGD	First Order Gaussian Differentiation
FP	False Positive
FN	False Negative
FPR	False Positive Rate
FMSA	Frequency at MSA
GCG	Gyrocardiogram
GDF	Gaussian Derivative Filtered
GDFM	Gaussian Derivative Filtered Mode
HS	Heart Sound
HR	Heart Rate
HRV	Heart Rate Variability
HRE	Heart Rate Envelope
HF	High Frequnecy

HPF	High Pass Filter
HC	Heart Cycle
IM	Isovolumic Moment
IC	Isotonic Contraction
IA	IM or IC Amplitude
IVCT	Isovolumetric Contraction Time
IVRT	Isovolumetric Relaxation Time
kNN	K-Nearest Neighbour
K	Kurtosis
LVET	Left Ventricular Ejection Time
LDV	Laser Doppler Vibrometry
LF	Low Frequency
LPF	Low Pass Filter
LDV	Laser Doppler Vibrometry
LBNP	Lower Body Negative Pressure
LDA	Linear Discriminant Analysis
LBDB	Long Breathing Database
MEMS	Micro-Electro-Mechanical Systems
MRI	Magnetic Resonance Imaging
MPI	Myocardial Performance Index
MO	Mitral Valve Opening
MC	Mitral Valve Closure
meanNN	Mean of all NN intervals
meanHR	Mean of Heart Rates
MVMD	Modified Variational Mode Decomposition
MCF	Multiscale Central Frequency
MRWE	Maximum Relative Wavelet Energy
MOS	Mean Opinion Score
MSA	Maximum Spectral Amplitude
NCC	Normalized Cross Correlation

NLMS	Normalized Least Mean Square
NN	Interval between two consecutive heartbeats
NN50	Count of successive NN intervals that differ by more than 50 ms
NZCP	Negative Zero Crossing Points
NBDB	Normal Breathing Database
NBayes	Naive Bayes
OPAMP	Operational Amplifier
OSP	Orthogonal Subspace Projection
PPG	Photoplethysmogram
PCG	Phonocardiogram
PEP	Pre-ejection Period
PTT	Pulse Transit Time
pNN50	Percentage of successive NN intervals that differ by more than 50 ms
pLF	Low Frequency Power (in HRV measurement)
pHF	High Frequency Power (in HRV measurement)
PCB	Printed Circuit Board
PZCP	Positive Zero Crossing Points
+P	Positive Predictivity
pAC	Post AC-point
Pr	Precision
Poly	Polynomial
QDA	Quadratic Discriminant Analysis
RF	Rapid Filling
RE	Rapid Ejection
RR	Interval between two consecutive R-peaks in ECG
RMSSD	Root Mean Square of the Successive Differences
RSDMK	Relative Squared Dominant Multiscale Kurtosis
RGE	Relative GDFM Energy
ROC	Receiver Operating Characteristic
RBF	Radial Basis Function

SCG	Seismocardiogram
SVM	Support Vector Machine
SA	Sino-atrial
SDNN	Standard deviation of all NN intervals
SDSD	Standard Deviation of Successive Differences (in HRV measurement)
SEE	Shannon energy
SE	Shannon entropy
Se	Sensitivity
SNR	Signal to Noise Ratio
Sp	Specificity
SBDB	Stopped (or Hold) Breathing Database
SAE	Stacked Autoencoder
TRI	Triangular Index (in HRV measurement)
TINN	Triangular Interpolation of NN Intervals
TP	True Positive
TN	True Negative
TPR	True Positive Rate
TNR	True Negative Rate
VMD	Variational Mode Decomposition
WT	Wavelet Transform
WBAN	Wireless Body Area Network

1

Introduction

Contents

1. Introduction

Improvement in early diagnosis, surveillance, and clinical intervention of cardiac ailments would help in reducing mortality-rate worldwide [1]. Current screening tools for assessment of cardiac-health include electrocardiography (ECG), phonocardiography (PCG), magnetic resonance imaging (MRI), echocardiography (ECHO), and computerized tomography (CT) scanning. Though ECG is considered as a standard diagnostic tool [2], there are few cardiovascular diseases such as structural defects in cardiac valves, which are so difficult to detect using ECG. These abnormalities do not affect the electrical conduction of myocardium, but these are manifested in vibration and acoustic signals produced by cardiac mechanics [3]. In acoustic-based diagnosis, auscultation of the heart sounds (HSs) is commonly used in clinical practice for identifying heart activities [4]. Due to having limited utility, manual auscultation or palpation cannot provide substantial cardiac information. In the palpation test, the cardiac pulsations, which are transmitted to the chest-surface, are perceived qualitatively via tactile sensing. Additionally, even a computer-aided analysis of these HSs are limited to provide valves' closing instants only. As a cardiac-induced chest wall vibrations, seismocardiogram (SCG) has an ability to identify clinical information like closing and opening instants of valves, rapid blood filling, and ejection through heart chambers, and so on [5]. Also, the recording process of the SCG is somewhat simpler and user-friendly than the other cardiac signal acquisition methods. Recent cardiovascular studies suggest seismocardiography as an emerging, popular, accessible, and effective tool for cardiac analysis and disease diagnostics in wearable healthcare [4,6]. Precise estimation of fiducial points of an SCG signal is a challenging research problem for its clinical usage. This dissertation centers around the delineation, analysis, and investigation of SCG signals.

The rest of this chapter is organized as follows. The first section 1.1 provides a brief description of SCG, its fiducial points, and the recording procedure of the signal. Section 1.2 presents the physiological aspects of the genesis of SCG morphology alongside with ECG. The challenges in the interpretation of the SCG waveform are presented in Section 1.3. Section 1.4 gives a brief idea to the delineation of the SCG signal and its applications. It also covers the literature surveys on progressive historical works for establishing the SCG and its delineation. Section 1.5 presents the motivation followed by the work-plan of the thesis. Finally, the organization of the thesis is presented via graphical-abstract in Section 1.6.

1.1 Seismocardiographic Signal

Seismocardiography is a non-invasive technique to measure precordial vibrations on the chest surface [5]. These vibrations are induced by cardiac movements and changes in blood-momentum in every cardiac cycle. A cardiac cycle consists of a systole and a diastole, and the SCG has the capability to reflect these cardiac mechanical activities [6]. Peaks and troughs of an SCG cycle represent the cardiovascular events, which are called fiducial points. Figure 1.1 shows an SCG signal with its temporal characteristics. The change in volume, pressure, and shape of the heart during different stages of the cardiac cycle produces vibrations on the ribs and tissues near the heart, and due to these variations, pulsations in the chest are generated. The first medical use of SCG was tried by Salerno and Zanetti [7], whereas Crow annotated it with the help of echocardiography (Doppler ultrasound imaging of the heart) in the early 1990s [8]. The SCG has the potential to be the best diagnostic tool for accurate and continuous heart monitoring for wearable healthcare systems.

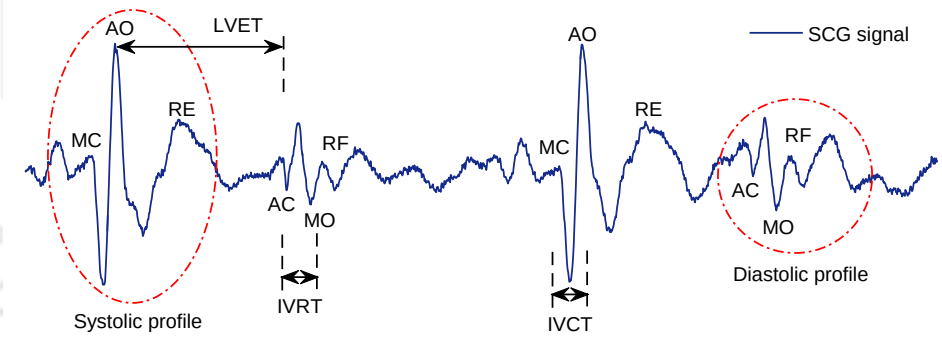

Figure 1.1: SCG signal with its fiducial points and time-intervals.

The SCG signal has a dynamic amplitude range, representing 5–10 mg (milli-gravity, g = 9.81 m/s^2) peak to peak typically [9] and extends up to 20–50 mg in the presence of motion artifacts. The frequency range of SCG ranges from 0.5 to 40 Hz, but its maximum energy lies in the infrasonic range ($\leq$30 Hz) [10]. Since the annotation for the SCG waveform has not been standardized yet, researchers try to annotate the SCG characteristic/fiducial points through mapping with other cardiovascular signals, such as echocardiogram, ECG, heart sound, and arterial blood pressure [11]. The characteristic points of SCG waveform and time intervals between them have clinical importance. Cardiac intervals, such as pre-ejection period (PEP), left ventricular ejection time (LVET), isovolumetric contraction time (IVCT), and isovolumetric relaxation time (IVRT) play vital roles in quantifying

Table 1.1: Fiducial points of SCG

MC	Mitral valve closure
IM	Isovolumic moment
AO	Aortic valve opening
IC	Isotonic contraction
RE	Rapid ejection
AC	Aortic valve closure
MO	Mitral valve opening
RF	Rapid filling

Table 1.2: Systolic and diastolic interval parameters

PEP	Pre-ejection period	Q – AO
LVET	Left ventricular ejection time	AO – AC
IVCT	Isovolumetric contraction time	MC – AO
IVRT	Isovolumetric relaxation time	AC – MO
EMD	Electromechanical delay (QS1)	Q – MC
EMS	Electromechanical systole (QS2)	Q – AC

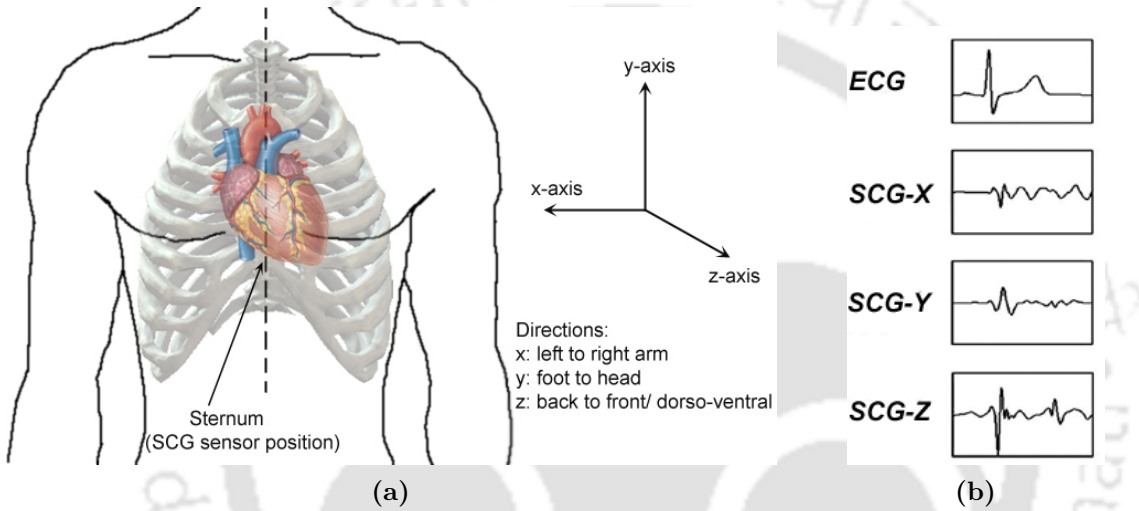

Figure 1.2: Recording of an SCG signal. (a) typical sensor location for recording, and (b) typical waveforms of 3-D SCG cycle along with concurrent ECG.

heart-fitness. These clinical parameters are listed in Tables 1.1 and 1.2, also shown in Figures 1.1 and 1.4. Other parameters in the form of interval-ratios such as PEP/LVET, myocardial performance index (MPI), and LVET/RR are also clinically important [12, 13], where MPI is defined as [12]: MPI = (IVCT+IVRT)/LVET. Thus, estimation of the SCG fiducial points is an important task.

Acquisition of SCG signals

This vibrational signal can be non-invasively acquired by placing a tri-axial accelerometer sensor on the precordial areas of the chest, generally at the lower end of the sternum on the xiphoid process [6]. In current scenarios, typically, the SCG is recorded from miniaturized accelerometers based on micro-electro-mechanical systems (MEMS) technology. By using a tri-axial accelerometer, the SCG components can be observed in all three orthogonal axes. An example of three dimensional (3-D) SCG for one cardiac cycle is illustrated in Figure 1.2(b). The orientation of acceleration axes are

described as follows: x = lateral component [left–right], y = longitudinal component [foot–head], and z = sagittal [dorso–ventral]; also shown in Figure 1.2(a). In most of the studies, the dorsoventral component of acceleration is focused because of its amplitude variations for corresponding heart events. The variations are more significant as compared to the other two axes.

1.2 Physiology behind Genesis of SCG Signal

The heart has two different pumps separated by a septum. Each of these pumps comprises two chambers– atrium and ventricle, as shown in Figure 1.3. Atrio-ventricular and semi-lunar valves again separate these chambers. Different phases of a cardiac cycle can be identified with the help of an SCG signal, and these instances/phases are mitral valve opening (MO), mitral valve closure (MC), aortic valve opening (AO), aortic valve closure (AC), isovolumic contraction time (IVCT), isovolumic relaxation time (IVRT), rapid filling (RF) and rapid ejection (RE) of blood through ventricles. In Figure 1.4, a typical SCG signal is shown for two cardiac cycles along with simultaneously recorded ECG. The mitral valve is closed when the blood completely enters from the left atrium to the left ventricle. As a result, the MC notch point is seen as a sudden positive deflection in the SCG signal. At this moment, electric impulse depolarizes Purkinje fibers, which results in major ventricular depolarization (R-wave in ECG) in the electro bio-potential measurement. Then, ventricles start contracting, which causes sharp inward wall motion, and decreases acceleration waves. It is the cause of the generation of the IM valley point. In the electrical conduction system, this indicates complete depolarization of

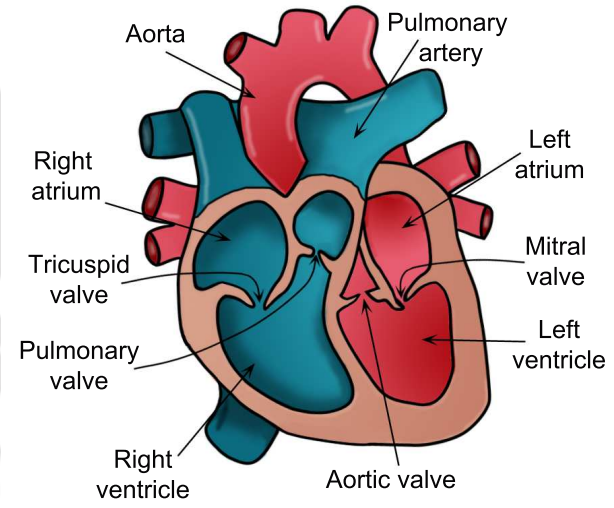

Figure 1.3: Physiological structure of the human heart

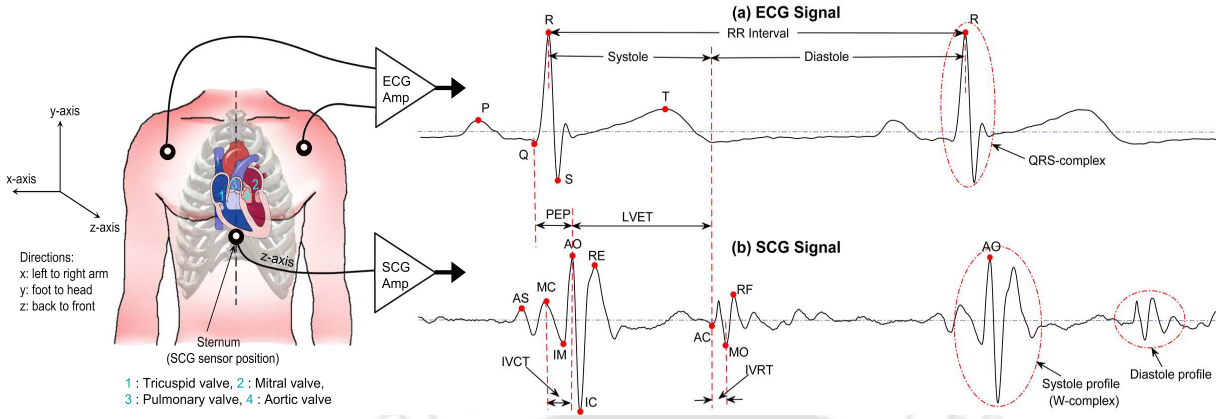

Figure 1.4: Simultaneous ECG and SCG recordings from CEBS database with annotations suggested by Crow *et al.*. **AS** : Atrial systole; **MC** : Mitral valve closure; **IM** : Isovolumic moment; **AO** : Aortic valve opening; **IC** : Isotonic contraction; **RE** : Rapid ejection; **AC** : Aortic valve closure; **MO** : Mitral valve opening; **RF** : Rapid filling; **PEP** : Pre-ejection period; **LVET** : Left ventricular ejection time; **IVCT** : Isovolumetric contraction time; **IVRT** : Isovolumetric relaxation time.

Purkinje fibers and basal depolarization of ventricles (S-wave in ECG). As enough pressure builds up, the apex moves inward, and the walls are swelled, so overall acceleration increases. This generates the AO peak point. By this time, the basal depolarization is completed. After the AO peak, a rapid twisting and inward wall motion decrease the acceleration due to the opening of the aortic valve. When the acceleration of inward wall motion stops, it gives the IC valley point. The higher pressure in the ventricle drastically increases the acceleration of blood in the aorta, which results in the RE peak point. In electrical conduction, an isoelectric line is traced corresponding to this condition. Then, the repolarization of the ventricle starts, which creates the onset of T-wave. As soon as the aortic valve closes, a slight rebound of heart acceleration gives the AC point. In ECG, the ventricular repolarization stops and produces offset of T-wave. Furthermore, atrial pressure increases when blood enters into the atrium. It causes a rise in the acceleration followed by a sudden fall in the acceleration due to the atrial myocardium contraction in the next phase. This action generates an isoelectric line. As soon as the mitral valve opens, the atrium volume decreases, that causes the generation of MO valley point. After a certain interval of time, the ventricle starts filling with blood, and the heart walls move outward, which augments the acceleration and produces the RF peak point. After some moments, the electric impulse travels from the SA node to the AV node for atrial depolarization. It produces P-wave. In this way, an SCG cycle is generated [8].

1.3 Parameters Affecting Signal Morphology

The relatively low amplitudes are observed in SCG vibrations, which can be easily corrupted by large vibrations, respiration noise and motion artifacts, including body movements and muscle-related disease [5,11]. The SCG signals corrupted with some of these noise sources are depicted in Figure 1.5. Proper interpretation of SCG signal features becomes difficult with the presence of these factors. Other factors such as heart rhythm, cardiac contractility (the intrinsic ability of cardiac muscles to contract), postural positions, blood viscosity, valvular function, and stiffness of blood vessels also affect the waveform morphology of the signal [4, 14]. SCG signal is susceptible to inter-subject variabilities such as age, gender, body mass index, and physical health conditions [14]. There are some difficulties and open issues regarding the SCG signal and its sensing, which needs to be taken into account before handling this signal.

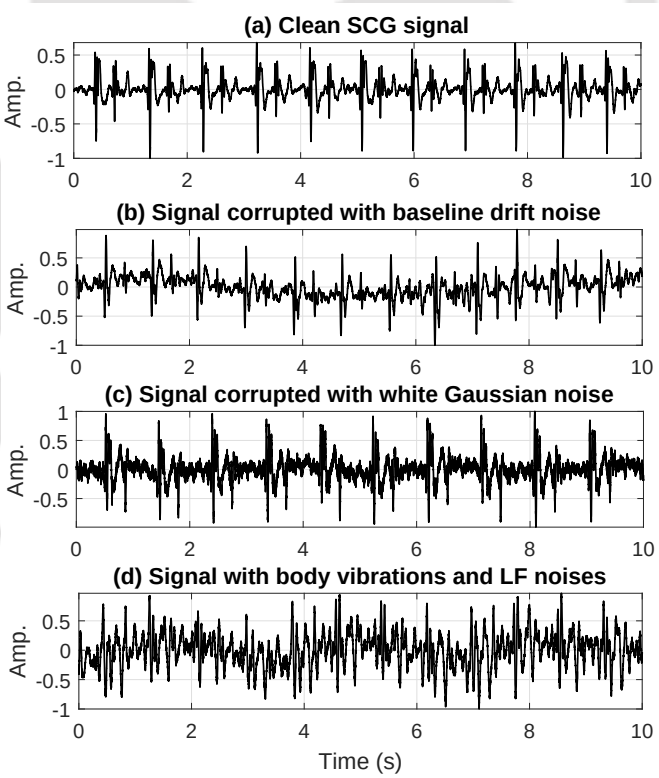

Figure 1.5: Different types of noises degrading the SCG signal quality. (a) A clean SCG signal, (b) Effect of respiratory baseline drift, (c) Effect of AWGN noise, and (d) Signal corrupted with body vibrations and LF artifacts.

Challenges from the signal point of view:

- Standardization is one of the biggest challenges in the SCG measurement [5]. Widely accepted annotation of fiducial points and their clinical relevance needs to be standardized universally analogous to P-QRS-T labeling in ECG [4].
- Selection of optimal axis for SCG measurement is a difficult task. The most accepted axis given in literature is the back to the front (dorsoventral) direction. The explorations of 3-D SCG in spatial distributions needs further investigation.
- The definition and standardization of the frequency range of SCG is required. In some existing literature, SCG is categorized as vibrations in the infrasonic range ($\leq$25 Hz) [15]. On the other side, some researchers indicate that some higher frequency components till 1000 Hz are present in SCG [16].

Challenges from sensing point of view:

- Accelerometer is more sensitive to motion artifact noise [2]. The investigation related to the effect of the sensor contact area is a challenging task to improve sensing mechanisms.
- Friction noise alters the vibrations. It arises from friction between the sensor and the skin or between sensor and clothes.

Additionally, the SCG signal gets affected with different respiratory phases (inhale and exhale), changes in lung-volume, subject postural position and motion, exercise and its recovery period, and change in measurement locations [4]. Respiration changes the lung volume and intrathoracic pressure, and hence the morphological variability of the SCG may be seen [4]. The body postures, such as sitting, standing, speaking, walking, and supine positions, during the SCG data acquisition usually affect the signal morphology [5, 6, 17]. Exercise augments the overall amplitude and power of the SCG signal, which is associated with the increased cardiac output, heart rate, and stroke volume. An increment in heart rate and contractility during exercise, decreases the LVET and PEP cardiac intervals. The variations in LVET and PEP can be detectable by SCG signal [6, 18]. The sensitivity of the sensor towards its placement on the chest locations is another unavoidable factor. Various anatomical locations on the chest surface, such as the sternum, the clavicle, and different intercostal spaces, have been taken into account when analyzing SCG signals [6, 16, 19]. Recently, a research

work [19] studied the morphological differences in SCG at the common valvular auscultation sites (aortic, pulmonary, tricuspid, and mitral). However, systematic and intensive examinations of these effects are lacking.

1.4 SCG, its Delineation and Applications - A Review

The fiducial points of the SCG cycle, such as AO, MC, IM, IC, RE, AC, MO, and RF, are essential cardiac phases corresponding to different mechanical activities of the heart. Their attributes such as amplitude, frequency, and temporal information in the SCG waveform and time intervals between them, have diagnostic abilities for cardiac health assessment [20]. The Delineation of SCG waveform refers to the determination of these fiducial points' attributes and the estimation of time intervals between the fiducial points, which are clinically significant for pathological interpretations of a cardiovascular system [21]. The delineation of an SCG signal helps in the evaluation of various cardiovascular parameters, such as heart rate variability (HRV) analysis, hemodynamic parameter estimation, and diagnosis of cardiovascular diseases. The delineation can also improve the ability of wearable SCG sensor nodes in the development of pervasive wireless body area networks [6]. Recent studies suggest its applications for assessing left-ventricular functions [22,23], heart- and respiration-rates [4,14], blood flow in coronary artery during angioplasty [7,22,23], valvular activities, and ventricular filling and ejection during ischemia [22]. A few applications of the SCG signal reported in the literature, are given as follows:

- Heartbeat detection and heart rate variability estimation [24–32]
- Detection of valvular defects [20]
- Mapping with other cardiovascular signals such as ECG, photoplethysmogram (PPG), phonocardiogram (PCG) and echocardiogram, and extracting their clinical information [9,33–36]
- Clinical diagnosis of cardiac pathological conditions such as coronary artery disease, atrial fibrillation, atrial flutter, and haemorrhage [7,22,37–40]
- Identification of respiratory phases: inhalation and exhalation [41,42]
- Estimation of hemodynamic parameters such as systolic and diastolic blood pressure, stroke volume, and cardiac output [43,44]. The volume of blood ejected from left ventricular in each

heart cycle is known as stroke volume, and cardiac output provides an estimate of blood volume ejected from the heart in a one-minute duration.

- Development of smart-garment based wearable healthcare system with integration of miniaturized MEMS accelerometer [6, 16, 45–50]

Foundation works on seismocardiography

In this section, we review the initial state-of-the-art works, that establish the SCG signal. The early usage of SCG in cardiac clinics faced barriers such as the large size of sensor-instrumentation, improper understanding of signal profiles, and inter- and intra-subjects' variabilities. However, these issues are well-addressed by the recent advances in signal processing tools and sensor technologies. The foundation research works in this field are discussed in chronological order below—

- The terminology of seismocardiography is inspired by seismology-based technology, where researchers study earthquakes and elastic wave propagation.

- In the early 1960s, Russian researchers R. Baevski and Bozhenko used the word seismocardiogram for the first time. They borrowed technology from seismology and recorded acceleration from heart activities [51], [52]. Unlike high accurate modern MEMS accelerometers, the Bozhenko's group measured signal by placing a magnetic-spring oscillator as an accelerometer on the chest wall. It generates current from induction coils due to acceleration. His group managed to monitor ECG and SCG simultaneously and analyzed them. Baevski's group tried to measure the heart vibrations by the same procedure as seismologists measure underground vibrations induced by earthquakes. Although using a different method, their signal quality was as well as what the Bozhenko's group had.

- At the initial stage, the SCG signal was used in the Russian aerospace-program [11]. Russian researchers applied this technology as a health monitoring procedure for their aerospace program. The first experimental test on a dog was done on the Sputnik-3. After that, the first SCG had also been measured during space flight in astronauts on Vostok 5 in 1963 [11].

- SCG was used for subject-health assessment onboard the *Sojus* spacecraft in the early 1970s [11]. Later, it was considered as part of their space experiments in the International Space Station (ISS) [53].

- The use of SCG in the clinical and commercial application was relatively slow. About twenty years later, Salerno and Zanetti did the first medical use of SCG in 1991, and it was commercialized by a company, *SeisMed Instruments, USA* [54].

- Through the year 1991 to 1994, various experiments were performed in medical fields using this SCG and other cardiovascular measuring techniques [7,8]. Simultaneous SCG and ECHO recordings were adequately analyzed, and a waveform nomenclature was developed for cardiovascular events. The SCG shows quantitative variations associated with blood-flow obstruction in the coronary artery during balloon angioplasty [7]. The experiments signified that SCG was more sensitive and carried more detailed information compared to ECG for the detection of coronary artery disease during exercise stress testing [38]. Also, it was demonstrated that the combined ECG and SCG could produce sensitivity and specificity comparable to radionuclide and ECHO recording schemes [11]. Later, the magnetic-field-compatibility of the SCG signal was shown by recording the SCG signal during MRI imaging [36].

- Due to the fact of a too heavy and bulky sensor to be placed on the sternum for a long time-period, SCG used in the early 1990s was not quite a success. Their study had provided significant experimental results in this field of research that provide the potential to reinvestigate this signal for researchers, when sensor and signal processing techniques are more developed and ready to be applied in SCG measurement.

- Due to the fast development of small-sized, low cost, low power, less noisy, and highly sensitive MEMS accelerometers, researchers can now record the heart induced vibrations with better accuracy and feasibility. A better quality SCG signal is possible with advanced signal acquisition and processing technology. It brings a new future for continuous monitoring of SCG to be applied in the clinical perspective and even in day-to-day healthcare.

- Also, new state-of-the-art modern sensor technologies provide portable, wearable, and wireless sensors that can be integrated and worn with clothes to acquire SCG signals during physical activities. In 2007, a smart garment based wearable healthcare system was introduced with an external tri-axial MEMS accelerometer for the recording of SCG signals alongside ECG and respiratory signals [16]. However, this textile-based smart garment was proposed earlier in 2005 for assessing cardiorespiratory system and subject-movement [55]. This idea was later improved

by Rienzo *et al.* [6], [47], [49]. They integrated a 3-axis MEMS accelerometer into electronics with textile ECG electrodes and a textile piezoresistive plethysmograph, and made a smart vest called *MagIC-SCG*. Using wearable-SCG, a wrist-watch was developed in 2017 to estimate blood pressure, called *SeismoWatch* [56]. It consists of an optical sensor alongside an accelerometer, which estimates the blood pressure by sensing the micro-vibrations traveling from the heart to the wrist when the SeismoWatch is attached to the sternum. The wearable SCG sensor-nodes were still based on either non-elastic piezoelectric membranes or rigid accelerometers. In 2019, an ultra-thin and stretchable electronic tattoo (e-tattoo) based sensor was introduced for simultaneous recording of ECG and SCG signals [57]. E-tattoo was integrated with the soft SCG sensor and a pair of soft gold ECG electrodes. It was named as soft electro-mechano-acoustic cardiovascular (EMAC) sensing tattoo, which was demonstrated to extract many cardiac time intervals. In early 2020, another system consisting of a wireless network of 12 sensor nodes called *SeisMote*, was designed for cardiac monitoring in daily life, telemedicine, and laboratory [58]. It can record ECG, PPG, and linear and rotational accelerations from various body areas. The linear and rotational chest-wall accelerations are known as SCG and gyrocardiogram (GCG) signals, respectively. These wearable devices are also summarized in Table 1.3.

Table 1.3: Summary of developed wearable devices for SCG signal acquisition. Abbreviations used in the table: 3D Accl—three orthogonal dimensional accelerometer; Resp.—respiratory signal; GCG—gyrocardiogram; #—number of; Lin—linear; Rot—rotational.

Reference	Wearable device	Accelerometer sensor			Recorded signals
		Type	# axes	Location	
2007 [16]	MagIC + 3D Accl	Lin	Triaxial	Left clavicle	SCG, ECG, Resp.
2011 [6, 47, 49]	MagIC-SCG	Lin	Triaxial	Sternum	SCG, ECG, Resp.
2017 [56]	SeismoWatch	Lin	Uniaxial	Sternum	SCG and PPG
2019 [57]	EMAC e-tattoo	Lin	Uniaxial	Precordial areas	SCG and ECG
2020 [58]	SeisMote	Lin, Rot	Triaxial	Lower sternum, right intercostal space, heart apex	SCG, ECG, GCG, PPG

- Recently, with standard signal sensing and processing technology, the acquisition of high-quality SCG signal becomes possible. In order to re-investigate the utility and feasibility of SCG for real-life cardiac health monitoring, a new dimension of research is emerging.

Existing sensing mechanisms

Recent advances in sensor technology are able to fabricate a miniatuatized and lightweight accelerometer, which facilitates an improved quality of SCG signal acquisition. We review different methods of SCG sensing mechanisms, which were used in the recent studies. These sensing methods are given as follows [4]:

- 1-D/3-D axis based piezoelectric accelerometers,
- 1-D/3-D axis based MEMS accelerometers,
- 3-D axial gyroscopes,
- Smartphone accelerometers and gyroscopes,
- Microwave Doppler radars,
- Airborne ultrasound surface motion camera (AUSMC).

The SCG signals might have one, two, or three axial and rotational components, which depend on the used sensor for signal acquisition. For instance, a uniaxial type accelerometer is usually used to acquire the dorso-ventral SCG component. However, combined triaxial-accelerometer and triaxial-gyroscope can extract information of heart-induced motion in three orthogonal axial and rotational directions. The SCG sensors are usually mounted on the sternum or its left-side lower border. However, many methods were used other chest locations also for SCG signal recording, including left clavicle, over the heart apex, and upside right sternal border [4]. The information of sensor-types, models, and their placements is summarized in Table 1.4.

The attachment of adhesive electrodes or sensors is not feasible for the recording of ECG or SCG signals in some applications, such as extremely infectious patients, burn patients, and premature babies. Thus, development of contactless and efficient SCG acquisition schemes are under investigation. An SCG measured through these techniques might also minimize skin coupling artifacts, which are more likely to be present in the SCG signals recorded using contact sensors placed on the body. The contactless methods include microwave Doppler radar, laser Doppler vibrometry (LDV), and airborne ultrasound imaging [4]. But, these approaches have limitations of their sensor cost and size.

Piezoelectric and MEMS based sensors are lighter and smaller sized than non-contact sensors. Thus, these kind of sensors may be utilized in clinical settings for day-to-day and continuous monitoring of subjects.

Table 1.4: Summary of existing accelerometer sensors used for the recording of SCG signals. Abbreviations used in the table: 1D—uniaxial; 2D—biaxial; 3D—triaxial; Accl—accelerometer; MEMS—micro electromechanical systems; SPh—smart phone; Gyro—gyroscope; ARS—angular rate sensor.

Reference	Sensor type	Sensor model	Sensor location
[59, 60]	1D-Accl	4381, Brüel & Kjær 393C, PCB Piezotronics	Above xiphoid
[61, 62]		DS1104, DSPACE	Xiphoid process
[19, 63]		LIS331DLH, STMicroelectronics	Mitral valve, tricuspid valve, aortic valve, pulmonary valve
[64]		N/A	Sternum
[65]	1D-MEMS-Accl	SCA620, Murata Electronic	Sternum–anterior chest
[66]	3D-Accl 1D-Accl	CXL01LF3, Crossbow Technology 7290-A, Endevco Microtron	Manubrium Xiphoid
[40, 67, 68]	3D-Accl	SCA610-C21H1A, Murata Electronic	1 cm above xiphoid
[69]		ViSi Mobile, Sotera Wireless	Chest wall
[70]		ADXL 335, Analog Devices	Chest wall
[71, 72]		356A32, PCB Piezotronics	Left sternal border along the 4th intercostal space
[73]		X6-2mini, GCDC	Left sternal border along the 4th intercostal space
[74]		356A32, PCB Piezotronics	Sternum, upper and lower sternum
[15, 17, 75]		BMA280, Bosch Sensortec GmbH	Mid-sternum
[76]		ADXL 354, Analog Devices	Mid-sternum, upper sternum, lower sternum Point of max impulse, below left clavicle, below right clavicle
[77]	3D-SPh-Accl	iPhone6, Apple	Midclavicular line and 4th intercostal space Belly above navel
[78, 79]		Xperia Z-series, Sony	Chest
[80, 81]	3D-MEMS-Accl	MMA 7361, Freescale Semiconductor	Heart apex
[82]		MMA 7361, Freescale Semiconductor	Above xiphoid
[83]		Analog Devices	2 cm above xiphoid
[84–86]		KXRB5-2042, Kionix MPU9150, Invensense	Left sternal border along the 3rd rib
[14, 87, 88]		MMA8451Q, Freescale Semiconductor	Sternum
[89]		MMA 7361, Freescale Semiconductor	Left sternal border along the 3rd rib
[90]		MMA8451Q, Freescale Semiconductor	Sternum, aortic valve, heart apex
[85]		TSD109C, Biopac Systems	Left sternal border along the 3rd rib

Continued on next page

Table 1.4 – *Continued from previous page*

Reference	Sensor type	Sensor model	Sensor location
[91]	3D-MEMS-Accl	LIS344ALH, STMicroelectronics	Heart apex
	2D-MEMS-Gyro	LPY403AL, STMicroelectronics	Lower back of subject between 2nd and 3rd lumbar vertebrae
[12]	3D-MEMS-Accl	MMA8451Q, Freescale Semiconductor	N/A
	3D-Gyro	L3GD20, STMicroelectronics	
[92]	3D-MEMS-Accl	SparkFun, Intel Edison	Sensor clipped on subjects clothes
	3D-MEMS-Gyro		
[93, 94]	Microwave Doppler radar	–	–
[95]	Laser Doppler vibrometer	PDV-100, Polytec	–
[96]	3D-MEMS-Accl	MMA8451Q, Freescale Semiconductor	Sternum
	3D-MEMS-ARS	MAX21000, Maxim Integrated	
[97]	AUSMC	Composed of the following sensors: - MA40S4S, Murata Electronics - FG-23629 Knowles microphone	30×40 cm^2 thoracic and abdominal surface

Existing SCG denoising approaches

The SCG signals are usually contaminated with noises from various sources, which include motion artifacts, friction noise, environmental vibrations, and sensor electro-mechanics. They lead to the wrong signal interpretation. Hence, the SCG denoising is considered as a preprocessing step. The denoising approaches can be categorized into two classes: (i) sensor-based, and (ii) signal processing-based. Under the sensor-based denoising category, a dual-sensor approach is suggested [98]. In this approach, the signals are acquired from posterior and anterior chest-surface. Then, a normalized least mean square (NLMS) filter is employed to remove the motion artifact from SCG signals. The use of multiple sensors, however, increases the system-complexity. The signal processing-based denoising

Table 1.5: Existing noise removal approaches used for SCG denoising.

Method	Technique	Application
[17, 40, 59–64, 69, 73–77, 83–86, 99–102]	Low-pass, High-pass, Band-pass, Notch filtering	Baseline drift, respiration and body-movement artifact removal
[6, 103]	Adaptive filtering	Motion artifact suppression
[104]	Averaging theory	Motion artifact suppression
[93]	Comb filtering	Removing breathing noise from radar signal
[17, 103, 105]	Empirical mode decomposition	Baseline drift, respiration and body movement artifact removal
[106]	Independent component analysis	Motion artifact suppression
[107]	Median filtering	–
[103]	Morphological filtering	–
[9]	Polynomial smoothing	Motion artifact suppression
[9, 92]	Savitzky-Golay filtering	Motion artifact suppression
[70, 103]	Wavelet denoising	Segmentation of HSs and SCG
[105]	Wiener filtering	–
[108]	Two-stage Kalman filtering	SCG artifacts

methods apply conventional band-pass filter [40,60,61,73,74,76,84,86], empirical mode decomposition (EMD) [17], ensemble empirical mode decomposition (EEMD) [105], Kalman filter [108], fuzzy neural network [109], NLMS based adaptive filter [89], median filter, and Savitzky-Golay filter [9] to remove

baseline drifts, body vibrations, and respiratory artifacts from SCG signals. The noise removal techniques used for SCG filtration are summarized in Table 1.5. However, more investigation is required in clinical and ambulatory settings.

Existing SCG delineation methods

This section presents the previous works on SCG delineation reported in the literature. The state-of-the-art techniques reported up to 2016 in this area have been well-reviewed in [5, 11]. Analyzing the SCG on its time-frequency distribution can provide more details about signal characteristics. However, existing delineation works mostly focused on either the time-domain or the frequency-domain approaches. There are many approaches, which prefer to detect the AO point before attempting to estimate other fiducial points. Because usually, it creates the largest peak in an SCG cycle. Extensive investigations were carried out for annotation of AO-phase in [10, 24, 28, 29, 60, 61, 110]. Most of these studies employed the ECG signal as a reference for finding out cardiac events from an SCG signal [24,61]. However, Some of existing approaches suggested algorithms to detect IM and IC points simultaneously [10,84,86]. While, [29] and [60] have developed approaches for estimating three various fiducial points, IM, AO, and IC. In some cases, gyroscopic recordings of the chest wall are also utilized to annotate SCG signals [84, 86].

Delineation helps in estimating cardiac time intervals, such as pulse transit time (PTT), LVET, PEP, IVCT, systolic, and diastolic time. To compute these, many delineation algorithms were developed with different performance levels, which were studied on both healthy individuals and cardiac patients [60, 111]. The electro-mechanical window (EMw) is characterized as the delay between the electrical systole and the mechanical systole. EMw is one of the important diagnostic markers for many cardiovascular diseases. Usually, ECG and heart sound signals are used to find EMw. However, SCG is suggested by Jain *et al.* as an alternate to HS for estimation of the EMw [82].

F. K.-Khavar *et al.* proposed a standalone delineation method for the SCG waveform [29]. The work is mainly focused on the determination of fiducial points such as IM, AO, and AC without using a reference ECG signal. The method consists derivation of multiple envelopes namely heart-rate envelope (HRE), AO and AC envelopes by using high pass filtering, absolute signal construction, and triple integration with optimal parameters (such as window-size and percentage of casualty index (PCI)). Finally, it detects the envelope-peaks of HR, AO, and AC, which are denoted by PHRE, PAOE, and PACE, respectively. By utilizing the extracted envelopes, the method locates the regions of the

SCG signal with IM, AO, and AC points. Although the exact peaks of these fiducial points cannot be located, the peak-locations can be determined within a time-window of 30 ms from PHRE, PAOE, and PACE locations. The SCG signals were measured with NI9205 in a supine position and lower body negative pressure (LBNP) condition. The LBNP dataset was collected from 18 subjects, one-hour data for each subject. In LBNP, the body's lower portion is placed in a seal packed chamber in which pressure is continuously lowered to -50 mmHg The method achieves timing differences of 9±8 ms, 9±9 ms and 6±9 ms for IM, AO, and AC, respectively. However, envelope construction is not found suitable for SCG signal having severe inter- and intra-beat variabilities. Determining the optimal peak of an envelope is itself a crucial task. Moreover, the window size is empirically selected for the integration task. In [28], H. Nguyen *et al.* proposed a new method to extract heartbeat waveform from the SCG time series for wearable devices. The method consists of the following steps: denoising by time-averaging, timing detection by maximum-likelihood (ML) estimator, generalized likelihood ratio (GLR) and thresholding. The method has been tested using measured SCG data in the z-direction with a sampling frequency of 200 samples/sec. Although the method gives a good estimate of the SCG waveform, it does not guarantee that the estimate is free from noises. Additionally, the selection of an empirical threshold for estimation is crucial. In this sequence, a methodology was presented by M. J. Tadi *et al.* for HRV estimation using SCG with the consideration of reference signal ECG [24]. Kubios HRV software is utilized to assess the HRV indices in the time and frequency domain. At first R-peaks in ECG are detected using well known Pan-Tompkins (PT) algorithm. After that, AO-peaks in the SCG are detected in two ways (i) PT algorithm, and (ii) ECG-SCG windowing technique. The windowing technique for AO-peak detection includes the following steps:

- Performing bandpass filtering for the frequency range of 4-50 Hz,
- Smoothing by moving average filter (10-20 ms),
- AO-peak detection in SCG using a search window of duration 90 ms from R-peak as a reference of the corresponding cycle.

Then, HRV parameters from time-domain analysis such as SDNN, NN50, RMSSD, TINN, and from frequency-domain analysis, such as pLF, pHF, LF/HF, are computed. The method has been validated using SCG data collected from 20 healthy young volunteers, 60 seconds data each. The SCG data has been recorded from a capacitive digital accelerometer (MMA8451Q) with a sampling rate of 800 Hz and 14 bits resolution. The method achieves high linear relationship and agreement (r>0.98) between

the HRV parameters computed from SCG and ECG. The timing error between heart rates obtained from SCG and ECG is 0.03±0.08 ms. The method does not completely rely on SCG recording, also depends on ECG. The selection of window size for the AO-peak search is empirical. For automatic annotation of AC and IM points in the SCG waveform, an algorithm was presented in [10]. The method extracts envelopes from a high-frequency cardiac acceleration (HFACC) signal with different envelope extraction methods such as absolute, Shannon energy, Hilbert, and cardiac sound characteristic wave (CSCW) envelope. These envelopes can be expressed as:

- Absolute envelope: $x_a(n) = |x(n)|$
- Shannon energy envelope: $x_{see}(n) = -|x(n)|^2 \log(|x(n)|^2)$
- Hilbert envelope: $x_h(n) = |\widehat{x}(n)|$; where "$\widehat{\cdot}$" is Hilbert transform operator
- Cardiac sound characteristic wave (CSCW) envelope (η): A vibration model of single degree of freedom is considered as–

$$\ddot{\eta} + 2\xi\rho\dot{\eta} + \rho^2\eta = \bar{S} \tag{1.1}$$

where $x(n)$ is input signal, $\bar{S}$ is amplitude normalized input signal, η, $\dot{\eta}$, $\ddot{\eta}$ denote envelope of $\bar{S}$, first and second derivatives of η, respectively. ρ and ξ denote resonant frequency and damping factor respectively. The method consists of the following steps: envelope extraction from an HFACC signal, its peak detection, selection of SCG processing-window based on detected envelope peaks, and estimation of extrema points. The algorithm of the method is presented by a block diagram, shown in Figure 1.6. The method has been tested on SCG data recorded from 85 subjects. The method achieves a detection

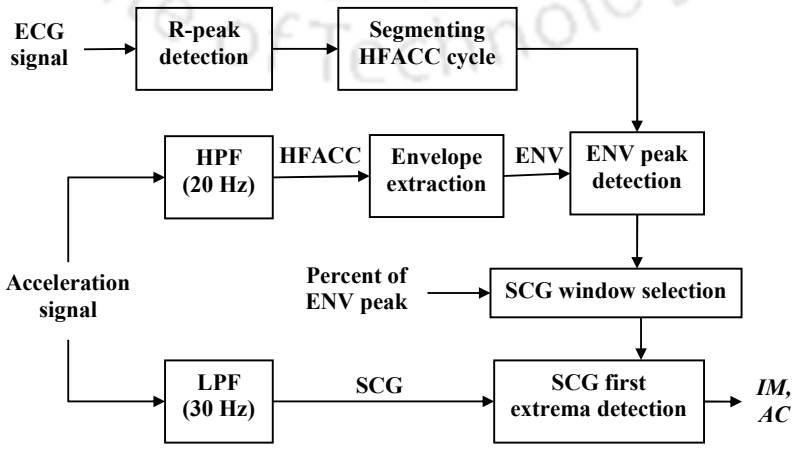

Figure 1.6: Block diagram representation of a previous delineation method, where the percentage of envelope peaks is used to select the SCG search window for IM and AC points.

accuracy of 98.1% for IM and 99% for AC for the private database. The accuracy may reduce when the MC has a greater amplitude than AO, and IM has a small deflection since the method directly depends on the instantaneous amplitude of the waveform. Y. Li *et al.* designed an approach for the segmentation of heartbeat waveform in the SCG using a matched filter [32]. The method consists following operations: extraction of the triangle template $w(m)$ from W-complex (systolic profile of SCG signal) by the means of search window for maxima and minima detection, construction of the FIR coefficients: $h(m) = w(N-m)$, matched filtering: $y(n) = \sum_{m=0}^{N-1} h(m)x(n-m)$ to enhance the W-complexes in SCG, and detection of maximum peaks of W-complexes in filtered signal. The detection of W-complexes is shown in Figure 1.7. Furthermore, differences between AO and R peaks are

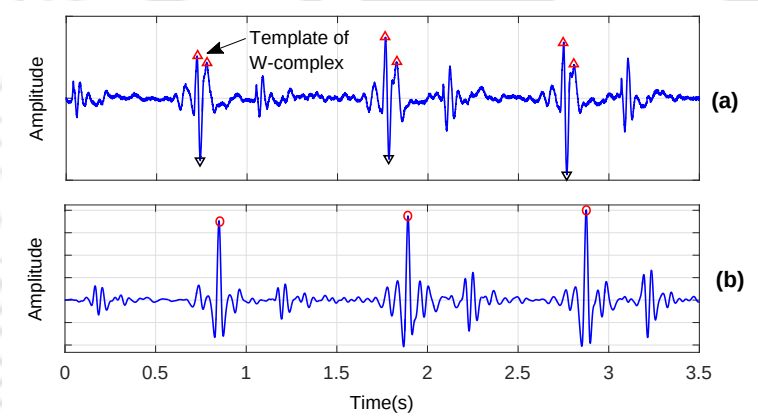

Figure 1.7: Detected W-complexes in matched-filtered signal. (a) Input SCG signal having triangular templates at W-complexes, and (b) matched filtered output with detected W-complex locations.

averaged for 30 heartbeats to predict the locations of upcoming W-complex peaks. The performance of the method is evaluated with the ECG and SCG signals with a sampling rate of 5 kHz from 20 healthy subjects while classical music listening in a supine position. The signals are collected from a publically available database, combined measurement of ECG, breathing, and SCG (CEBS). The method achieves a detection accuracy of 98.74% and a sensitivity of 99.33%. In this method, preprocessing for denoising is not required, but for each cardiac cycle, filter coefficients need to be updated. Otherwise it would fail on abnormal beats. Another algorithm to detect W-complex was presented by Xu *et al.* via multiscale edge detection scheme [112]. The method has been tested using SCG data recorded from 15 healthy subjects (one-minute data from each subject). However, the selection of amplitude threshold and scales are purely empirical in this method. Rienzo *et al.* estimated parameters PEP and LVET using an ECG signal as a reference [6]. The heartbeat waveform is extracted from the SCG using detected ECG R-peaks. Then, PEP and LVET parameters are estimated using extracted

SCG heartbeats, ensemble averaging of five beats, and linear regression scheme. The method has been validated on SCG data collected from six subjects, with a sampling rate of 200 Hz and 12 resolution bits. The beat averaging is not a suitable operation to perform when ectopic beats are present. A delineation algorithm was devised to detect IM, AO, and AC fiducial points of an SCG signal with and without using the reference ECG signal [60]. The method consists of the following operations:

- Computing heart-rate, systolic, and diastolic envelopes using HPF and moving average filtering of different orders,
- Masking the systolic and diastolic profiles,
- Approximating the IM, AO and AC points using extrema detection from search windows,
- Probabilistic decision making.

The method is validated on SCG data recorded from 105 individuals. The algorithm has a good accuracy with the root mean square error of less than 5 ms. In [113], the SCG systole points are annotated using calibration, heartbeat detection, and prototype matching scheme. G. Shafiq *et al.* proposed an algorithm to estimate the systolic time intervals [61]. It contains Butterworth filtering, SCG beat segmentation using ECG R-peaks, ensemble averaging of beats, formulation of initial and sliding heartbeat templates, maxima detection in the initial template as AO point, and localization of search window for AO peak detection in the sliding template using previous beat AO peak information. The method is tested on SCG data with sampling rate of 500 Hz collected from 4 healthy subjects. It achieves the limits of agreement -1.3 to 2.67 ms for AO point detection. Another method was proposed for the detection of IM and AC points using wavelet generation schemes and gap-filling techniques [110]. It employs an approach for heart rate envelope generation and estimates an exact location of IM points. By utilizing the IM locations, the method then yields a less accurate peak estimation of AO and AC points. Although overall performance of this method is good, it has the biggest limitation that the parameters of the algorithm have a high dependency on the subject-characteristics. In [84], the GCG signals, which indicate the rotational component of heart-induced chest wall vibrations, were utilized as a reference for the annotation of SCG signals. A triaxial MEMS accelerometer and a triaxial MEMS gyroscope are integrated in an inertial measurement unit, which is used for the detection of IM and AC fiducial points. The method consists of calculation of axial and rotational kinetic energies, peak

detection and annotation scheme. The kinetic energies are computed as follows:

$$E_{axial} = \frac{1}{2}mv^2 \tag{1.2}$$

$$E_{rot} = \frac{1}{2}\left(I_x\omega_x^2 + I_y\omega_y^2 + I_z\omega_z^2\right) \tag{1.3}$$

where, m and v correspond mass and linear velocity of the sensing unit, and $\omega_{x,y,z}$ and $I_{x,y,z}$ denote the angular speed and moments of inertia of the sensor in three directions, respectively. For estimation of both fiducial points (IM, AC), E_{rot} signal was found useful. It was also demonstrated that the y-axis energy-waveform of the GCG is less sensitive to walking artifacts. It may be useful in annotating SCG signals in ambulatory conditions.

Application works

- **Study on cardiac-diseases using SCG:** The application of an SCG signal has been extended not only for healthy subjects but also for cardiac patients. In the existing literature, various methods illustrated the importance of SCG-waveform delineation for the diagnosis of cardiac diseases, such as atrial flutter, atrial fibrillation, valvular, and coronary artery diseases [4]. A summary of SCG parameters is provided in Table 1.6 used for diagnosing different cardiac conditions.

Table 1.6: Reported SCG parameters for cardiac disease diagnosis.

Cardiac disease	Delineation parameter used for diagnosis
Atrial flutter [40]	MC, AO, AC, MO
Atrial fibrillation [37, 65, 78, 88]	AO-AO interval
Myocardial ischemia [7, 22, 38]	AO and RF amplitudes
Haemorrhage [39]	LVET interval
Valvular disease	MC, AO, AC, MO
Hypertension [59]	PEP, LVET
Myocardial infarction [39]	AC, MC
Heart Failure [75, 76]	PEP, Normalized-SCG

- **Study on breathing-patterns using SCG:** Long term irregularities in respiratory rhythms often affect the heart and the lung functions. Hence, the identification of breathing patterns is

an essential task to avoid related diseases. In medical diagnosis, breathing patterns give important information to detect various life-threatening diseases, including cardiovascular diseases like arrhythmias, cardiac arrest and sepsis, and diseases due to lung dysfunctions such as asthma, pneumonia, chronic obstructive pulmonary disease (COPD), hypercarbia and pulmonary embolism [114]. Fear, anxiety, and extensive exercises could also produce abnormal breathing symptoms even in healthy individuals. During the breathing inhalation time, the diaphragm contracts and moves down, the chest surface expands, pressure in the intrathoracic cavity reduces, each of the lungs inflates, and the heart moves almost linearly with the displacement of diaphragm [20]. The hemodynamic variations, such as changes in blood volume, turbulence, and pressure caused due to decreased intrathoracic pressure, affect the morphological structure of the SCG signal [20]. The morphology of an SCG signal is affected by different respiratory conditions, and so, the SCG can not only be used to measure cardiac health but also to assess lung fitness [4], [115]. In our previous work [115], significant changes in SCG morphologies are shown for different respiratory events. Breathing patterns may be categorized into three states, *viz.*, breathlessness, normal breathing, and long and labored breathing. Sudden shortness of breath, also known as acute/chronic dyspnea, is a serious pathological condition [116]. The severe abnormalities in lung and heart are the major causes of these conditions in most of the cases. It is to be mentioned that the physical examinations cannot always diagnose these conditions [116]. The SCG would be helpful in establishing physiological-relationship for cardiorespiratory, which would also be applicable to cardiopulmonary exercise testing (CPET).

In the existing literature, a few research works have been suggested using ECG or SCG signals for the detection of respiratory information, such as extraction of breathing rate sequence and detection of sleep apnea. To identify the respiratory inhale and exhale phases, the SCG signal may also be used [41,42,68,117,118]. Zakeri *et al.* devised an approach to analyze the SCG beats for the recognition of respiratory phases [68]. In this approach, an SCG beat is segmented into identical-sized blocks in temporal and spectral domains, and average values from the blocks are used as features. After that, a support vector machine (SVM) is used to select an optimal feature-group which gives a higher identification-rate. Another method was proposed in this direction, which considers an averaged value of 512 data points of each of the systolic-profiles as a feature, and subsequently, an SVM is used for identification of breathing phases [41]. The aforementioned

schemes use R-peaks of temporally concurrent ECG signals for the segmentation of SCG cycles. In [118], it was demonstrated that all SCG cycles can be categorized into the inhale and exhale phases with the help of a respiratory signal. In this direction, a frequency-domain SCG signal analysis is suggested by Pandia *et al.* [42]. The entire frequency range is splitted into two spectral bins corresponding to 5 and 10 Hz, and discrimination between the inhalation and exhalation phases is statistically done in the 10–40 Hz frequency range. As preliminary work, we presented a method for the characterization of two breathing states by analyzing morphological differences of an SCG waveform [115]. However, the variation of morphological characteristics of the SCG signal due to different respiratory conditions is still needed to be extensively investigated.

1.5 Motivation and Objectives

Delineation of the SCG signal is highly essential for its usage in a clinical setting. However, SCG delineation is a challenging research problem. The task is even more complex and difficult when the signal is severely affected by noises and inter- and intra-beat variabilities. Most of the state-of-the-art methods are not efficient in the presence of abnormal beats and noise. In addition, many clinical parameter extraction methods are focused on estimating the prominent AO peaks. However, they mostly use a fixed windowing scheme. For example, they determine maxima as AO peak in SCG just after R-peak in the ECG signal. The use of any fixed window-size is not appropriate for a signal having abnormal and irregular heart rhythms, especially when AO peak has a smaller amplitude than peak corresponding to mitral valve closure (MC) or rapid ejection (RE) instant under a systole profile. Most of the methods are not completely relying on the SCG signal for the delineation task. Their approaches rely on other cardiac signals alongside with the SCG, recorded from multiple sensors, which in turn increases the overall complexity of the systems. However, multimodality of the SCG with other cardiac signals may help in its delineation by estimating other critical points appropriately. Existing methods mainly employ time-domain approaches. In time-frequency representations, the earlier methods are not investigated in depth. More explorations are needed for analyzing signal characteristics in data-independent and data-adaptive based time-frequency decomposition techniques. Moreover, the existing methods are limited to estimate only a few fiducial points, through which the characterization of both systolic and diastolic profiles of the SCG would not be possible. There is no systematic approach for automated standalone noise-robust SCG delineation to extract all the clinical

information from the heart. Moreover, the effects of body movement, posture, and respiration are needed to be analyzed that influence the characteristics of the SCG signal. Thus, motivated by the above study points, the objectives of the thesis are given as follows:

- To develop automatic delineation frameworks for an SCG signal, which would include detection of systole and diastole profiles, determination of various SCG fiducial points, and estimation of temporal durations between them. The delineation includes two approaches, standalone and secondly, with the assistance of other cardiac signals such as ECG and PPG.
- To design and develop the SCG acquisition hardware for the recording of the signal.
- To establish the mapping of SCG with other cardiac signals using delineation for extracting robust clinical information of heart cycle events such as hemodynamic parameters, heart rate variability parameters, and contractility parameters.
- To study the effect of respiratory-effort levels onto the SCG morphology, which would employ machine learning approaches to show the potentials of delineated features for the classification of SCG signals.

1.6 Thesis Outline

The contribution of the present thesis is illustrated in Figure 1.8. It includes three major blocks, which are signal acquisition, delineation of the SCG waveform, and its applicability. The signal acquisition block represents the development of hardware for SCG signal recording. Along with that, the acquisition also allows the recording of concurrent ECG and PPG signals. The second block, SCG delineation, represents four different approaches for the estimation of fiducial points with and without the help of reference cardiac signals. Two different applications are shown in the third block by analyzing the morphological structures of the SCG profiles. It describes one of its applications in fundamental heart sound extraction and its characterization, and another in cardiorespiratory analysis to show the ability of delineated SCG parameters. The planning of the proposed investigations attempted in this thesis is as follows: Chapter 2 presents our designed SCG acquisition system. It further describes the approaches for standalone SCG delineation, which do not rely on any other cardiac signal. These delineation techniques are mainly employed to estimate the AO fiducial point. Whereas, Chapter 3 presents the delineation approaches, which take into consideration of other cardiac

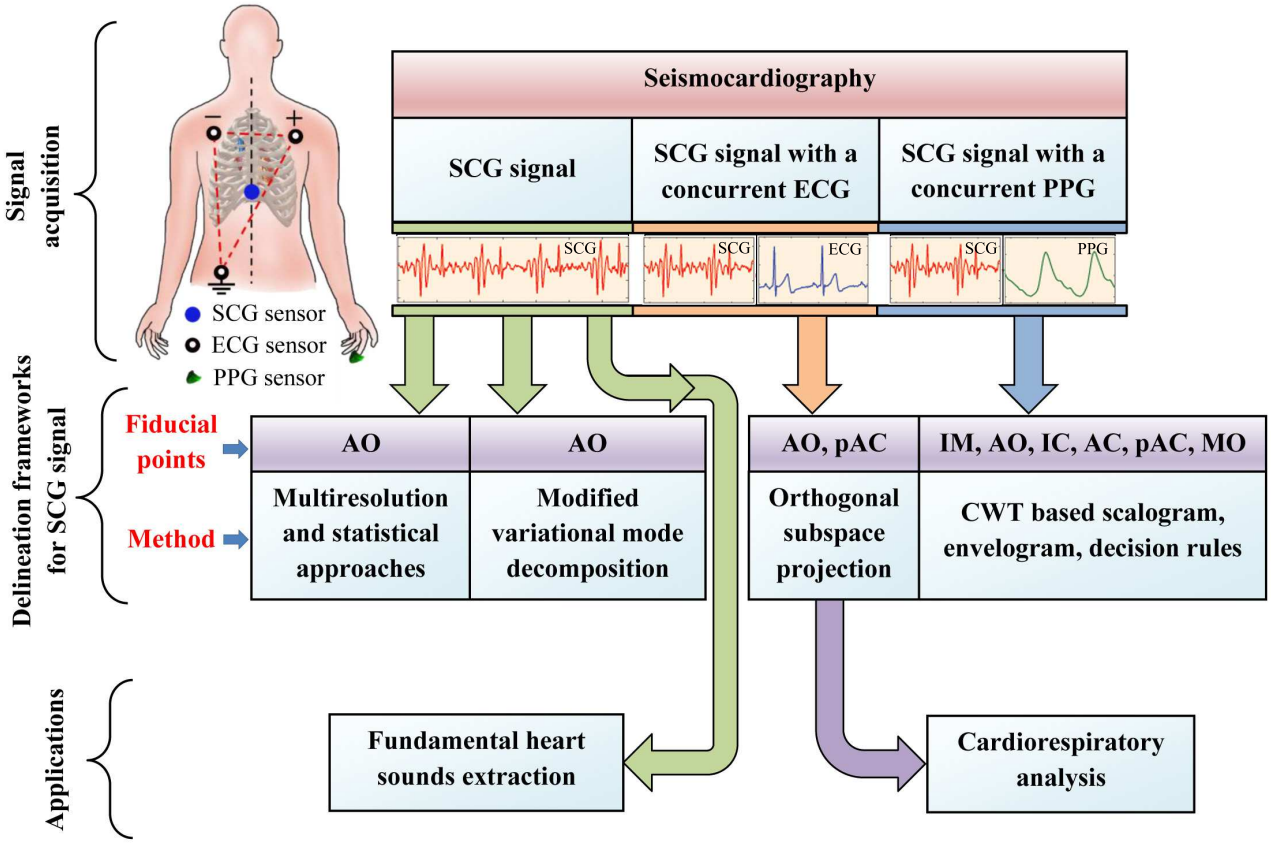

Figure 1.8: Graphical abstract describing dissertation work-flow

signals such as ECG and PPG signals. In Chapter 4, the utility of the SCG signal is shown to extract the fundamental heart sounds, which are S_1 and S_2 sounds. Chapter 5 presents the analysis of SCG morphological features for the identification of respiratory-effort levels. It utilizes the hybrid features of the SCG signal, including fiducial and non-fiducial features, for the characterization of breathing-states. A summary of the thesis with the major contributions of the present work is discussed in Chapter 6.

2

SCG Waveform Delineation - Standalone Approaches

Contents

This chapter presents two proposed standalone approaches for SCG signal delineation. The delineation of the SCG signal does not need any reference cardiac signal (such as ECG) in these methods. The methods are focused on estimating the aortic valve opening, i.e., AO fiducial point. In general, the AO point in the SCG signal generates a prominent peak under a cardiac cycle. Hence, detection of the AO point can be considered as the primary step for delineating other fiducial points. Also, the cardiac intervals, such as PEP, LVET, and IVCT, cannot be estimated without AO instant information. However, the estimation of PEP requires a Q-wave of ECG along with the SCG signal. Thus, the AO point plays a major role in finding these diagnostic features of the heart. Along with its applications in HRV analysis, AO phase detection has many real-life applications in continuous monitoring and diagnostic applications. Some of them are as follows:

- Hemodynamic parameter estimation with the help of PEP and LVET intervals
- Systolic blood pressure estimation using AO and other fiducial points
- Pulse pressure and pulse transit time estimation using duration of AO to foot of PPG pulse
- Diagnosis of valvular defects and other various cardiovascular diseases such as:
  - Coronary artery disease (myocardial ischemia): With the help of AO and RF amplitudes
  - Atrial flutter: With the help of locations of AO and other fiducial points from 3-D SCGs
  - Atrial fibrillation: With the help of heartbeat sequence derived from AO points
  - Haemorrhage: With the help of LVET interval

However, the estimation of the AO fiducial point is a crucial task in an SCG signal. Two different studies are carried out to address this issue using the time-frequency analysis of the signal. The first study is based on a multiscale decomposition of the SCG signal using discrete wavelet transformation. For localizing the AO points, multiscale statistical approaches are employed for quantification of usefulness and effectiveness of extracted subbands and further, signal reconstruction from them. With improved performance, another study is performed using a data-adaptive modified variational mode decomposition (VMD) based scheme. For an automatic tuning of controlling parameters, the traditional VMD model is modified, which is further used for SCG filtering, followed by Gaussian derivative filtering. The rest of the chapter is organized as follows: the designed hardware for SCG signal acquisition is described in Section 2.1. The proposed multiresolution and statistical approaches based method is presented in Section 2.2. Section 2.3 describes our second standalone approach based on the proposed MVMD model. Finally, a summary is provided in Section 2.4.

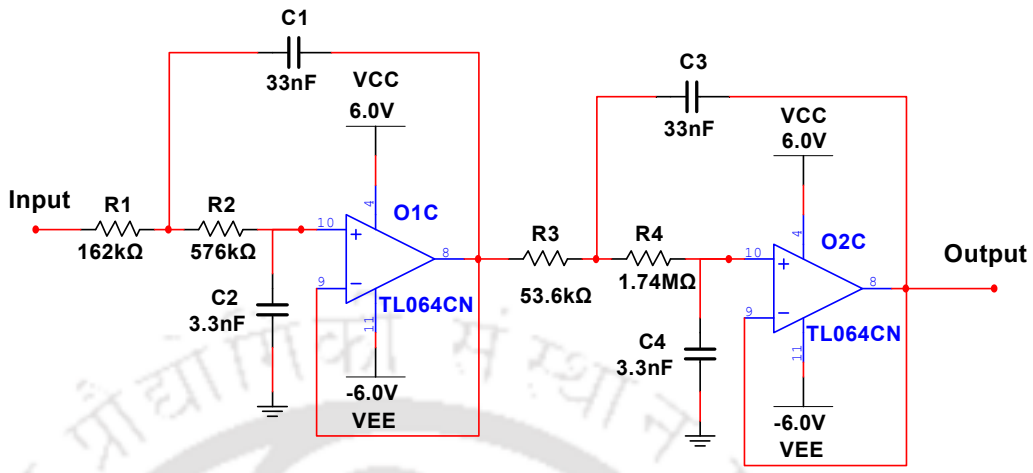

Figure 2.1: Schematic of electronic circuitry of Butterworth low pass filter for SCG signal acquisition.

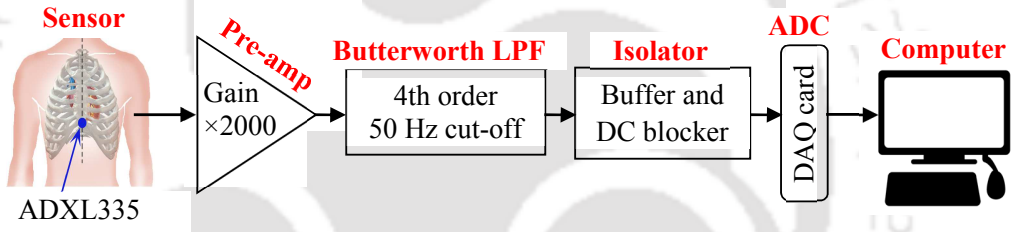

Figure 2.2: Overview of our designed system for SCG signal acquisition.

2.1 Hardware and Data Collection

A small electronic circuit board is developed for recording of the SCG signals noninvasively. The system consists of a low-cost and miniaturized MEMS-based accelerometer sensor (ADXL335, ±3 g) [119], a pre-amplifier, a fourth-order Butterworth low pass filter (LPF), a buffer, data acquisition system (Biopac MP150), and a PC with the AcqKnowledge interfacing software. Initially, an acceleration signal is pre-amplified by an active amplifier with a gain of 2000. The SCG signal is band-limited to 50 Hz frequency using the Butterworth LPF. Two second-order filters are cascaded to design this LPF filter, where both the filters are configured in a Sallen-Key topology. A schematic of the electronic circuitry of designed unit-gain LPF is shown in Figure 2.1. The low-power quad-package based JFET-input operational amplifiers (opamp), TL064, are used as active amplifiers. The schematic of our SCG monitoring system and designed PCB are shown in Figures 2.2 and 2.3, respectively. The PCB also has the facility of wireless data transmission via Bluetooth scheme. The experimental set-up for signal

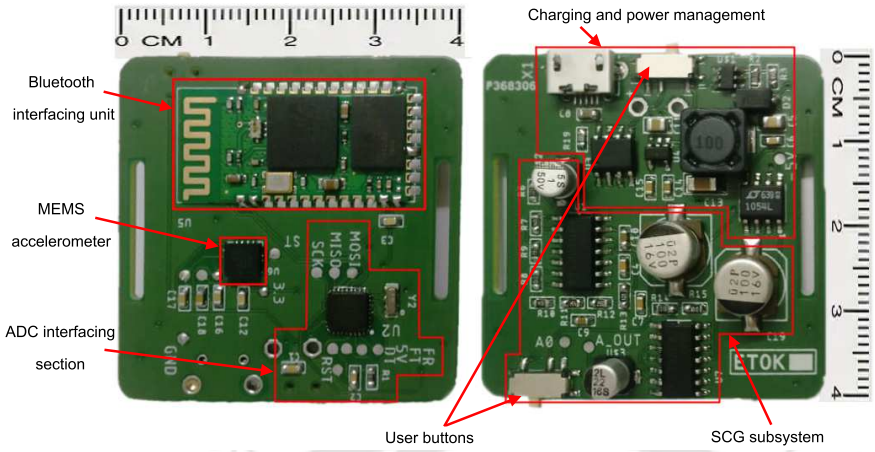

Figure 2.3: Back and front views of our designed PCB for SCG signal recording.

Figure 2.4: Experimental setup for SCG signal acquisition.

recording is shown in Figure 2.4, where the subject is lying in a supine position during the signal recording process. The sensor is placed on the chest with the help of an elastic chest-band.

The SCG signals are acquired by mounting the sensor node near the lower end of the sternum on the chest wall. Additionally, the ECG (Lead-II) and the PPG (at fingertip) signals were also acquired in a standard-setting procedure. All these three signals are digitized and synchronized using the Biopac MP150 DAQ system at a sampling rate of 1 kHz. After getting ethical approval from the institutional review board, the signals are recorded from healthy subjects with their proper consent.

2.2 Multiresolution and Statistical Approaches Based Method

A standalone AO peak detection algorithm is proposed based on dominant multiscale kurtosis (DMK) and dominant multiscale central frequency (DMCF) in the multiresolution domain using wavelet. Based on proposed DMK and DMCF based criteria, probable AO peaks rich subbands are selected,

[1]This work has been published in IEEE Journal of Biomedical and Health Informatics, 2019 (Refer *List of Publications* page for details).

and the signal is reconstructed. Further, the reconstructed signal is enhanced for AO peaks with weights, which are based on proposed relative squared dominant multiscale kurtosis (RSDMK). Finally, AO peaks are detected using Shannon energy (SEE) and autocorrelation features based envelope construction scheme, and Gaussian derivative filtering based peak detection logic.

2.2.1 Proposed method for AO peak detection

The wavelet transform has the ability to represent a signal in different subbands [112], [30]. It may be applied for the time-frequency analysis of non-stationary signals like SCG and characterization of its profiles [30]. The inner cross product of the scaled and translated version of basis wavelet and the signal is used to estimate the wavelet coefficients, $w_{l,m}$ [120]

$$w_{l,m} = \langle x(t), \psi_{l,m}(t) \rangle \tag{2.1}$$

where, $x(t)$ represents input signal, $\psi_{l,m}(t)$ is scaled by a factor l and translated by a factor m of basis wavelet, and $w_{l,m}$ denotes m^{th} coefficient at the l^{th} level of decomposition. The bandwidth of l^{th} level subband is defined as $\Delta f_l \in [2^{-l-1}\mathrm{F_S},\ 2^{-l}\mathrm{F_S}]$, where $\mathrm{F_S}$ is the sampling frequency. A multiresolution pyramidal filterbank is used to implement the dyadic wavelet decomposition framework. Any finite energy signal can be decomposed using the L^{th}-order wavelet filterbank structure using a discrete wavelet transform (DWT). If $x[n]$ $(n = 1, 2, ..., N)$ is a discrete SCG signal, then the DWT is given by:

$$x[n] = \sum_{l=1}^{L} \sum_{m=-\infty}^{\infty} cD_l(m)\psi_{l,m}[n] + \sum_{m=-\infty}^{\infty} cA_L(m)\phi_{L,m}[n] \tag{2.2}$$

where, $l = 1, 2, ..., L$; $cD_l(m)$ and $cA_l(m)$ denote m^{th} detail and approximation coefficient of l^{th} level, respectively; $\psi[n]$ and $\phi[n]$ correspond to wavelet and scaling functions, respectively. If $D_l[n]$ and $A_l[n]$ denote the reconstructed subbands from detail and approximation coefficients of l^{th} level, the reconstructed signal can be written as the sum of sub-signals as:

$$x[n] = \sum_{l=1}^{L} D_l[n] + A_L[n] \tag{2.3}$$

These subband signals are togetherly expressed as:

$$B_\gamma[n] = \begin{cases} D_l[n], & \gamma = 1, 2, ..., L \\ A_L[n], & \gamma = L + 1 \end{cases} \tag{2.4}$$

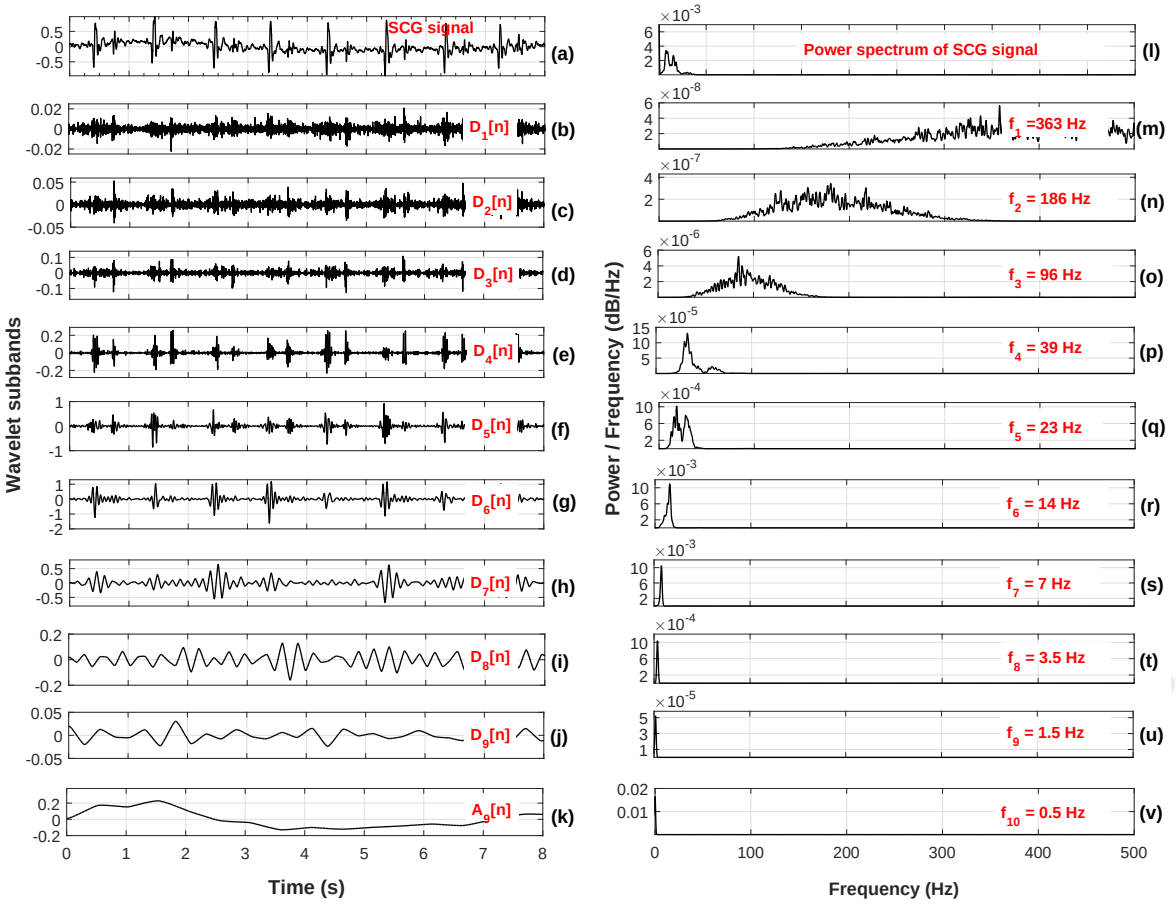

Figure 2.5: Decomposition of an SCG signal using DWT with spectral distributions. (a) SCG signal, (l) power spectrum of SCG signal, (b)-(k) wavelet subband signals, and (m)-(v) power spectrum densities with dominant multiscale central frequencies (DMCF).

It is expected that the information contained in an SCG signal is decomposed at different scales, including W-complex, diastole complex, low and high-frequency artifacts, and noises. Figure 2.5 shows signal decomposition using the biorthogonal-3.9 mother wavelet and the associated power spectrums. The lower subbands (D_1-D_3) capture high-frequency components, while slow varying signal components are observed in higher subbands (D_4-D_9, A_9).

2.2.1.1 Proposed dominant multiscale kurtosis (DMK)

The kurtosis estimate indicates the sharpness of the peak of probability distribution [121]. The multiscale kurtosis (MK) facilitates the measurement of Gaussianity of each extracted subband, (i) Gaussian if kurtosis is equal to 3, (ii) sub-Gaussian if kurtosis is less than 3, and (iii) super-Gaussian if kurtosis is greater than 3 [121]. The multiscale kurtosis of reconstructed detailed subband signals

is given as:

$$\lambda_{D_l} = \frac{\frac{1}{N}\sum_{n=1}^{N}\left(D_l[n] - \overline{D}_l[n]\right)^4}{\left(\frac{1}{N}\sum_{n=1}^{N}\left(D_l[n] - \overline{D}_l[n]\right)^2\right)^2} \tag{2.5}$$

The multiscale kurtosis of reconstructed approximation subband signal is defined as:

$$\lambda_{A_L} = \frac{\frac{1}{N}\sum_{n=1}^{N}\left(A_L[n] - \overline{A}_L[n]\right)^4}{\left(\frac{1}{N}\sum_{n=1}^{N}\left(A_L[n] - \overline{A}_L[n]\right)^2\right)^2} \tag{2.6}$$

where, $n = 1, 2, ..., N$ and $\overline{(\cdot)}$ corresponds to mean operator. For mathematical simplification to include λ_{D_l} and λ_{A_L}, the dominant multiscale kurtosis (DMK) is expressed as:

$$\lambda_\gamma = P \cdot \lambda_{D_{(l=\gamma)}} + Q \cdot \lambda_{A_L} \tag{2.7}$$

$$P = \left\lceil \frac{L+1-\gamma}{L+1-\gamma+\epsilon} \right\rceil; \quad Q = \left\lfloor \frac{\gamma}{L+1} \right\rfloor \tag{2.8}$$

where, subband index $\gamma = 1, 2, ..., L+1$; $\lceil\cdot\rceil$ and $\lfloor\cdot\rfloor$ represent ceiling and flooring operations, respectively. In this, ϵ is a very small real positive number ($\epsilon \to 0$). It could be hypothesized that in the presence of a systolic or diastolic profile in an SCG segment in reconstructed subband signal, the signal has a super-Gaussian behavior. In Figure 2.6, different morphologies of systolic profiles and respective power spectrums are shown. When kurtosis is estimated for each of these systole profiles, it is found to have a value of greater than 3. This justifies the super-Gaussianity behavior of these profiles.

2.2.1.2 Proposed dominant multiscale central frequency (DMCF)

The central frequency of a signal provides an idea of the centroid of the corresponding power spectrum [122]. The multiscale central frequency (MCF) is computed as the center-of-gravity of the power spectrum of each of the subbands. The MCF of reconstructed detailed subband signals is defined as:

$$f_{D_l} = \left(\frac{\sum_f f|D_l(f)|^2}{\sum_f |D_l(f)|^2}\right) \tag{2.9}$$

where, $\sum_f := \sum_{f=0}^{\infty}$ is the summation over all the signal frequencies. The MCF of reconstructed approximation subband signal is defined as:

$$f_{A_L} = \left(\frac{\sum_f f|A_L(f)|^2}{\sum_f |A_L(f)|^2}\right) \tag{2.10}$$

where, f denotes frequency, and $|D_l(f)|^2$, $|A_L(f)|^2$ are the power spectrums of l^{th} detailed and L^{th} approximation subband, respectively. For mathematical simplification to include f_{D_l} and f_{A_L}, the

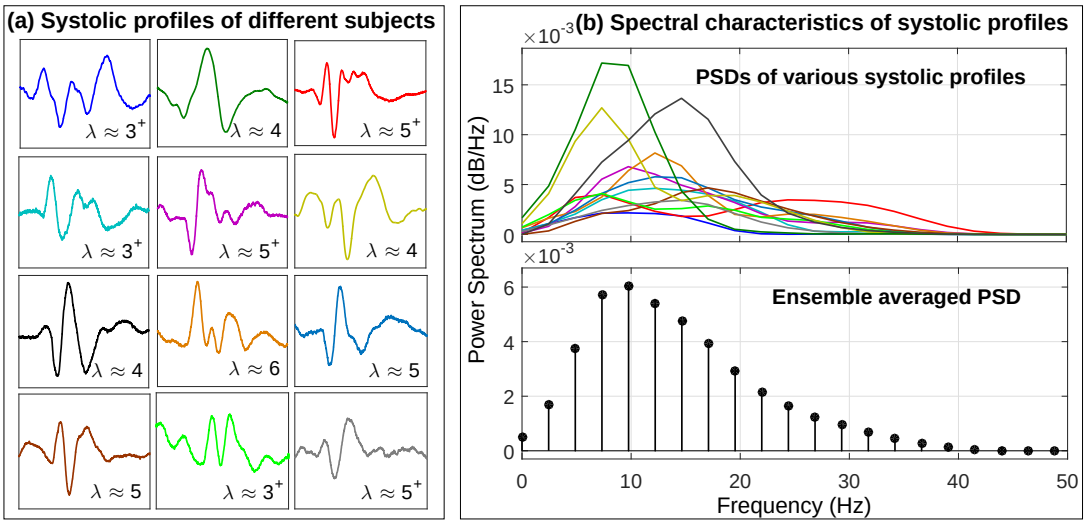

Figure 2.6: Systolic profiles of SCG for 12 individuals with spectrums (CEBS database). (a) Different profiles of systole regions with kurtosis (λ) values, (b) spectral characteristics of these systole profiles and their ensemble average.

dominant multiscale central frequency (DMCF) is expressed as:

$$f_\gamma = P \cdot f_{D_{(l=\gamma)}} + Q \cdot f_{A_L} \tag{2.11}$$

It is desirable to exclude subbands whose central frequencies do not follow the systolic profile. The main energy concentration of the systolic profile lies below 40 Hz [40]. Figure 2.6(b) also justifies the consideration of subbands having DMCF in the frequency range of 6 – 45 Hz, approximately.

2.2.1.3 Proposed method for selection of important subbands

After reconstructing sub-signals at different wavelet scales, it is essential to identify subbands having significant systolic profiles. The DMK and DMCF are used to eliminate undesired subband signals. The DMK rejects those subbands which show Gaussian or sub-Gaussian characteristic ($\lambda_\gamma \leq 3$), and this is due to the presence of low-frequency signal components and artifacts. Higher DMK values ($\lambda_\gamma > 3$) for subband signals indicate peakedness in their distribution due to the presence of prominent AO peaks in the signal. Thus, based on this criterion, a modified set of subbands Θ_λ is created as:

$$\gamma^* = \underset{\gamma}{arg}(\lambda_\gamma \geq 4) \tag{2.12}$$

$$\Theta_\lambda = B_{\gamma^*}[n] \tag{2.13}$$

where, γ^* ($\gamma^* \in [1, L+1]$) is the index of the selected subbands from DMK based criterion. Similarly,

DMCF is considered to exclude the subband signals whose central frequencies do not follow the systolic profile frequency (6 – 45 Hz) range. To create a new set of subbands, the argument Θ_f is taken as:

$$\gamma^\dagger = \underset{\gamma}{arg}(6 \leq f_\gamma \leq 45) \tag{2.14}$$

$$\Theta_f = B_{\gamma^\dagger}[n] \tag{2.15}$$

where, $\gamma^\dagger$ ($\gamma^\dagger \in [1, L+1]$) is the index of the selected subbands from DMCF based criterion. Based on DMK and DMCF, a set of subbands, $B_q[n]$, is derived as:

$$B_q[n] = \Theta_\lambda \cap \Theta_f := \left\{ B_q[n] \middle| B_q[n] \subset B_\gamma[n] \right\} \tag{2.16}$$

where, subband index $q = 1, 2, ..., L_s$ and $1 \leq L_s \leq \min\{length(\gamma^*), length(\gamma^\dagger)\}$. All selected subbands from both the criteria carry information of AO peaks in the SCG signal.

2.2.2 Emphasizing systolic profiles

The signal with systolic profiles needs emphasis for better identification of peaks. It is proposed to use relative squared dominant multiscale kurtosis (RSDMK) to give weights to the desired components. The RSDMK weights w_q are computed from the selected subbands as the normalized sum of squared DMK:

$$w_q = \frac{\lambda_q^2}{\sum_{q=1}^{L_s} \lambda_q^2} \tag{2.17}$$

where, $q = 1, 2, ..., L_s$ and $\sum_q w_q = 1$. Based on non-linear weights, the reconstructed signal $x_r[n]$ is estimated as:

$$x_r[n] = \sum_{q=1}^{L_s} w_q . B_q[n] \tag{2.18}$$

It is expected to get sharper transitions and significant impulsive patterns at the AO peaks using these weights. Also, it has a better ability to suppress noisy-spikes.

2.2.2.1 Envelope construction

A time series of autocorrelation coefficient (ACoef) with a fixed lag on Shannon energy (SEE) envelope can approximately locate the AO peaks in the signal. The combination of both operators can identify the rise in the signal value, and it corresponds to AO peaks of the signal. The SEE is computed as $S_e[n] = -x_r^2[n]\log_2(x_r^2[n])$, where $x_r[n]$ is reconstructed signal [123]. The ACoef time series is

computed as:

$$Ac[j] = \sum_{m=-\infty}^{\infty} \{Sw_j[m]Sw_j[m+\mathrm{D}]\} \tag{2.19}$$

where, $Sw_j[m] = S_e[m + (j-1)\mathrm{O}]$, represents windowed version of $S_e[n]$, j $(j = 1, 2, .., J)$ denotes its short time window number, m $(m = 1, 2, .., M)$ denotes its sample index, O denotes amount of overlapping between consecutive windows, and the D is a fixed lag. The SEE envelope gives a better estimate in the presence of sudden low or high dynamic amplitudes in the SCG signal. While other envelope extraction methods such as absolute [123], energy [123], analytic signal envelope [123], and Shannon entropy [123] do not perform well in such conditions. The performance of all these extraction methods is shown in Figure 2.11. To suppress other than systole regions, the computed ACoef time series on the SEE envelope is smoothed using a low pass filter. Further, it is thresholded with a data adaptive global threshold, which results in a pulse train, and it is denoted by $tsac[n]$.

2.2.2.2 Peak detection and localization

The local maxima from each pulse of $tsac[n]$ is approximated as an AO peak. These peaks are estimated by first-order Gaussian differentiation (FOGD), which is computed as [124]:

$$d[i] = w[i+1] - w[i], \quad i = 1, 2, ..., I-1 \tag{2.20}$$

where, $d[i]$ provides the slope corresponding to each of the samples, and $w[i] = e^{-(i-I/2)^2/(\sigma^2 I)}$ is a I-point Gaussian window. The parameters σ^2 (variance) and I (window length) change the characteristic of FOGD. After filtering the thresholded signal $tsac[n]$, FOGD sequence $y[n]$ is computed as:

$$y[n] = \sum_{k=-\infty}^{\infty} d[k] \cdot tsac[n-k] \tag{2.21}$$

If the wave corresponding to the peak is considered as a Gaussian window, then the negative zero crossing points (NZCPs) of $y[n]$ provide the peak locations of input signal [124]. It is denoted by $p[v]$, where $v = 1, 2, ..., V$, and V is total number of approximated AO peaks in the SCG signal. Figure 2.12(f) illustrates the FOGD filtering process of $tsac[n]$ with all the detected NZCPs. Finally, the AO peak is more properly localized using a symmetric extrema search window centered around each NZCP as $p[v] \pm \frac{W}{2}$, where W denotes the width of the search window.

A block diagram of the proposed AO peak detection method is shown in Figure 2.7. Initially, the SCG signal is segmented into non-overlapping blocks of 10 s duration each. In the pre-processing stage,

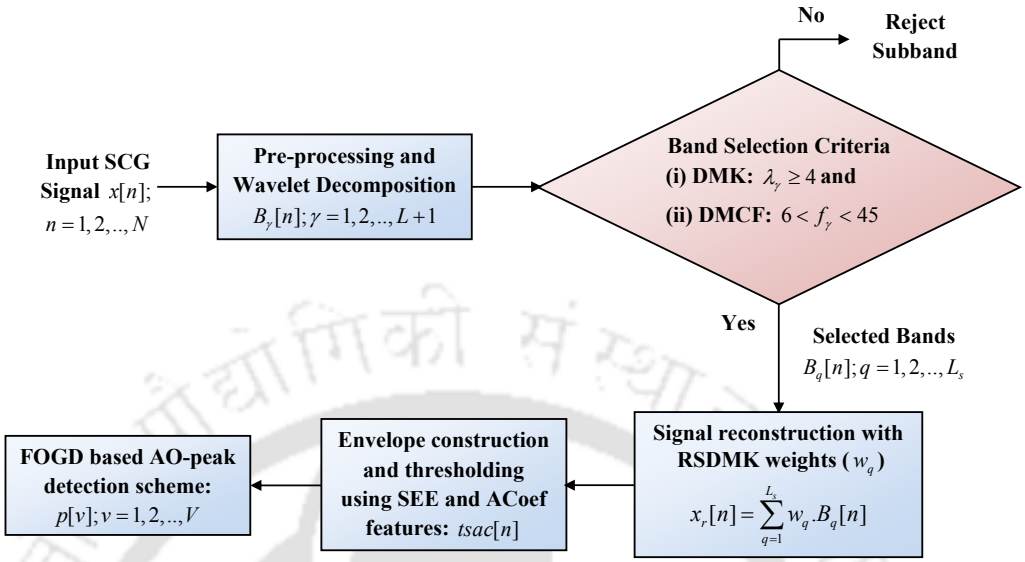

Figure 2.7: Block diagram of the proposed AO peak detection framework.

a fifth-order median filter is applied on zero mean, amplitude normalized N-samples SCG segment $x[n]$. Then, the signal is decomposed into approximate and detailed subbands using DWT. Using proposed DMK and DMCF criteria, subbands containing AO peaks are selected. With the selected subbands, the SCG signal is reconstructed with the help of RSDMK weights. Envelope construction using SEE and autocorrelation is suggested to find AO peaks. Data-adaptive global thresholding is performed on the constructed envelope in order to suppress the regions other than systolic profiles. Finally, a Gaussian derivative filtering based peak detection scheme is applied to localize the valid AO peaks.

2.2.3 Results and discussion

The proposed AO-peak detection framework is tested using the combined measurement of ECG, breathing, and seismocardiogram (CEBS) database, available at the Physionet archive [125]. The signals are recorded using a Biopac MP36 signal acquisition system (Santa Barbara, CA, USA) from 20 healthy individuals. The sampling rate for each channel is 5 kHz. However, signals are re-sampled to 1 kHz for our study. The SCG dataset includes signals with narrow systolic profile, wider systolic profile, motion artifacts, trending effect, baseline drift, sudden variations in systolic profile amplitudes and patterns, irregularity in cardiac rhythms, cases with lower AO amplitudes and strong diastolic profile patterns. The mean is removed from the signal and amplitude is normalized. It is pre-

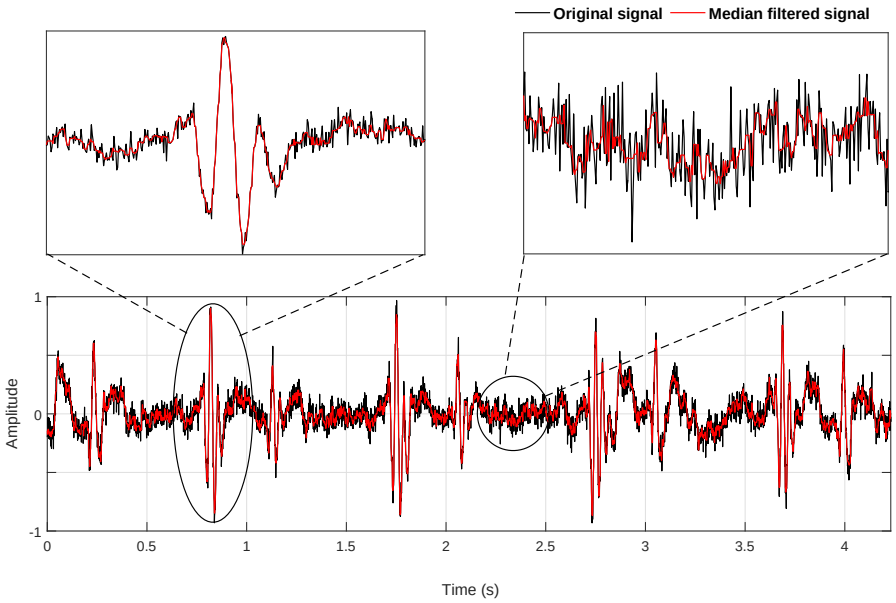

Figure 2.8: Median filtering of the SCG signal in preprocessing stage. By magnifying the two selected regions, it is illustrated that median filtering reduces the intermittency in the signal, while preserving the diagnostic information i.e. it does not affect the profile morphologies.

processed by applying a fifth-order median filter. This improves the quality of the signal and reduces high frequency noises. The reduction of intermittency, irregularity and high frequency body vibrations improves the accuracy of AO-peak detection. It is illustrated in Figure 2.8.

Using the biorthogonal-3.9 mother wavelet, the signal is decomposed into nine levels. The biorthogonal-3.9 wavelet has morphological similarity with the systolic profile. The clinical information is significantly segregated, including W-complex, diastole complex, low- and high-frequency noises at different wavelet scales (Figure 2.5). The lower subbands (D_1–D_3) capture high frequency signal noises, while slow varying signal components are seen in higher subbands (D_4–D_9, A_9). The information of systolic profiles is captured in subbands D_4–D_7 in most of the cases. In Figure 2.9, four cases of subband selection and signal reconstruction are shown. In case (I) AO>MC and AO>RE: Figure 2.9(a) and Figure 2.9(e) show the original and reconstructed signals whereas Figure 2.9(b) and Figure 2.9(c) show DMK and DMCF based subband selection criteria, respectively. Figure 2.9(d) shows the selected subbands. Similarly, other cases (II) MC>AO and RE>AO, (III) RE>AO, and (IV) diastole $\approx$ systole are shown. Based on proposed criteria, there are four selected subbands D_4–D_7 in cases (I) and (II), while three subbands D_4–D_6 are selected in cases (III) and (IV). However, the reconstructed signal produces significant impulses only at AO peaks under systolic profiles in all the cases. The proposed

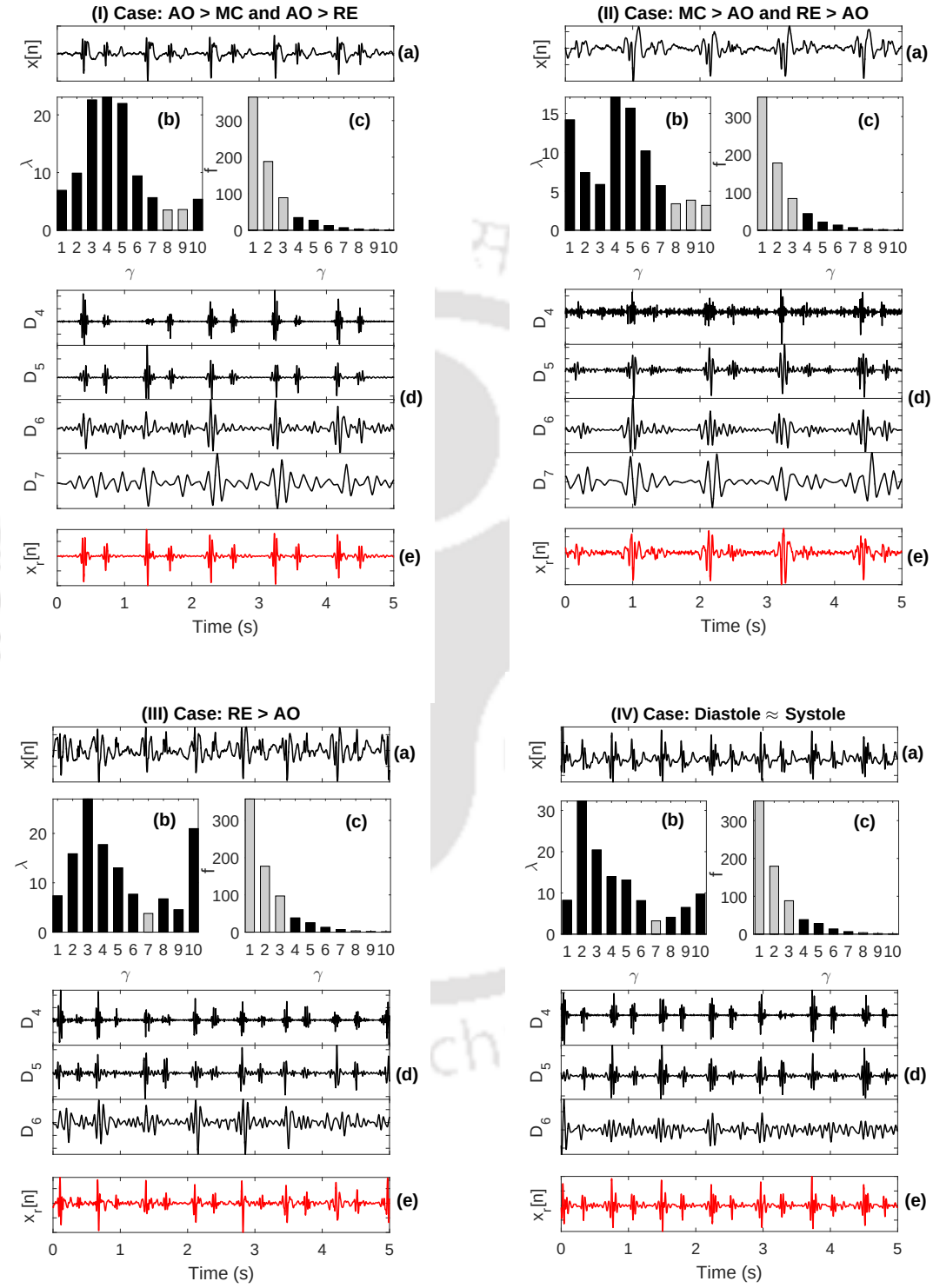

Figure 2.9: Subband selection based on DMK and DMCF and reconstruction of signals in four different morphological cases: amplitude of (I) AO>MC and AO>RE, (II) MC>AO and RE>AO, (III) RE>AO and (IV) diastole ≈ systole. (a) SCG signal, (b) DMK based criterion, (c) DMCF based criterion, (d) selected subband set from both criteria, and (e) reconstructed signal using RSDMK weights. Note that the subbands satisfying each of the criteria are highlighted in dark black bar in (b) and (c).

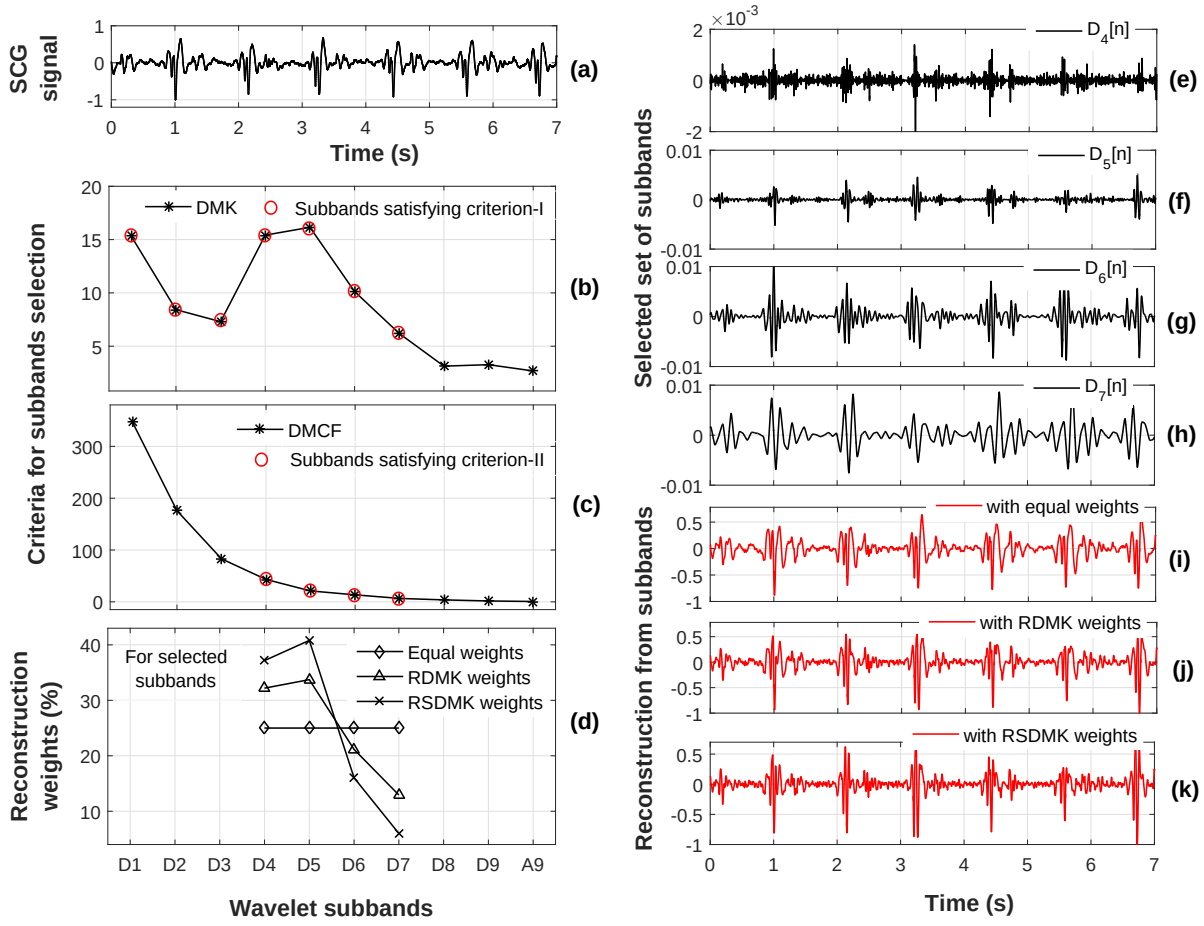

Figure 2.10: Generation of reconstructed signal from wavelet subbands. (a) Test SCG signal, (b)-(c) selection of subbands using DMK and DMCF based criteria, (d) three types of percentage of weights, (e)-(h) selected set of bands, (i)-(k) three types of reconstruction corresponding to three types of weights.

RSDMK weights are linearly combined with the selected subbands. The selected subbands from both the criteria are D_4, D_5, D_6 and D_7 as shown in Figure 2.10(e)–(h) for an SCG signal (Figure 2.10(a)), and signal reconstruction using RSDMK weights is shown in Figure 2.10(k). The qualitative analysis shows that sharper transitions are achieved at AO peak instants by our proposed weighting method in contrast to the methods which use equal and relative DMK (RDMK) weights, as shown in Figure 2.10(i) and (j), respectively. For AO peak detection, it is necessary to construct the envelope of the signal. It is observed that absolute, energy, and analytic-signal envelopes provide more spiky patterns on high amplitude AO regions and provide small deflections on low amplitude AO regions, whereas Shannon energy-based envelope provides uniformity in all AO peak variations throughout the beats (Figure 2.11). In order to suppress the regions other than systolic profile, the ACoef time

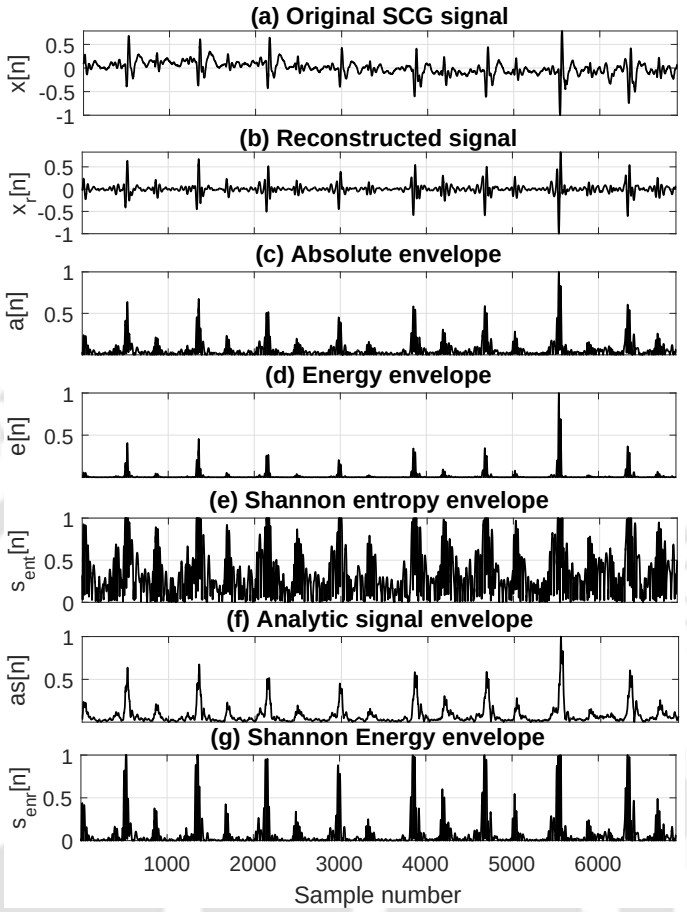

Figure 2.11: Different envelope extraction methods: (a) $x[n]$: original signal, (b) $x_r[n]$: reconstructed signal, (c) $a[n]$: absolute envelope, (d) $e[n]$: energy envelope, (e) s_{ent}: Shannon entropy envelope, (f) $as[n]$: analytic signal envelope, (g) s_{enr}: Shannon energy envelope.

series ($Ac[n]$) with fixed lag 10 is estimated from the SEE envelope, and $Ac[n]$ is smoothed with a sixth-order Butterworth low-pass filter with a cutoff frequency of 65 Hz (Figure 2.12(d)). It is thresholded to eliminate remaining significant larger diastolic profiles with a data adaptive global threshold τ; $\tau = 2 \cdot std\{Ac[n]\}$, where $std\{\cdot\}$ corresponds to a standard deviation operator. The resultant pulse train obtained from smoothed ACoef time series is denoted as $tsac[n]$ (Figure 2.12(e)). Finally, AO peaks are detected by FOGD based filtering technique with $I = 2.5\mathrm{F_s}$ ($\mathrm{F_s}$: signal sampling frequency) and $\sigma^{-1} = 0.02I = 0.05\mathrm{F_s}$, and corrected by a symmetric search window of duration $W = 0.3\mathrm{F_s}$. These processes are shown in Figure 2.12(f)–(g).

2.2.3.1 Performance evaluation

The AO-peak detection rates for signals in CEBS database [125] are evaluated. Three quantitative parameters, accuracy (ACC), sensitivity (Se), and positive predictivity (+P) are calculated as ACC =

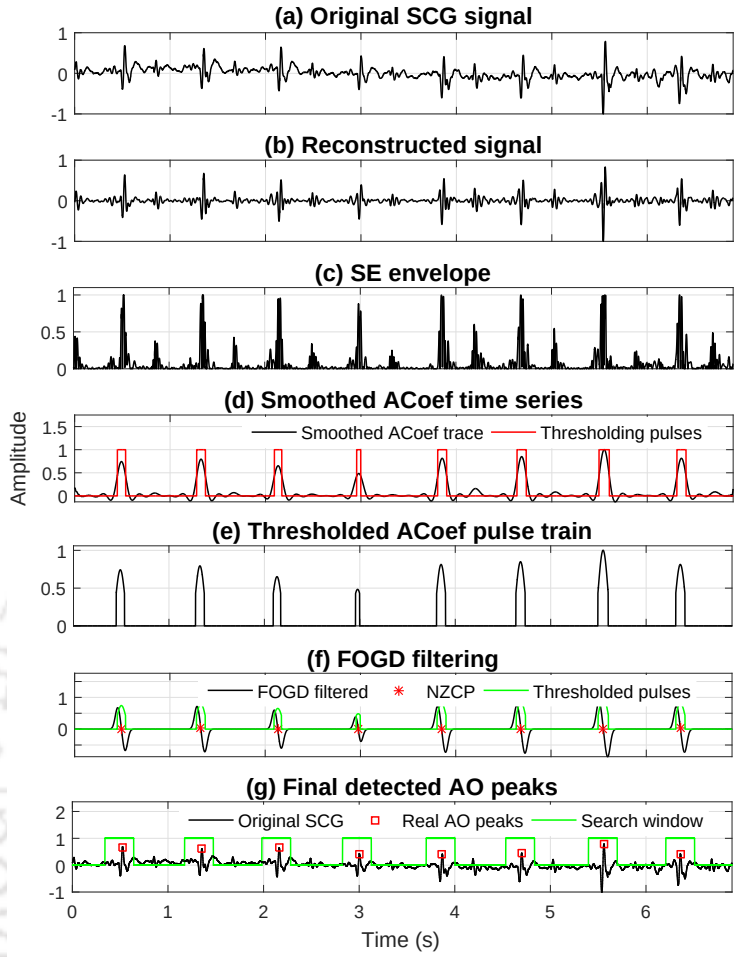

Figure 2.12: Illustrates the performance of the proposed AO peak detection method. (a) Original SCG signal, (b) reconstructed signal from selected subbands, (c) SEE envelope, (d) ACoef time series, (e) thresholded signal, (f) output of FOGD filtering and NZCPs, and (g) output of the AO peak localization stage.

$(\frac{\text{TP}}{\text{TP+FP+FN}}) \times 100\%$, Se $= (\frac{\text{TP}}{\text{TP+FN}}) \times 100\%$, and +P $= (\frac{\text{TP}}{\text{TP+FP}}) \times 100\%$. In this, true-positive (TP) signifies that AO-point is accurately identified, false-negative (FN) signifies that AO-point is missed, and false-positive (FP) signifies that AO-point is falsely identified due to a noise spike.

Table 2.1 summarizes the performance of the proposed method in terms of ACC, Se, and +P. The SCG recordings 001, 003, 011, 014, 018, and 020 produce more false-positives, and the recordings 012, 016, 017, and 018 produce more false-negatives. However, our proposed algorithm achieves a significant improvement in the case of AO-peak detection under time-varying systolic and diastolic morphologies and the presence of noises and artifacts. In some of the instances, the AO point is not a prominent peak in the SCG signal, and the amplitude of the MC or RE peak is greater than the amplitude of the AO peak. If the wave associated with the MC or RE point has a slower varying component in

Table 2.1: Performance evaluation: 20 basal stated healthy subjects.

SCG record	Signal quality	TP (beats)	FP (beats)	FN (beats)	Se (%)	+P (%)	ACC (%)
001	I, II, AC, UD	209	62	12	94.57	77.12	73.85
002	I, SD	204	0	1	99.51	100	99.51
003	V, AWGN, AC, UD, BD	219	122	10	95.63	64.22	62.39
004	I, NHR	214	0	3	98.62	100	98.62
005	I, IV, AWGN, NHR	228	20	13	94.61	91.94	87.36
006	I, AC, UD	200	3	6	97.09	98.52	95.69
007	II, SD	160	10	20	88.89	94.12	84.21
008	III, II, NHR	297	5	19	93.99	98.34	92.52
009	I, SD	201	1	5	97.57	99.50	97.1
010	I, NHR	204	0	1	99.51	100	99.51
011	I, IV	223	74	1	99.55	75.08	74.83
012	IV	242	8	27	89.96	96.80	87.36
013	I, NHR, HFN	237	1	1	99.58	99.58	99.16
014	IV, I, NHR, HFN	204	52	20	91.07	79.69	73.91
015	I, HFN, NHR	209	19	10	95.43	91.67	87.82
016	I, HFN	205	0	33	86.13	100	86.13
017	I, BD	208	0	33	86.31	100	86.31
018	I, IV, AC, UD	236	61	32	88.06	79.46	71.73
019	I	210	0	0	100	100	100
020	II, III, AC, UD, BD	205	150	23	89.91	57.75	54.23
Overall	–	4315	588	270	94.3	90.19	85.61

Terms used for data interpretation - I: case with AO>MC and AO>RE, II: case with AO<MC and AO<RE, III: case with RE>AO, IV: case with diastole≈systole, V: hybrid combination of I-IV, AC: abrupt change, UD: unrecognizable distorted beats, SD: small diastole, AWGN: additive white Gaussian noise, BD: baseline drift, NHR: normal heart rhythm, and HFN: high frequency noise.

the systolic profile, it can be easily eliminated during reconstruction by our proposed algorithm. The proposed algorithm produces 588 FP, and 270 FN beats out of a total of 4585 analyzed beats. Our method achieves overall detection rates as an average sensitivity of 94.3%, an average prediction rate of 90.19%, and a mean accuracy of 85.61%.

The poor accuracy is due to the presence of different artifacts, which degrade the signal quality. In the CEBS database, SCG records b003, b017, and b020 are severely affected by baseline drifts. However, the proposed method performs well in the presence of baseline drifts. Records b001, b003, b006, b018, and b020 contain abrupt changes and unrecognizable distorted beats. Figure 2.13 illustrates the detection performance of the SCG signal, which consists of distorted beats and unrecognizable heart rhythms. These signals are even very difficult to annotate manually. For such instants, the proposed algorithm gives a large number of misdetections.

In addition, the records b001, b007, and b020 have smaller AO peak morphologies than RE, and the record b011 has similar diastolic structures as systolic profiles. For these cases, the proposed

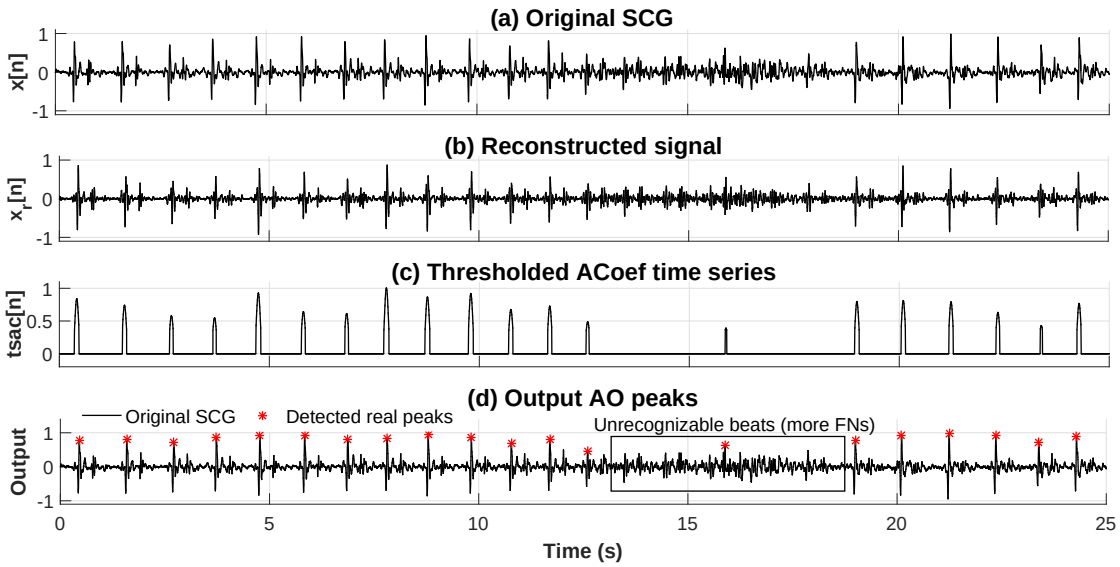

Figure 2.13: Performance of the proposed detection algorithm in the presence of unrecognizable and distorted heartbeats. (a) Original SCG, (b) wavelet reconstructed signal, (c) thresholded ACoef signal, and (d) detected real AO-peaks.

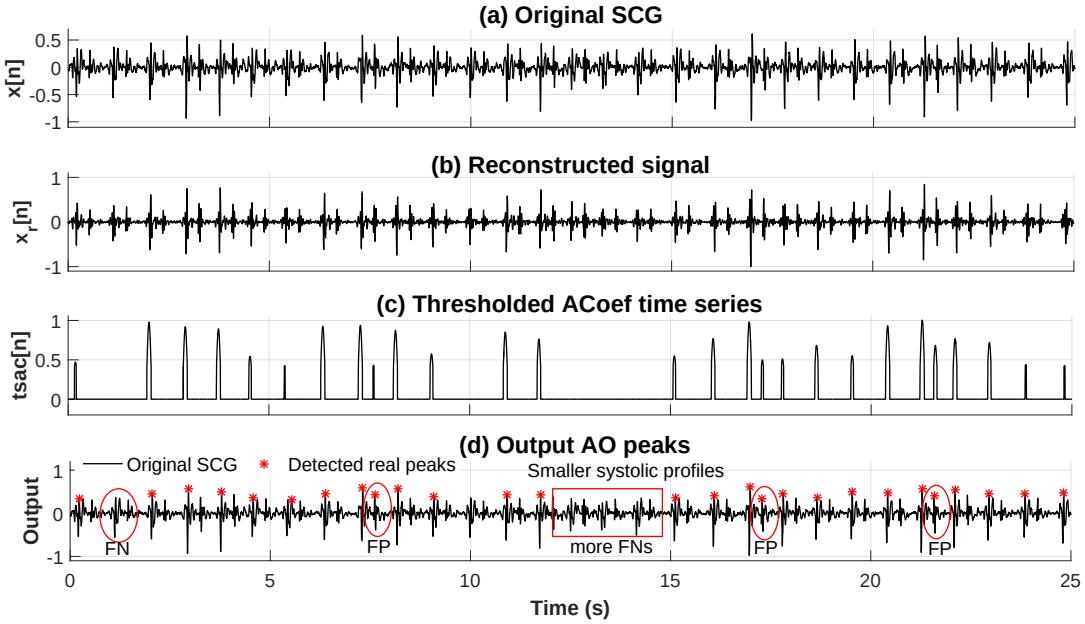

Figure 2.14: Performance of the proposed AO peak detection algorithm in the presence of smaller systolic profiles and larger diastolic profiles. (a) Original SCG, (b) wavelet reconstructed signal, (c) thresholded ACoef signal, and (d) detected real AO-peaks.

method produces more FPs and FNs. The performance of the proposed method for the SCG signal having numerous smaller systolic profiles is presented in Figure 2.14.

Records b001 and b006 have larger variations in AO amplitudes. Our method gives more FPs for two records, 003 and 020, across all the records in the database due to their distorted beats and spurious spikes. Thus, by eliminating these two records (003 and 020), the overall performance are

Table 2.2: Comparison of the proposed method with previous state of the art methods for AO peak detection

Method	Subject position	Accelerometer	Test databases	F_S (Hz)	Tested on (duration; subjects)
[60]	Supine	Brüel Kjær 4381	SFU_GYM, BGH, TC	NA	6846 beats; 105
[24]	Supine	MMA8451Q	TRC Lab	800	1300 beats; 20
[61]	Supine	DSPACE	KNU	500	45 minutes; 5
[110]	Supine	Brüel Kjær 4381	Negative Pressure	NA	NA; 18
[48]	Supine	ST LIS3LV02DL	Gnocchi ONLUS	200	8 minutes; 2
[12]	Sleep	MMA8451Q	ISS Expedition	200	36000 beats; 1
[29]	Supine	Brüel Kjær 4381	LBNP data	NA	21610 beats; 18
		ST LIS344ALH	CEBS	5000	4585 beats; 20
Proposed	Supine	ST LIS344ALH	CEBS	5000	4585 beats; 20

Method	Need of ECG	Defected beat rejection	Performance
[60]	Yes	Yes	Se (%): 74, 68, 42
	No	Yes	Se (%): 32, 14, 21
[24]	Yes	No	–
[61]	Yes	No	FN: 8
[110]	No	Yes	ACC (%): 96.2±4.2
[48]	Yes	No	–
[12]	Yes	Yes	+P (%): 99.9
[29]	No	No	Timing error: 9±9 ms
	No	No	Se: 90%, +P: 88%, ACC: 83%
Proposed	No	No	Se: 94%, +P: 90%, ACC: 86%

achieved as Se = 94.5%, +P = 93.4% and ACC = 88.65%. It is to be noted that most of the well established state-of-the-art methods directly rely on ECG R-wave [24, 61]. Moreover, some of the methods use temporal envelopes [10, 29], which cannot be implemented when the signals have more inter-beat and intra-beat variabilities. In Table 2.2, a detailed comparison of the proposed method with previous AO peak detection methods is given. An average timing difference of 9±9 ms is reported in AO peak detection over 21610 cardiac cycles [29]. In [60], the authors reported an overall average detection rate per individual recordings (DRI) of 32%, 14%, and 21% for three test datasets in different cardiac conditions without using ECG. The DRI is very much similar to the parameter "sensitivity" used in our study. Unlike the methods proposed in [60, 110], and [12], the performance of our method is satisfactory even in the presence of low-quality beats during the experimentation.

To show the applicability of the proposed method in HRV estimation, the cardiac cycles extracted from estimated AO peaks are compared with the RR intervals of ECG signals. All twenty SCG records of duration 30 s with concurrent ECG are taken for the study. Using the well-known Pan-

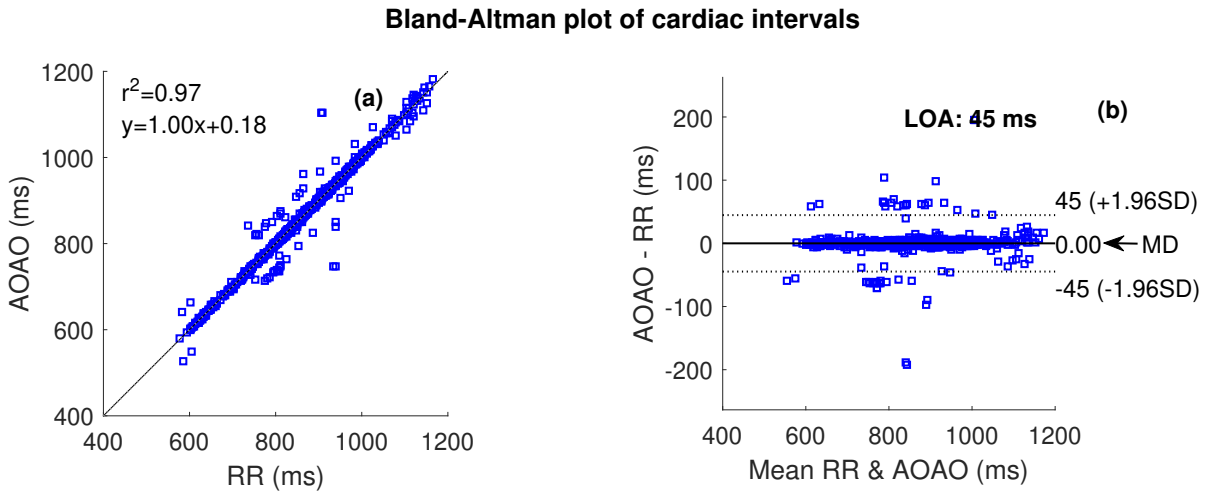

Figure 2.15: Comparison of heartbeats extracted from RR and AO-AO intervals using (a) correlation plot, and (b) Bland-Altman plot. In correlation plot, root mean squared error is achieved as 23 ms. Limits of agreement in 95% confidence intervals are shown in dotted lines. (Abbreviations used— r^2: Pearson's R-squared correlation coefficient, LOA: limits of agreement, MD: mean difference, SD: standard deviation of difference).

Tompkins method, R-peaks in the ECG are detected. The comparison is shown via correlation and Bland-Altman plots in Figure 2.15. A high correlation coefficient (R-squared $r^2 = 0.97$) and a large population-size (>93% data) under 95% limits of agreement (LOA) reveals good correlation and agreement, respectively. Hence, the proposed method may be used for HRV analysis application.

2.2.3.2 Noise stress test

The SCG signal is normally affected by different types of noises, such as baseline drift, additive white Gaussian noise (AWGN), motion artifact, friction noise, interference from respiratory efforts, and power line interference. In this study, some noises encountered in the CEBS database are examined by our method, and we observed that the proposed algorithm is robust to these external noises and physiological interferences. The effectiveness of the proposed algorithm can be observed in the presence of various noises, as shown in Figure 2.16. It shows the detection performance when the SCG signal has amplitude variations between consecutive AO-peaks and is contaminated with AWGN noise (signal-to-noise ratio 1 dB) and severe baseline trending effect. For these kinds of SCG recordings, the proposed algorithm can give 100% true detections.

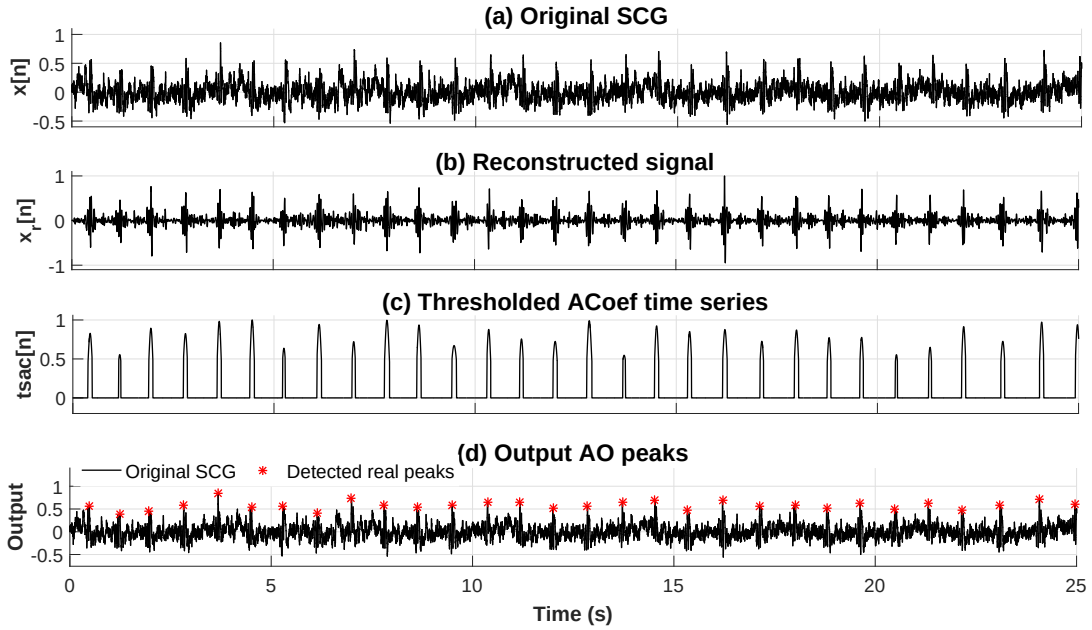

Figure 2.16: Detection performance of the proposed algorithm under AO peak amplitude variations, baseline drifts and AWGN noise. (a) Original SCG, (b) wavelet reconstructed signal, (c) thresholded ACoef signal, and (d) detected real AO-peaks. Our method gives an accuracy of 100% in these cases.

2.2.4 Conclusion

In this study, a multiresolution and statistical approaches based algorithm for standalone automated AO peak detection of the SCG signal is proposed. The AO peaks can be detected without ECG R-wave as a reference. The multiscale wavelet decomposition is carried out to get signal components in different wavelet subbands. The subbands having possible AO peaks are selected by a newly proposed DMK and DMCF based criteria. The systolic profiles are enhanced using RSDMK weights. The envelope of a systolic profile is extracted using the SEE operator, followed by the autocorrelation feature. Finally, AO peaks are approximated using a FOGD filtering based approach. The method is tested and validated on publically available CEBS database. The proposed method achieves a mean sensitivity of 94%, a mean prediction rate of 90%, and a mean detection accuracy of 86%, approximately over 4585 analyzed beats. The performance results show that the proposed method is comparable to the methods reported in the literature. Additionally, our method can give good accuracies even with a very less number of analyzing beats. The salient point of this method is that both time and frequency information are jointly employed. A novel combination of temporal-based DMK and spectral-based DMCF criteria is used for subband selection. At any step of the proposed algorithm, temporal based thresholding is not performed. Thus, it may show good performance on

tachycardia and bradycardia arrhythmic test cases. However, it requires extensive validations with real-time arrhythmic signals. The limitation of the method is that it is unable to produce proper reconstruction for many amplitude-varying signals, since it suffers from hard band-limits for their subbands. Due to that, its performance slightly reduces. Our current research work mainly deals with the SCG database acquired from healthy individuals, and so, the detection of the parameters of SCG signals acquired from cardiac patients constitutes future research in this direction.

2.3 Modified Variational Mode Decomposition Based Method

This approach presents a data-adaptive time-frequency distribution technique to resolve and analyze the SCG signal for a better harmonic representation. The variational mode decomposition (VMD) is preferred over other methods such as wavelet transform (WT), empirical mode decomposition (EMD), and their variants [122]. In VMD, the common problem of EMD, known as the mode-mixing problem, is removed without creating noise assisted ensembles, unlike EEMD and complete ensemble empirical mode decomposition with adaptive noise (CEEMDAN) [122]. In wavelet methods, WT suffers from hard band limiting for each subband and is not a data-adaptive approach, and adaptive WT *i.e.* EWT suffers from the need to pre-define the boundaries of filter bank [122]. Thus, VMD-based signal decomposition is opted in the current work.

We propose a noise-robust AO peak detection system without using a reference ECG. The VMD is applied for suppressing baseline drift from the signal, and it extracts significant modes of the signal. The manual selection of important input parameters such as mode bandwidth constraint (α) and the number of modes (K) in the traditional VMD is a crucial task. It has motivated us to propose a modified VMD (MVMD), which is able to provide an optimal combination of parameters α and K for SCG signal decomposition. Gaussian derivative filtered modes (GDFM) are obtained in order to enhance the systolic profiles of the extracted modes. Probable AO peaks rich GDFMs are selected based on proposed relative GDFM energy (RGE), and finally, the signal is reconstructed. The AO peaks are approximated by our envelope construction technique and Hilbert transform-based peak detection logic. Finally, valid AO peaks are determined with the help of a cardiac cycle envelope (CCE).

[2]This work has been published in IEEE Sensors Journal, 2020 (Refer *List of Publications* page for details).

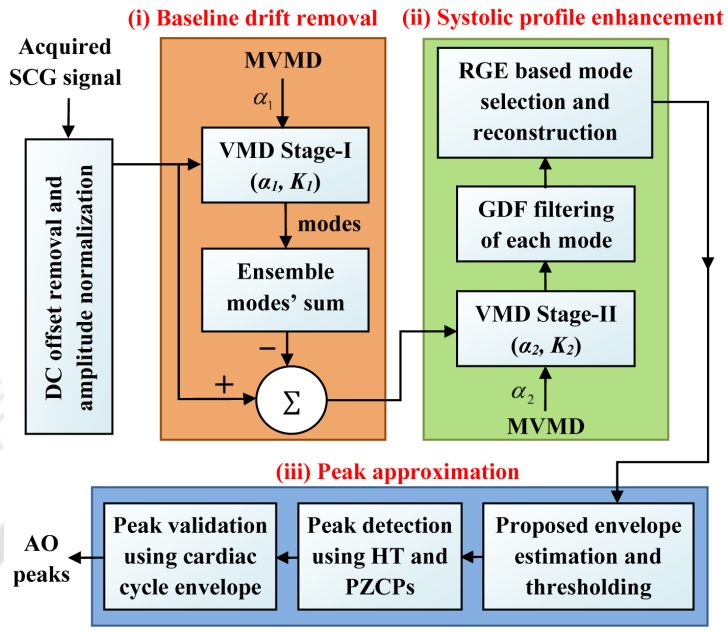

Figure 2.17: Block diagram of the proposed AO peak detection framework.

2.3.1 Proposed AO peak detection method

The VMD is able to reduce the limitations of other signal decomposition techniques such as EMD, WT, and their variants [122]. However, for a particular application, it does not have an ability to automatically control the allowable bandwidth in each mode, which is very crucial for signal decomposition task. To avail of this facility, a modified VMD is proposed.

A schematic block diagram of the proposed AO instant detection scheme is illustrated in Figure 2.17. It consists of three modules: (i) baseline drift removal, (ii) enhancement of systolic profiles, and (iii) peak approximation. Initially, a zero mean and amplitude normalized SCG signal, affected by baseline drift, is denoised by the first stage of VMD decomposition. For each stage of decomposition, the optimal balancing parameter of data fidelity constraint is determined by our MVMD optimization model. Furthermore, enhancement of systolic profiles involves following operations: representation of diagnostic information in the form of modes using second stage VMD decomposition, Gaussian derivative filtering (GDF) of modes, selection of appropriate modes using RGE criterion, and signal reconstruction with squared RGE weights. In our proposed method, the AO peaks are estimated by an envelope construction method followed by a Hilbert transform-based peak detection scheme. Finally, true AO peaks are identified with the help of a CCE envelope.

2.3.1.1 Proposed modified VMD (MVMD) based SCG filtering

The VMD is an adaptive and non-recursive data decomposition model, which computes the relevant spectral bands and the associated modes [122]. It can decompose a signal into a set of modes in such a way that modes collectively reconstruct the input signal in a least-square sense. Extracted modes are band-limited about central frequencies, which are updated in each iteration. The main constituents of VMD are Wiener filter for noise reduction, Hilbert transform for unilateral band analytic signal, and harmonic mixing for frequency translation into baseband. A real valued multicomponent signal $x(t)$ may be decomposed using VMD into a finite number of modes $m_k(t)$, which are mostly centered around a central frequency ω_k. The bandwidth of each mode is assessed as follows: (i) construction of an analytic signal for each mode m_k, (ii) mixing of each mode with an exponential ($e^{-j\omega_k t}$) tuned to the corresponding estimated ω_k, (iii) performing squared L^2-norm operation on the gradient. The resultant constrained variational problem is following [122]:

$$\min_{m_k,\omega_k} \sum_{k=1}^{K} \left\| \frac{\partial}{\partial t} \left\{ \left[m_k(t) + j\left(\frac{1}{\pi t} * m_k(t)\right)\right] e^{-j\omega_k t} \right\} \right\|_2^2 \quad \text{s.t.} \sum_{k=1}^{K} m_k(t) = x(t) \tag{2.22}$$

where '$*$' is convolution operator. $\{m_k\}$:=$\{m_1, m_2, ..., m_K\}$ and $\{\omega_k\}$:=$\{\omega_1, \omega_2, ..., \omega_K\}$ denote the set of modes of the signal $x(t)$ and the corresponding central frequencies, respectively. This constraint optimization problem (2.22) is solved by using Lagrange multipliers and a quadratic penalty term. The quadratic penalty term is used to stimulate reconstruction fidelity, if additive white Gaussian noise is present. Moreover, Lagrange multipliers are generally used to enforce constraints strictly. The resultant unconstrained problem is as follows:

$$\begin{aligned}\mathcal{L}(m_k, \omega_k, \lambda) = \alpha \sum_{k=1}^{K} \left\| \frac{\partial}{\partial t} \left([m_k(t) + j\widehat{m}_k(t)]\, e^{-j\omega_k t} \right) \right\|_2^2 \\ + \left\| x(t) - \sum_{k=1}^{K} m_k(t) \right\|_2^2 + \left\langle \lambda(t), x(t) - \sum_{k=1}^{K} m_k(t) \right\rangle\end{aligned} \tag{2.23}$$

where, α denotes the balancing parameter of the data fidelity constraint and $\widehat{(\cdot)}$ is Hilbert transform operator. Then, the alternate direction method of multipliers (ADMM) is used to solve Eq. (2.23). The algorithm for complete optimization of VMD is summarized in Algorithm 1 (steps 1 to 9), where

Algorithm 1 Pseudocode for proposed MVMD optimization

Initialization: K, $\alpha = 10$, $\mathrm{F_H}$
Input: $x(n)$
Initialize: $\widetilde{m}_k^1$, ω_k^1, $\widetilde{\lambda}^1$, $n \leftarrow 0$
repeat
  $n \leftarrow n + 1$ ▷ Number of iterations
  for $k = 1$ to K **do**
    Update $\widetilde{m}_k$ for all frequencies $\omega \geq 0$:

$$\widetilde{m}_k^{n+1} \leftarrow \frac{\widetilde{x}(\omega) - \sum_{i<k} \widetilde{m}_i^{n+1}(\omega) - \sum_{i>k} \widetilde{m}_i^{n}(\omega) + \frac{\widetilde{\lambda}^n(\omega)}{2}}{1 + 2\alpha(\omega - \omega_k^n)^2} \tag{2.24}$$

    Update ω_k:

$$\omega_k^{n+1} \leftarrow \frac{\int_0^\infty \omega |\widetilde{m}_k^{n+1}(\omega)|^2 d\omega}{\int_0^\infty |\widetilde{m}_k^{n+1}(\omega)|^2 d\omega} \tag{2.25}$$

  end for
  Update $\widetilde{\lambda}$ for all frequencies $\omega \geq 0$:

$$\widetilde{\lambda}^{n+1}(\omega) \leftarrow \widetilde{\lambda}^n(\omega) + \tau \left(\widetilde{x}(\omega) - \sum_k \widetilde{m}_k^{n+1}(\omega) \right) \tag{2.26}$$

until convergence criterion: $\sum_{k=1}^{K} \frac{\|\widetilde{m}_k^{n+1} - \widetilde{m}_k^n\|_2^2}{\|\widetilde{m}_k^n\|_2^2} < \epsilon$
if any $\omega_k > \mathrm{F_H}$, $\forall\ k = 1 : K$ **then**
  repeat

$$\Delta_k = \omega_k - \mathrm{F_H} \tag{2.27}$$

$$\eta = \frac{\max(\Delta_k)}{\sum_k |\Delta_k|} \tag{2.28}$$

$$\alpha \leftarrow \alpha(1 + \eta) \tag{2.29}$$

    Repeat steps 1 to 9 with updated α
  until all $\omega_k \leq \mathrm{F_H}$, $\forall\ k = 1 : K$
end if
if any $D_k := (\omega_{k+1} - \omega_k) < 0$, $\forall\ k = 1 : K - 1$ **then**
  repeat

$$\eta = \frac{\min(D_k)}{\sum_k |D_k|} \tag{2.30}$$

$$\alpha \leftarrow \alpha\,(1 - |\eta|/2) \tag{2.31}$$

    Repeat steps 1 to 9 with updated α
  until all $\omega_k \leq \mathrm{F_H}$, $\forall\ k = 1 : K$
end if
Output: $\alpha_{\text{optimum}} \leftarrow \alpha$

$\widetilde{(\cdot)}$ is Fourier transform operator. Minimization of the argument of unconstrained problem (2.23) with respect to m_k and ω_k shows Wiener filter behaviour (Eq. (2.24)) and expression for center of gravity of the respective mode's power spectral density (Eq. (2.25)), respectively. The mode in the temporal domain is estimated as the real part of the inverse Fourier transform of the respective filtered analytic signal. The VMD process depends on numerous input quantities: the number of the modes (K), the bandwidth constraint (α), the initial central frequency (ω), the tolerance for convergence condition (ϵ), and the time step of the dual ascent (τ).

The variational mode decomposition mainly depends on two major parameters: the bandwidth constraint (α) and the number of modes (K). For a specific event detection, the optimal selection of both the parameters is essential. The parameter α controls the bandwidth of a mode, and K controls the distribution of energy. A large value of α allows small frequency bands in the decomposed modes and provides less spectral separability among the modes. Similarly, a small value of α yields the modes with large bandwidths, which are highly separable in the spectral domain [122].

The modified VMD (MVMD) automatically update α for a given number of modes. The model is initialized with a small α (say, α=10) and a fixed K value. The model employs VMD recursively until the following two nested criteria are satisfied:

- **Criterion 1:** Each of the decomposed modes must have central frequency less than a fixed cut off frequency F_H. In other cases, α is incremented by $(\eta/100)\%$, where η is maximum normalized central frequency difference from F_H. Thus, α is updated adaptively with F_H. The updation of α is given by Eqs. (2.27)–(2.29) in Algorithm 1. After updating α, VMD is applied to the signal, and criterion 1 verifies the estimated ω_k's of decomposed modes repeatedly until this criterion is satisfied.

- **Criterion 2:** The central frequencies of consecutive modes must be in the increasing order. Otherwise, α is decremented by a small value of $(\eta/200)\%$, where η is the minimum normalized difference of consecutive central frequencies. Thus, α is being updated with central frequency variations. The updation of α is given by Eqs. (2.30)–(2.31) in Algorithm 1, where $D_k = \omega_{k+1} - \omega_k$. Subsequently, the signal is decomposed with an updated version of α, and the estimated ω_k's are cross-checked by criterion 2 recursively. Optimum α is obtained when this criterion is satisfied.

The SCG signal, denoted by $x[n]$ $(n = 1, 2, ..., N)$, is decomposed using two stage VMD. The decompositions are done to remove low-frequency (LF) artifacts and to segregate all the essential SCG informative components. The LF artifacts mainly reside in the frequency range of 0 to 1.5 Hz, and the major systole profile information of the SCG lies under 45 Hz frequency [3]. Thus, the parameter F_H is set at 1.5 Hz in stage-I for capturing LF artifacts and 45 Hz in stage-II for estimating systole profile components. In the first stage of VMD, $x[n]$ is decomposed in two modes ($K = 2$) with $\alpha = 8 \times 10^6$, which is determined from the proposed MVMD model. This process is shown in

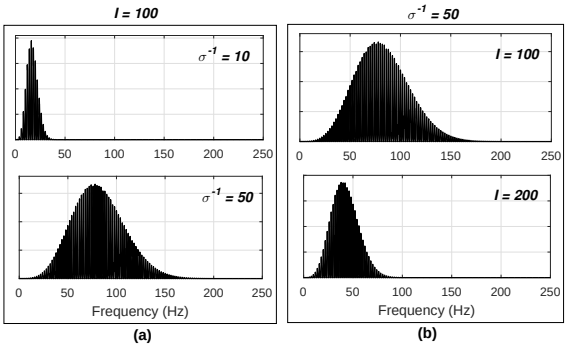

Figure 2.18: Effects of GDF parameter variation (I, σ) on magnitude spectrum. This experiment is performed on multi-sinusoid signal having all harmonic components of 2 Hz frequency in the range of 0–200 Hz.

Figure 2.22. It captures baseline drift in the first mode and other low frequency motion artifacts in the second mode as shown in Figure 2.22(b)–(c), which combinedly show the trend of the input signal. The detrended SCG signal is estimated as:

$$x_d[n] = x[n] - \sum_{\phi=1}^{2} m_{\phi}^{\mathrm{I}}[n] \tag{2.32}$$

where ϕ denotes the mode index, $m_{\phi}^{\mathrm{I}}[n]$ represents decomposed modes of the first stage of the VMD process, and $x_d[n]$ is the resulting detrended signal.

In the second stage, all information (systolic profile, diastolic profile, and motion artifacts) present in the detrended SCG are resolved into different modes, which are denoted by $m_{\gamma}^{\mathrm{II}}[n]$ (γ corresponds mode index for second stage VMD) individually. For this purpose, an average value of α is obtained by the proposed MVMD model for four number of modes. To represent the relevant systolic profile information, a minimum of four modes are found optimal. From the decomposition results, as shown in Figure 2.23(a) for $\alpha = 800$, it is observed that modes containing diagnostic information are spectrally separated. It is desired to select the modes having significant systolic profile information. Before this, the information of the systolic profile is enhanced from each of the modes by a Gaussian derivative filtering technique.

2.3.1.2 GDF filtering for emphasizing systolic profiles

To emphasize the systolic profile components present in each mode, Gaussian derivative filtering (GDF) is applied. The creation of a Gaussian window is parameterized on the length I and the standard deviation σ to select the specific frequency band. For a fixed σ, the small I value yields high-frequency components in the filtered output and vice-versa (Figure 2.18). The cut-off frequency

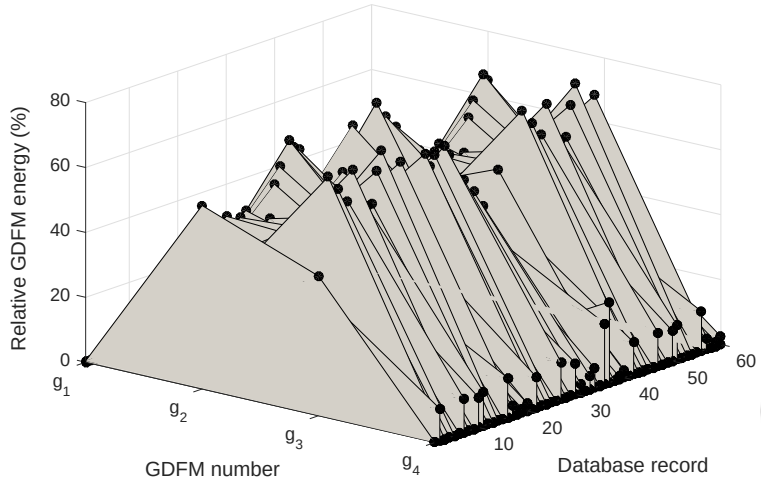

Figure 2.19: RGE contribution by each GDFM for CEBS database.

of Gaussian smoothing window is related to σ as $\sigma^{-1} = (\frac{\mathrm{F}_c}{\mathrm{F}_s/2})I$. The F_c and F_s are cut-off and sampling frequency, respectively. Low σ value decreases the width of the window and minimizes the discontinuity at the boundaries. However, it increases the spectral width of the main lobe and decreases the side-lobe levels [126]. The I-point Gaussian window is generated as [126]:

$$w[i] = e^{-\frac{1}{2\sigma^2}\left[\frac{i}{(I-1)/2}\right]^2} \qquad 0 \leq |i| \leq \frac{(I-1)}{2} \tag{2.33}$$

The first order Gaussian derivative coefficients are computed as $d[j] = w[j+1] - w[j]$, where $j = 1, 2, .., I-1$. Then, each Gaussian derivative filtered mode (GDFM) is estimated as:

$$g_\gamma[n] = \sum_{k=-\infty}^{\infty} d[k] \cdot m_\gamma^{\mathrm{II}}[n-k] \tag{2.34}$$

where, $g_\gamma[n]$ represents GDFM corresponding to γ^{th} mode of the second stage VMD decomposition, *i.e.*, $m_\gamma^{\mathrm{II}}[n]$. Both the parameters σ and I change the characteristic of GDFM. These parameters are chosen in such a way that the energy of the systolic profile in each of the modes would be maximum. For a fixed value of $I = 210$, the spread parameter σ is determined as 0.05 to obtain a cut-off frequency of 45 Hz. In this way, SCG systole components present in each of the VMD modes get boosted, while the energies of other profile components are reduced in all the GDFMs. This is depicted in Figure 2.23(b), which clearly shows that g_2 and g_3 contain systolic components of SCG, and they possess more energies. In addition to that, g_2 and g_3 show perfect AM-FM characteristics.

2.3.1.3 Proposed relative GDFM energy (RGE) criterion

Proper selection of GDFMs is important for accurate AO peak detection. The optimal GDFM having higher energy of systolic profile is selected using relative GDFM energy (RGE). The RGE measures the amount of systole energy shared by each GDFM, which is defined as:

$$e_\gamma = \left(\sum_{n=1}^{N}(g_\gamma[n])^2\right) \Big/ \left(\sum_{\gamma=1}^{4}\sum_{n=1}^{N}(g_\gamma[n])^2\right) \tag{2.35}$$

where, e_γ represents the RGE contribution by γ^{th} GDFM. The percentage RGE contribution by each GDFM is depicted in Figure 2.19 for each of the 60 records of the CEBS database. It is observed that g_2 and g_3 exhibit major energy contribution in all the cases. Based on maximizing the RGE criterion across all the modes, a reconstructed signal ($s[n]$) is created as:

$$\gamma^* = \underset{\{\gamma=1,2,..,4\}}{arg\ max}\,[e_\gamma] \tag{2.36}$$

$$s[n] = \begin{cases} e_{\gamma^*}^2 g_{\gamma^*} + e_{\gamma^*-1}^2 g_{\gamma^*-1} & \text{if } |e_{\gamma^*} - e_{\gamma^*-1}| < \rho \\ e_{\gamma^*}^2 g_{\gamma^*} + e_{\gamma^*+1}^2 g_{\gamma^*+1} & \text{if } |e_{\gamma^*} - e_{\gamma^*+1}| < \rho \\ g_{\gamma^*} & \text{otherwise} \end{cases} \tag{2.37}$$

where, γ^* denotes the optimal mode number. The tolerance for RGE difference, denoted by ρ is chosen as 20% for better precision. Eq. (2.37) confirms that the maximum two modes are enough to represent the harmonics of an enhanced systolic region.

2.3.1.4 Envelope construction scheme

The reconstructed signal $s[n]$ follows the characteristics of an AM-FM signal. It is observed that the profiles of $s[n]$ are symmetric with respect to x-axis. Based on this fact, an upper envelope (U_{env}) is constructed by exploiting maximum slope information in every small segment of $s[n]$. Similarly, a lower envelope (L_{env}) is constructed from minimum slope information. The linear interpolation scheme is used to get these envelopes. Our proposed algorithm for construction of U_{env} and L_{env} envelopes is given in Algorithm 2. In order to emphasize the envelope of $s[n]$, a resultant envelope is constructed by the difference of U_{env} and L_{env} as: $\text{D}_{\text{env}} = \text{U}_{\text{env}} - \text{L}_{\text{env}}$. The results of D_{env} computation are illustrated in Figure 2.20. Then, a thresholding operation is performed on D_{env} to suppress other than

Algorithm 2 Pseudocode for envelope construction

Initialize: $i \leftarrow 1$, $z \leftarrow \{1$ for $\mathrm{U_{env}}\}$ or $\{-1$ for $\mathrm{L_{env}}\}$, $l \leftarrow 1$, x: test signal, L_w: width for interpolation, i: sample index

1: **repeat**

2: Compute the index exhibiting maximum slope information:

$$idx = \underset{\{j\}}{arg\ max} \left[\left(\frac{x_j - x_i}{j - i} \right) z \right] \qquad (2.39)$$
$$j = (i+1), (i+2), .., (i+L_w)$$

3: Update sample index: $i \leftarrow i + idx$

4: Store sample index: $\beta_l \leftarrow i$

5: Increment loop index: $l \leftarrow l + 1$

6: **until** criterion: $(i + L_w) \geq length(x_i)$

7: Interpolate linearly all the adjacent points (β, x_β)

Output: Envelopes: $\mathrm{U_{env}}$ and $\mathrm{L_{env}}$

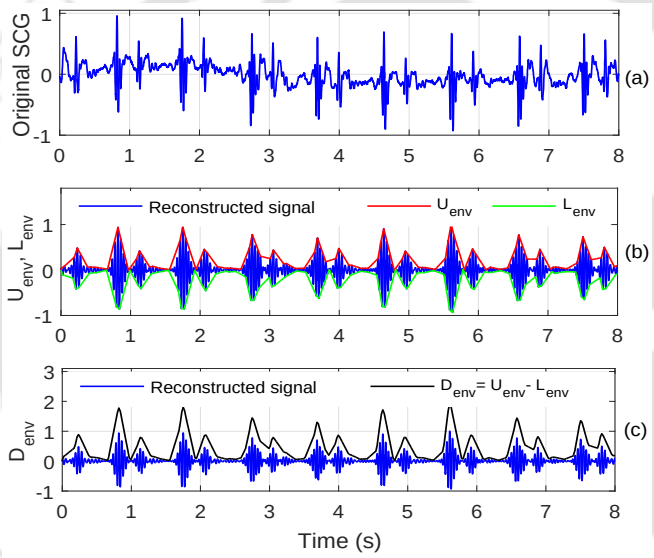

Figure 2.20: Envelope construction process. (a) SCG signal, (b) $\mathrm{U_{env}}$, $\mathrm{L_{env}}$: upper and lower envelopes on $s[n]$, and (c) $\mathrm{D_{env}}$: resultant envelope.

systole regions as:

$$\mathrm{T_{env}[n]} = \begin{cases} \mathrm{D_{env}[n]}, & \text{if } \mathrm{E_{env}[n]} > \tau \\ 0, & \text{otherwise} \end{cases} \qquad (2.38)$$

where $\tau = 2 \cdot std\{\mathrm{E_{env}}[n]\}$ and $std\{\cdot\}$ denotes standard deviation. $\mathrm{E_{env}}$ denotes the instantaneous energy of $\mathrm{D_{env}}$ and $\mathrm{T_{env}}$ is the thresholded envelope. Figure 2.24(c) and (d) show the process of thresholding the $\mathrm{D_{env}}$ signal.

2.3.1.5 AO peak detection scheme

The pulses of $\mathrm{T_{env}}$ and their peaks are used to approximate the AO peaks in the SCG signal. To detect AO peaks in the SCG signal, Hilbert transform (HT) is applied to $\mathrm{T_{env}}$ signal. The positive zero-

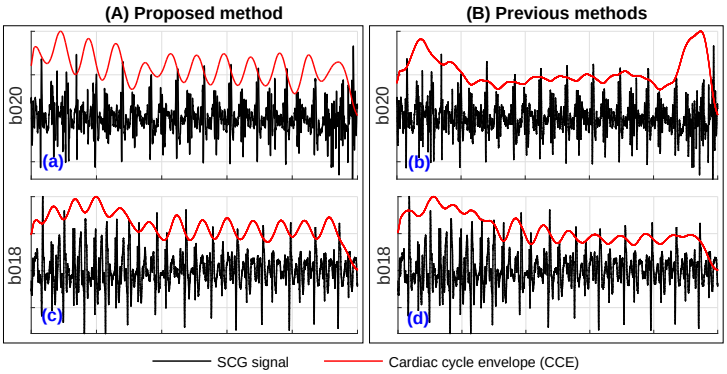

Figure 2.21: Performance of CCE construction on two different SCG data: b020 and b018. (A) Proposed scheme, and (B) previous CCE extraction methods.

crossing points (PZCP) of Hilbert transformed envelope provides an exact estimation of T_{env} signal peaks, which is shown in Figure 2.24(e). It is the first level approximation of AO peaks. Finally, all the AO peaks are localized in the SCG signal using a 70 ms extrema search window centered around approximated peaks, and the results are shown in Figure 2.24(f).

2.3.1.6 True peak identification using cardiac cycle envelope

To reduce the number of false detections, valid AO peaks are identified with the help of a cardiac cycle envelope (CCE). The CCE construction on the SCG signal is inspired by the method proposed in [29,60]. The only difference in our method is that it relies on GDFMs instead of direct SCG signal. The important GDFMs are selected based on their cardiac periodicity behavior. Initially, each of the GDFMs is smoothed using a zero-phase moving average filter of order 400 ms. The periodicity of each smoothed GDFM is determined by the autocorrelation measure. The GDFMs showing heart rates 40–200 bpm, are selected. In addition, the difference between the second peak and first valley must be at least 250 ms in the autocorrelation for selecting important GDFMs. The signal reconstructed from selected GDFMs is employed for absolute envelope construction, and triple integration [29] is applied to obtain the CCE envelope. The performance of the proposed CCE construction is better than the prior methods [29,60], and the comparative results are shown in Figure 2.21. The detected AO peaks within 350 ms duration of consecutive CCE-peaks are treated as valid AO peaks. Moreover, the information of time intervals between successive valid AO peaks indicates heart rates, which can also be used for HRV analysis.

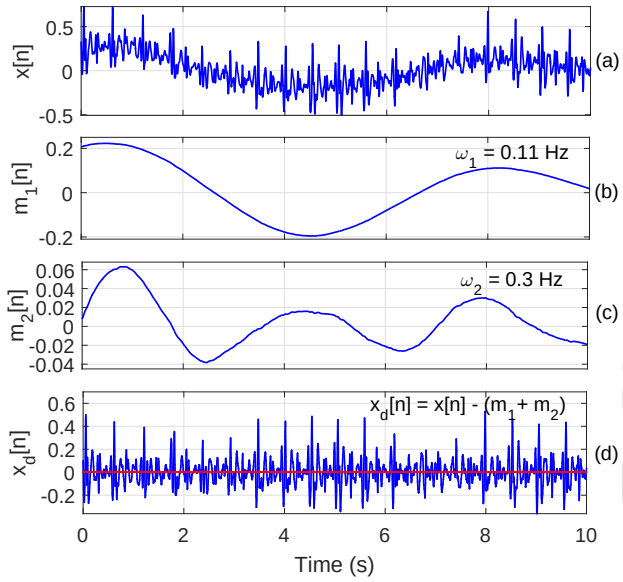

Figure 2.22: Removal of LF artifacts in the first stage of VMD. (a) Input SCG, (b)–(c) decomposed modes, and (d) detrended signal, which is free from baseline drift and other LF artifacts.

2.3.2 Results and discussion

2.3.2.1 Data collection

The SCG signals were recorded from the xiphoid process on chest walls of five male subjects (demographics: 28±3 yrs, 74±5 kgs) in two different sessions, first with normal breathing for 5 minutes and subsequently, with holding breath for 40 s. The signals were recorded using a self-built SCG acquisition circuit at IIT Guwahati (IITG), by taking proper consent of subjects.

Besides the testing with our real-time registrations of 10 signals, the proposed method is also tested with 20 SCG signals, taken from standard CEBS database (publically available at Physionet archive), recorded from 20 basal stated subjects [125]. The SCG database contains signals with trending effect, baseline drift, motion artifact, wider systolic profile, narrow systolic profile, sudden changes in systolic profile amplitudes and patterns, irregular cardiac rhythms, cases with lower AO amplitudes and strong diastolic profile patterns.

2.3.2.2 Experiment

A ten seconds segmented data from SCG signal is fed into the proposed algorithm. At first, very low-frequency contents, including the baseline drifts, are removed from the acquired SCG signal in the first stage of VMD decomposition. It uses a large α ($\alpha = 8\times10^6$) for decomposing the signal into two modes.

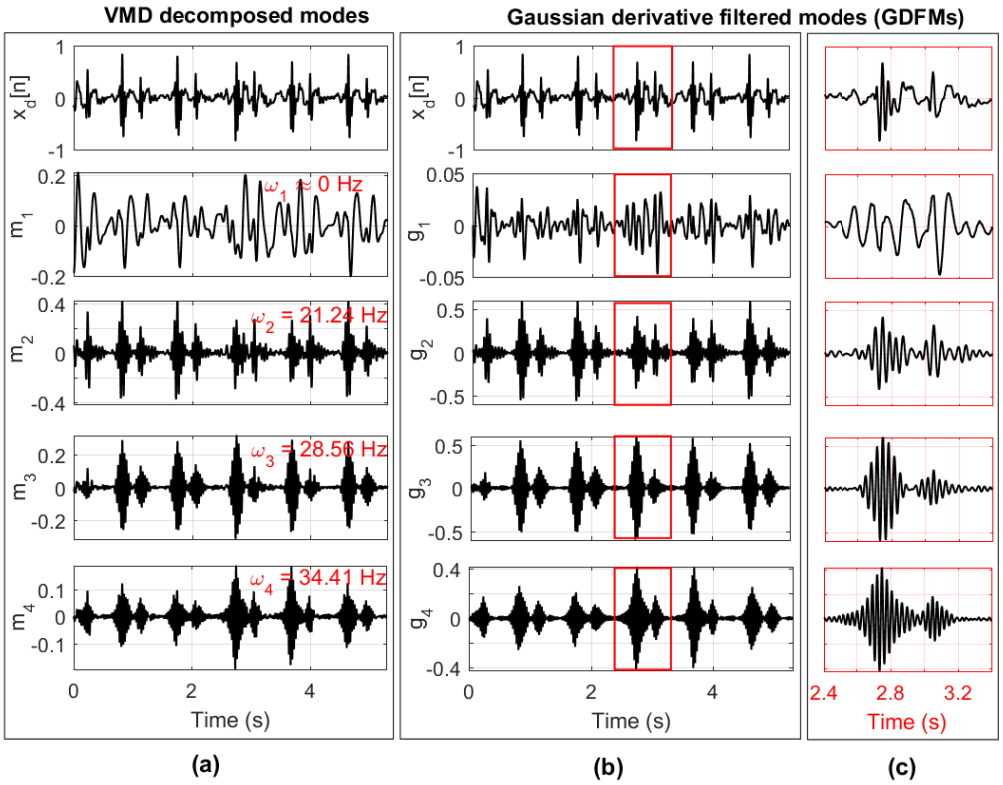

Figure 2.23: Mapping of clinical information into different modes by second stage of VMD [panel (a)] and corresponding GDFMs [panel (b)]. Third beat of every GDFM represented by red rectangular box is magnified in panel (c).

First mode provides baseline drift, whereas other low frequency artifacts are captured by the second mode as shown in Figure 2.22. These modes are subtracted from the signal to obtain a detrended signal (Figure 2.22(d)). Further, the components of resulting signal are segregated into four modes with $\alpha = 800$ in the second stage of VMD (in Figure 2.23(a)). Their central frequencies are 0, 21.24, 28.56, and 34.41 Hz, respectively. The slow varying signal components are captured by lower mode m_1, which does not carry systolic profile information. Whereas, higher modes m_2, m_3 and m_4 carry AO peak information, which are enhanced in GDFMs g_2, g_3 and g_4 (Figure 2.23(b)). Significant GDFMs with rich AO peaks are selected by using the proposed RGE criterion. The squared RGE weights are linearly combined with the selected modes to reconstruct the signal. It is evident from Eq. (2.37) that one or two modes are enough to capture the maximum systole energy. Then, systole envelopes are constructed by considering maximum slope information in a time-varying window of length $L_w = 150$ ms (Figure 2.24(c)). The HT-based technique approximates the AO peaks, and they are corrected by a symmetric search window of duration 70 ms. These steps are illustrated in Figure 2.24(e)–(f).

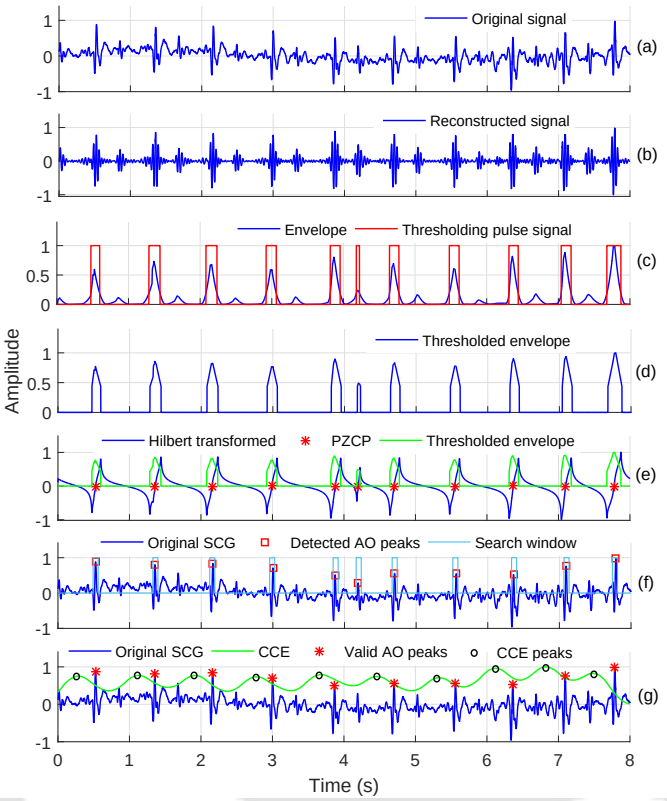

Figure 2.24: Complete AO peak detection process using the proposed framework. (a) Original SCG, (b) reconstructed signal, (c) envelope D_{env}, (d) thresholded envelope T_{env}, (e) HT of T_{env} and PZCPs, (f) detected AO peaks from search windows around PZCPs, and (g) validated AO peaks with the help of CCE.

Finally, the detected AO peaks are validated using the CCE-peaks, as shown in Figure 2.24(g). All the experiments were performed on MATLAB R2015b in a 64-bit Microsoft Windows-10 Home platform with Intel Core-i.7 CPU (1.8 GHz) and 8-GB RAM. The average computation time for the execution of the proposed algorithm on an SCG segment is approximately 3.09 s.

2.3.2.3 Performance evaluation

The computational complexity of the proposed method mainly relies on signal decomposition process. As the number of decomposition increases, reconstruction error reduces. However, CPU execution time and space requirement become slightly higher [127]. The performance of the proposed AO peak detection method is analyzed for entire basal stated recordings of the CEBS database and both sessions of the IITG database. Four quantitative benchmarks, namely, the detection error rate $\left(\text{DER} = \frac{\text{FP+FN}}{\text{TP+FN}}\right)$, the sensitivity $\left(\text{Se} = \frac{\text{TP}}{\text{TP+FN}}\right)$, the positive predictivity $\left(\text{+P} = \frac{\text{TP}}{\text{TP+FP}}\right)$ and the accuracy $\left(\text{ACC} = \frac{\text{TP}}{\text{TP+FP+FN}}\right)$ are calculated [128]. In the CEBS database, SCG records b001, b003, b005, b011, b014, b018, and b020 contain significant artifacts and noises. The severe baseline drifts

Table 2.3: Performance evaluation on signals from CEBS database (TP: true positive, FP: false positive, and FN: false negative)

SCG record	TP (beats)	FP (beats)	FN (beats)	DER (%)	Se (%)	+P (%)	ACC (%)
b001	216	14	5	8.6	97.74	93.91	91.91
b002	204	3	1	1.95	99.51	98.55	98.08
b003	205	14	24	16.59	89.52	93.61	84.36
b004	215	0	2	0.92	99.08	100	99.08
b005	236	2	5	2.9	97.93	99.16	97.12
b006	201	6	5	5.34	97.57	97.10	94.81
b007	178	2	2	2.22	98.89	98.89	97.80
b008	313	5	3	2.53	99.05	98.43	97.51
b009	199	9	7	7.77	96.60	95.67	92.56
b010	204	4	1	2.44	99.51	98.08	97.61
b011	222	7	2	4.02	99.11	96.94	96.10
b012	265	1	4	1.86	98.51	99.62	98.15
b013	236	0	2	0.84	99.16	100	99.16
b014	221	7	3	4.46	98.66	96.93	95.67
b015	218	2	1	1.37	99.54	99.09	98.64
b016	235	0	3	1.26	98.74	100	98.74
b017	240	0	1	0.41	99.59	100	99.59
b018	231	31	37	25.37	86.19	88.17	77.26
b019	209	0	1	0.48	99.52	100	99.52
b020	212	12	16	12.28	92.98	94.64	88.33
Overall	4460	119	125	5.18	97.37	97.44	95.1

are seen in records b003, b017, and b020. Records b001, b003, b006, b018, and b020 have sudden variations and unrecognizable distorted beats. In records b001, b007, and b020, AO peak magnitude is smaller than RE, while large diastolic profile patterns are observed in b011. Moreover, records b001 and b006 contain large amplitude variations of AO peaks.

The overall performance of the proposed method is summarized in Table 2.3. It is observed that b001, b003, b018, and b020 produce more FPs, while more FNs are observed for records b003, b018, and b020. However, our proposed method can accurately locate AO-peaks in the presence of noises and artifacts. Also, our method can determine AO peaks even for varying systolic and diastolic profiles. Our method cannot perfectly identify AO point when the associated wave with the MC/RE has a high-frequency component, and the corresponding peak has an amplitude greater than the AO peak. However, the method is found effective under the presence of either of the conditions. The proposed method produces 119 FP and 125 FN beats for a total number of 4585 analyzed beats. The method achieves a mean sensitivity of 97.37% with a standard deviation of 3.6%, mean prediction rate of 97.44% with a standard deviation of 3%, mean accuracy of 95.1% with a standard deviation

Table 2.4: Comparison of proposed method with previous standalone methods for AO peak detection

Method	Test datasets	(#B; #S)	Performance
[60]	SFUGYM, BGH, TC	6846; 105	Se: 32, 14, 21
[110]	Negative Pressure	NA; 18	ACC: 96.2±4.2
[29]	LBNP data	21610; 18	Timing error: 9±9 ms
	CEBS†	4585; 20	Se: 90, +P: 88, ACC: 83
Proposed-DWT	CEBS	4585; 20	Se: 94, +P: 90, ACC: 86
Proposed-MVMD	CEBS	4585; 20	Se: 97, +P: 97, ACC: 95

Note that #B: number of analyzed beats, and #S: number of subjects for data acquisition. Performance metrics such as Se, +P, and ACC are in terms of %. †: Method [29] is implemented for CEBS data set. Original manuscript does not report performance metrics for CEBS data.

of 5.8%, and mean error rate of 5.18% with a standard deviation of 6.4%. In the case of the IITG database, our method produces 96.7% Se, 96.4% +P, 93.4% ACC, and 6.9% DER over 1961 SCG beats. A detailed comparison of the proposed framework with the previous standalone AO peak detection methods is provided in Table 2.4. Most of the existing methods for AO peak detection entirely depend on R-waves of the ECG signal [24, 61]. In addition, methods relying on temporal envelopes may not be perfect for signals with more inter-beat variability [10, 29]. In [29], the authors reported a mean timing error of 9±9 ms in AO peak detection for 21610 cardiac cycles. The overall mean detection rate per individual recordings (DRI) of 32%, 14% and 21% are observed for three datasets with different heart conditions [60]. The DRI measure closely resembles to the *sensitivity* used in our study. Unlike [60] and [110], our method performs satisfactorily even in the presence of poor quality beats and large inter-beat variability. Our previous work (Section 2.2) based on discrete wavelet transformation (DWT), achieved 94% Se, 90% +P, and 86% ACC on CEBS data. The MVMD based proposed method outperforms this also.

An experiment is also performed to show the possible use of our method in HRV analysis application. For this, the cardiac cycles extracted from the AO peaks of an SCG are compared with the RR intervals of concurrent ECG signals. All the twenty records of duration 30 s are considered for the study. The comparison is shown via regression and Bland-Altman plots in Figure 2.25. It shows Pearson's R-squared correlation coefficient equal to 0.98, which reveals a strong correlation, while a good agreement can be observed in the Bland-Altman plot. This experiment supports the proposed MVMD-based method for the use of HRV estimation in the future.

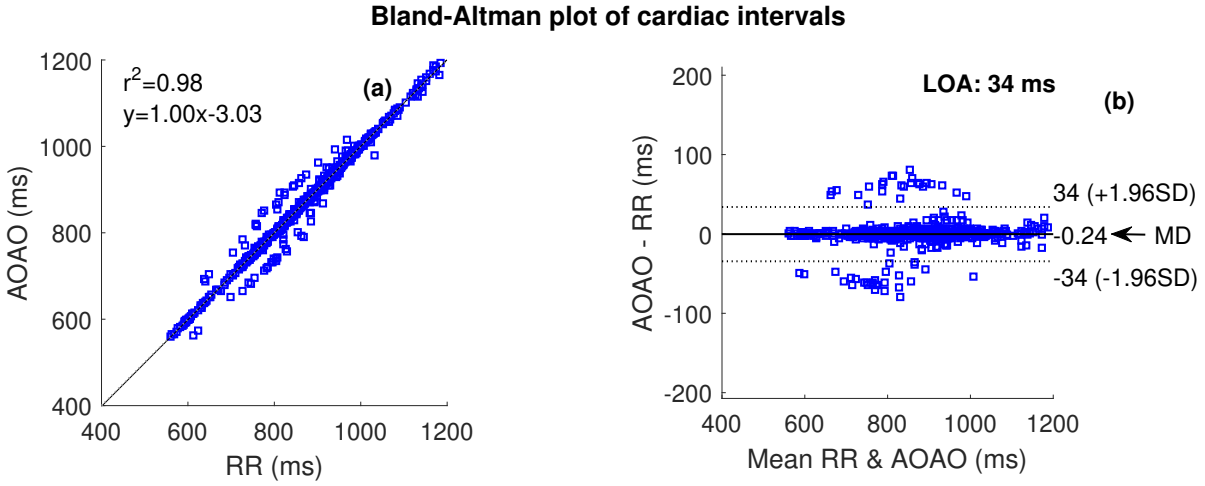

Figure 2.25: Comparison of heartbeats extracted from RR and AO-AO intervals using (a) correlation plot, and (b) Bland-Altman plot. In correlation plot, root mean squared error is achieved as 17 ms. Limits of agreement in 95% confidence intervals are shown in dotted lines.(Abbreviations used— r^2: Pearson's R-squared correlation coefficient, LOA: limits of agreement, MD: mean difference, SD: standard deviation of difference).

Table 2.5: Performance of our method under various AWGN noise levels

Performance metric →		**Se** (%)	**+P** (%)	**ACC** (%)	**DER** (%)
Signal without noise		97.42	97.45	95.16	5.06
AWGN corrupted signal	**SNR 35 dB**	97.42	97.45	95.16	5.06
	SNR 20 dB	97.42	97.38	95.09	5.21
	SNR 5 dB	96.59	96.31	93.53	7.11
	SNR 0 dB	96.24	96.06	93.09	7.7

2.3.2.4 Performance in noisy condition

The performance of the proposed method is evaluated by adding additive white Gaussian noise (AWGN). The initial one minute signals (b001-b020, CEBS database) are considered for this noise stress test. For a given signal, it is important to set accurate noise power to get the desired SNR level. Let the observed input signal is $s_o[n] = x_o[n] + \mathrm{Q} \cdot w_o[n]$, where $x_o[n]$, Q, and $w_o[n]$ are clean signal, noise constant and AWGN noise, respectively. The constant Q can be derived as

$$\mathrm{Q} = \sqrt{\left(\sum_{n=1}^{N} x_o^2[n]\right) \Big/ \left(10^{\left(\frac{SNR}{10}\right)} \cdot \sum_{n=1}^{N} w_o^2[n]\right)} \tag{2.40}$$

where SNR signifies desired SNR in dB after adding noise. Table 2.5 shows performance of the proposed method for different noise levels. The method gives Se = 97.42%, +P = 97.45%, ACC = 95.16%, and DER = 5.06% for SCG signals at 35 dB SNR. In addition to that, Se = 96.24%, +P =

Table 2.6: Overall detection performance results for different body postures and exercises

Scenarios	#Beats	Se (%)	+P (%)	ACC (%)	DER (%)
SuNB	167	97.85	97.35	95.52	4.84
SuSB	151	100	100	100	0
Sitting	187	95.3	98.21	93.8	6.42
Standing	193	96.26	96.11	92.63	7.98
SuER*	195	96.56	98.84	95.5	4.57

*To show the physiological modulation effect under SuER, the data was recorded just after two subsequent exercises: rope-skipping (60 s) and plank (60 s).

96.06%, ACC = 93.09%, and DER = 7.7% are achieved at SNR of 0 dB, which shows almost similar results obtained for 35 dB SNR. This test reveals the robustness of the proposed method for AWGN noise. The performance of the method is also evaluated for different body postures and exercises in real-time scenarios. Five different scenarios, such as supine position with normal breathing (SuNB) and supine position with stopped breathing (SuSB), sitting and standing positions, and exercise-recovery (SuER) are studied. In such scenarios, the protocols for the signal-measurement are shown in the following video link: `https://www.youtube.com/watch?v=qXcO_g90270`. The overall performance for three subjects for aforementioned scenarios is summarized in Table 2.6. For the SuSB, the accuracy is found 100% when 151 beats are analyzed. The lowest accuracy, 92.63% is found when the signal is recorded in a standing position. The consistency observed relating different performance metrics suggests the proposed algorithm may be reliable for in-field data.

2.3.3 Conclusion

In this study, the MVMD based framework for AO peak detection in the SCG signal is proposed. This method does not use ECG as a reference. The main contribution of our proposed MVMD model is the selection of optimum α for any application-specific VMD-based decompositions. In our method, the baseline drift is suppressed using the first stage of VMD. Then, systolic profiles are enhanced using the second stage of VMD, Gaussian derivative filtering, RGE criterion-based mode selection, and signal reconstruction with squared RGE weights. Subsequently, the envelope on a systolic profile is constructed based on extracted slope information. Finally, AO peaks are estimated by the Hilbert transform-based approach, and the valid peaks are identified using CCE-envelope. The proposed method achieves an average DER of 5%, an average Se of 97%, an average +P of 97%, and an average ACC of 95%, approximately over 4585 analyzed beats for CEBS database. For real-time

IITG database, 96.7% Se, 96.4% +P, 93.4% ACC, and 6.9% DER are achieved over 1961 SCG beats. The evaluation results clearly show that our method is comparable to the methods presented in the literature, as it produces good accuracies on a very less number of test beats. Also, the experimental results of our method show its noise robustness. However, the proposed method needs to be tested with real-time pathological SCG signals for clinical validations. Along with HRV analysis, the presented research-work would be very helpful to estimate other cardiac phases and their time intervals in an SCG cycle.

2.4 Summary

In this chapter, two standalone approaches are presented for the delineation of SCG signals to get an estimate of AO instants. The prominent AO phase information is suggested to extract as a primary step by these approaches, which can help in estimating other fiducial points of an SCG. These methods use time-frequency analysis based signal decomposition techniques. The first approach resolves the signal using data-independent discrete wavelet transformation, selects appropriate subbands using DMK and DMCF based criteria, and reconstructs using RSDMK weights. The detection performance for AO instants is improved in the second method that uses a data-adaptive MVMD model. It also consists of operations, such as GDF filtering of modes, relative GDFM energy extraction, construction of upper envelopes, and CCE envelopes. The MVMD-based approach outperforms others by producing an average Se of 97%, an average +P of 97%, and an average ACC of 95% for CEBS basal-stated data. These standalone approaches have substantial abilities to be used in cardiac clinics with an independent SCG signal. However, the association of SCG with other cardiac signals may help in estimating its many fiducial points with ease. In other words, multimodal cardiac analysis can surely improve diagnostic accuracy. Hence, in the next chapter, we will discuss the SCG delineation with the assistance of other cardiac signals to estimate more fiducial points.

3

SCG Waveform Delineation with the Assistance of Other Cardiac Signals

Contents

For proper characterization of both systolic and diastolic profiles of the SCG, the fiducial points associated with these profiles need to be estimated accurately. This chapter presents the proposed delineation frameworks for the SCG signals with the use of other cardiac signals as reference. The developed methods can estimate various cardiac phases from an SCG cardiac cycle, such as AO, IM, IC, pAC, AC, and MO. The chapter includes two different approaches. The first approach is based on the orthogonal subspace projection technique. With the help of a concurrent ECG signal, it estimates two important fiducial points from systole and diastole of the SCG signal, AO and pAC points, respectively. By analyzing the heart cycles, the parameter-extraction is validated with R-peaks of the ECG signal. In the second approach, we utilize the PPG signal as a reference to localize the fiducial points, IM, AO, IC, AC, pAC, and MO in the SCG waveform. Additionally, it can also compute the clinical time intervals IVRT and LVET using extracted points. The localization of SCG-diastole is a challenging task, which is made possible with the use of a PPG signal. The method includes processing of PPG-scalogram, construction of signal-envelopes, and development of histogram-based decision rules. The delineated parameters are also able to identify two respiratory events. The current chapter is organized as follows: the ECG-assisted proposed orthogonal subspace projection-based framework is presented in Section 3.1. Section 3.2 provides details of our PPG-assisted second approach for SCG-delineation. Finally, the chapter is summarized in Section 3.3.

3.1 ECG Assisted Delineation Framework

Due to inter-beat and intra-beat variabilities present in an SCG signal, the detection of AO and postAC peaks are very difficult. In this work, the AO and postAC peaks under systolic and diastolic profiles of SCG are estimated to design a heart cycle extraction framework. Most of the existing methods for SCG-cycle extraction are based on fixed windowing techniques such as- (i) determining maxima as AO peak in SCG just after R-peak in ECG, and (ii) FIR moving average smoothing with a fixed window size to get the heart cycle. As discussed earlier (Section 1.5), the use of any fixed-size window is not suitable for a signal having abnormal and irregular heart rhythms, especially when AO peak has a smaller amplitude than peak corresponding to mitral valve closure (MC) or rapid ejection (RE) instant under a systole profile.

The AO peaks are detected using the orthogonal subspace projection of an SCG signal onto

[3]This work has been published in Elsevier journal of Biomedical Signal Processing and Control, 2019 (Refer *List of Publications* page for details).

the ECG subspace. The projected signal provides more precise locations of the AO peaks. The Gaussian differentiator based scheme is employed to obtain the information of AO instants. After that, postAC peaks are detected using simple diastolic window analysis on estimated AO-AO intervals. The detections of these fiducial points are validated with manual annotations. A temporal detection error is selected as a metric to evaluate the performance of the proposed method. For validation of heart cycle extraction, an additional performance metric namely, normalized cross-correlation (NCC) is also investigated between R-peaks of the ECG and estimated fiducial points of the SCG signal.

3.1.1 Methods for heart cycle extraction

A unique framework for detection of AO and postAC peaks is proposed to extract heart cycles from an SCG signal. The intervals between consecutive peaks may be used for heart cycle extraction. The subspace projection technique is used to detect AO peaks with the help of concurrent ECG signal as a reference. Thereafter, peak after AC point is determined under diastolic profile using simple windowing technique on each of the detected AO-AO intervals.

3.1.1.1 AO instants detection

The information of SCG that is linearly related to concurrent ECG, can be extracted by projecting SCG signal on ECG subspace. The ECG subspace can be created by ECG signal and its variations. Let's ECG and simultaneously recorded SCG (z-component) signals are denoted by $\mathbf{e}$ and $\mathbf{s}$, respectively. The subspace of ECG is created by $\mathbf{e}$ and set of its delayed versions. This is expressed as $\mathbb{U}$ as shown in Figure 3.1. It represents the linear relationship of $\mathbb{U}$ and $\mathbf{s}$ as:

$$\mathbb{U}\mathbf{x} = \mathbf{s} \tag{3.1}$$

where $\mathbf{x}$ denotes the set of parameters used for $\mathbb{U}$ to approach $\mathbf{s}$. In least square error sense, the best estimate of $\mathbf{x}$ is given as [129]:

$$\widehat{\mathbf{x}} = (\mathbb{U}^{\mathrm{T}}\mathbb{U})^{-1}\mathbb{U}^{\mathrm{T}}\mathbf{s} \tag{3.2}$$

And the best estimate of $\mathbf{s}$ on the subspace of $\mathbb{U}$ is found using subspace projection as [129]:

$$\widehat{\mathbf{s}} = \mathbb{U}\widehat{\mathbf{x}} \tag{3.3}$$

$$\widehat{\mathbf{s}} = \mathbb{U}(\mathbb{U}^{\mathrm{T}}\mathbb{U})^{-1}\mathbb{U}^{\mathrm{T}}\mathbf{s} \tag{3.4}$$

$$\widehat{\mathbf{s}} = \mathbf{P}\mathbf{s} \tag{3.5}$$

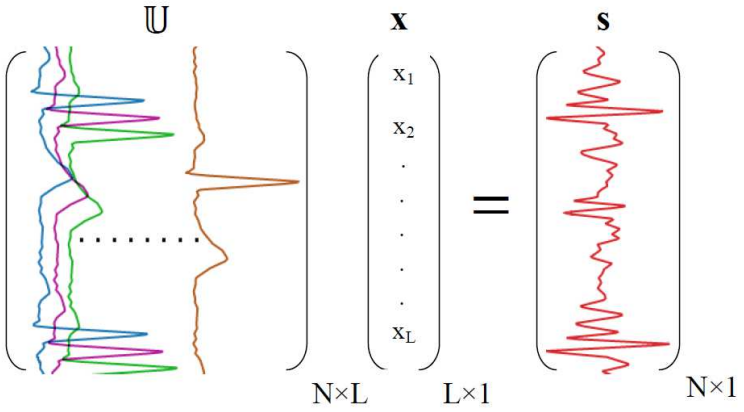

Figure 3.1: Relationship of $\mathbb{U}$ space with $\mathbf{s}$ for subspace projection.

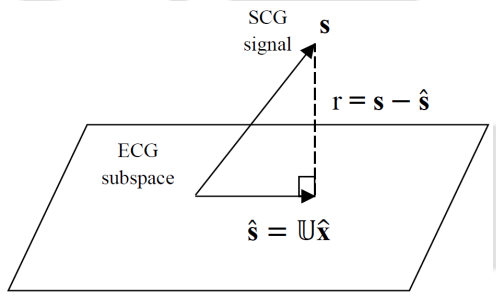

Figure 3.2: Projection of SCG signal on to ECG subspace.

where, $\mathbf{P}$ ($\mathbf{P} = \mathbb{U}(\mathbb{U}^{\mathrm{T}}\mathbb{U})^{-1}\mathbb{U}^{\mathrm{T}}$) denotes the projection matrix of size N × N. The error generated due to projection, also known as projection error or residue, '$\mathbf{r}$' will always be orthogonal to $\mathbb{U}$ [129]. This is shown in Eq. (3.8).

$$\mathbf{r} = \mathbf{s} - \widehat{\mathbf{s}} \tag{3.6}$$

$$\mathbf{r} = \mathbf{s} - \mathbb{U}\widehat{\mathbf{x}} \tag{3.7}$$

$$\mathbb{U}^{\mathrm{T}}\mathbf{r} = \mathbb{U}^{\mathrm{T}}(\mathbf{s} - \mathbb{U}\widehat{\mathbf{x}}) = 0 \tag{3.8}$$

The projection of $\mathbf{s}$ on to $\mathbb{U}$ is shown in Figure 3.2. The projected sequence $\widehat{\mathbf{s}}$ provides significant impulses on the locations of AO peaks in SCG. The process yields proper pre-processed signal for further analysis of the SCG. In addition to this, the profiles associated with these impulses show the characteristics like QRS-complexes of ECG as they have spectral range of around 6 to 20 Hz. Thus, first order Gaussian differentiator (FOGD) based logic is applied for detection of peaks of these impulses [3], which provide AO instants in SCG signal.

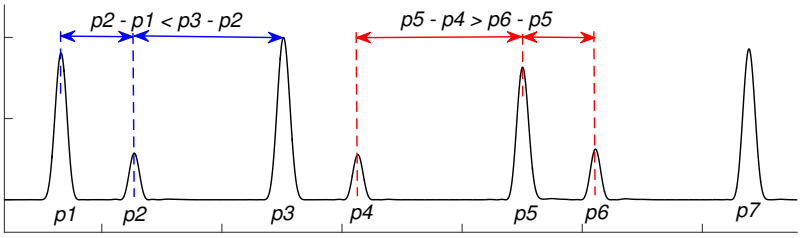

Figure 3.3: Distance pair of systole and diastole envelopes in SCG signal

3.1.1.2 PostAC (pAC) instants detection

Estimation of diastolic profile parameters is always a challenging task in an SCG signal. It has more inter-beat and intra-beat variabilities. We have attempted to develop a simple method to detect peak just after AC point under diastole, say postAC point. In a cardiac cycle, diastolic profile is always nearer to its preceding systolic profile [110]. It is also shown in Figure 3.3 that distance of systolic-diastolic location pairs $(p1, p2)$, $(p3, p4)$, and $(p5, p6)$ are less than distance of diastolic-systolic location pairs $(p2, p3)$, $(p4, p5)$, and $(p6, p7)$, respectively. Utilizing this fact, we divide each of the consecutive AO-AO intervals at their midpoint (M_1), which is expressed as:

$$M_1 = \frac{AO_1 + AO_2}{2} \tag{3.9}$$

where AO_1 and AO_2 are onset and offset AO peak locations to extract an SCG cycle, respectively. At this point, we can claim strongly that the diastolic profile resides between AO_1 and M_1. Again the interval between AO_1 and M_1 is divided at their midpoint (M_2) to have expectation of diastolic profile in M_2 to M_1 interval as shown in Figure 3.5(a). The expressions for M_2 is given as:

$$M_2 = \frac{AO_1 + M_1}{2} = \frac{3AO_1 + AO_2}{4} \tag{3.10}$$

Hence, each of the SCG cycles (consecutive AO-AO intervals) is segmented from M_2 to M_1 locations. These segments are subjected for mean subtraction and amplitude normalization. To reduce irregularity present in the data, a moving average filtering is applied subsequently. In general, this segment suffers with a large trend, due to which detection of the maximum point as the postAC event may be wrong. To avoid this situation, the smoothed segment is high pass filtered using a butterworth IIR filter with an empirical cut-off frequency of 10 Hz. The next step is to find the maxima of the processed segment, which is addressed as postAC event in the SCG cycle. The complete process is shown in Figure 3.5.

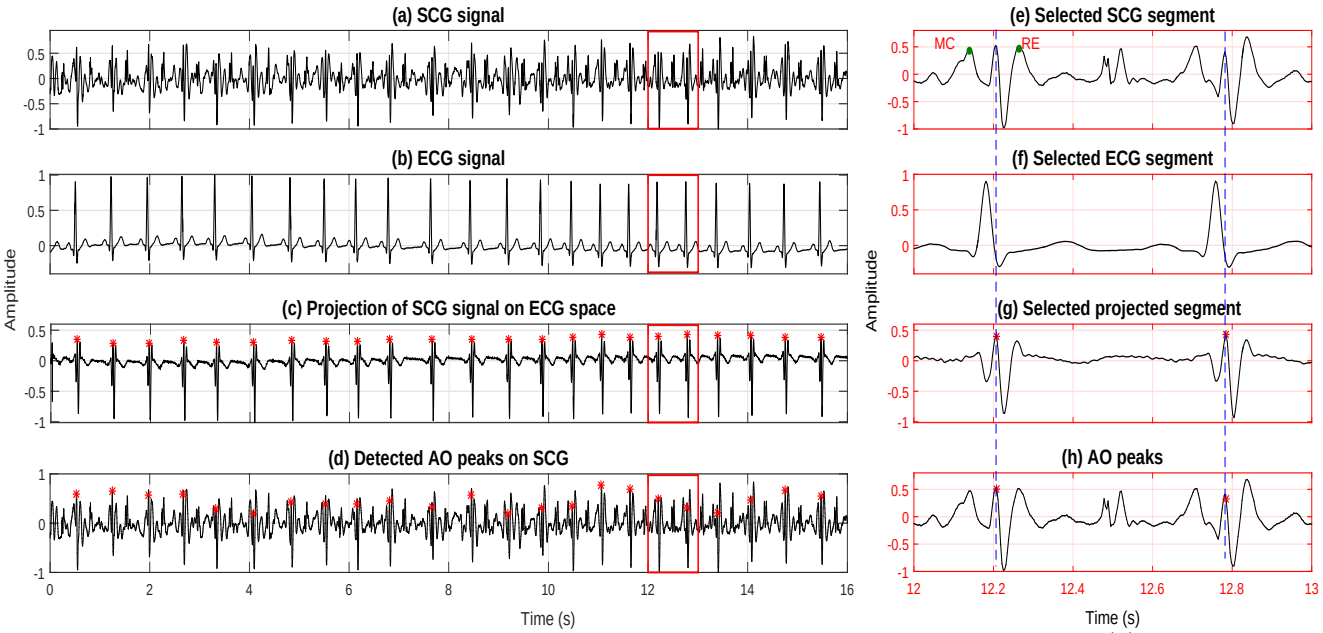

Figure 3.4: AO peak detection using subspace projection of SCG signal on to ECG space. (a) SCG signal $\mathbf{s}$, (b) concurrent ECG signal $\mathbf{e}$, (c) projected SCG signal $\widehat{\mathbf{s}}$ and detected peaks using FOGD based scheme, (d) AO peaks on SCG by projecting peaks of $\widehat{\mathbf{s}}$, and (e)-(f) magnified versions of corresponding signals from red rectangular boxes in (a)-(d), respectively.

3.1.2 Results and discussion

3.1.2.1 Description of the database

The proposed method is tested and validated using concurrent ECG and SCG signals of CEBS database [125]. The database includes simultaneous recordings of ECG, SCG and respiration signals, collected from twenty healthy individuals. The recorded signals have varying wave morphologies with trending effects, inter-beat and intra-beat variabilities, small and large motion artifacts. The signal acquisition was done in supine position during three different states: basal (b), music listening (m) and music paused (p). However, we are considering ECG (lead-II) and dorso ventral SCG signals from basal stated records b001-b020 in this work.

3.1.2.2 Experimental results

The SCG and ECG signals are resampled at a sampling rate of 300 Hz for this study. These signals are firstly processed with mean removal and amplitude normalization process. Then, ECG subspace $\mathbb{U}$ is created by ECG signal and its delayed realizations. The selection of number of delayed realizations is purely empirical. In this experiment, minimum ten number of realizations are found suitable. The subspace projection of $\mathbf{s}$ onto ECG space $\mathbb{U}$ is found by Eq. (3.3)–(3.5). This projected signal $\widehat{\mathbf{s}}$

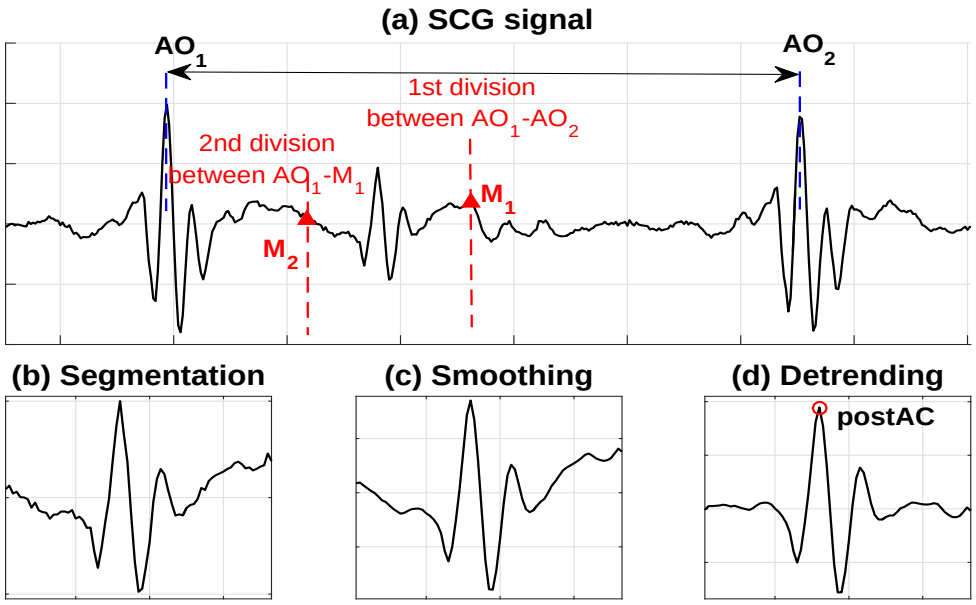

Figure 3.5: Detection of postAC instants in SCG signal. (a) SCG waveform, (b) segmented diastole, (c) smoothing operation, and (d) postAC peak on detrended diastole.

provides sharp transitions at the places of AO peaks. The peaks of these profiles are detected using FOGD based algorithm [3]. The experimental results of the proposed AO peak detection method on an SCG signal having prominent and non-prominent AO peaks is shown in Figure 3.4. Figure 3.4(a) and (b) show concurrent SCG and ECG signals, respectively. Figure 3.4(c) depicts the projection of SCG signal onto ECG space, while (d) shows detected maximas of the projection as AO peaks on the SCG signal. The selected regions of Figure 3.4(a)-(d) are magnified, which are shown in (e)-(h), respectively. The segments are selected in Figure 3.4(a)-(d) by uniform red rectangular boxes. It is observed that our method performs extremely well even in the presence of very smaller amplitudes of AO peaks. These results are further analyzed in section 3.1.2.3. In order to extract heart cycles, each of the AO-AO intervals is extracted from systole analysis. These intervals are further used for postAC peak detection under diastole analysis. For each AO-AO interval, we segment data from M_2 to M_1 location as shown in Figure 3.5(a)-(b). Then, segmented diastole is smoothed out using FIR moving average filter of window size 7 ms (Figure 3.5(c)). Subsequently, to remove the trend, a filtering operation is applied on it using sixth order butterworth high pass filter of cut-off frequency 10 Hz (Figure 3.5(d)). Finally, the instant corresponding to maximum value of detrended data is determined as postAC point. Similarly, intervals between consecutive postAC peaks can also be considered as heart cycles from diastole analysis. Figure 3.6 shows the experimental results of the proposed

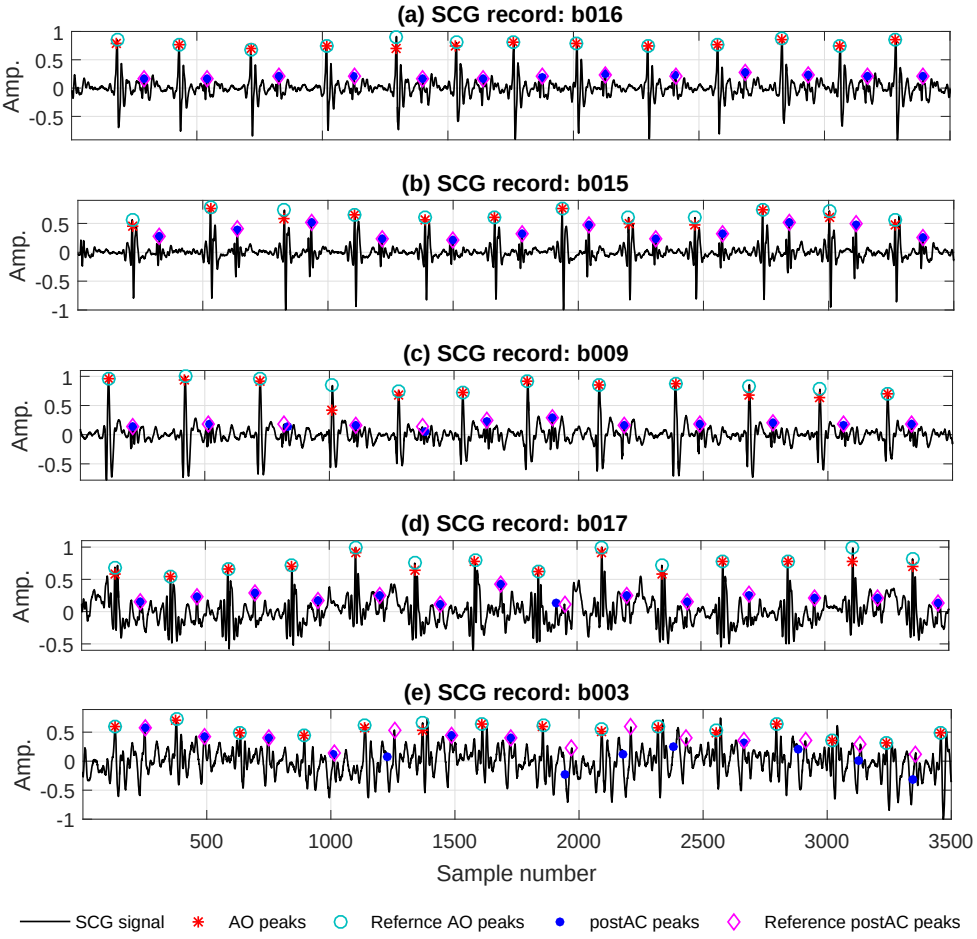

Figure 3.6: Experimental results of the proposed method applied on different SCG signals having various wave morphologies. Detected AO and postAC peaks are highlighted along with their manual annotations.

method on five different SCG recordings having different wave patterns. The SCG signals depicted in Figure 3.6(a)–(d) have normal heart rhythms, Figure 3.6(c) shows SCG data with very small diastolic profiles, and the signals shown in Figure 3.6(d)–(e) have large baseline drifts. In addition, the signal in Figure 3.6(e) is having distorted and unrecognizable beat patterns. By comparing the detections with manually annotated AO and postAC peaks, it can be said that our method works satisfactory.

3.1.2.3 Performance evaluation

The detection of postAC peaks depends on the correct detection of AO peaks. The misdetection of AO peaks may lead to wrong interpretation of postAC points. However, our proposed method for detection of AO and postAC peaks is robust to noise, artifacts and inter-beat variabilities (Figures 3.4–3.6). Figure 3.4 shows the AO peak detection results using our proposed method with cases: (i) AO

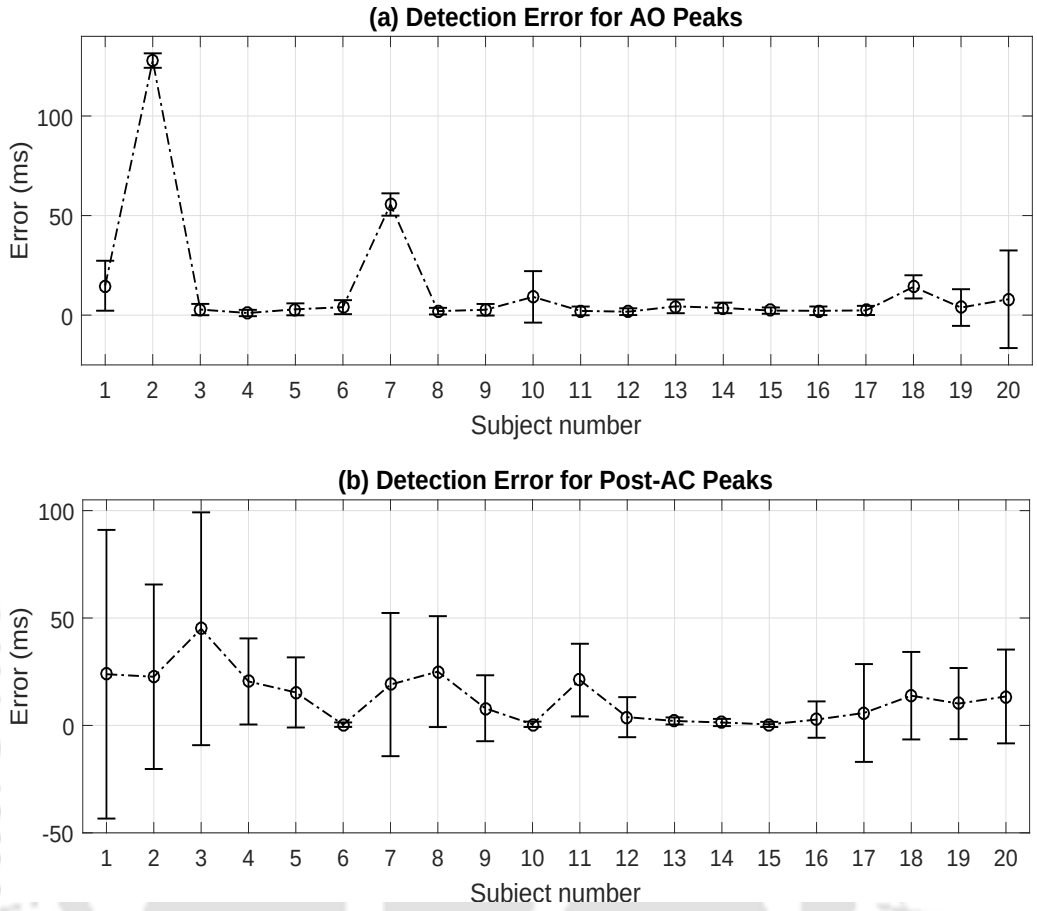

Figure 3.7: Performance of the proposed method using error-plots (mean±standard deviation) for twenty basal stated subjects. (a) AO peak detection error, and (b) postAC peak detection error.

peak has larger amplitude than MC and RE peaks (in first beat of Figure 3.4(e)), and (ii) AO peak has smaller amplitude than MC and RE peaks (in second beat of Figure 3.4(e)). Still our method achieves 100% true detections throughout the data. The experimental results demonstrate that the proposed method is superior to the methods which use fixed window segment after R-peaks to detect the AO peaks. To evaluate the performance of the proposed method, temporal errors are analyzed between detected and manually annotated AO and postAC peaks, respectively. So, twenty seconds SCG data is manually annotated for AO and postAC peaks from twenty basal stated subjects, and absolute errors are found for both. The temporal errors in detection of AO and postAC peaks are shown in Figure 3.7(a) and (b), respectively. The mean errors in AO peak detection is approaching to zero with very small deviations except for subjects 2 and 7. The reason behind the increased error is due to having very low frequency systole morphologies in subjects 2 and 7. In addition, minimum mean errors are achieved with little higher deviations for postAC detection. Since our method did not

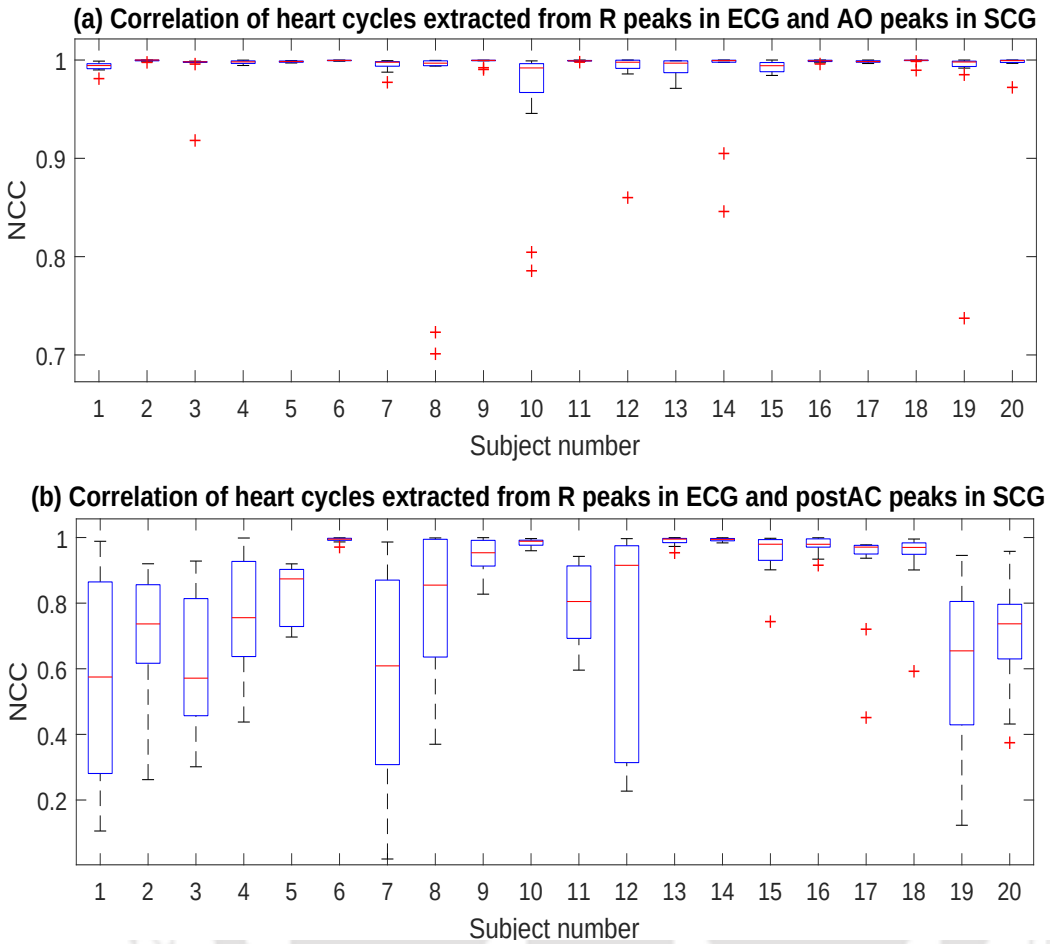

Figure 3.8: Boxplot representation for normalized cross correlation (NCC) of heartbeats extracted from ECG and SCG signals. (a) NCC of heartbeat intervals extracted from RR and AO-AO intervals, and (b) NCC of heartbeat intervals extracted from RR and postAC-postAC intervals.

produce any false positive or false negative for the peak detection task, it outperforms other methods of SCG cycle extraction. This quantitative analysis provides an idea about a good performance of the proposed method towards heart cycle extraction using both AO and postAC peaks. An important hemodynamic parameter, left ventricular ejection time (LVET) is defined by the interval between AO and AC instances, which can also be estimated based on detection results of AO and postAC instances.

3.1.2.4 Correlation of heartbeats extracted from ECG and SCG signals

Another experiment is conducted to validate the performance of the proposed method. The heart cycles are extracted in ECG using consecutive R-peaks, while this is done in SCG via AO peaks and postAC peaks. Each of the recordings from the database is segmented into 10 s blocks for 2 minutes duration in the experimentation. The well-known Pan Tompkins algorithm is employed for R-peak detection [130]. The time interval series from successive R-to-R, AO-to-AO, and pAC-to-pAC are

determined from each of the blocks, and normalized cross correlation (NCC) of AO-AO and pAC-pAC are computed with RR intervals for each subject. The NCC is defined as [124]:

$$\mathrm{NCC}_i = \frac{\sum_{l=1}^{H}(ff_i(l) - \overline{ff}_i)(rr(l) - \overline{rr})}{\sqrt{\sum_{k=1}^{H}(ff_i(k) - \overline{ff}_i)^2 \sum_{t=1}^{H}(rr(t) - \overline{rr})^2}} \tag{3.11}$$

where i $(i = 1, 2)$ denotes index for AO-AO and postAC-postAC interval time series, respectively. $\overline{rr}$ is the mean of RR interval time series $(rr(l))$, and $\overline{ff}_i$ is the mean of interval series $ff_i(l)$, which is obtained from i^{th} fiducial point. H represents the number of heartbeats considered for the study. The boxplot representations for NCC of AO-AO with RR, and postAC-postAC with RR are shown in Figure 3.8(a) and (b), respectively. It is observed that AO-AO shows strong correlation with RR for all the subjects, while postAC-postAC shows more variability in the correlation as compared to AO-AO intervals. The records 2 and 7 produce relatively high, but constant temporal errors. Therefore, the estimation of heart rhythms from the SCG signal does not get affected as shown in Figure 3.8. The results show the robust detection of AO peaks by the proposed method, while more temporal errors in detecting pAC produces less heartbeat correlation with RR intervals. Hence, it can be said that the trace of heart cycles achieved by the proposed method almost follow the heart cycle trace obtained by a concurrent ECG signal.

Apart from correlation, the evaluation of the heart-cycle estimation should also be done to check the agreement with RR intervals. It is shown via Bland-Altman plots for both AO-AO and pAC-pAC intervals in Figures 3.9 and 3.10, respectively, where all the signals are taken for one minute duration in this study. From these figures, it is also justified that AO-AO intervals provide better correlation and agreement with RR intervals as compared to pAC-pAC intervals. Thus, the estimated AO peaks are more reliable in heart cycle extraction and HRV estimation for the presented ECG-assisted method.

3.1.3 Conclusion

In the above study, a unified framework is developed for extracting SCG heart cycles using two approaches: (i) AO-AO intervals from systolic profiles, and (ii) postAC-postAC intervals from diastolic profiles, with concurrent ECG signal as a reference. The SCG signal is projected on ECG space using subspace projection for detecting AO peaks. Subsequently, postAC peaks are detected by processing the SCG cycles constructed by AO-AO intervals. The detection of postAC peaks consists

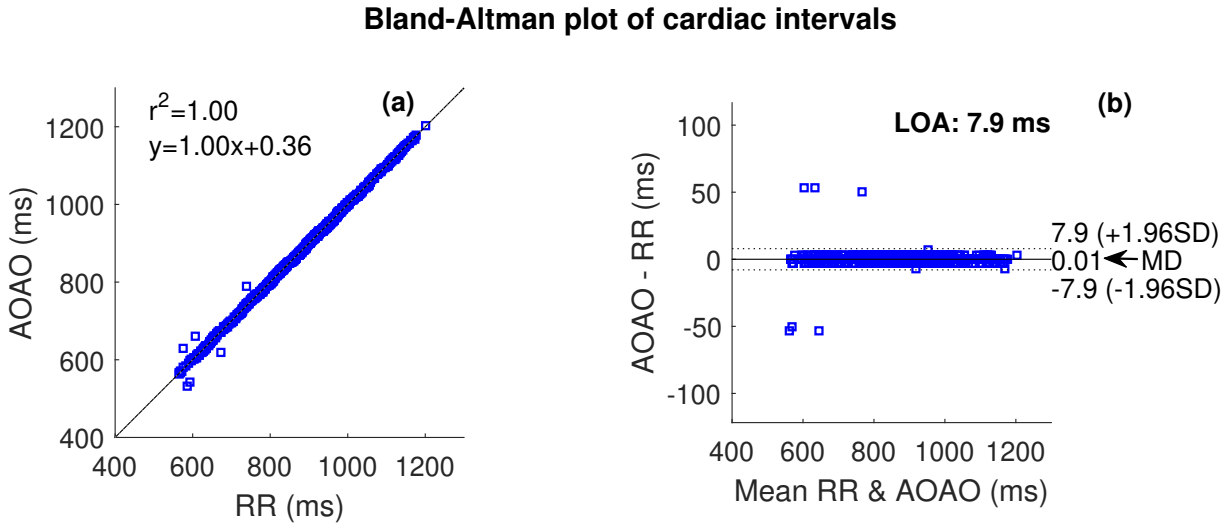

Figure 3.9: Comparison of heartbeats extracted from RR and AO-AO intervals using (a) correlation plot, and (b) Bland-Altman plot. In correlation plot, root mean squared error is achieved as 4 ms. Limits of agreement in 95% confidence intervals are shown in dotted lines. (Abbreviations used— r^2: Pearson's R-squared correlation

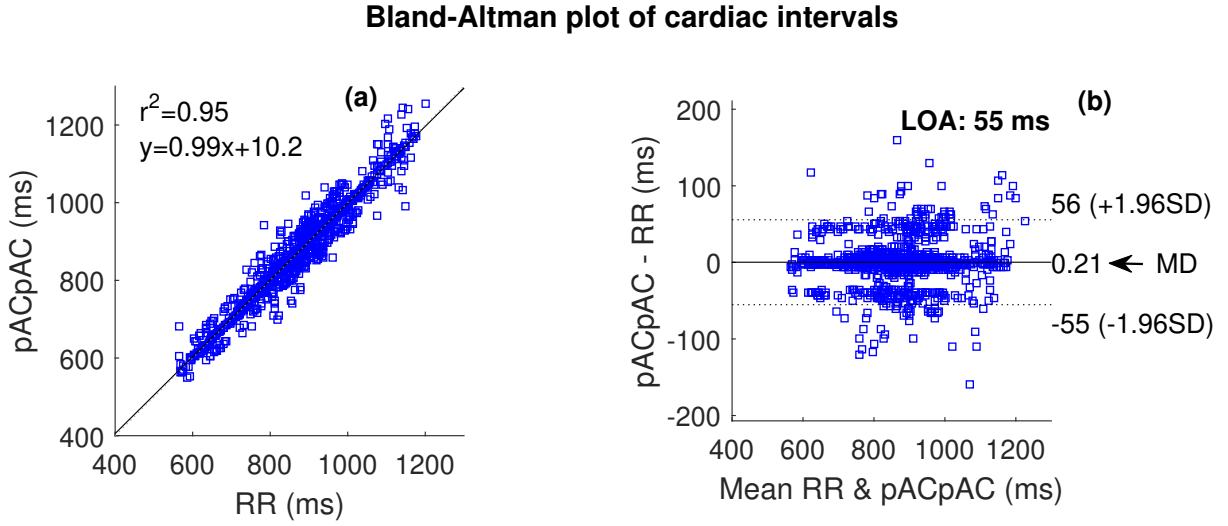

Figure 3.10: Comparison of heartbeats extracted from RR and pAC-pAC intervals using (a) correlation plot, and (b) Bland-Altman plot. In correlation plot, root mean squared error is achieved as 28 ms. Limits of agreement in 95% confidence intervals are shown in dotted lines. (Abbreviations used— r^2: Pearson's R-squared correlation coefficient, LOA: limits of agreement, MD: mean difference, SD: standard deviation of difference).

segmentation, moving average filtering, high pass IIR filtering, and determining maxima point. The overall performance results show that the proposed framework produces little higher detection errors for postAC peaks, while it produces errors closed to zero for AO peaks. The heart cycle intervals extracted from SCG are well correlated with concurrent ECG cycles. The quantitative analysis of

the proposed method enables its applicability in the direction of heart cycle extraction and heart rate variability analysis. The proposed work can also be extended for hemodynamic parameter extraction.

3.2 PPG Assisted Delineation Framework

In Section 3.1, ECG assisted delineation method is proposed, where pAC points are detected by processing the consecutive AO-AO intervals. Thus, it is not able to estimate the pAC peak before the first, and after the last systolic profile (or AO point) in a segment. Additionally, it is limited to detect only two fiducial points. To address the drawbacks, another method is developed. A delineation framework is proposed to identify most of the fiducial points, such as IM, AO, IC, AC, pAC and MO, with the help of a photoplethysmogram (PPG) signal. Figure 3.11 illustrates the simultaneous recordings of ECG, fingertip-PPG, and SCG signals. Rhythmic variations of blood-volume at different parts of the body is generally observed due to the pumping actions of the heart, which is indicated by a PPG signal [131]. Usually, the PPG sensor is worn on finger-tip for achieving highest signal strength [131].

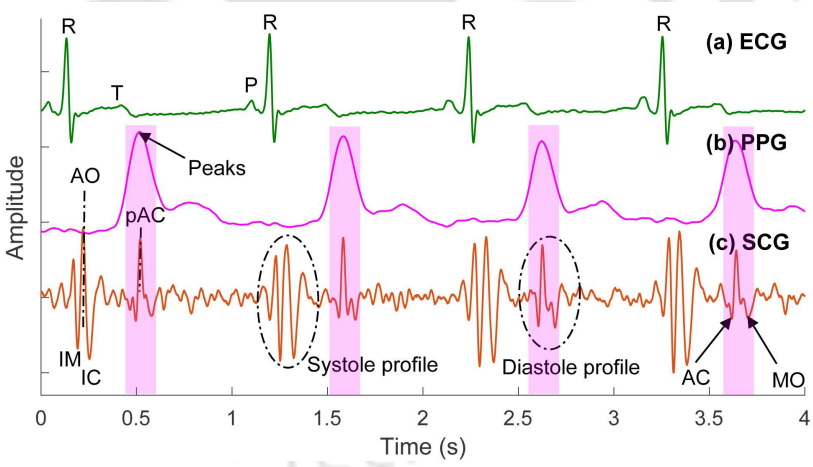

Figure 3.11: Simultaneous recordings of ECG, fingertip-PPG and SCG signals.

Typically, the AO point creates a prominent peak under the systolic profile of the SCG signal [132]. Thus, other informative systolic points may be estimated with the help of the AO peaks. However, delineation of an SCG diastole profile is still a challenge, and the task is even more complicated when both systole and diastole profiles have similar characteristics. It is observed in Figure 3.11 that the diastole delineation would be comparatively easier with the help of a PPG signal. This is due to the

[4]This work has been published in IEEE Transactions on Instrumentation and Measurement, 2020 (Refer *List of Publications* page for details).

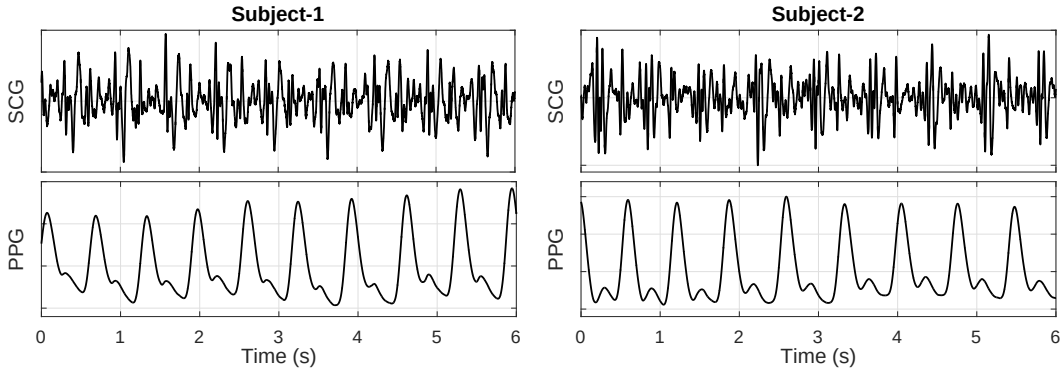

Figure 3.12: Difficulty in localization of an SCG profile in presence of interbeat and intrabeat variabilities in contrast to PPG signals.

fact that projections of PPG peaks lie on AC-to-MO segments of an SCG signal. The PPG signal is less noisy, while an SCG signal changes its basic characteristics if the sensor placement is affected by the body movements. As illustrated by a concurrently recorded SCG and PPG signals from two subjects in Figure 3.12, it is difficult to localize an SCG profile due to inter and intra beat variabilities. Moreover, the existing methods are limited to estimate only a few fiducial points, through which the characterization of both systolic and diastolic profiles of the SCG would not be possible.

To address these issues, a PPG-assisted automatic delineation framework for an SCG signal is proposed, which can estimate IM, AO, IC, AC, pAC and MO fiducial points in systole and diastole profiles. The framework can also estimate two important cardiac intervals, namely IVRT (AC-to-MO) and LVET (AO-to-AC). Multiscale scalogram is employed for spectro-temporal localization of nonstationary and nonlinear signals [133]. To analyze the SCG waveform, a PPG signal is employed and wavelet scalogram-based time-frequency analysis is performed onto it. An envelope construction method is proposed and decision rules are used for estimation of fiducial points. In addition, one of its applications is presented in respiratory-event analysis in order to show the ability of the delineated points. Since a change in the respiratory effort-level affects the morphology of the SCG waveform [4], [115], the fiducial points of an SCG signal may be used in assessing the fitness of a respiratory system. As an extension of the proposed delineation work, the breathlessness (shortness of breath or dyspnea) and normal breathing conditions are perfectly discriminated by the delineated points. The proposed method is elaborately discussed in the following sections.

3.2.1 Proposed SCG delineation method

Wavelet transform (WT) represents a signal as linear combinations of a basis function-set and its variations. The variation is achieved by means of scaling (l) and shifting (m) parameters of a single mother wavelet function $\psi(t)$. So, signal $x(t)$ can be analyzed using WT as [134]:

$$w_{l,m}\{x\} = \frac{1}{\sqrt{l}} \int_{-\infty}^{+\infty} x(t)\psi^* \left(\frac{t-m}{l}\right) dt,\ l > 0 \tag{3.12}$$

where, $w_{l,m}$ represents m^{th} wavelet coefficient at l^{th} scale and the asterisk ($*$) is a complex conjugate operator. Since, the second derivative of a Gaussian function (*Gaus-2*) has a morphological similarity with the pulsatile profile of a PPG signal [135, 136], it is chosen as the mother wavelet for continuous wavelet transform (CWT). The prototype wavelet $\psi(t)$ can be defined as [137]:

$$\psi(t) = -\frac{dg(t)}{dt} = \mathrm{C}(1-t^2)e^{-t^2/2} \tag{3.13}$$

where, $g(t)$ and C denote a Gaussian function $\mathcal{N}(0,\ 1)$ and normalization factor, respectively.

3.2.1.1 Processing of scalogram

A scalogram shows 3-D multiscale distributions of signal components with the help of wavelet transformation [133], [137]. It indicates the relative wavelet energy for each coefficient $w_{l,m}$, which is obtained as [137]:

$$E_{l,m} = |w_{l,m}|^2 \tag{3.14}$$

$$S_{l,m} \longleftarrow \frac{E_{l,m}}{\sum_l \sum_m E_{l,m}} \tag{3.15}$$

where, $E_{l,m}$ and $S_{l,m}$ denote wavelet energy density and scalogram, respectively. A PPG-scalogram is obtained by processing an input PPG signal upto 150 scales, which is illustrated in Figure 3.13. The corresponding scalogram is shown in Figure 3.13(b) and subsequently, its all possible two dimensional interpretations are shown in Figure 3.13(c)–(f). From this representation, a time series of maximum relative wavelet energy (MRWE) is obtained irrespective to the scales as shown in Figure 3.13(c). A larger MRWE value corresponds maximum resemblance between the wavelet function and the pulsatile waveform, which in turn gives an indication of the presence of PPG peaks. Thus, the MRWE signal is selected for further analysis. The PPG signal is detrended and subsequently, added up with the MRWE signal to emphasize the PPG-peaks and to suppress other spurious peaks. The detrending process removes the baseline-drift (BD) from the signal, which uses a high pass filtering scheme. The

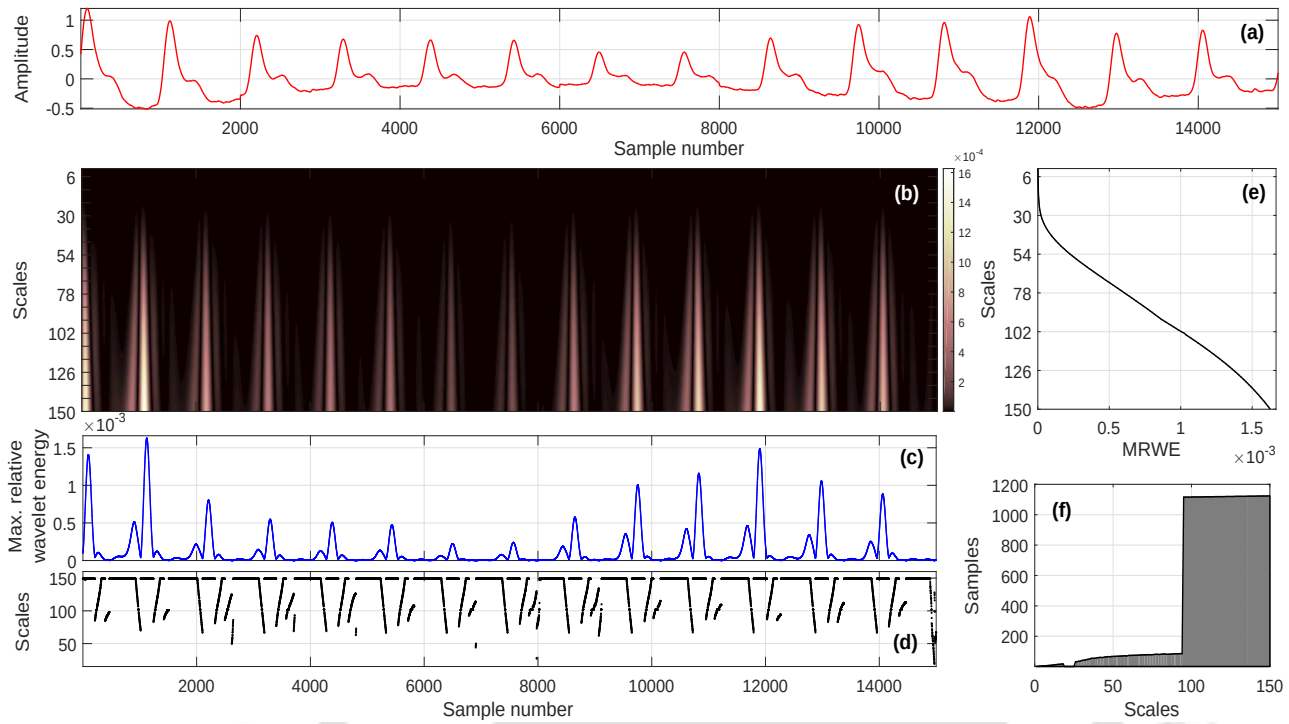

Figure 3.13: Scalogram of PPG signal. (a) Input PPG signal, (b) PPG scalogram, (c) change of maximum relative wavelet energy (MRWE) with time, (d) scales corresponding to MRWE, with respect to samples, (e) predominating energy (MRWE) with the higher scales, and (f) overlapping area of time and scales.

signal produced by ensembled-sum is denoted by $x_p^*[n]$.

3.2.1.2 Proposed envelope construction scheme

The Shannon entropy (SE) and Shannon energy (SEE) based envelopes produce minima point for higher normalized-signal-amplitude. The methods for estimating envelopes such as absolute, energy, analytic signal, SE and SEE were compared in [3]. The ensembled-sum signal $x_p^*[n]$ is employed for envelope construction using SE and SEE as shown in Figure 3.14(b)–(e). They provide bifurcated profiles for input peaks having large relative amplitudes. Hence, a modified transfer characteristic is proposed as shown in Figure 3.14(f), which can effectively estimate the envelope profile of $x_p^*[n]$ by creating sharp impulses at the locations of PPG-peaks (Figure 3.14(g)). In contrast to other methods, it emphasizes the PPG-peaks without bifurcation and suppresses the other regions relatively better. The proposed profile can be obtained via fitting an exponential curve in a least square sense. Mathematically, it can be represented via two exponential expressions, $(1 - e^{-qx})$ and $1/(1 + e^{-qx})$, where x corresponds to the input vector. Hence, the function for fitting of the desired characteristic

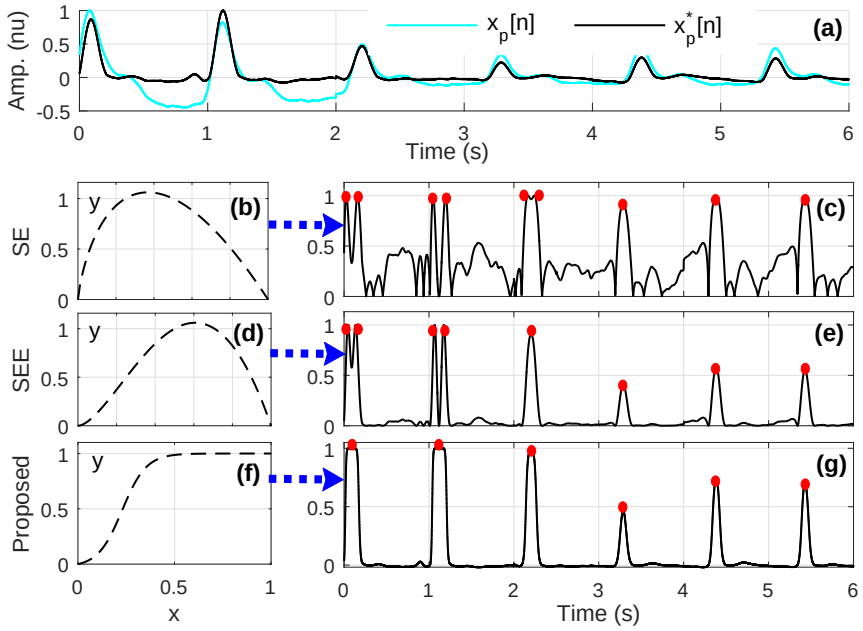

Figure 3.14: Performance comparison of the proposed envelope construction for $x_p^*[n]$. (a) PPG and ensemble sum signal; (b)-(g) transfer characteristics and envelope profile estimation using using SE, SEE and the proposed method. Red dots denote local peaks of the envelope impulses.

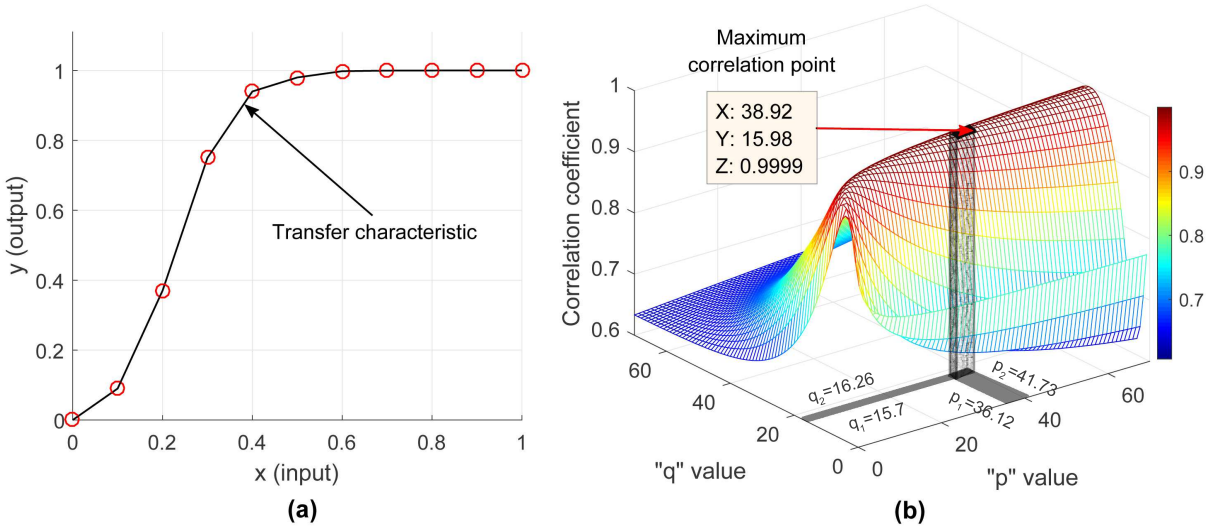

Figure 3.15: Estimation of modeling parameters. (a) Desired transfer characteristic in a piecewise linear fashion, and (b) mesh plot representing variations of correlation for obtained characteristic corresponding to curve fitting parameters 'p' and 'q' [Eq. (3.16)]. Estimated parameters corresponding to maximum correlation are highlighted with 95% confidence interval using gray color bands. Transfer function produced by fitted parameters achieves maximum correlation.

can be expressed as:

$$y = \frac{1 - e^{-qx}}{1 + pe^{-qx}}, \quad \forall x \in [0, 1], \quad p, q \in \mathbb{N} \tag{3.16}$$

To achieve the desired profile, the modelling parameters p and q need to be estimated for different input values. Figure 3.15 shows a variation of correlation between desired and estimated characteristic. The estimated transfer characteristic is achieved by varying the parameters. The fitted parameters are also highlighted with 95% confidence intervals, which are presented by gray rectangular patches in p-q plane. By the usage of fitted p and q parameters, the designed model shows the highest correlation with the desired characteristic as shown in Figure 3.15(b). Thus, in an average least square sense, parameters p and q are estimated as 39 and 16, respectively. In the proposed method, this envelope extraction scheme is used for the detection of true PPG-peaks and later, for the estimation of AO peaks.

3.2.1.3 Detection of PPG-peaks

This developed model is applied to the ensembled-sum signal $x_p^*[n]$ to get the desired envelope profile. The envelope provides localization of PPG-peaks in the form of sharp impulses. The peaks of these impulses can be easily identified using simple amplitude-temporal based thresholding schemes.

3.2.1.4 Delineation of diastolic regions

The diastole profiles of an SCG signal are estimated with the help of PPG signals at the initial stage. The detected PPG-peaks are found useful in estimating the pAC peaks in SCG-diastole profile. The pAC point corresponds to the maxima in an SCG diastole, and it can be located by searching the peaks of a PPG signal with the help of a narrow and symmetric window. Subsequently, a proposed set of amplitude-histogram based decision rules can be employed for estimation of adjacent fiducial points (AC and MO) as follows:

- **Amplitude-Histogram based Proposed Decision Rules:** The decision rules (Algorithm 3) block is employed on both diastole and systole profiles of an SCG signal. At first, each of the SCG diastolic profiles is segmented into two small blocks adjacent to pAC peaks, and all local peaks are detected for both the blocks. It is observed that amplitude of the peaks gradually decreases from pAC locations. Hence, each of the blocks is employed for the following set of operations. Five frequency bins are created to show the distribution of local peaks with respect to the pAC point under a segmented block of diastole profile as listed in step 5 (Algorithm 3). Subsequently, all the frequency bins are scanned sequentially (F^1–F^5) to find non-zero elements (local peaks). In the scanning process, the first bin corresponding to have non-zero elements is

Algorithm 3 Proposed decision rules

Inputs: $x_s[n]$, $pks_{i=1,2,\ldots,\#pks}$
// $x_s[n]$ corresponds to the input SCG signal
// pks corresponds to pAC peaks for diastole delineation (or AO peaks for systole delineation)
1: Segment the SCG profiles into two blocks:
$\text{blockA}_i = x_s[(pks_i - 100 \text{ ms}) : pks_i]$
$\text{blockB}_i = x_s[pks_i : (pks_i + 200 \text{ ms})]$
2: Identify all local peak-locations of blockA and blockB.
3: **for** $b = [1, 2]$ **do** // Selection of blockA ($b = 1$) and blockB ($b = 2$).
4: **for** $i = 1$ to $\#pks$ **do**
5: **(a)** Compute amplitude histogram of local peaks:

$$\text{frequency bins} \begin{cases} F_i^1 \leftarrow \text{peaks lying in amplitude range } (80 - 100\%] \text{ of } pks_i \\ F_i^2 \leftarrow \text{peaks lying in amplitude range } (60 - 80\%] \text{ of } pks_i \\ \vdots \quad \vdots \quad \vdots \quad \vdots \quad \vdots \\ F_i^5 \leftarrow \text{peaks lying in amplitude range } (0 - 20\%] \text{ of } pks_i \end{cases}$$

6: **(b)** Estimate first significant peak nearest to pks_i
7: **for** $j = 1$ to 5 **do**
8: **if** $n(F_i^j) \geq 1$ **then**
// where $n(\cdot)$ denotes number of elements.
9: $P_{1i} \leftarrow$ Peak nearest to pks_i in frequency bin F_i^j;
10: break **for loop**;
11: **end if**
12: **end for**
13: **(c)** Detect minimum points between P_{1i} and $pks_i \rightarrow Min_i$
14: **end for**
15: $M_b \leftarrow Min$; // Estimated fiducial point adjacent to pks.
16: **end for**
Outputs: Fiducial points: M_1, M_2 and pks

observed and selected for further investigation. Among all these local peaks from the selected bin, the first significant peak closest to pAC is estimated, say P_1. Then, the segment P_1 to pAC is applied for minima search for both the blocks, which can estimate AC and MO fiducial points.

3.2.1.5 Delineation of systolic regions

Once the fiducial parameters of the diastolic region are determined, delineation is carried out for the systole. If the fiducial points, AC, pAC and MO are perfectly determined, then it is possible to precisely localize diastolic profiles in the SCG signal. Usually, both systolic and diastolic profiles share the same spectral range and/or have similar amplitude strengths. Due to that, identifying systolic profile in the presence of diastolic profile in an SCG cycle becomes a great challenge. Thus, the diastole profiles are masked in the SCG signal by replacing their corresponding samples with zero amplitude levels. Typically, the AO peak possesses the prominent amplitude under a systole profile. But, its actual location cannot always be found by determining the maxima of the masked-SCG-cycle, which

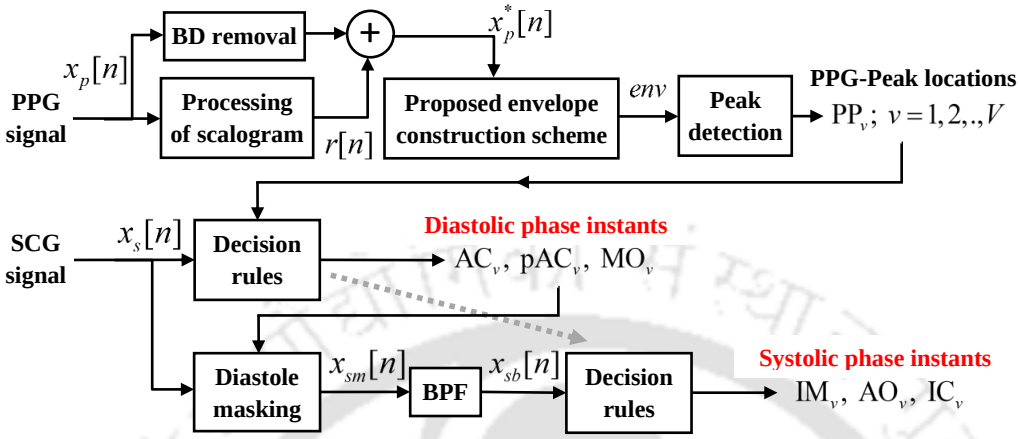

Figure 3.16: Block diagram of the proposed method.

is created by a segment between any two same diastole-fiducials. The reason behind is sometimes, the AO peak has a smaller amplitude than MC or RE, which are the peaks adjacent to AO in SCG signal. The SCG segment, IM-AO-IC shows frequency range typically higher than other wave-segments in the SCG-systole. So, the masked-SCG is bandpass filtered in a relatively higher frequency range of 20–30 Hz. Due to that, the AO peaks are emphasized in the resulting signal. Then, its upper envelope is extracted and subsequently, its instantaneous energy signal is employed to the proposed envelope construction technique (Eq. (3.16)). Finally, the locations of all the AO peaks, which are indicated through impulses in the resultant signal, are detected using simple thresholding and peak correction scheme. As like diastole profile, the proposed decision rules (Algorithm 3) are subsequently applied to the masked-SCG signal with detected AO peaks. It can localize two another systole fiducial points, IM and IC.

A block diagram of the proposed method for estimation of cardiac phases is shown in Figure 3.16. Initially, MRWE signal is extracted from the PPG-scalogram, which is further summed-up synchronously with the BD-suppressed PPG signal. Subsequently, an envelope is constructed on the output signal using the proposed scheme, and PPG-peaks are detected. The PPG-peaks can detect the pAC peaks in the SCG signal. Other essential diastole phase instants, AC and MO are estimated using the proposed decision rules. After this process, the diastole profiles are localized and masked in the SCG signal, and subsequently, bandpass filtering is employed to estimate the AO instants. Similarly, other important systole phase instants, IM and IC are estimated using the proposed decision

Table 3.1: Demographics of subjects and their recording information

#Signals	#Subjects	Sex	Age(y)	Wt.(kg)	Ht.	HR(bpm)	#Systoles	#Diastoles
16	8	M	28.75 ±2.31	71.63 ±7.85	5'7.6" ±2.6"	79.18 ±10.93	3429	3425

HR corresponds heart-rate, which is expressed in terms of beats per minute (bpm).

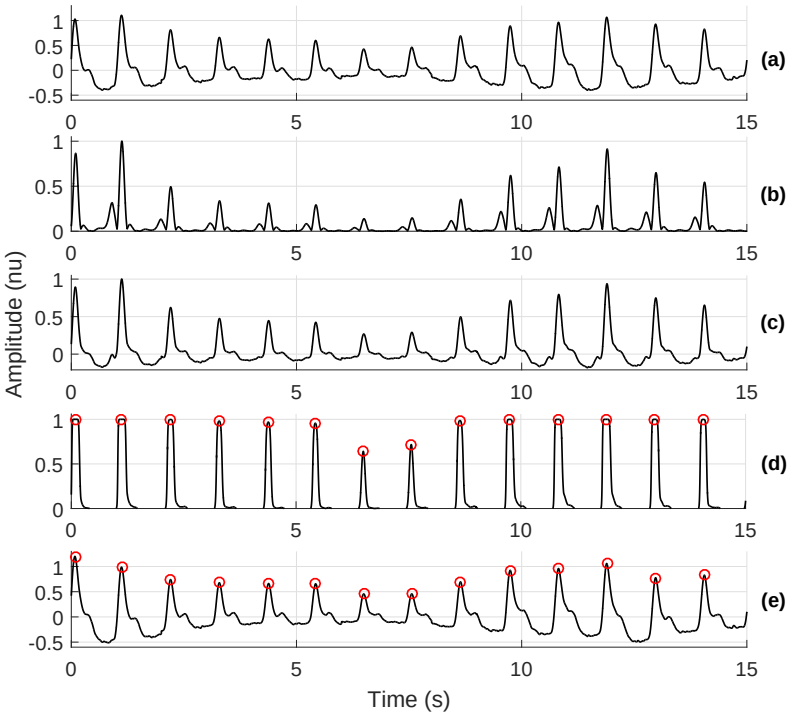

Figure 3.17: Peak detection process of a PPG signal having amplitude variabilities. (a) Input PPG signal, (b) MRWE signal, (c) detrended PPG + MRWE, (d) envelope, and (e) peaks of the PPG.

rules. Two important cardiac time intervals, namely LVET and IVRT can also be determined using the estimated AO, AC and MO parameters.

3.2.2 Results and discussion

3.2.2.1 Measurement protocol and data acquisition

The SCG signals were acquired from eight male subjects using our developed signal acquisition system, which has been described earlier in Section 2.1. The demographics of involved subjects and the recording information are tabulated in Table 3.1. Along with the SCG signal, other cardiac signals ECG and PPG were recorded in two different sessions: normal breathing for 5 minutes followed by holding breath for 50 s. So, breathlessness condition is artificially achieved for every subject by holding or stopping his respiratory activity. With an ethical approval and proper consent of subjects, the SCG signals were recorded. Subjects are advised to be in a supine position during both the sessions.

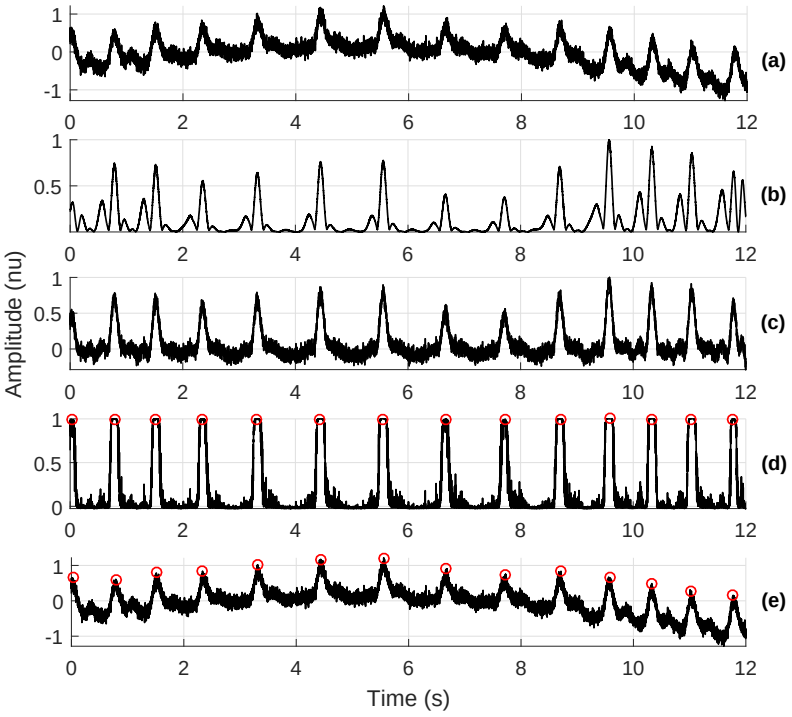

Figure 3.18: Peak detection process of a noisy PPG signal affected from AWGN and baseline drift noises. (a) Input PPG signal, (b) MRWE signal, (c) detrended PPG + MRWE, (d) envelope, and (e) peaks of the PPG.

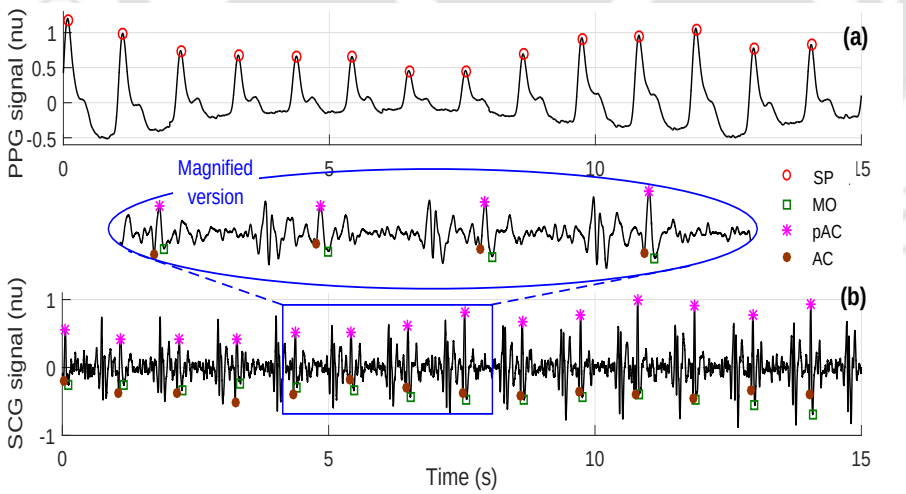

Figure 3.19: Determination of parameters of SCG diastoles with the help of PPG peaks. (a) PPG signal with its peaks, (b) SCG signal with detected fiducial points (AC, pAC and MO) of diastoles using the proposed decision rules.

3.2.2.2 Experiment

The proposed method is tested and validated with 16 different signals. According to breathing pattern, entire data can be divided into normal breathing (NBDB) and stopped breathing (SBDB) datasets.

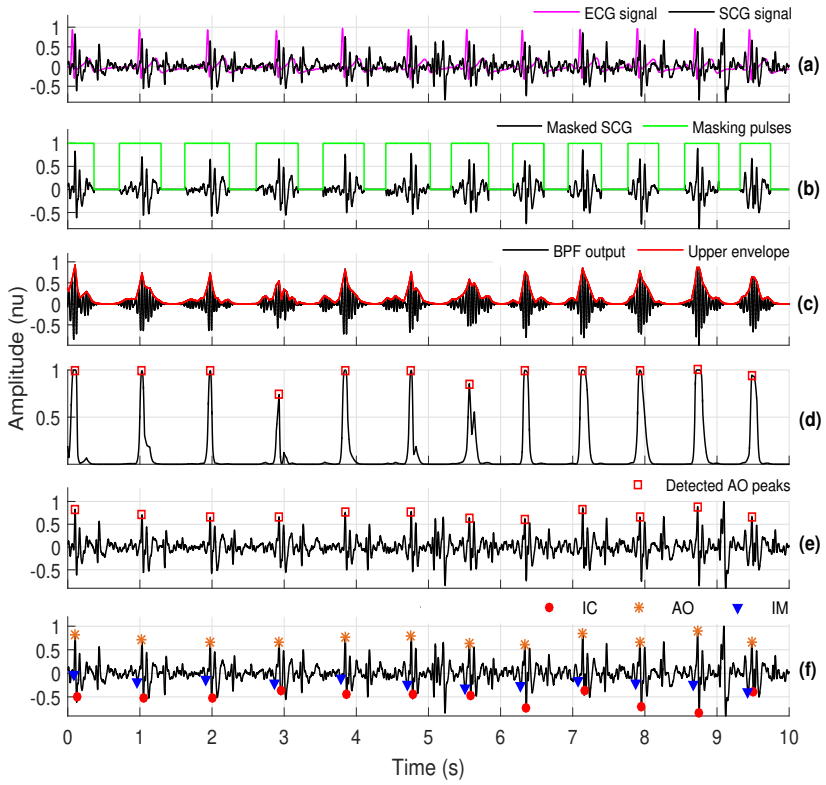

Figure 3.20: Delineation process for systolic profiles of SCG. (a) Input SCG signal, (b) masking of diastole boundaries with the help of estimated diastolic fiducial points, (c) band pass filtered signal and its upper envelope construction, (d) final envelope created by using the proposed envelope scheme, (e) detected AO instants, and (f) estimated IM and IC instants using the decision rules.

The proposed method employs simultaneously recorded SCG and PPG signals, while ECG is used as a reference signal for manual annotation of the SCG signal. The proposed delineation framework is employed on each of the signals with a 10 s time window. The PPG-peaks are determined initially with the help of wavelet scalogram, as shown in Figures 3.17 and 3.18, which further helps in locating the pAC-peaks under SCG diastole profiles. Subsequently, the adjacent fiducial points AC and MO are estimated using the proposed histogram based decision rules. It is illustrated with an example in Figure 3.19. The localization of diastolic region helps in precise detection of AO peaks under systole profiles, and the neighborhood fiducial points (IM and IC) can also be located with the help of same decision rules. The entire process of estimation of systolic parameters is shown in Figure 3.20. For both the profiles in the SCG waveform, the proposed envelope construction scheme helps in indicating the prominent peak locations.

3.2.2.3 Performance evaluation

The performance of the proposed delineation framework is analyzed for all the estimated parameters of both systolic and diastolic profiles. The proposed method is tested with SCG signals of NBDB and SBDB databases. The performance is evaluated using three quantitative measures namely, the sensitivity $\left(\text{Se} = \frac{\text{TP}}{\text{TP+FN}}\right)$, the positive predictivity $\left(+\text{P} = \frac{\text{TP}}{\text{TP+FP}}\right)$ and the accuracy $\left(\text{ACC} = \frac{\text{TP}}{\text{TP+FP+FN}}\right)$, where TP, FP and FN have their usual meaning [128]. The overall performance in the estimation of systolic fiducial points AO, IM and IC is summarized in Table 3.2. The proposed method achieves average accuracies (in %) of 95.2, 88.18 and 85.32 for AO, IM and IC points, respectively, on NBDB database, while 90.08, 86.09 and 89.13 are achieved for AO, IM and IC, respectively, on SBDB database. The maximum sensitivity and positive predictivity are found in the detection of prominent AO peaks as compared to other systolic points.

In a similar manner, the performance in the estimation of diastolic fiducial points pAC, AC and MO is summarized in Table 3.3. The proposed method achieves mean accuracies (in %) of 98.96, 97.55 and 94.54 for pAC, AC and MO points, respectively, on NBDB database, while 98.27, 95.06 and 95.06 are achieved for pAC, AC and MO, respectively, on SBDB database. The maximum sensitivity and positive predictivity are found in the detection of pAC instants as compared to other diastolic points, which are 99.04 and 99.93 for NBDB, respectively, and 99.58 and 98.69 for SBDB, respectively. The obtained results clearly show the excellent performance of our delineation method.

With the estimated AO and pAC peaks, the feasibility of the proposed method could be analyzed for heartbeat extraction and HRV estimation applications. For this purpose, cardiac intervals obtained from AO-AO and pAC-pAC intervals are compared with the ones derived from RR intervals. The comparison is shown via correlation and Bland-Altman plots for both AO-AO and pAC-pAC intervals in Figures 3.21 and 3.22, respectively. In this experiment, all the signals are taken for 30 s duration. From these figures, it is observed that large values of obtained Pearson's R-squared correlation coefficient ($r^2 = 0.97$ and 1) and large population coming under 95% limits of agreement reveal good correlation and agreement. However, the pAC-pAC intervals provide much better correlation and agreement with RR intervals as compared to AO-AO intervals. Thus, the estimated pAC peaks are more reliable in HRV estimation for the presented PPG-assisted method.

Table 3.2: Performance of the proposed method in the detection of systolic fiducial points

	Record	AO Instant Detection			IM Instant Detection			IC Instant Detection		
		Se(%)	**+P**(%)	**ACC**(%)	**Se**(%)	**+P**(%)	**ACC**(%)	**Se**(%)	**+P**(%)	**ACC**(%)
NBDB	s01a	99.11	99.7	98.81	96.73	97.31	94.2	99.1	99.4	98.52
	s02a	90.98	91.48	83.88	90.98	91.48	83.88	90.98	91.48	83.88
	s03a	98.28	99.31	97.61	79.11	79.93	66	85.27	86.16	75
	s04a	97.65	98.31	96.04	96.31	96.96	93.49	88.26	88.85	79.46
	s05a	95.51	95.73	91.61	88.42	89.26	79.91	94.56	94.79	89.89
	s06a	99.54	98.87	98.42	97.27	96.61	94.05	99.77	99.09	98.87
	s07a	98.91	99.56	98.47	98.47	99.12	97.61	75.49	75.99	60.95
	s08a	97.31	99.45	96.79	97.04	99.18	96.27	96.51	99.45	95.99
	Overall	**97.16 ±2.8**	**97.8 ±2.86**	**95.2 ±5.13**	**93.04 ±6.63**	**93.73 ±6.61**	**88.18 ±10.9**	**91.24 ±8.16**	**91.9 ±8.18**	**85.32 ±13.25**
SBDB	s01b	100	100	100	100	100	100	100	100	100
	s02b	75.41	86.79	67.65	75.41	86.79	67.65	75.41	86.79	67.65
	s03b	95.74	97.83	93.75	91.49	93.48	86	95.74	97.83	93.75
	s04b	88.24	88.24	78.95	86.54	88.24	77.59	86.54	88.24	77.59
	s05b	98.33	98.33	96.72	98.33	98.33	96.72	95	95	90.48
	s06b	100	100	100	100	100	100	100	100	100
	s07b	96.55	94.92	91.8	94.83	93.22	88.71	96.55	94.92	91.8
	s08b	94.92	96.55	91.8	83.05	84.48	72.06	94.92	96.55	91.8
	Overall	**93.65 ±8.27**	**95.33 ±5.12**	**90.08 ±11.26**	**91.21 ±8.92**	**93.07 ±6.1**	**86.09 ±12.63**	**93.02 ±8.25**	**94.92 ±4.98**	**89.13 ±11.14**

Overall performances are given in terms of mean ± standard deviation.

Table 3.3: Performance of the proposed method in the detection of diastolic fiducial points

	Record	pAC Instant Detection			AC Instant Detection			MO Instant Detection		
		Se(%)	**+P**(%)	**ACC**(%)	**Se**(%)	**+P**(%)	**ACC**(%)	**Se**(%)	**+P**(%)	**ACC**(%)
NBDB	s01a	98.81	100	98.81	98.21	99.7	97.92	98.21	99.4	97.63
	s02a	98.9	100	98.9	98.9	100	98.9	98.36	99.45	97.82
	s03a	99.32	99.66	98.98	98.97	99.31	98.3	99.32	99.66	98.98
	s04a	99.33	100	99.33	97.64	98.31	96.03	97.98	98.64	96.68
	s05a	98.82	100	98.82	98.58	99.76	98.35	96.22	97.37	93.78
	s06a	98.86	99.77	98.64	98.41	99.77	98.18	97.72	99.08	96.84
	s07a	98.25	100	98.25	95.84	97.77	93.79	95.4	97.1	92.77
	s08a	100	100	100	99.46	99.46	98.93	90.03	90.03	81.86
	Overall	**99.04 ±0.52**	**99.93 ±0.14**	**98.96 ±0.52**	**98.25 ±1.12**	**99.26 ±0.8**	**97.55 ±1.77**	**96.65 ±2.95**	**97.59 ±3.2**	**94.54 ±5.53**
SBDB	s01b	100	100	100	100	100	100	98.15	98.15	96.36
	s02b	100	89.55	89.55	100	89.55	89.55	95	87.69	83.82
	s03b	100	100	100	100	100	100	97.83	97.83	95.74
	s04b	100	100	100	100	100	100	98.08	98.08	96.23
	s05b	100	100	100	100	100	100	100	100	100
	s06b	98.28	100	98.28	87.72	89.29	79.37	94.74	94.74	90
	s07b	100	100	100	96.49	96.49	93.22	100	100	100
	s08b	98.33	100	98.33	98.33	100	98.33	98.33	100	98.33
	Overall	**99.58 ±0.78**	**98.69 ±3.69**	**98.27 ±3.6**	**97.82 ±4.27**	**96.92 ±4.78**	**95.06 ±7.45**	**97.77 ±1.98**	**97.06 ±4.17**	**95.06 ±5.54**

Overall performances are given in terms of mean ± standard deviation.

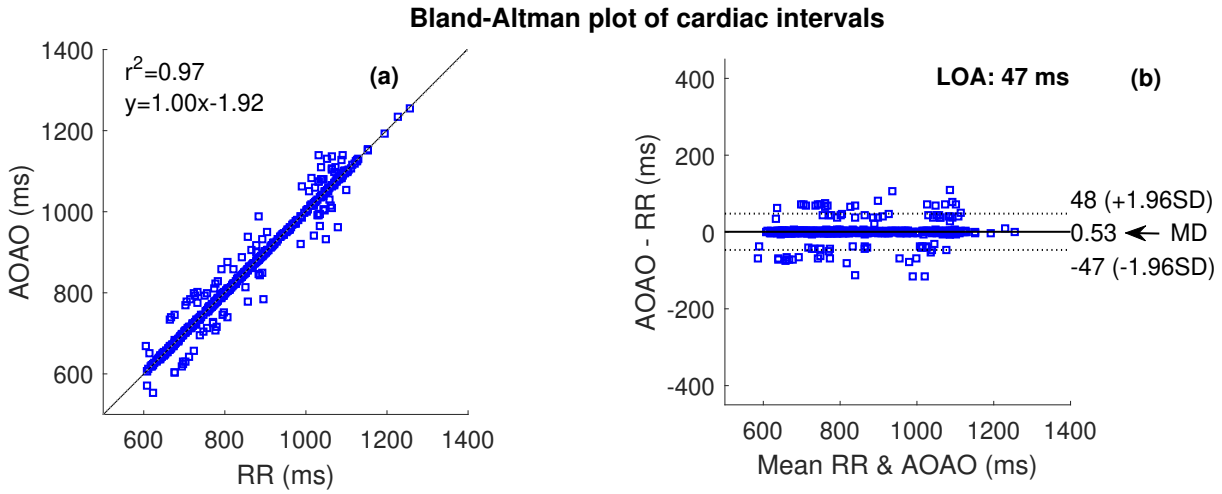

Figure 3.21: Comparison of heartbeats extracted from RR and AO-AO intervals using (a) correlation plot, and (b) Bland-Altman plot. In correlation plot, root mean squared error is achieved as 24 ms. Limits of agreement in 95% confidence intervals are shown in dotted lines. (Abbreviations used— r^2: Pearson's R-squared correlation

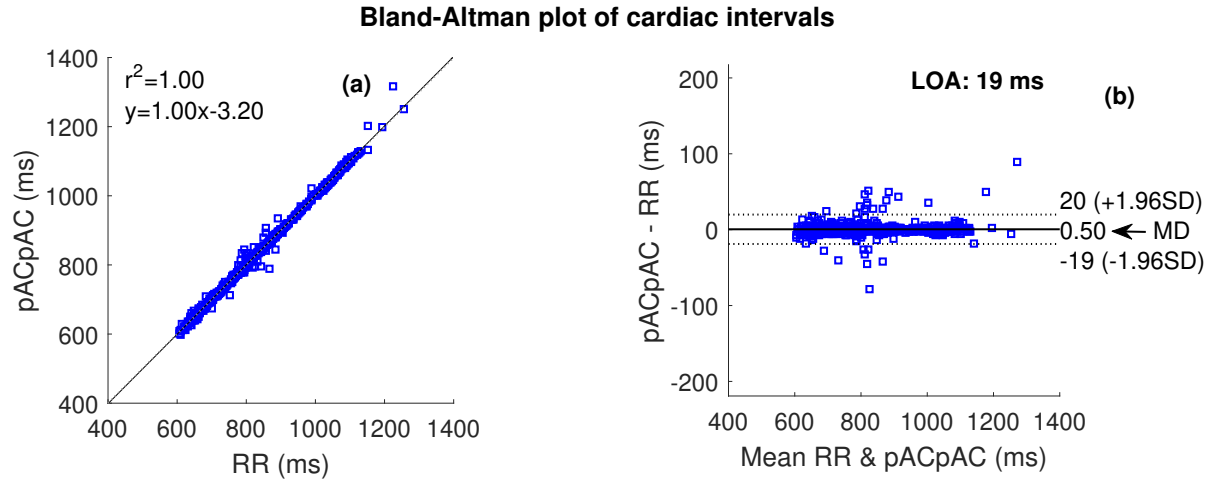

Figure 3.22: Comparison of heartbeats extracted from RR and pAC-pAC intervals using (a) correlation plot, and (b) Bland-Altman plot. In correlation plot, root mean squared error is achieved as 9.9 ms. Limits of agreement in 95% confidence intervals are shown in dotted lines. (Abbreviations used— r^2: Pearson's R-squared correlation coefficient, LOA: limits of agreement, MD: mean difference, SD: standard deviation of difference).

3.2.2.4 Performance comparison

To show the effectiveness of the current PPG assisted framework, its performance is compared with our ECG assisted delineation framework. Both the databases, NBDB and SBDB, are used to evaluate the performance of both the methods. The evaluations are performed for two fiducial points, AO and pAC. Their performance results are tabulated in Tables 3.4 and 3.5, respectively. It is evident from Table 3.4 that the AO peak detection performance is comparable with the ECG assisted method. In

Table 3.4: Performance comparison of AO peak detection on NBDB and SBDB data

Methods	#Beats	Se (%)	+P (%)	ACC (%)
Proposed ECG assisted method	768	98.42	96.83	95.54
Proposed PPG assisted method		96.11	96.97	93.49

Table 3.5: Performance comparison of pAC peak detection on NBDB and SBDB data

Methods	#Beats	Se (%)	+P (%)	ACC (%)
Proposed ECG assisted method	764	91.6	97.39	89.59
Proposed PPG assisted method		99.54	99.41	98.95

contrast, the detection accuracy of the pAC peak is found relatively very poor in the ECG assisted method (Table 3.5). This analysis exhibits the usefulness of our PPG assisted method for delineation of SCG systolic and diastolic points.

3.2.2.5 Applicability in respiratory-effort level identification

The delineated parameters can be used for detection and classification of many cardiovascular events. The variation in respiratory-effort levels is one of the affecting factors of the SCG morphology [4], [115]. Hence, the fiducial points of an SCG signal can be used in assessing the fitness of a respiratory system. Figure 3.23 shows the effect of normal and stopped breathing of an individual onto simultaneously recorded ECG and SCG signals. The ECG derived respiratory effort signals are also shown for these

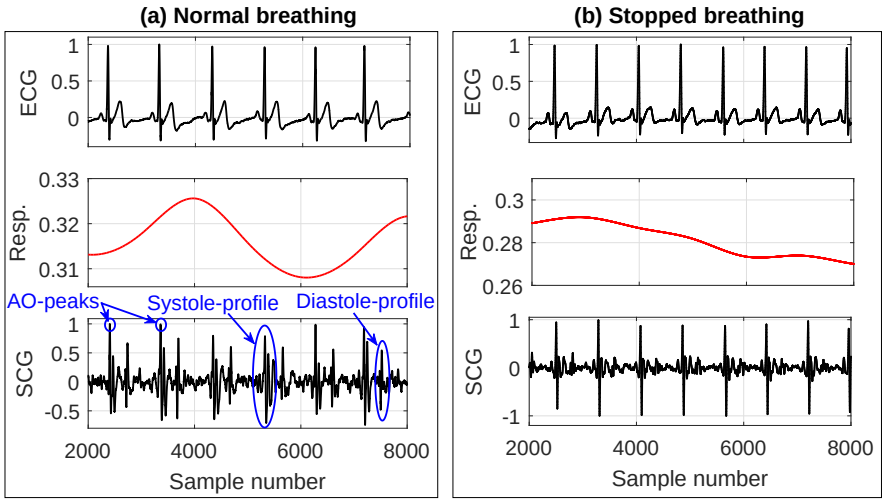

Figure 3.23: Simultaneous recordings of ECG and SCG signals. Morphological variation can be observed in SCG signal under normal and stopped breathing. Respiratory effort signal is derived from ECG signal.

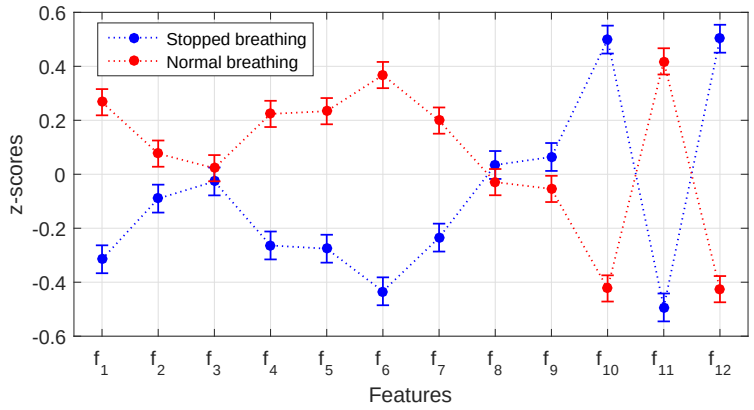

Figure 3.24: Error-bar graph provides distribution of extracted features for both the classes. The distribution is shown via statistical parameters mean (red/blue color dot) and standard deviation (symmetric vertical lines around mean).

cases just for the reference. These signals are extracted by tracing the variation of QRS complexes in consecutive heartbeats, which is obtained by principal component analysis based approach [138]. This figure shows the HR variations against breathing levels, which can be observed on ECG as well as SCG signals. But, a significant variation can be noticed on SCG morphologies as compared to ECG signals. Hence, the selection of the SCG signal can be an appropriate option in this regard.

To show the applicability of the proposed framework, a study of SCG-based cardiorespiratory analysis is performed. For this, the effect of respiratory effort levels reflected in SCG-morphology is observed. Based on morphological variations, the respiratory conditions of a subject can be categorized as normal breathing and breathlessness conditions. A set of twelve extracted features ($\mathrm{f}_k \in \mathbb{R}^{12},\ k = 1, 2, ..12$) is studied for this purpose, and they are AO-AO interval derived heart-rate (HR), relative timing information of AO, IC, AC, pAC and MO with respect to IM, normalized signal amplitudes corresponding to IM, AO, IC, AC, pAC and MO points. The features are extracted from each of the cardiac cycles and normalized. In this study, a 40 s SCG-segment from each of the signals is used for feature extraction. The distributions of normalized features are displayed in Figure 3.24 in terms of mean±standard-deviation. More discriminative and independent features are selected after a statistical analysis of feature distributions and the use of standard T-test procedure. The selected features are $\mathrm{f}_{k^*} \in \mathbb{R}^8,\ k^* = 1, 2, 5, 6, 7, 9, 10, 11$ for this event classification task. Finally, support vector machine (SVM) with RBF kernel is used to identify the breathlessness condition. The choice of training and test cycles is done using the standard 10-fold cross-validation technique [139].

The classification performance is evaluated and compared with various other classifiers. The per-

Table 3.6: Performance results of different classifiers for breathlessness detection with 10-fold cross validation

Features	Metrics	SVM		kNN			Naive	Discrim. Ana.	
		RBF	Linear	Fine	Med.	Coarse	Bayes	LDA	QDA
All	Acc	**97.25**	89.70	96.70	94.64	84.06	85.71	89.57	92.73
	TPR	**96.72**	93.12	97.01	95.53	85.29	85.61	93.73	94.32
	FPR	**2.29**	13.22	3.54	6.08	16.99	14.22	13.97	8.63
SF*	Acc	**98.35**	87.23	96.02	95.61	84.90	79.40	88.19	87.65
	TPR	**97.32**	89.83	95.81	95.53	87.99	75.79	92.83	91.92
	FPR	**0.76**	14.99	3.81	4.31	17.76	17.51	15.74	15.98

Abbreviations – SVM: support vector machine, RBF: radial basis function, kNN: K-nearest neighbour, Fine: kNN with $K = 5$, Medium: kNN with $K = 11$, Coarse: kNN with $K = 101$, LDA: linear discriminant analysis based classifier, QDA: quadratic discriminant analysis based classifier. Here, K denotes number of neighbors in the kNN classifier.
*SF: selected feature-set. Note that all the metrics are presented here in terms of %.

formance evaluation is done with three measurement parameters, true positive rate $\left(\text{TPR} = \frac{\text{TP}}{\text{TP+FN}}\right)$, false positive rate $\left(\text{FPR} = \frac{\text{FP}}{\text{TN+FP}}\right)$, and recognition accuracy $\left(\text{Acc} = \frac{\text{TP+TN}}{\text{TP+TN+FP+FN}}\right)$ [140]. The average performance metrics are tabulated in Table 3.6. The SVM-RBF based classifier outperforms others by producing these metrics as 97.25, 96.72 and 2.29, respectively for considering all features, and 98.35, 97.32 and 0.76, respectively for considering selected feature-set. Figure 3.25 shows the estimated receiver operating characteristic (ROC) curves plotted between TPR and FPR, and area under the ROC curve (AUC) for the identification of SB class. The best performance is achieved with the SVM-RBF classifier. This experiment validates that the delineated parameters from the proposed method could be employed not only for the cardiac analysis, but also for the assessment of respiratory system.

3.2.3 Conclusion

In this work, a novel framework is proposed for delineation of systole and diastole parameters of an SCG signal with the help of a temporally concurrent fingertip-PPG signal. The proposed SCG delineation framework is mainly based on wavelet scalogram, envelope construction scheme, and decision rules. It gives a better estimation of PPG-peaks, estimation of diastole-phases (AC, pAC, and MO) in the SCG, and estimation of systole-phases (IM, AO, and IC) in SCG. Along with the delineated parameters, LVET and IVRT time-intervals can also be estimated. The experimental results on NBDB and SBDB databases show very promising results, and so, the proposed framework may be applied for cardiac-cycle event detection for pathological interpretations. The salient point of the proposed method is its

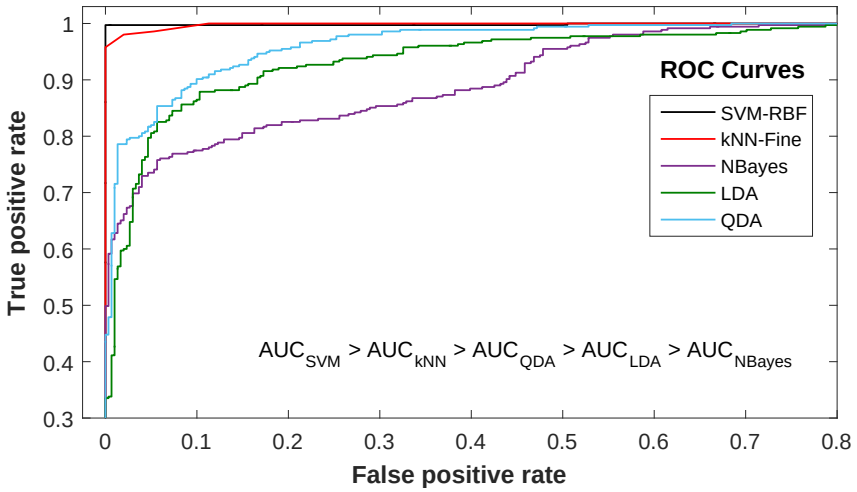

Figure 3.25: ROC of different classifier-models on selected features. SVM-RBF based classifier outperforms others by achieving the largest AUC of 0.9986.

ability to estimate six important cardiac phases simultaneously and characterize events associated with both systolic and diastolic regions. Additionally, as an application, the information extracted from the estimated fiducial points can be used to identify normal breathing and breathlessness conditions. The SVM-RBF classifier gives good results on our selected feature-set. However, the framework needs to be tested with cardio- and respiratory related pathological scenarios for its clinical applications.

3.3 Summary

In this chapter, we present the delineation frameworks for systole and diastole profiles of the SCG signal, which take the help of other cardiac signals as reference. In the first approach based on ECG-assisted delineation, orthogonal subspace projection is used to project the SCG signal onto the ECG subspace for estimating the AO peaks. Subsequently, the pAC peaks are estimated by processing the SCG cycles constructed by AO-AO intervals. Whereas second approach uses the fingertip-PPG signal as a reference to obtain the information of many SCG-parameters such as IM, AO, IC, AC, pAC, and MO. The fiducial points estimated from the proposed method characterize the whole SCG cycle, including its systole and diastole profiles. The qualitative and quantitative analysis of the results shows quite better performances for our delineation methods. The ability of the delineated parameters obtained from our PPG assisted delineation method is shown to detect the breathlessness condition of a subject. In the next chapter, we will discuss the extraction of fundamental heart sounds and their characterization by analyzing the morphological structure of SCG signals.

4

Extraction of Fundamental Heart Sounds: A Pilot Study

Contents

The heart-sound (HS) signal indicates closing instants of atrioventricular and semilunar valves. The SCG signal is generated by cardiac mechanical functions, blood flow, and valvular opening and closing activities. Thus, it is expected that the information about HS is embedded in the SCG signal. This chapter presents a small preliminary study to assess the reliability in extracting fundamental heart sounds from an SCG signal. The proposed method employs a discrete wavelet transform for signal decomposition, and subsequently, the center of gravity (CoG) of the power spectrum for each of the subbands is computed. The proposed method can optimally select wavelet subbands for any combination of sampling frequencies of the signal and number of decomposition levels. Based on the proposed CoG criterion, the signal is reconstructed from selected subbands, and the instantaneous Hilbert envelope is constructed for localizing peaks of the signal. Finally, a simple decision rule is applied to annotate S1 and S2 sounds of the PCG signal. Experimental results show that the heart sound waves S1 and S2 can be well localized with the help of one SCG cycle without using a reference ECG cycle. The organization of this chapter is as follows: the description of heart sound and its association with SCG are discussed in Section 4.1. Section 4.2 explains the application of the SCG signal for the extraction of PCG-components using the proposed method. In Section 4.3, the experimental results of our method are analyzed to evaluate its performance. Finally, the chapter is summarized in Section 4.4.

4.1 Heart Sound Extraction from Sternal Seismocardiography

The temporal-association among ECG, SCG, and phonocardiogram (PCG) is shown in Figure 4.1. Among other modalities, heart sound, also called PCG signal represents cardiac mechanical functions such as closures of AV and semilunar valves. Two fundamental heart sounds (HS)– S1 (first HS) and S2 (second HS) are prominent during auscultation. Sometimes, two more heart sounds S3 (third HS) and S4 (fourth HS) may be heard due to exercise or pathology [141]. An accelerometric SCG signal consists of both infrasonic and sonic components up to 1 kHz [11]. So, one important research problem is to develop a suitable method for extracting heart sound from mechanical vibrations in the form of an SCG signal. The frequency components of the fundamental heart sound waves cover the lower sonic range, *i.e.*, less than 150 Hz [141]. There are many standard methods for segmenting heart sounds [142]. Thus, the clinical features from systole and diastole profiles of SCG and PCG signals can provide vital information about the heart mechanical activities.

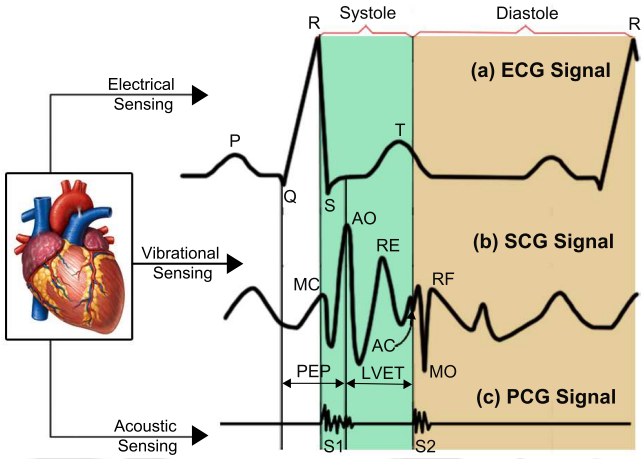

Figure 4.1: Simultaneous recording of ECG, dorso-ventral SCG and PCG signals.

So, the main objective of this research work is to extract fundamental heart sounds from dorso-ventral component of a 3-D SCG signal. In the existing literature, the PCG cycles are extracted using zero-phase Chebyshev digital high pass filter with ECG signal as a reference [34]. The heart sounds are extracted by removing the smoothed part from the SCG signal by the Savitzky-Golay filter [9]. These extractions are done using time-domain features of the SCG signal, which are not reliable in the presence of artifacts and interbeat variabilities in the SCG signal. In this work, a unified multiresolution and center frequency based framework is proposed for extracting fundamental HS without using a reference ECG signal. The proposed framework provides the flexibility of selecting any number of wavelet decomposition levels for any sampling frequency of the signal. It looks at their energy concentration by peak localization from the systolic and diastolic periods of the heart cycle. We also used an SCG signal to extract heart rates from the derived HS signal, and our experimental results clearly show that the heart rate patterns obtained by our method almost follow the heart rate patterns obtained by an ECG signal.

4.2 Proposed Heart Sound Extraction Method

A zero mean amplitude normalized SCG signal denoted by $x[n]$ $(n = 1, 2, ..., N)$ is first filtered by a fifth-order median filter. The filtered SCG data is re-sampled at 1000 samples/s and divided into non-overlapping segments of 10 s each for further processing. A schematic block diagram of the proposed heart sound extraction and its fundamental waves' peak-detection scheme is illustrated in Figure 4.2.

[5]This work has been published in IEEE Signal Processing Letters, 2018 (Refer *List of Publications* page for details).

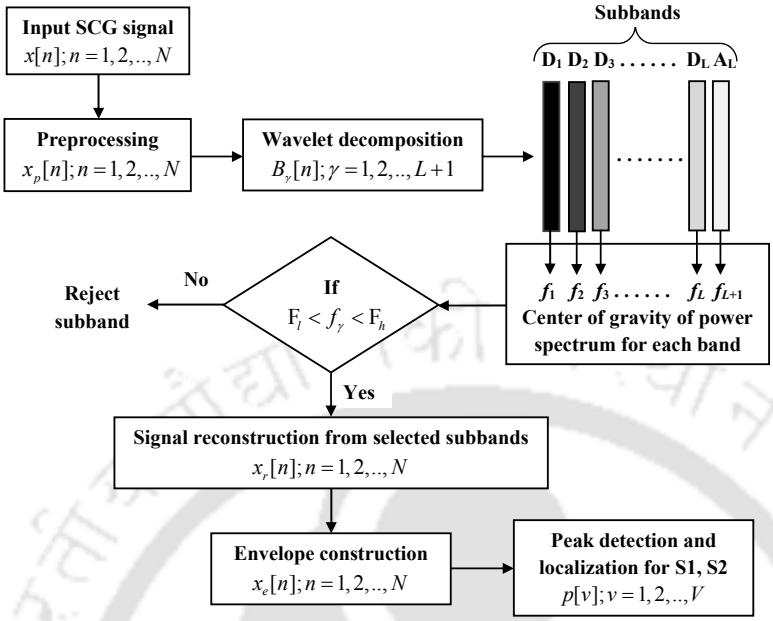

Figure 4.2: Proposed heart sound extraction and its peak detection framework.

4.2.1 Signal decomposition and reconstruction

The preprocessed signal $x_p[n]$ is decomposed using discrete wavelet transform (DWT) with *Biorthogonal 3.9* (bior3.9) basis function. This basis function is selected as it has morphological similarity with the SCG signal. The DWT segments diagnostic and clinical features of SCG in various subbands [30]. The wavelet filterbank structure is designed for L^{th}-order decomposition as:

$$x_p[n] = \sum_{i=1}^{L} D_i[n] + A_L[n] \tag{4.1}$$

where, $D_i[n]$, $A_i[n]$, $(i = 1, 2, ..., L)$ correspond reconstructed subband signals from i^{th}-level detailed and approximation coefficients, respectively. These sub-signals are togetherly expressed as:

$$B_\gamma[n] = \begin{cases} D_\gamma[n], & \gamma = 1, 2, ..., L \\ A_L[n], & \gamma = L+1 \end{cases} \tag{4.2}$$

4.2.1.1 Proposed CoG-based criterion for subband selection

The subbands, whose center of gravities (CoG) of the power spectrums, do not follow the frequency range of HS– S1 and S2 (30–150 Hz [141]) are rejected. The CoG of power spectrum for γ^{th} subband is computed as:

$$f_\gamma = \frac{\int_0^\infty f|\bar{S}_\gamma(f)|^2 df}{\int_0^\infty |\bar{S}_\gamma(f)|^2 df} \tag{4.3}$$

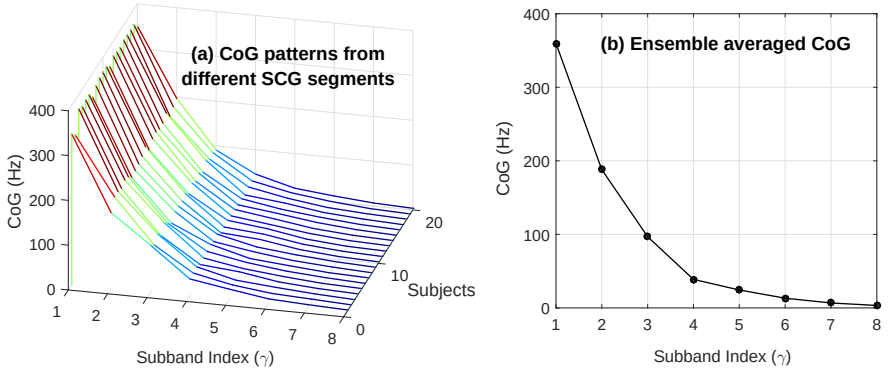

Figure 4.3: Exponential nature of CoG patterns of power spectrums for seven decomposition levels. (a) set of CoGs from different subjects, and (b) ensemble averaged CoG.

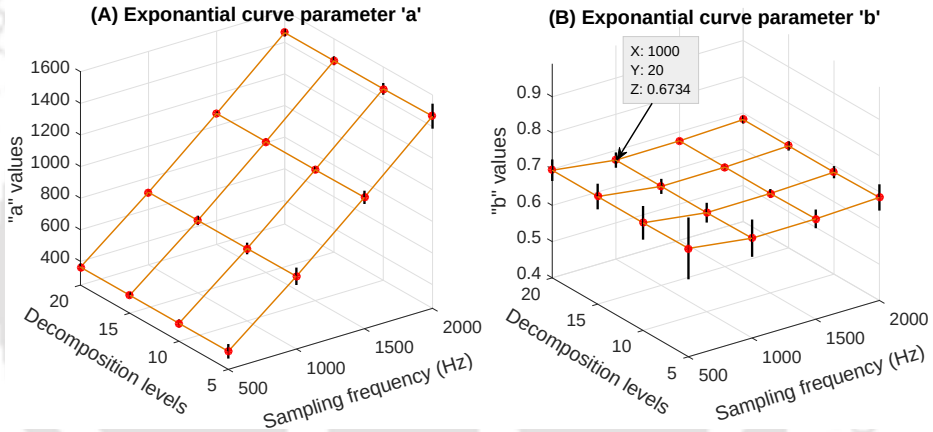

Figure 4.4: Variations of exponential curve fitting parameters with respect to sampling frequency and number of decomposition levels (Eq. (4.4)). Dots indicate parameter values in the grid, and symmetric vertical lines on those dots indicate the range of parameter values in 95% confidence interval.

where, f and $|\bar{S}_\gamma(f)|^2$ denote frequency and power spectrum of γ^{th} subband, respectively. These CoG-patterns follow exponential decay with respect to the extracted subbands, which is shown in Figure 4.3. Thus, ensemble averaged CoG from different subjects can be modelled as:

$$f_\gamma = ae^{-b\gamma} \tag{4.4}$$

where, a and b are exponential parameters, which need to be estimated for different combinations of sampling frequencies (F_s) and number of decomposition levels (L) to generalize Eq. (4.4). Figure 4.4 shows variations of these fitted parameters with respect to F_s (500 to 2000 Hz) and L (5 to 20) for 95% confidence intervals. The parameter a varies with F_s in a linear fashion irrespective of L (Figure 4.4(A)), while it is observed that parameter b remains constant with the variations of F_s and

L (Figure 4.4(B)). Thus, in an average sense, parameters a and b are estimated as:

$$a \approx \mathrm{C}F_s \; ; \quad b \approx 0.673 \tag{4.5}$$

where C = 5/7 and Eq. (4.4) is updated as:

$$f_\gamma = \frac{5}{7} F_s e^{-0.673\gamma} \tag{4.6}$$

$$\gamma \approx -1.486 \log_e \left(\frac{7 f_\gamma}{5 F_s} \right) \tag{4.7}$$

As the selection criterion for subbands, the range 20 Hz (F_l) to 160 Hz (F_h) is selected with a little tolerance.

$$\left\lceil -1.486 \log_e \left(\frac{7\mathrm{F}_h}{5F_s} \right) \right\rceil \leq \gamma \leq \left\lfloor -1.486 \log_e \left(\frac{7\mathrm{F}_l}{5F_s} \right) \right\rfloor \tag{4.8}$$

$$\left\lceil -1.486 \log_e \left(\frac{224}{F_s} \right) \right\rceil \leq \gamma \leq \left\lfloor -1.486 \log_e \left(\frac{28}{F_s} \right) \right\rfloor \tag{4.9}$$

where $\lceil \cdot \rceil$ and $\lfloor \cdot \rfloor$ denote ceiling and flooring operations, respectively. Finally, the signal is reconstructed by considering the selected subbands for $\mathrm{F}_l < f_\gamma < \mathrm{F}_h$, which is denoted by $x_r[n]$. The reconstructed signal is expected to provide a good correlation with the concurrent HS signal. This model provides application-specific optimal wavelet subbands irrespective of the sampling frequency and decomposition levels.

4.2.2 Envelope construction and peak detection

An envelope is constructed in order to localize the peaks of local waves (S1 and S2) in the HS signal extracted from SCG. The Hilbert transform based analytic signal envelope ($x_e[n]$) is computed as:

$$x_e[n] = \sqrt{(x_r[n])^2 + (\widehat{x}_r[n])^2} \tag{4.10}$$

where $\widehat{(\cdot)}$ is Hilbert transform operator. A moving average FIR filtering (window length 50 ms) based smoothing operation is performed to avoid small spurious spikes in the estimated envelope. To detect the peaks of S1 and S2, the Hilbert transform is applied to the smoothed envelope. The positive zero crossings (PZCs) of Hilbert transformed envelope provides an estimation of S1 and S2 peaks. Finally, proper peak localization in the derived PCG signal is performed by a 300 ms extrema search window, which is centered around the estimated peaks. So, the exact heart sound peaks ($p[v]$ in Figure 4.2) are obtained.

Algorithm 4 Automatic annotation of S1 and S2 peaks

1: $[p[v]] \leftarrow$ **HS_Peak_Detection**$(x_r[n])$.
2: $[s[n]] \leftarrow$ **Construct_Sparsity**$(x_r[n], p[v])$.
Input: $s[n]$, $p[v]$.
3: $\widetilde{\text{S1}} \leftarrow$ **arg max**$(s[n])$.
4: S1 $\leftarrow \widetilde{\text{S1}}$.
5: Update S1 location: $s_1loc \leftarrow [s_1loc\ ;\ \text{S1}]$.
6: Forward scanning with $w[m]$ $(m = 1, .., \text{M})$ after S1:
S1 $\leftarrow$ **arg max**$(s[n] \cdot w[m + \text{S1} + \text{M}/2])$.
7: Repeat from Step 5 until forward scanning is complete for $s[n]$.
8: S1 $\leftarrow \widetilde{\text{S1}}$.
9: Backward scanning with $w[m]$ $(m = 1, .., \text{M})$ before S1:
S1 $\leftarrow$ **arg max**$(s[n] \cdot w[m - \text{S1} - \text{M}/2])$.
10: Update S1 location: $s_1loc \leftarrow [s_1loc\ ;\ \text{S1}]$.
11: Repeat from Step 9 until backward scanning is complete for $s[n]$.
12: $s_1loc \leftarrow$ **Ascending_Sort**(s_1loc).
13: $s_2loc \leftarrow$ **arg max**$(s[s_1loc(i) + 1 : s_1loc(i + 1) - 1])$.
Output: Prominent S1 and S2 peak instants– s_1loc, s_2loc.

4.2.3 Annotation of S1 and S2 peaks

After estimating peaks present in the systolic and diastolic regions of derived PCG signal $x_r[n]$, it is essential to categorize and label the peaks as S1 and S2. In order to annotate peaks, a sparse signal $s[n]$, containing only the estimated peaks is constructed from $x_r[n]$. Basically, $s[n]$ contains zero elements and deflections on determined peak locations $p[v]$. It is supposed to get relatively large amplitudes in S1 waves depending on the placement of the sensor in the body areas. The SCG is recorded at the lower end of the sternum on the xiphoid process, which is very near to tricuspid and mitral area (S1 louder). Thus, the maximum of $s[n]$ is assigned as S1, which is the first labelling step. A fixed duration scanning window ($w[m]$; $m = 1, 2, .., M$) is used in both forward and backward direction from the labelled S1 to find maximas corresponding to S1 peaks. Then, S2 peaks are determined as maximas of $s[n]$ between every two consecutive S1 peak instants. The pseudocode for automatic labelling of S1 and S2 is given in Algorithm 4.

4.3 Results and Discussion

For our experimentations, the SCG signals are taken from the CEBS database, publicly available at Physionet archive [125], which includes ECG, SCG, and respiration signals with varying wave morphologies for healthy subjects. The input SCG signal $x[n]$ is preprocessed with a median filter, which suppresses high-frequency noises, but it preserves clinical information. Furthermore, DWT-based signal decomposition is performed on the preprocessed signal $x_p[n]$ into seven levels. As fundamental

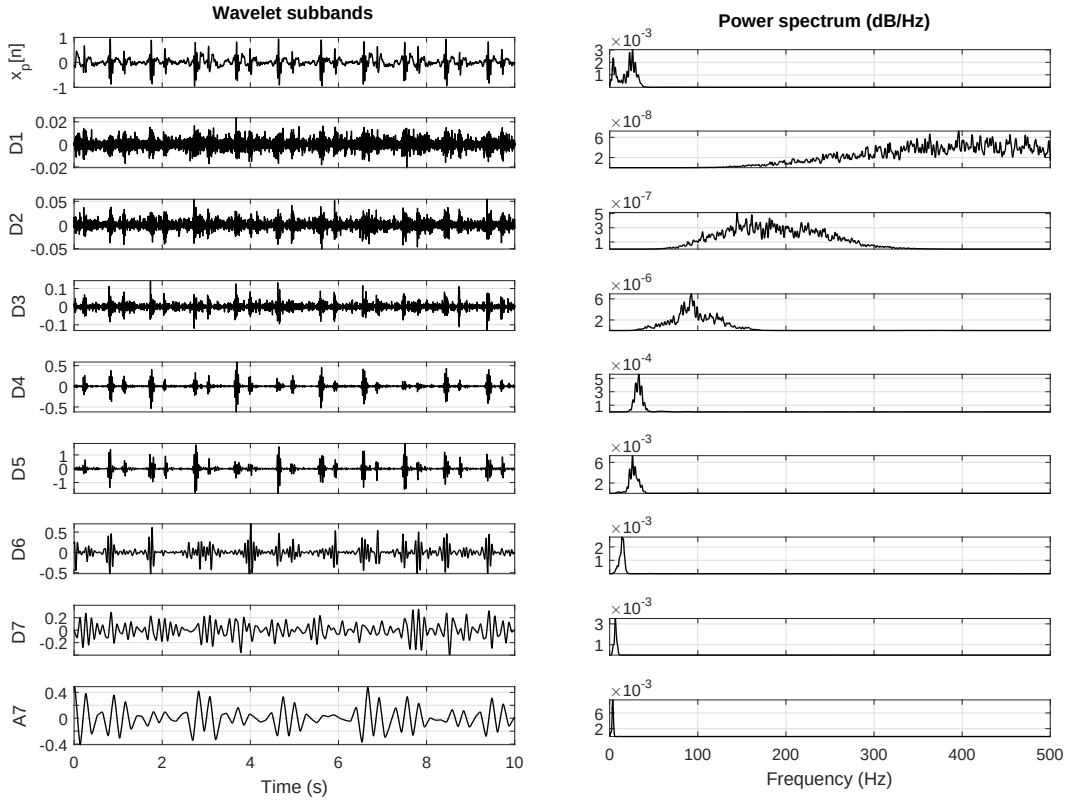

Figure 4.5: Signal decomposition using wavelet transform (Left panel) and their corresponding power spectral densities (Right panel).

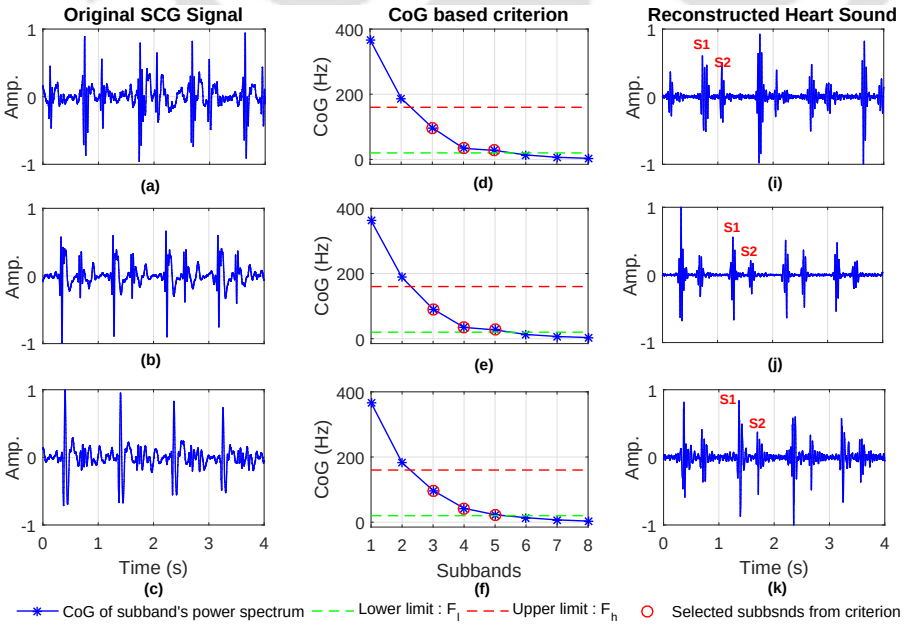

Figure 4.6: HS extraction from SCG signals from different subjects by selecting subbands with CoG based criterion. (a)–(c) show input SCGs from three different subjects, and corresponding selected subbands are shown in (d)–(f); and reconstructed PCGs are shown in (i)–(k), respectively.

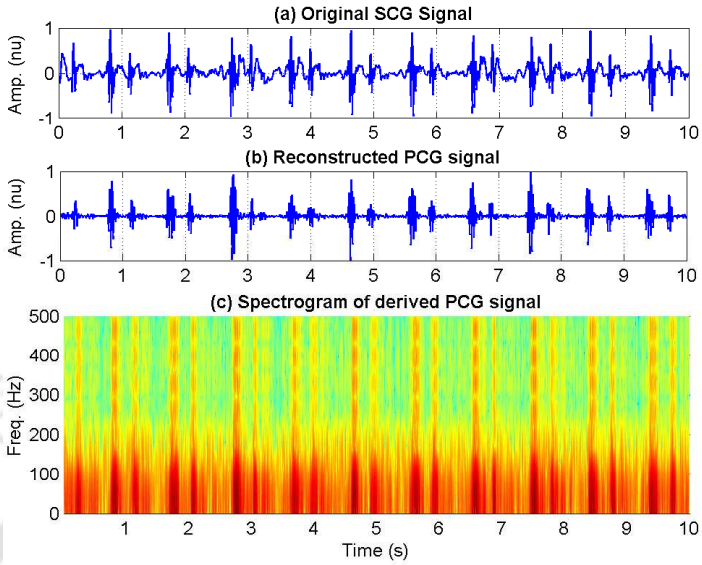

Figure 4.7: Time-frequency representation of the derived heart sound signal using spectrogram. The major energy distributions are limited to 150 Hz.

heart sounds reside in the higher frequency range (>30 Hz) and so, no further decomposition is needed to emphasize lower frequency bands. An example of SCG signal decomposition and the corresponding power spectrum of each of the subbands are illustrated in Figure 4.5. The wavelet decomposition of $x_p[n]$ provides an approximation subband A_7 and seven detailed subbands D_1-D_7. It is seen (Figure 4.5) that most of the S1 and S2 components reside in D_3-D_5 subbands.

The optimal subbands which convey heart sound information, are selected on the basis of CoG of power spectrums of the subbands. The CoG corresponds to the central frequency, where the maximum power of the spectrum is concentrated. The proposed CoG criterion is applied to wavelet subbands to select optimal bands, and the PCG signal is reconstructed. Subbands 3, 4, and 5 are selected for F_s=1000 and L=7 by Eq. (4.9). The HS extraction process by this criterion is shown in Figure 4.6. In addition, the spectrogram of the derived PCG signal is computed by the STFT processing window of 15 ms duration, which is shown in Figure 4.7(c). It is observed that major energies corresponding to the HSs remain below 150 Hz.

The Hilbert transform is employed on the derived PCG signal $x_r[n]$ for envelope construction, and subsequently, it is also used for finding peaks of S1 and S2 waves. The smoothed analytic signal envelope $x_e[n]$ constructed from $x_r[n]$ is shown in Figure 4.8(c). Figure 4.8(d) shows the Hilbert transformed envelope $h_e[n]$ and zero crossings at positive slopes. Finally, a symmetric search window is employed to find the real peaks in $x_r[n]$ around detected zero crossings of $h_e[n]$. The peak detection

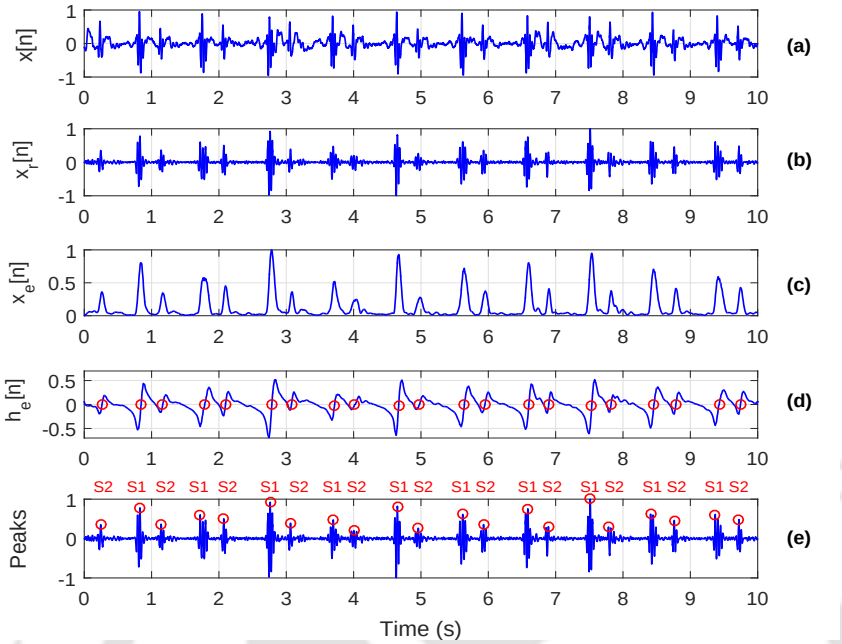

Figure 4.8: Peak detection process of S1 and S2 waves. (a) SCG signal, (b) reconstructed PCG, (c) smoothed envelope, (d) Hilbert transformed envelope with PZCs, (e) detected real S1, S2 peaks, but not annotated.

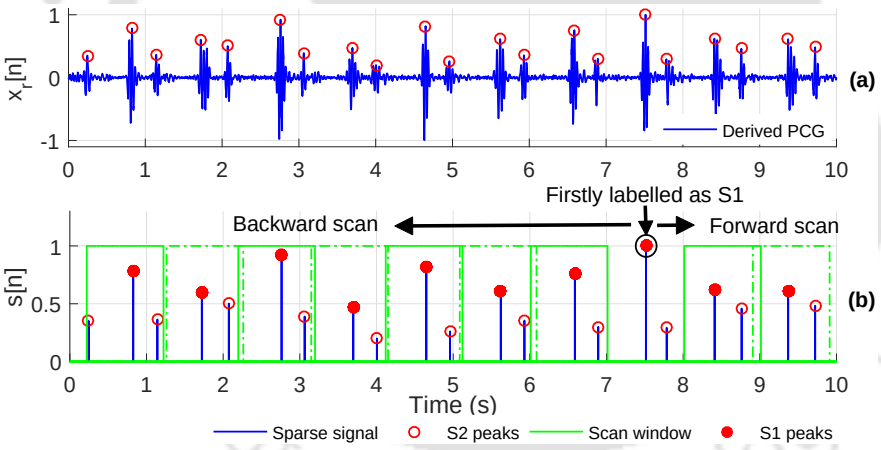

Figure 4.9: Peak annotation process of S1 and S2 in derived PCG signal. (a) extracted PCG with non-labelled peaks, (b) labelled S1 and S2 peak instants.

process in PCG is shown in Figure 4.8.

After detecting all the peaks, annotation is done on the sparse signal $s[n]$ by a scanning window of duration 800 ms with a translation of 400 ms. Heart sound S1 and S2 peaks are labeled by using our proposed Algorithm 4, which is shown in Figure 4.9. Another experiment is also performed to extract heart rate information from the derived PCG signal. For this purpose, five different SCG signals from the CEBS database are processed for 60 s each, and heart rates are extracted by using the estimated S1-S1 intervals and S2-S2 intervals. These results are compared with the results extracted from ECG

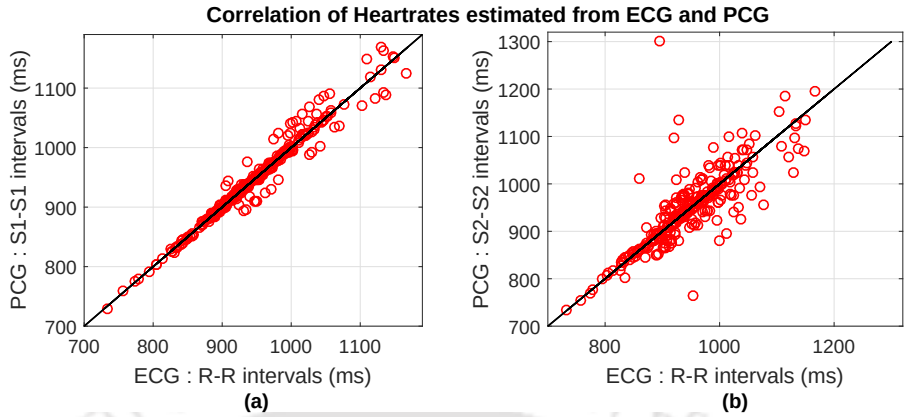

Figure 4.10: Correlation between extracted heartrates from ECG and SCG-derived PCG for: (a) R-R and S1-S1 intervals, and (b) R-R and S2-S2 intervals.

R-R intervals, and this is illustrated in Figure 4.10. It is observed that the correlation between S1-S1 and R-R intervals is stronger, and also, the scattering of S2-S2 intervals relating to R-R intervals is higher. All these experimental results clearly show that the derived PCG signal can be efficiently employed for heart rate variability analysis like ECG-based analysis. Additionally, mean opinion scores (MOS's) from five clinical experts (doctors) are recorded to evaluate the quality of clinical features of SCG-derived S1, S2, and entire PCG signals. The extracted PCG signals are played back to them, and they compared it with the heart sounds of healthy subjects with their perceived clinical knowledge during auscultation by stethoscope. They have provided their opinion scores on a 5 point scale. The average MOS's for S1, S2, and PCG are 4.31, 4.33, and 4.26, respectively.

4.4 Summary

In this chapter, we present a framework for extracting the PCG signal from a dorso-ventral component of a 3-D SCG signal. The subbands are extracted by discrete wavelet decomposition, and the important subbands are selected by our proposed CoG criterion. The proposed data-dependent frequency domain CoG feature is found effective in selecting important subbands. It localizes the peaks of fundamental heart sounds without any other reference cardiac signals. Finally, the Hilbert transform is employed for constructing signal envelope and peak detection. A simple decision rule-based strategy is proposed for automatic annotation of heart sound peaks. The PCG signal obtained by processing an SCG signal is investigated for the feasibility of heart rate variability analysis, and it shows promising results. The performance evaluation of our method is done by using different types of SCG signals

from the CEBS database. The qualitative analysis and listening test show that the performance of the proposed method is quite satisfactory. However, quantitative validations with real PCG signals are required for possible clinical applications. Along with the heart sound information, the SCG also carries information related to respiratory events. The morphology of the SCG signal is usually affected by the breathing-patterns. Thus, the next chapter presents another applicability of SCG morphology in the cardiorespiratory analysis. To identify breathing-condition of a subject, the SCG-characteristics are investigated.

5

Cardiorespiratory Analysis

Contents

This chapter presents the utility of SCG signals for the identification of respiratory-effort levels. In this study, we analyze the SCG morphological variations under varying respiratory-efforts level. The development of alarming devices for health monitoring via body area networks (BANs) has been receiving substantial interest recently. As an m-health application, the automatic breathing-state assessment system can be employed in many electronic devices like tablets, smart phones, e-whiteboards, smart watches, and health-bands [143]. Recent cardiovascular studies suggest that the SCG has greater potential to be a diagnostic tool for early prediction of cardiac diseases in wearable healthcare [4, 6]. The wearable healthcare appliances integrated with an SCG-based system have a great potential for wireless wearable BANs [6]. Many factors affect the SCG signal morphology, such as body movement, posture, and respiration. This study is mainly focused on the analysis of SCG morphology under varying respiratory-effort levels. It uses hybrid morphological features of the SCG signal, including fiducial and non-fiducial features for the characterization of breathing-states.

The objective of this study is to propose an SCG-based breathing-state detector for healthcare applications. The proposed framework is designed to identify different breathing patterns, namely breathlessness, regular/normal respiration, and long and labored breathing. The labored breathing is an abnormal pattern characterized by a symptom of increased breathing effort. All these patterns are abbreviated as SB, NB, and LB for stopped, normal, and long breathing, respectively. The proposed breathing-state detector needs a concurrent ECG signal to extract the SCG cycles. A set of statistical-, amplitude-, time-, and spectral-based features of the SCG signal is extracted. In our method, stacked autoencoder (SAE) based neural network (NN) architecture is used for identification of different breathing levels. An accurate estimation of fiducial points is a difficult and computationally expensive task. Hence, to make the system low complex, only a few fiducial information such as AO and diastole boundaries are utilized. The rest of the chapter is organized as follows: Section 5.1 presents the proposed methodology. The experimental results are presented in Section 5.2. Finally, it is summarized in Section 5.3.

5.1 Proposed Breathing State Detection Method

The SCG beat morphologies can indicate respiratory-effort levels. As shown in Figure 5.1, the waveform characteristics of SCG signals changes for SB, NB, and LB breathing patterns. More specifically, SCG signals in breathlessness condition have peaky-distributed beat patterns having almost constant

[6]This work has been published in IEEE Sensors Journal, 2020 (Refer *List of Publications* page for details).

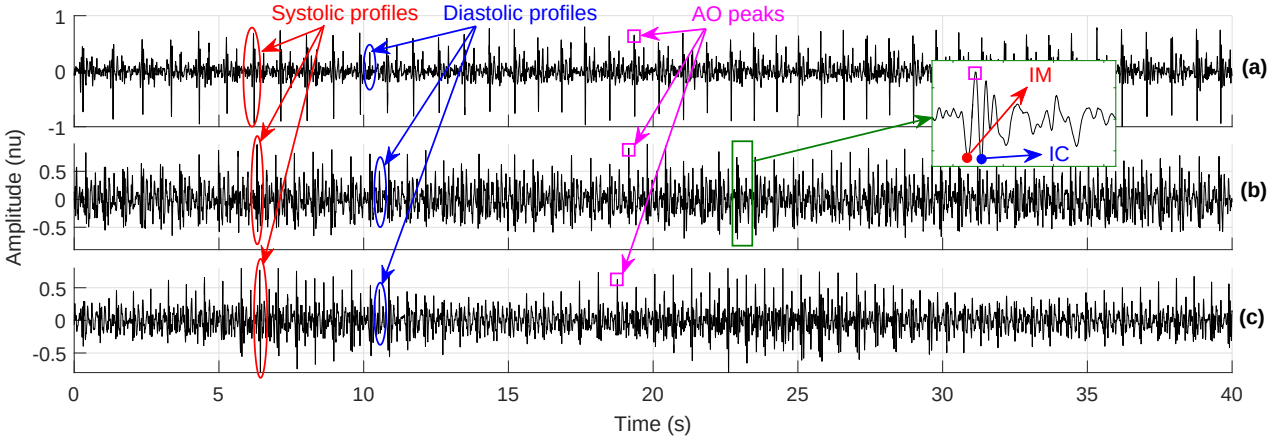

Figure 5.1: Annotated SCG signals in three breathing scenarios: (a) breathlessness, (b) normal breathing, and (c) long breathing. Morphological variations can be observed in all three respiratory patterns, where signals were collected from a single subject.

amplitude and regular heart-rhythm, while relatively more variations of amplitude and heart-rhythm are observed during normal breathing. Large amplitude-modulated type beat patterns with varying heart-rates are observed in long breathing conditions. In order to identify different breathing states, the features which can identify morphological variations of an SCG signal due to different breathing conditions need to be extracted. The overview of the proposed methodology is illustrated in Figure 5.2. The proposed work is carried out in three major phases. In Phase-I, signal-database was generated followed by feature extraction in Phase-II. Finally, classification is done to identify the degree of breathing levels (SB, NB and LB).

5.1.1 Database creation

For the breathing level identification purpose, the dorso-ventral SCG and concurrent ECG (Lead-II) signals are acquired from healthy male subjects. Chosen subjects have following demographics, age: 28.75±2.31 yrs, weight: 71.63±7.85 kg, height: 5'7.6"±2.6", heart-rate: 79.18±10.93 bpm. The signals are recorded in three sessions: normal breathing for 5 minutes (NB), holding breath for 50 s (SB), and long respiration for 2 minutes (LB). So, two breathing conditions, namely breathlessness as well as long- and labored-respiratory data are artificially generated. The signals are sampled at a frequency of 1 kHz. All the signals were recorded using our self built data acquisition system (DAS). The description of the designed DAS is provided in Section 2.1, also can be found in [132]. The recording process was approved by the institutional ethical review board.

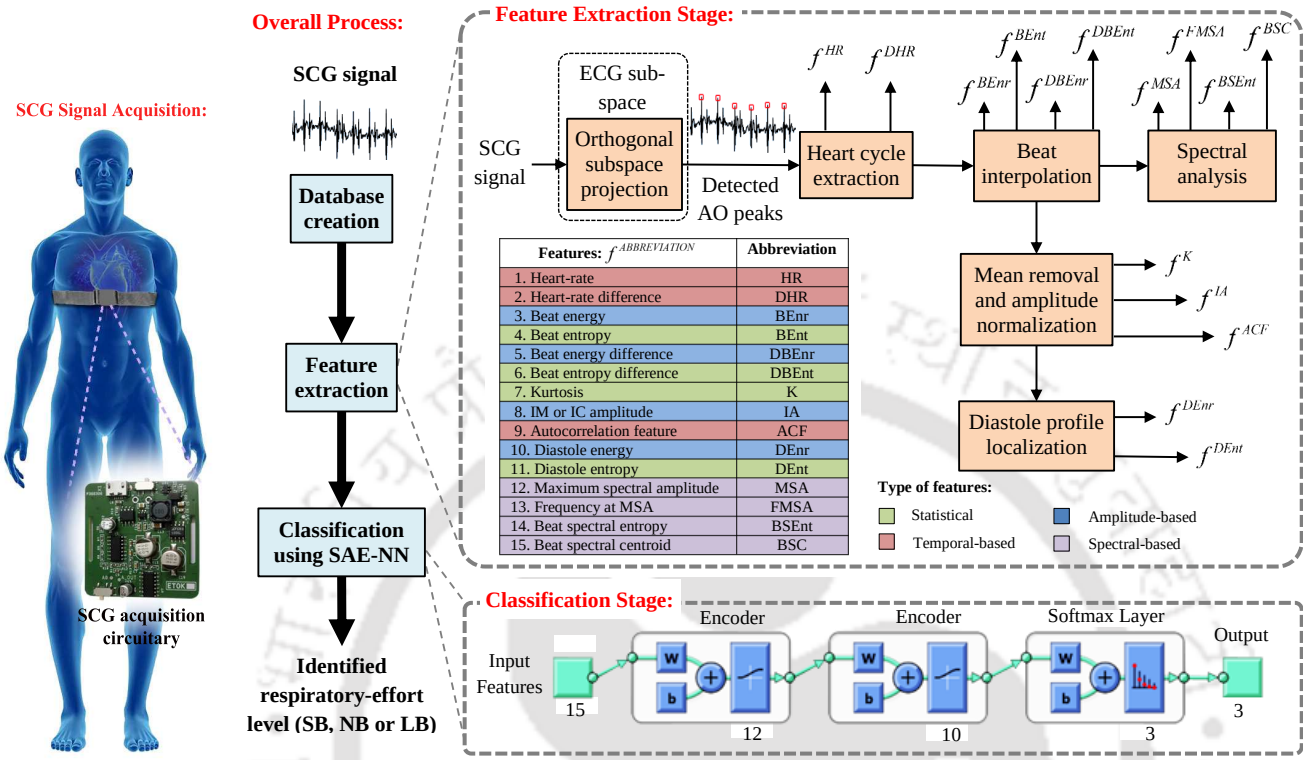

Figure 5.2: Overview of the proposed method for identification of the respiratory-effort levels. The numeric details shown in the classification stage represent numbers of nodes at different layers of SAE-NN classifier. For instance, there are 15 input features, and both sequential encoders and softmax layer produce 12, 10 and 3 output nodes, respectively.

5.1.2 Feature extraction

A number of features are extracted from an SCG signal, and these features are mainly based on statistical, amplitude, temporal and spectral information of the signal. These features can uniquely relate the SCG morphology with the respiration rate. The extraction process of all these features are illustrated in Figure 5.2. A detailed description of feature extraction steps is provided below.

5.1.2.1 Orthogonal subspace projection

The proposed method is mainly based on the extraction of SCG cycles, which relies on accurate detection of prominent AO peaks in the SCG. The estimation of AO peaks is performed using an orthogonal subspace projection (OSP) scheme [144]. With the projection of an SCG signal onto ECG subspace, the details of SCG signal which are linearly related to the details of an ECG signal can be estimated. The ECG subspace is created by the original ECG signal and its delayed versions [144]. The linear relationship of an SCG signal $\mathbf{s}$ and the corresponding ECG subspace $\mathbb{U}$ can be expressed

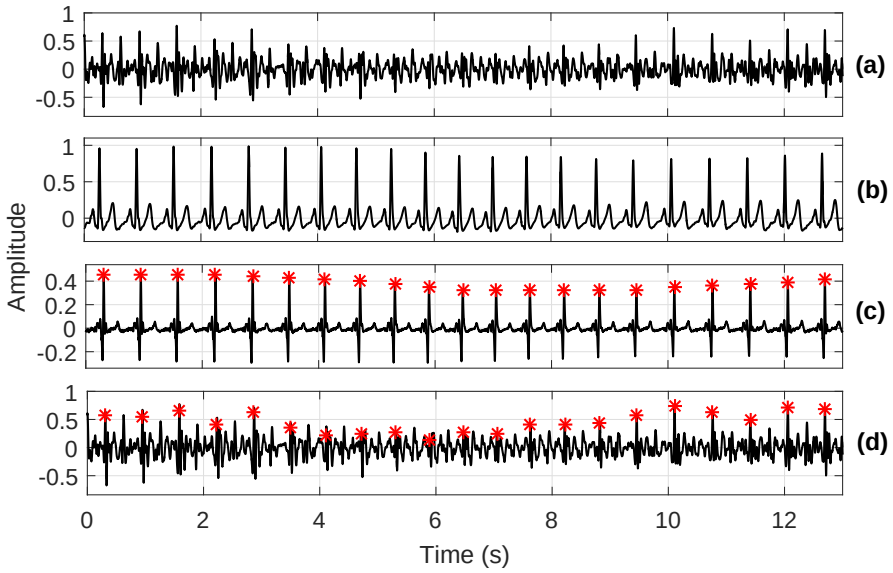

Figure 5.3: AO peak detection process using orthogonal subspace projection. (a) an SCG signal $\mathbf{s}$, (b) concurrent ECG signal for creation of its subspace $\mathbb{U}$, (c) projected sequence $\widehat{\mathbf{s}}$ and its estimated peaks using the FOGD scheme, and (d) detected AO peaks in the SCG.

as follows [144]:

$$\mathbb{U}\mathbf{x} = \mathbf{s} \tag{5.1}$$

The best estimate of $\mathbf{s}$ on subspace $\mathbb{U}$ is found by using a subspace projection as [144]:

$$\widehat{\mathbf{s}} = \mathbb{U}(\mathbb{U}^T\mathbb{U})^{-1}\mathbb{U}^T\mathbf{s} \tag{5.2}$$

Finally, a first order Gaussian differentiator (FOGD) based logic is applied to the projected sequence $\widehat{\mathbf{s}}$, which ultimately indicates the locations of AO peaks in the SCG signal. The entire AO peak detection process is shown in Figure 5.3. This OSP-based AO peak detection scheme has also been explained in Section 3.1.1.1.

5.1.2.2 Heart cycle extraction

In our proposed method, the estimated AO instants are used to extract heart cycles (HC) in the SCG signal. Changes of breathing levels indirectly alter oxygen content present in the blood, and so, the heart pumping rates change accordingly. Thus, heart rate (HR) variations can indicate respiratory effort levels. In order to extract the heart cycles, the intervals between consecutive AO instants are estimated and two different features, namely heart rate (f^{HR}) and heart rate difference (f^{DHR}) are

estimated as follows:

$$\mathrm{HC}_i = \mathrm{AO}_{i+1} - \mathrm{AO}_i \tag{5.3}$$

$$f_i^{HR} = 60/\mathrm{HC}_i \tag{5.4}$$

$$f_i^{DHR} = \left| f_i^{\overline{HR}} - f_{i-\mathrm{D}}^{\overline{HR}} \right| \tag{5.5}$$

where, $|\cdot|$ is absolute value operator; $i = 1, 2, ..., (\mathrm{P}-1)$, and P denotes total number of AO peaks present in the SCG segment. $f^{\overline{HR}}$ makes f^{HR} to be a circular sequence, and the delay parameter D is judiciously chosen as 3 for identifying long breathing patterns.

5.1.2.3 Beat interpolation

After utilizing temporal information of an SCG signal for indicating heart beats, all the beat-durations are normalized to a fixed length. The resulting interpolated SCG beats are used to estimate the following features: beat energy (f^{BEnr}), beat entropy (f^{BEnt}), beat energy difference (f^{DBEnr}), and beat entropy difference (f^{DBEnt}). The beat energy is expressed as:

$$f_i^{BEnr} = \frac{1}{L} \sum_{l=0}^{L-1} \left(\bar{\mathbf{s}}^i[l] \right)^2 \tag{5.6}$$

where, $\bar{\mathbf{s}}^i[l]$ $(l = 0, 1, .., L-1)$ denotes i^{th} interpolated SCG beat, $i \in [1, \mathrm{P}-1]$. For the computation of f^{DBEnt} feature, the amplitude level of beat $\bar{\mathbf{s}}[l]$ is normalized, say $\bar{\mathbf{s}}_1[l]$, such that $\bar{\mathbf{s}}_1[l] \in [0, 1]$ and $\sum_l \bar{\mathbf{s}}_1[l] = 1$. It expresses the distribution of relative components in a beat as:

$$\bar{\mathbf{s}}_1[l] \longleftarrow \frac{\bar{\mathbf{s}}[l] - \mathrm{M}_{\bar{\mathbf{s}}}}{\sum_{l=0}^{L-1} \left(\bar{\mathbf{s}}[l] - \mathrm{M}_{\bar{\mathbf{s}}} \right)} \tag{5.7}$$

where, $\mathrm{M}_{\bar{\mathbf{s}}} = \underset{l=0:L-1}{min} (\bar{\mathbf{s}}[l])$. Hence, the beat entropy can be expressed as:

$$f_i^{BEnt} = -\sum_l \bar{\mathbf{s}}_1^i[l] log(\bar{\mathbf{s}}_1^i[l]) \tag{5.8}$$

The difference features corresponding to beat energy and beat entropy are computed as:

$$f_i^{DBEnr} = \left| f_i^{\overline{BEnr}} - f_{i-\mathrm{D}}^{\overline{BEnr}} \right| \tag{5.9}$$

$$f_i^{DBEnt} = \left| f_i^{\overline{BEnt}} - f_{i-\mathrm{D}}^{\overline{BEnt}} \right| \tag{5.10}$$

where, $f^{\overline{BEnr}}$ and $f^{\overline{BEnt}}$ denote circular versions of f^{BEnr} and f^{BEnt} sequences, respectively.

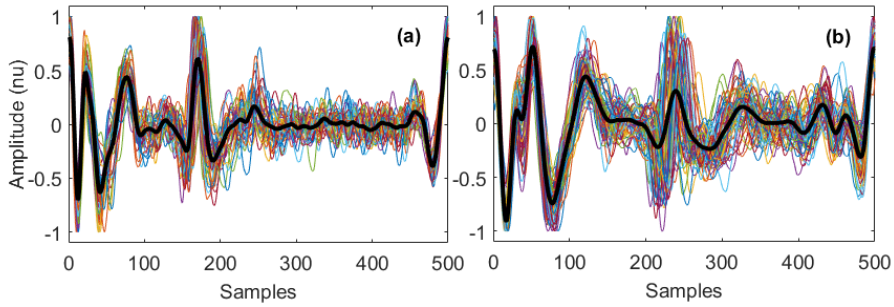

Figure 5.4: Interpolated SCG beats after DC-offset removal and amplitude normalization for two subjects in (a) and (b). All the inter-beats are displayed along with their ensemble-averaged beat (in dark black colour).

5.1.2.4 Mean removal and amplitude normalization

After the estimation of beat energy and entropy features, DC-offset is subtracted from $\bar{\mathbf{s}}_1[l]$, and the amplitude is normalized by its maximum value. This normalized beat, also denoted by $\bar{\mathbf{s}}_2[l]$, is shown in Figure 5.4. Under this, three morphological features, namely kurtosis (f^K), IM or IC amplitude (f^{IA}) and auto-correlation feature (f^{ACF}) are extracted from the SCG beat $\bar{\mathbf{s}}_2[l]$, which are described as follows:

- **Kurtosis (K):** It estimates the peakedness of the distribution for SCG beat $\bar{\mathbf{s}}_2[l]$. It is defined as [3]:

$$f_i^K = \frac{\frac{1}{L}\sum_{l=0}^{L-1}\left(\bar{\mathbf{s}}_2^i[l] - \mathrm{M}_{\bar{\mathbf{s}}_2^i}\right)^4}{\left(\frac{1}{L}\sum_{l=0}^{L-1}\left(\bar{\mathbf{s}}_2^i[l] - \mathrm{M}_{\bar{\mathbf{s}}_2^i}\right)^2\right)^2} \tag{5.11}$$

  where, $\mathrm{M}_{\bar{\mathbf{s}}_2^i} = \frac{1}{L}\sum_{l=0}^{L-1}\bar{\mathbf{s}}_2^i[l]$. As compared to other breathing patterns, larger Kurtosis values correspond to breathlessness conditions [115].

- **Autocorrelation feature (ACF):** The ACF feature is extracted from each of the beats as follows [3]:

$$f_i^{ACF} = \sum_{l=-\infty}^{\infty}\{\bar{\mathbf{s}}_2^i[l]\bar{\mathbf{s}}_2^i[l+P]\} \tag{5.12}$$

  where, the parameter P denotes a fixed lag. The ACF feature can detect interbeat variabilities and body vibrations resulted from varying respiration rates.

- **IM/IC amplitude (IA):** The IA is extracted by computing the maximum negative signal-strength of each beat $\bar{\mathbf{s}}_2$ [115]. It indicates the amplitude of either IM or IC fiducial point.

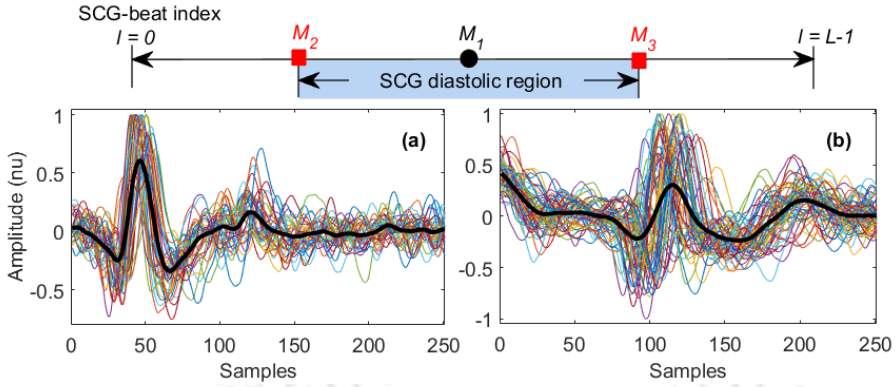

Figure 5.5: Segmented SCG diastole-profiles after DC-offset removal and amplitude normalization for two subjects in (a) and (b). All the inter-beats are displayed along with their ensemble-averaged beat (in dark black colour).

This feature is used to measure the amplitude sharpness of an SCG cycle induced by varying breathing-pattens. It can be expressed as:

$$f_i^{IA} = \underset{l=0:L-1}{min}\,(\bar{\mathbf{s}}_2^i[l]) \tag{5.13}$$

5.1.2.5 Diastole profile localization

In order to extract the diastolic features, the SCG diastole is segmented as follows. Initially, the beat $\bar{\mathbf{s}}_2$ is divided at its middle (say M_1 point). The SCG systole can be localized in a segment between M_2 and M_3 points, where M_2 and M_3 are the mid-points of segments between start-point and M_1, and between M_1 and end-point, i.e.,

$$M_1 = \frac{(L-1)}{2};\quad M_2 = \frac{(L-1)}{4};\quad M_3 = \frac{3(L-1)}{2}$$

The segmentation of diastolic region is also shown in Figure 5.5 along with diastole profiles segmented from two subjects. To capture morphological variabilities especially in diastole profiles, two features, diastole Energy (f^{DEnr}) and diastole entropy (f^{DEnt}) are extracted. The expression of f^{DEnr} is given as follows:

$$f_i^{DEnr} = \frac{1}{M_3 - M_2 + 1}\sum_{l=M_2}^{M_3}\left(\bar{\mathbf{s}}_2^i[l]\right)^2 \tag{5.14}$$

Usually, the SCG-diastole produces relatively smallest energy in breathlessness condition as compared to other breathing conditions. Thus, f^{DEnr} can be a dominant feature to detect breathing events. Subsequently, diastole entropy (f^{DEnt}) feature is extracted on $\mathbf{d}_1[n]$ ($\mathbf{d}_1[n] \in [0,1]$), which has a zero

minima and it is normalized by its elemental-sum value as:

$$\mathbf{d}[n] = \bar{\mathbf{s}}_2[M_2, M_2+1, M_2+2, ..., M_3] \tag{5.15}$$

$$\mathbf{d}_1[n] \longleftarrow \frac{\mathbf{d}[n] - \mathrm{M}_{\mathbf{d}}}{\sum_{n=M_2}^{M_3} (\mathbf{d}[n] - \mathrm{M}_{\mathbf{d}})} \tag{5.16}$$

where, $\mathrm{M}_{\mathbf{d}} = \underset{n=0:M_3-M_2}{min}(\mathbf{d}[n])$ and the expression for f^{DEnt} is given as:

$$f_i^{DEnt} = -\sum_n \mathbf{d}_1^i[n] log(\mathbf{d}_1^i[n]) \tag{5.17}$$

5.1.2.6 Spectral analysis

Four spectral features namely, maximum spectral amplitude (f^{MSA}), frequency at MSA (f^{FMSA}), beat spectral centroid (f^{BSC}), and beat spectral entropy (f^{BSEnt}) are extracted from magnitude-spectrum of each of the interpolated beats ($\bar{\mathbf{s}}_1^i[l]$). Suppose, $\bar{\mathbf{s}}_1[l]$ and $\bar{\mathbf{S}}_1[f]$ are Fourier transformation pairs, and $|\bar{\mathbf{S}}_1[f]|$ denotes the magnitude spectrum. Then, f^{MSA} and f^{FMSA} features are expressed as:

$$f_i^{MSA} = \underset{f=0,1,..,F_s/2}{max} \left(|\bar{\mathbf{S}}_1^i[f]| \right) \tag{5.18}$$

$$f_i^{FMSA} = \underset{f=0,1,..,F_s/2}{arg\ max} \left(|\bar{\mathbf{S}}_1^i[f]| \right) \tag{5.19}$$

where, F_s denotes sampling frequency of the signal. The MSA and FMSA features characterize the beat by its dominating spectral component, which changes with varying respiration-rates. Similarly, the beat spectral centroid (BSC) and the beat spectral entropy (BSEnt) measure the center-of-gravity of the beat-spectrum and spectral randomness, respectively. Their expressions are given as follows:

$$f_i^{BSC} = \frac{\sum_f f|\bar{\mathbf{S}}_1^i[f]|}{\sum_f |\bar{\mathbf{S}}_1^i[f]|} \tag{5.20}$$

$$f_i^{BSEnt} = -\sum_f \mathbf{S}_n^i[f] log(\mathbf{S}_n^i[f]) \tag{5.21}$$

where, $\mathbf{S}_n[f]$ corresponds to normalized $\bar{\mathbf{S}}_1[f]$ i.e., $\mathbf{S}_n[f] = \bar{\mathbf{S}}_1[f]/(\sum \bar{\mathbf{S}}_1[f])$.

Finally, all the extracted features are concatenated together to create a feature vector ($\mathbb{R}^{15}$) corresponding to each of the SCG-beats.

5.1.3 Stacked autoencoder-based model for identification of breathing conditions

Autoencoder is a neural network with an input layer, a hidden layer, and an output layer as shown

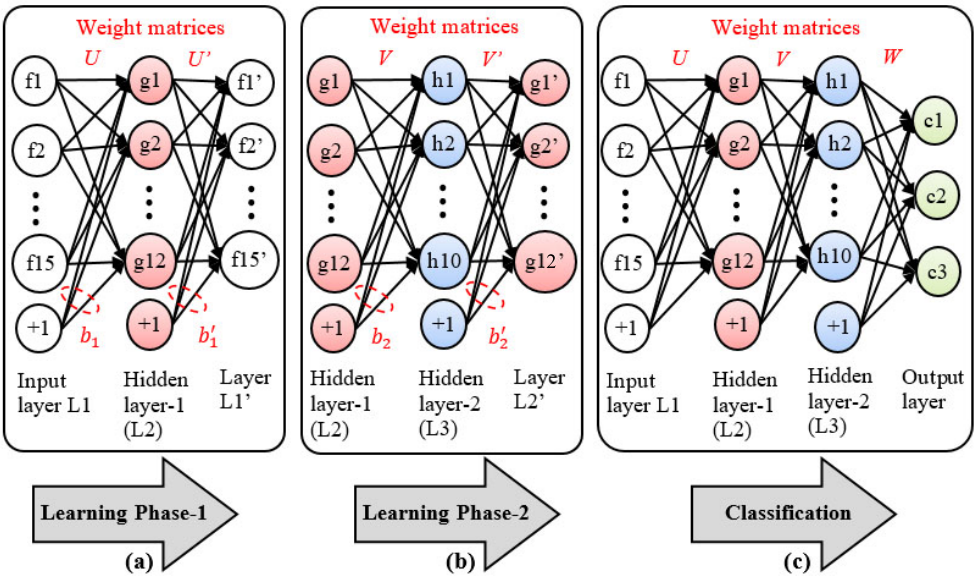

Figure 5.6: Proposed network configuration to develop stacked autoencoder (SAE) based classifier for identification of breathing-patterns. (a) autoencoder for layer L2, (b) autoencoder for layer L3, and (c) SAE for classification.

in Figure 5.6(a) and (b). The autoencoder is trained to reconstruct input data using encoding and decoding processes [145]. Let x and b be the input vector and bias, respectively, then the hidden space is expressed as $z = \phi(Ax + b)$, where 'z' is mapping or code vector, 'A' denotes the encoding weight matrix, and the linear or nonlinear nature of mapping can be set by activation function $\phi(\cdot)$. Similarly, the decoder maps the hidden space data to the input vector as, $\widehat{x} = \phi'(A'z + b')$. In general, $\phi'(\cdot)$ is considered linear, since input data belongs to the space of real numbers [146]. The learning of connection weights corresponding to encoding (A) and decoding (A') is achieved by minimizing the cost function given in [147]:

$$J = \frac{1}{2R}\sum_{r=1}^{R}\sum_{k=1}^{K}(x_{kn} - \widehat{x}_{kn})^2 + \frac{\lambda}{2}\left(\sum_{N,K} A^2 + \sum_{K,N}(A')^2 + \sum_{N} b^2 + \sum_{K}(b')^2\right) + \beta\sum_{j=1}^{N}\mathrm{KL}(\rho \parallel \widehat{\rho}_j) \quad (5.22)$$

where, input and output layers have equal K nodes, and the hidden layer has N nodes, thus $A \in \mathbb{R}^{N\times K}$, $A' \in \mathbb{R}^{K\times N}$, $b \in \mathbb{R}^{N\times 1}$, and $b' \in \mathbb{R}^{K\times 1}$. The used parameters R, λ, and β denote total number of observations in the dataset, weight regularization, and sparsity regularization parameters, respectively. KL, which represents Kullback-Leibler divergence, acts as a sparsity penalty component [147]. The indices ρ and $\widehat{\rho}$ correspond to desired and average activation values, respectively.

For classification, the sparse autoencoders are stacked together and a combined neural network

Table 5.1: Foldwise overall accuracies of the proposed SAE classifier

Folds	1	2	3	4	5	6	7	8	9	10	**Average**
Acc (%)	89.47	88.70	88.70	96.52	91.30	93.04	90.43	93.04	91.23	92.11	**91.45**

architecture is created. This is called as stacked autoencoder (SAE), where the weights are usually learned in a greedy manner [146]. Figure 5.6 shows the proposed SAE network configuration for identification of respiratory rates. It is an ensemble of two sparse autoencoders with a soft-max classifier. As shown in Figure 5.6, during the first learning phase, hidden space g is trained on input feature vector f to obtain the parameters U, U', b_1 and b_1'. While, the next hidden layer h is trained on the g space to get the parameters V, V', b_2 and b_2'. Subsequently, the output of the last hidden layer is fed into a soft-max classifier. Finally, all the SAE layers are used as a single unified model, and this model is fine-tuned for performance improvement as shown in Figure 5.6(c).

5.2 Results and Discussion

Initially, OSP-based AO peak detection algorithm is employed to estimate AO peaks of an SCG signal. The detected AO peaks are used to identify SCG cycles. Subsequently, fifteen significant features are extracted on each of the SCG cycles. The final feature set is represented as: $f^{final} = \{f^{HR}, f^{DHR}, f^{BEnr}, f^{BEnt}, f^{DBEnr}, f^{DBEnt}, f^{K}, f^{IA}, f^{ACF}, f^{DEnt}, f^{DEnr}, f^{MSA}, f^{FMSA}, f^{BSEnt}, f^{BSC}\}$. An NN architecture using SAE is proposed for classification, which can handle the feature engineering on its own. The parameters used in the proposed SAE are as follows: number of neurons in hidden layers equal to 12 and 10, respectively. The values of λ and β are 0.001 and 4, respectively. The sparsity proportions for hidden layers are selected as 0.5 and 0.35, respectively. The efficiency of the proposed approach is established based on standard quantitative statistical assessments. The performance measures used are recognition accuracy (Acc), precision (Pr), true positive rate (TPR), true negative rate (TNR) and F1-score. The aforementioned metrics can be computed using following expressions: Acc $= \frac{\text{TP+TN}}{\text{TP+TN+FP+FN}}$, Pr $= \frac{\text{TP}}{\text{TP+FP}}$, TPR $= \frac{\text{TP}}{\text{TP+FN}}$, TNR $= \frac{\text{TN}}{\text{TN+FP}}$, and F1-score $= \frac{2\times\text{Pr}\times\text{TPR}}{\text{Pr+TPR}}$. The experimentation was performed with 10-fold cross validation for 1147 SCG-beats, collected from eight subjects. The analyzed data were taken for 40 s duration from each of the three breathing patterns. Table 5.1 lists the foldwise recognition accuracies produced by the proposed method. The average overall recognition accuracy of 91.45% is achieved. Additionally, ac-

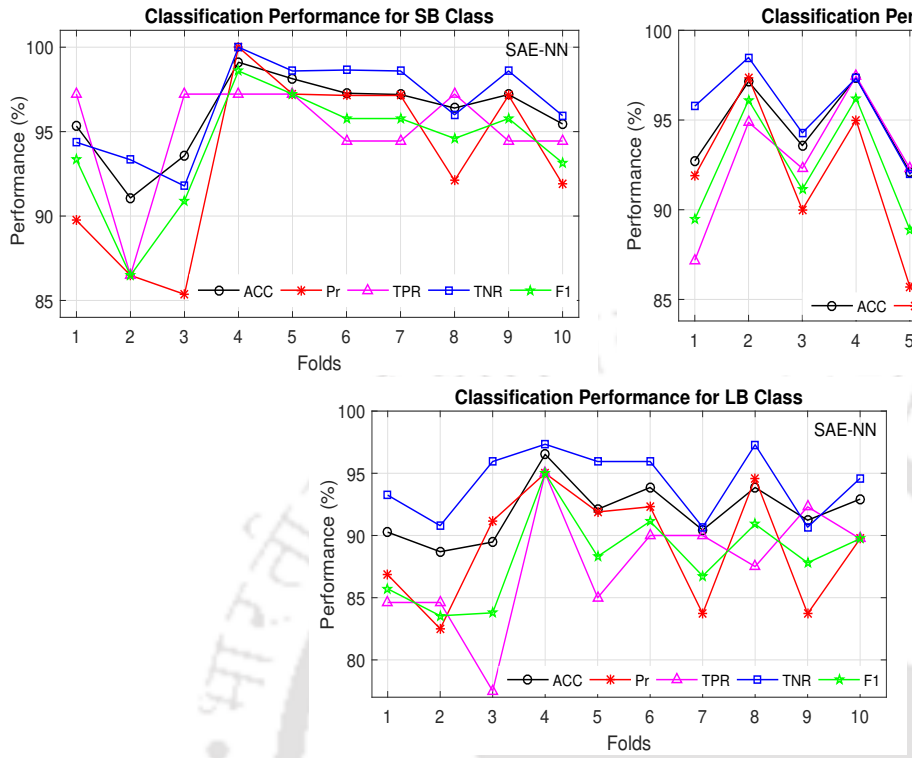

Figure 5.7: Classification performance of the proposed method for identification of different respiratory-patterns.

curacies in identifying SB, NB, and LB breathing-patterns are determined. The performance results are shown in Figure 5.7 for different folds. It is observed that average accuracies achieved for classification of SB, NB and LB classes are in the range of 96–97%, 94–95%, and 91–92%, respectively. The average performance results for all these breathing classes are tabulated in Table 5.2. The av-

Table 5.2: Average performance of the proposed SAE-based approach

Resp. Levels	Acc	Pr	TPR	TNR	F1-score
SB	96.07	93.42	95.04	96.59	94.16
NB	94.52	92.38	92.05	95.87	92.16
LB	91.94	89.15	87.63	94.24	88.27
Average*	**94.17**	**91.65**	**91.57**	**95.56**	**91.53**

Note that Acc, Pr, TPR, TNR and F1-scores are given in %.
*Average performance indexes for all respiratory levels.

erage achieved precision rate from all three classes is 91.65%. The average TPR value obtained is in the range of 91–92%. The averaged TNR and F1-score are approximately, 95.56% and 91.53%. The performance of the proposed method is also evaluated in the other two cross-validation analyses, namely leave-one-subject-out and leave-one-sample-out. To evaluate the performance unbias to the

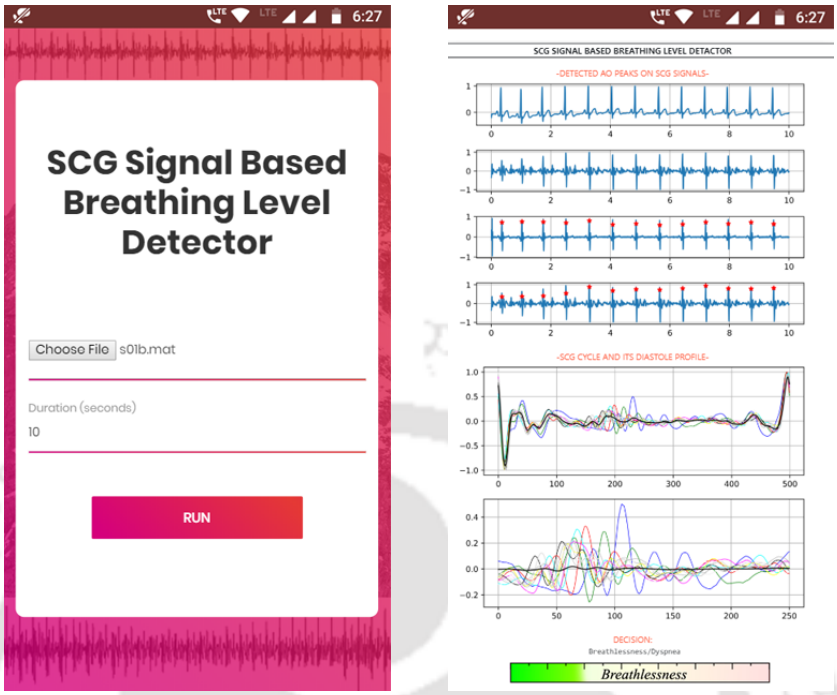

Figure 5.8: Snapshots of our developed mobile application for breathing state detection.

test-subjects, leave-one-subject-out cross-validation analysis is performed. In this study, one subject is considered for testing, and the model is trained with the remaining subjects. This experiment is repeated for all the subjects, leaving a subject out each time. With this cross-validation analysis, the method produces an average overall accuracy of 73.46% irrespective of the classes. Under the leave-one-sample-out cross-validation scheme, every heartbeat is repeatedly used for the testing process, and reminders of the data are used to train the model. It is a good way to validate, but relatively takes much time for computation. The overall mean accuracy is obtained as 90.67%. All the performance results indicate the efficacy of the proposed method, and our proposed framework has a great potential in the domain of automatic identification of degree of breathing. The snapshots of the developed mobile application are illustrated in Figure 5.8. In this example, it is shown that an SCG signal of duration 10 s is recorded under breathlessness condition, and subsequently, it is successfully identified by the proposed framework.

5.2.1 Performance comparison

The proposed technique is compared with other conventional classifiers, namely SVM (with different kernels, namely RBF, linear and polynomial), kNN (with different number of neighbours), naive Bayes,

Table 5.3: Performance comparison in terms of overall accuracy (%) obtained from 10-folds experimentation

Proposed	SVM			kNN			Naive		
SAE-NN	RBF	Linear	Poly3	K=5	K=10	K=100	Bayes	LDA	QDA
91.45	90.50	86.84	89.19	89.45	87.53	77.52	71.32	85.10	85.01

Random forest			AdaBoost (Ns = 50)		
Nl = 30	Nl = 100	Nl = 200	Nl = 100	Nl = 200	Nl = 300
89.1	90.8	90.1	90	90.5	90.3

Nl and Ns denote number of learners and number of splits, respectively.

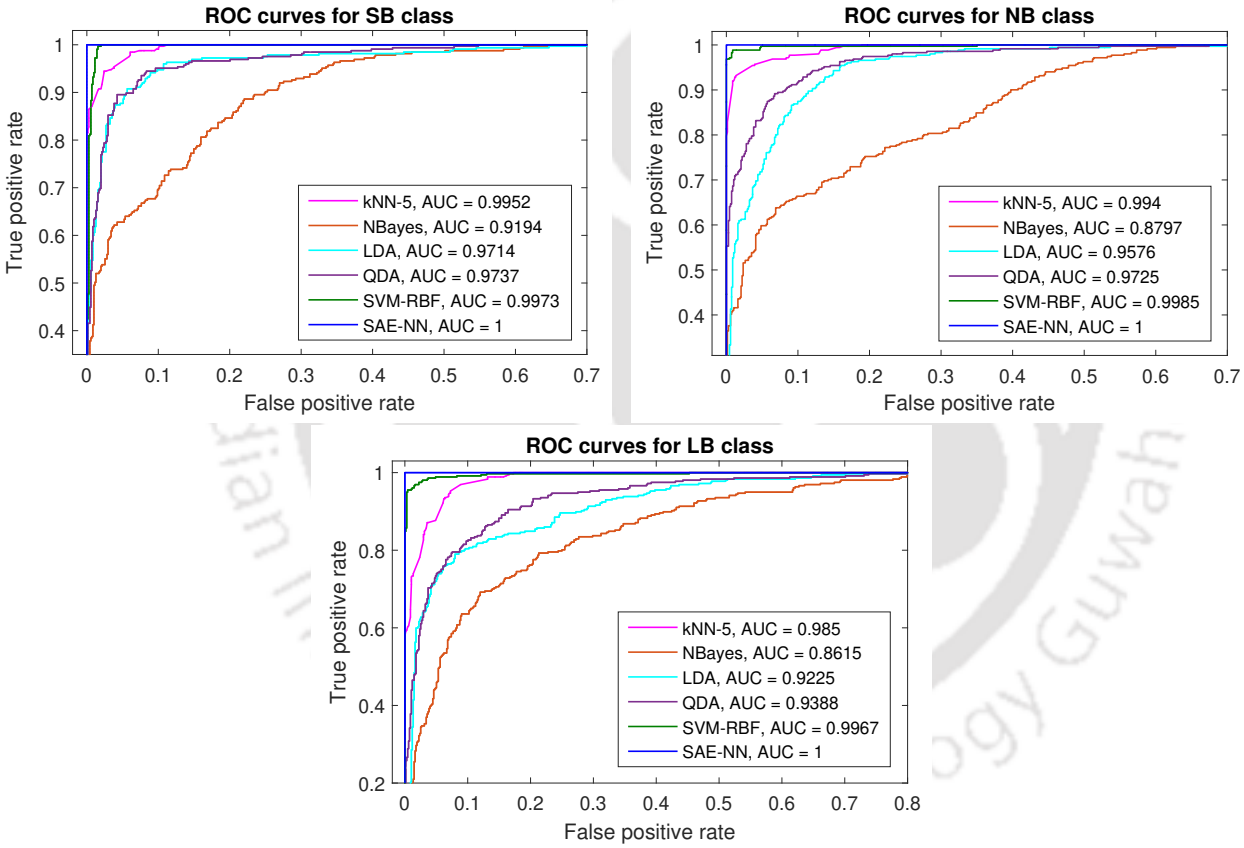

Figure 5.9: ROC curves of different classifiers. Note that AUC represents area under the ROC curve and false positive rate is computed as: FPR = 1 − TNR.

ensemble classifiers, linear discriminant analysis (LDA), and quadratic discriminant analysis (QDA) based classifiers. We deployed a statistical based feature analysis technique called multi-variate feature analysis (MANOVA) [148] technique to select dominant features for comparison of different classifiers. The features only having less than *5% level of significance* are considered for this study. All the fifteen features are accepted as all of them show more than *5% level of significance*. The performance

comparison of our method with different classifiers is shown in Table 5.3. The results clearly show that the proposed method outperforms other conventional methods. Also, ROC curves for all these classifiers are shown in Figure 5.9.

5.3 Summary

In this chapter, an SCG based breathing-state detector is presented for healthcare applications. The proposed method can accurately identify the degree-of-breathing, such as breathlessness, normal breathing, and long and labored breathing conditions. The concurrent ECG signal is also used to extract the SCG cycles using an OSP-based scheme, and each of the cycles is used for feature extraction. A set of features is extracted from the SCG signal, which conveys the information of hemodynamic changes and physiological movement of lung and heart muscles due to varying breathing-rates. For the classification of different breathing patterns, an SAE-based NN architecture is proposed. The performance of our method is evaluated on 1147 SCG cycles in different breathing scenarios. The quantitative-assessment results clearly show that the proposed method may be deployed for many day-to-day life and clinical applications. One major finding of this research work is that the SCG signal can be used not only for cardiac health measurement but also for the assessment of respiration-rates and lung fitness.

6

Conclusions

Contents

According to the American Heart Association, there will be a sudden increase in the prevalence of heart failure by 2030, and the overall costs of patient healthcare will also be increased. As a result of this, there will be insufficiency in medical experts per patient. Thus, there is a compelling requirement to transfer care from hospitals to home environments to provide more convenience and accessibility to the patient and reduce the overall costs of care. For this purpose, a smart system that allows noninvasive and nonintrusive wearable sensing of cardiac signals, their processing through intelligent methods and algorithms, and drawing a clinical decision is beneficial to implement remote monitoring in home-healthcare. It would allow us to assess cardiac-health regularly and reduce the chances of disease-progression if any.

In this thesis, the delineation frameworks for the SCG signals and their analysis in two different applications are investigated. The developed methods and algorithms improve the robustness of SCG delineation and analysis, and therefore significantly improve home monitoring of cardiac health for healthy controls and cardiac patients. In Chapter 1, a basic idea of the SCG signal, its acquisition, genesis, challenges of analyzing its morphology, and open issues are provided. Along with these, it also includes a brief introduction about SCG delineation and a literature survey of previously reported methods on this. Chapter 2 presents our developed SCG acquisition system and two different approaches for standalone SCG delineation. The approaches do not require any other cardiac signal for the estimation of AO peaks. These delineation frameworks are mainly developed to estimate the prominent AO fiducial point from an SCG cycle. In Chapter 3, two other delineation frameworks are presented, in which the reference ECG and PPG cardiac signals are taken into account, respectively. These methods are able to characterize the SCG systoles and diastoles by estimating many fiducial points of an SCG cycle. Chapter 4 provides an application of the SCG signal to extract the fundamental heart sounds and to characterize them. Another application is shown in the cardiorespiratory analysis by analyzing the SCG profiles in Chapter 5. Thus, it provides the classification of SCG signals in different respiratory-effort levels. The chapter presents a hybrid feature-based approach for the identification of three breathing states. The presented quantitative analysis of the proposed delineation methods enables their applicability in various directions such as heart cycle extraction and heart rate variability analysis. The proposed work can also be extended for hemodynamic parameter extraction and diagnosis of various cardiac disorders. The current chapter is organized as follows: the major contributions of this thesis are presented in Section 6.1. Possible future works are provided in Section

6.2.

6.1 Summary of Contributions

The major contributions of our work reported in this thesis are as follows:

- The fingertip-PPG signal is first-ever investigated for the SCG delineation. It is found most suitable for the diastole delineation. The presented PPG assisted method is able to estimate up to six crucial SCG fiducial points, through which the characterization of both systolic and diastolic profiles of the SCG is made possible.
- An algorithm is devised to estimate the optimal bandwidth-constraint parameter of the VMD model for a given number of modes. The algorithm would be applicable to any application-specific VMD decomposition process.
- Information related to fundamental heart sounds is extracted from an accelerometric SCG signal.
- The effect of respiratory-effort levels onto the SCG morphology is analyzed using the proposed fiducial and non-fiducial based discriminative features.

6.2 Scope for the Future Work

The delineation can be employed in numerous applications such as continuous cardiac-health monitoring and diagnosis of cardiovascular diseases. The dissertation points towards some interesting future directions. Despite various investigations in the field, still, some limitations and open issues are there, which need to be addressed in future works.

The beat-patterns of the SCG signals vary with many factors such as sensor location, body movements, gender, age, and heart displacements. In addition, they are often corrupted from various noise sources. However, out of them, removal of motion artifacts is a challenge. This problem needs to be addressed in future work. A universally accepted standardization is still awaiting for the fiducial points of the SCG signal. Moreover, another question regarding SCG genesis is an open issue despite having several studies. It requires more attention from researchers in this field. Additionally, mathematical and system modelings are required to simulate more realistic SCG signals. The simulated signals would be useful for understanding the signal characteristics and pre-clinical studies. A database consisting of artificial SCG signals for different cardiac-disorders can be created. Proper modelling can encourage

the researchers in this field. The delineated fiducial points can be employed for the analysis of SCG signals collected from cardiac patients of various disorders. More research-efforts are required in the direction of cardiovascular disease diagnosis. In addition, an analysis of multichannel SCG recordings corresponding to different chest locations in all three x, y, and z directions needs to be done to investigate the spatial variability of the signal. This would also help to localize the cardiac-disorders on different sections of heart. Analysis of SCG signals under rigorous physical exercises would be helpful to understand the cardio-mechanical activities in such conditions. Moreover, an exercise augments the symptoms of coronary artery disease, which can help reducing false negative rates in diagnosing such diseases. The creation of a common large archive and dataset is much needed for the researchers those are interested to analyze the cardiovascular signals. The database should include the variety of clean and noisy raw-signals from healthy controls and cardiac patients. Also, the combined information of other cardiac signals with that of SCG signal may lead to a multi- or hybrid-modalily with increased clinical diagnosis ability for cardiac diseases. It also provides an understanding of cardiac activity in different aspects. This may produce more complex and useful features which will need a increased use of machine learning methods.

The methods and algorithms devised and presented by this thesis facilitate the delineation, characterization, and analysis of systole and diastole profiles of an SCG signal using various standalone and other cardiac-signal assisted approaches with better robustness and improved performance. The delineated parameters claim to provide in-depth information of the mechanical-heart and thoracic movement. They could be employed in many clinical and non-clinical applications, such as estimation of cardiac health parameters (like systolic time intervals, hemodynamic parameters, HR, and HRV indices), respiratory analysis and lung fitness, diagnosis of various cardiac disorders, human posture and other activity detection, and so on. Additionally, this dissertation would be helpful in understanding the underlying physiology and functions of the heart. It also provides the analysis of SCG signals for two different applications. However, a large scale study is needed for more clinical reliability of these applications, breathing-states detection in Chapter 5 and fundamental heart sounds derivation in Chapter 4, on healthy controls and cardiac patients.

A

Developed Graphical User Interfaces

Contents

Graphical user interfaces (GUIs) are quite helpful in showing the output-behavior and applicability of their algorithms. They allow a visual approach of interacting with graphical elements, which make the systems convenient at the end-user level. In this appendix section, we present our developed GUIs based on mobile- and computer-interaction.

A.1 Mobile Application for Continuous Monitoring of SCG Signals

For a continuous screening of cardiac mechanics, an android-based mobile application (m-app) is developed. It facilitates the continuous monitoring of SCG signals, which displays the live recording in a running mode from right to left in the visualizer panel. This m-app wireless interfaces with our designed SCG acquisition electronic-board circuitry (Chapter 2.1), and fetches the SCG data via Bluetooth technology. The interfacing is shown in Figure A.1. Besides the data visualization feature, it has the facility of storage of a long-data, which is sampled at 250 Hz and has a resolution of 10 bits.

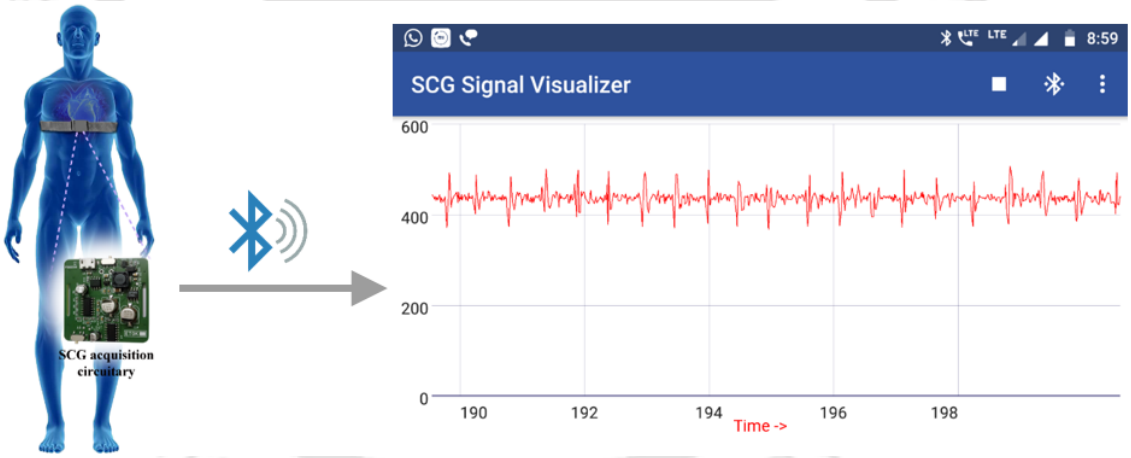

Figure A.1: Developed mobile-based SCG monitoring application interacting with data-acquisition circuitry.

A.2 MATLAB-based GUIs for AO Instant Detection

Microsoft Windows OS-based, a GUI interfacing system is developed using MATLAB (MathWorks, Inc.) environment for the detection of AO peaks in the SCG signal. The system uses the algorithm of multiresolution and statistical approaches-based SCG delineation (Chapter 2.2). The system can test the SCG signals at various sampling frequencies, signal lengths, and SNR levels. After the AO peak detection, the system computes and displays the AO-AO interval time series. This time series is further employed for heart rate variability analysis. Under this analysis, essential HRV parameters are

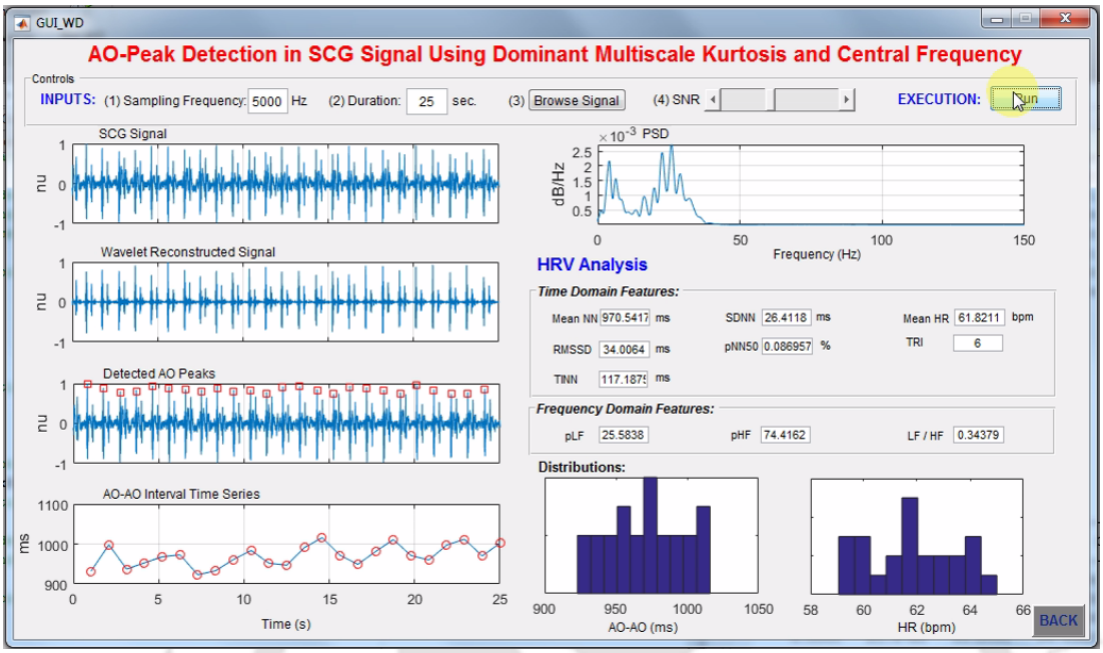

Figure A.2: GUI for HRV parameters estimation using a multiresolution-based SCG delineation method.

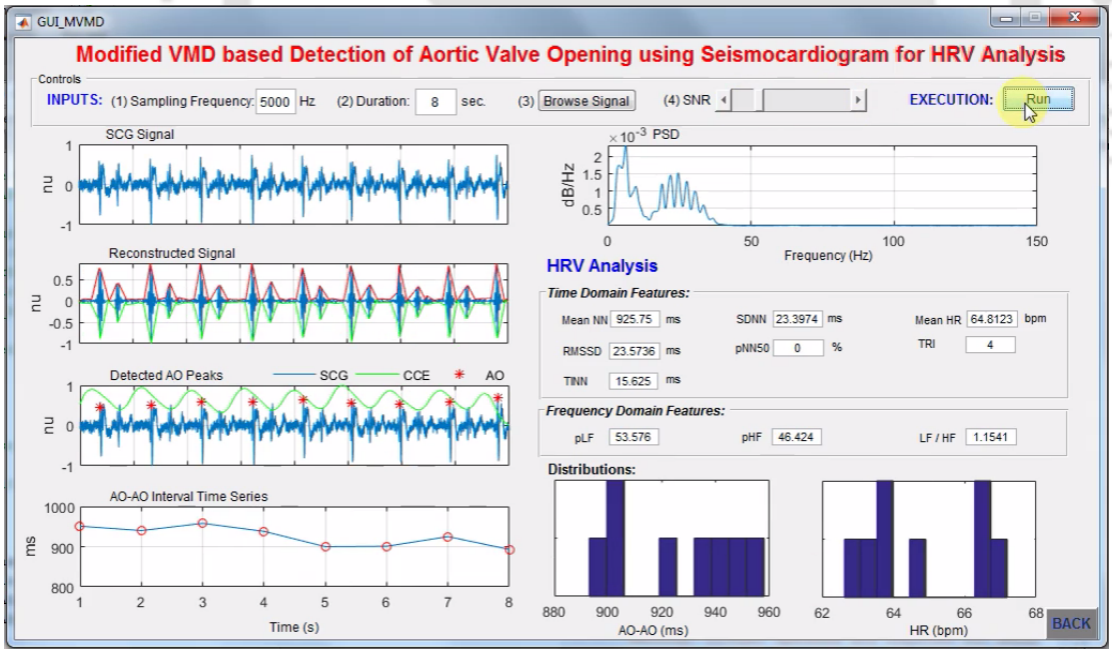

Figure A.3: GUI interface for HRV parameters estimation using a MVMD-based SCG delineation method.

computed and shown by using the algorithm proposed in [149]. The system estimates following HRV parameters: (i) time-domain features, such as meanNN, SDNN, meanHR, RMSSD, pNN50, TRI, and TINN, (ii) frequency-domain features, such as pLF, pHF, and LF/HF, and (iii) distribution graphs of AO-AO intervals, and heart rates. A snapshot of designed GUI is shown in Figure A.2.

A similar GUI system is developed for the HRV parameter estimation using detected AO peak locations in the SCG signal. The developed GUI uses the algorithm of our MVMD based model (Chapter 2.3) for AO instant detection. The interface of designed GUI is illustrated in Figure A.3. Both the above-mentioned GUIs are developed on the MATLAB R2015b platform. Launching of these Windows-executable applications needs a MATLAB runtime environment.

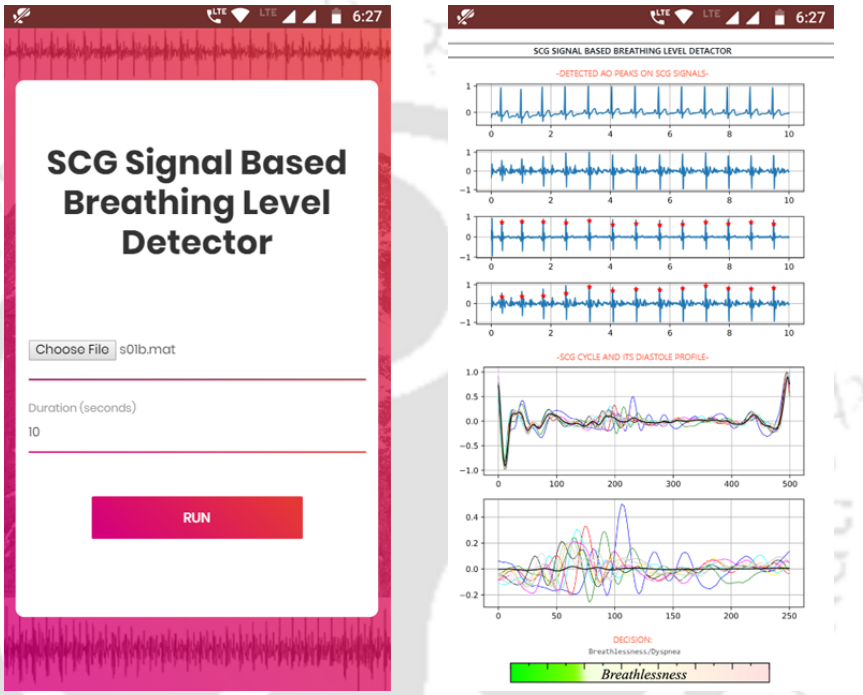

Figure A.4: Snapshots of our developed mobile application for breathing states detection.

A.3 Mobile Application for Identification of Breathing Patterns

An android-based mobile application is designed for the identification of three breathing patterns, SB, NB, and LB, using the SCG and ECG signals. The m-app uses the algorithm of hybrid morphological features-based breathing state detection, mentioned in Chapter 5. The interfaces of the developed mobile application are shown in Figure A.4. In this example, it is shown that an SCG signal of duration 10 s is recorded under breathless condition, and subsequently, it is successfully identified by the proposed framework.

List of Publications

Journal Publications

1. Tilendra Choudhary, M.K. Bhuyan, and L.N. Sharma, "Delineation and Analysis of Seismocardiographic Systole and Diastole Profiles," **IEEE Transactions on Instrumentation and Measurement**, 2020. doi: 10.1109/TIM.2020.3007295

2. Tilendra Choudhary, L.N. Sharma, M.K. Bhuyan, and K. Bora, "Identification of Human Breathing-States Using Cardiac-Vibrational Signal for m-Health Applications," **IEEE Sensors Journal**, 2020. doi: 10.1109/JSEN.2020.3025384

3. Tilendra Choudhary, L.N. Sharma, and M.K. Bhuyan, "Automatic Detection of Aortic Valve Opening using Seismocardiography in Healthy Individuals," **IEEE Journal of Biomedical and Health Informatics**, vol. 23, no. 3, pp. 1032–1040, 2019.

4. Tilendra Choudhary, M.K. Bhuyan, and L.N. Sharma, "A Novel Method for Aortic Valve Opening Phase Detection Using SCG Signal," **IEEE Sensors Journal**, vol. 20, no. 2, pp. 899–908, 2020. doi: 10.1109/JSEN.2019.2944235

5. Tilendra Choudhary, L.N. Sharma, and M.K. Bhuyan, "Heart Sound Extraction from Sternal Seismocardiographic Signal," **IEEE Signal Processing Letters**, vol. 25, no. 4, pp. 482–486, 2018.

6. Tilendra Choudhary, M.K. Bhuyan, and L.N. Sharma, "Orthogonal Subspace Projection based Framework to Extract Heart Cycles from SCG Signal," **Biomedical Signal Processing and Control, Elsevier**, vol. 50, pp. 45–51, 2019.

Journals Under Review

1. Tilendra Choudhary, M. Das, L.N. Sharma, and M.K. Bhuyan, "Analyzing SCG Methodology for Heart Rate Variability Measurement: A Feasibility Study," **IEEE Sensors Letters**, 2020.

2. M. Das, Tilendra Choudhary, L.N. Sharma, and M.K. Bhuyan, "Accelerometric Method for Cuffless Continuous Blood Pressure Measurement," **IEEE Sensors Journal**, 2020.

Conference Publications

1. Tilendra Choudhary, L.N. Sharma, and M.K. Bhuyan, "Suppression of Artifacts from Seismocardiogram Signal using Two-Stage Kalman Filtering Model," in **Proc. IEEE Intr. Conf. SPCOM, Bangalore**, 2018, pp. 417–421.

2. Tilendra Choudhary, L.N. Sharma, and M.K. Bhuyan, "Standalone Heartbeat Extraction in SCG signal using Variational Mode Decomposition," in **Proc. IEEE Intr. Conf. Wireless Communications, Signal Processing and Networking (WiSPNET), Chennai**, 2018, pp. 1–4.

3. Tilendra Choudhary, L.N. Sharma, and M.K. Bhuyan, "SPECTRACENTROGRAM: A Time-Frequency Distribution for Signal Processing Applications," in **Proc. IEEE Intr. Conf. Intelligent Informatics and BioMedical Sciences (ICIIBMS), Thailand**, 2018, pp. 1–5.

4. Tilendra Choudhary, M.K. Bhuyan, and L.N. Sharma, "Effect of Respiratory Effort Levels on SCG Signals," in **Proc. IEEE Region 10 Symposium (TENSYMP)**, 2019, pp. 143–146.

Patents Filed

1. Tilendra Choudhary, L.N. Sharma, and M.K. Bhuyan, "Method and Technology for Accelerometric Signal Recording of a Novel Vibrocarotidogram (ViCG) with Seismocardiogram (SCG)," Indian Patent, 2020. Ref. No.: 202031026802

2. Tilendra Choudhary, L.N. Sharma, and M.K. Bhuyan, "Device and Method for Seismocardiography Recording and Monitoring in Mobile Device for Healthcare Applications," Indian Patent, 2020. Ref. No.: 202031027314

Bibliography

[1] C. M. Otto, "Timing of aortic valve surgery," *Heart*, vol. 84, no. 2, pp. 211–218, 2000.

[2] Y. Hu, E. G. Kim, G. Cao, S. Liu, and Y. Xu, "Physiological acoustic sensing based on accelerometers: A survey for mobile healthcare," *Annals of Biomedical Engineering*, vol. 42, no. 11, pp. 2264–2277, 2014.

[3] T. Choudhary, L. N. Sharma, and M. K. Bhuyan, "Automatic detection of aortic valve opening using seismocardiography in healthy individuals," *IEEE Journal of Biomedical and Health Informatics*, vol. 23, no. 3, pp. 1032–1040, May 2019.

[4] A. Taebi, B. E. Solar, A. J. Bomar, R. H. Sandler, and H. A. Mansy, "Recent advances in seismocardiography," *Vibration*, vol. 2, no. 1, pp. 64–86, 2019.

[5] O. T. Inan, P. F. Migeotte, K. S. Park, M. Etemadi, K. Tavakolian, R. Casanella, J. Zanetti, J. Tank, I. Funtova, G. K. Prisk, and M. D. Rienzo, "Ballistocardiography and seismocardiography: A review of recent advances," *IEEE Journal of Biomedical and Health Informatics*, vol. 19, no. 4, pp. 1414–1427, July 2015.

[6] M. D. Rienzo, E. Vaini, P. Castiglioni, G. Merati, P. Meriggi, G. Parati, A. Faini, and F. Rizzo, "Wearable seismocardiography: Towards a beat-by-beat assessment of cardiac mechanics in ambulant subjects," *Autonomic Neuroscience*, vol. 178, no. 1–2, pp. 50 – 59, 2013.

[7] D. M. Salerno, J. M. Zanetti, L. A. Green, M. R. Mooney, J. D. Madison, and R. A. V. Tassel, "Seismocardiographic changes associated with obstruction of coronary blood flow during balloon angioplasty," *The American Journal of Cardiology*, vol. 68, no. 2, pp. 201 – 207, 1991.

[8] R. S. Crow, P. Hannan, D. Jacobs, L. He dquist, and D. M. Salerno, "Relationship between seismocardiogram and echocardiogram for events in the cardiac cycle," *American Journal of Noninvasive Cardiology*, vol. 8, no. 1, pp. 39–46, 1994.

[9] K. Pandia, S. Ravindran, R. Cole, G. Kovacs, and L. Giovangrandi, "Motion artifact cancellation to obtain heart sounds from a single chest-worn accelerometer," in *IEEE International Conference on Acoustics, Speech and Signal Processing*, March 2010, pp. 590–593.

[10] F. Khosrow-khavar, K. Tavakolian, A. P. Blaber, J. M. Zanetti, R. Fazel-Rezai, and C. Menon, "Automatic annotation of seismocardiogram with high-frequency precordial accelerations," *IEEE Journal of Biomedical and Health Informatics*, vol. 19, no. 4, pp. 1428–1434, July 2015.

[11] J. M. Zanetti and K. Tavakolian, "Seismocardiography: Past, present and future," in *2013 35th Annual International Conference of the IEEE Engineering in Medicine and Biology Society (EMBC)*, July 2013, pp. 7004–7007.

[12] M. Di Rienzo, E. Vaini, and P. Lombardi, "An algorithm for the beat-to-beat assessment of cardiac mechanics during sleep on earth and in microgravity from the seismocardiogram," *Scientific Reports Nature*, vol. 7, no. 1, p. 15634, 2017.

[13] M. O. Poliac, J. M. Zanetty, D. Salerno, and G. L. Wilcox, "Seismocardiogram (scg) interpretation using neural networks," in *Computer-Based Medical Systems, 1991. Proceedings of the Fourth Annual IEEE Symposium*, May 1991, pp. 288–295.

[14] M. J. Tadi, E. Lehtonen, T. Hurnanen, J. Koskinen, J. Eriksson, M. Pänkäälä, M. Teräs, and T. Koivisto, "A real-time approach for heart rate monitoring using a hilbert transform in seismocardiograms," *Physiological measurement*, vol. 37, no. 11, p. 1885, 2016.

[15] Y. Chuo, K. Tavakolian, and B. Kaminska, "Evaluation of a novel integrated sensor system for synchronous measurement of cardiac vibrations and cardiac potentials," *Journal of medical systems*, vol. 35, no. 4, pp. 445–455, 2011.

[16] P. Castiglioni, A. Faini, G. Parati, and M. D. Rienzo, "Wearable seismocardiography," in *2007 29th Annual International Conference of the IEEE Engineering in Medicine and Biology Society*, Aug 2007, pp. 3954–3957.

[17] A. Q. Javaid, H. Ashouri, A. Dorier, M. Etemadi, J. A. Heller, S. Roy, and O. T. Inan, "Quantifying and reducing motion artifacts in wearable seismocardiogram measurements during walking to assess left ventricular health," *IEEE Transactions on Biomedical Engineering*, vol. 64, no. 6, pp. 1277–1286, June 2017.

[18] M. D. Rienzo, E. Vaini, P. Castiglioni, P. Meriggi, and F. Rizzo, "Beat-to-beat estimation of lvet and qs2 indices of cardiac mechanics from wearable seismocardiography in ambulant subjects," in *2013 35th Annual International Conference of the IEEE Engineering in Medicine and Biology Society (EMBC)*, July 2013, pp. 7017–7020.

[19] W. Lin, W. Chou, P. Chang, C. Chou, M. Wen, M. Ho, W. Lee, M. Hsieh, C. Lin, T. Tsai, and M. Lee, "Identification of location specific feature points in a cardiac cycle using a novel seismocardiogram spectrum system," *IEEE Journal of Biomedical and Health Informatics*, vol. 22, no. 2, pp. 442–449, March 2018.

[20] A. Taebi, "Characterization, classification, and genesis of seismocardiographic signals," Ph.D. dissertation, University of Central Florida, 2018.

[21] K. Sørensen, S. E. Schmidt, A. S. Jensen, P. Søgaard, and J. J. Struijk, "Definition of fiducial points in the normal seismocardiogram," *Scientific reports*, vol. 8, no. 1, p. 15455, 2018.

[22] D. M. Salerno and J. Zanetti, "Seismocardiography for monitoring changes in left ventricular function during ischemia," *Chest*, vol. 100, no. 4, pp. 991 – 993, 1991.

[23] A. W. Scherhag, S. Pfleger, C. Ceconi, W. Voelker, J. Gehring, U. Staedt, and D. L. Heene, "Evaluation of signal-averaged cardiokymography for the detection of ischemic left ventricular dysfunction," *International Journal of Cardiology*, vol. 59, no. 3, pp. 305 – 312, 1997.

[24] M. J. Tadi, E. Lehtonen, T. Koivisto, M. Pänkäälä, A. Paasio, and M. Teräs, "Seismocardiography: Toward heart rate variability (hrv) estimation," in *Medical Measurements and Applications (MeMeA), 2015 IEEE International Symposium on*, May 2015, pp. 261–266.

[25] A. Laurin, A. Blaber, and K. Tavakolian, "Seismocardiograms return valid heart rate variability indices," in *Computing in Cardiology 2013*, Sept 2013, pp. 413–416.

[26] M. S. Imtiaz, R. Shrestha, T. Dhillon, K. A. Yousuf, B. Saeed, A. Dinh, and K. Wahid, "Cardiac cycle and heart rate calculation based on seismocardiogram," in *Electrical and Computer Engineering (CCECE), 2013 26th Annual IEEE Canadian Conference on*, May 2013, pp. 1–5.

[27] M. A. García-González, A. Argelagós-Palau, M. Fernández-Chimeno, and J. Ramos-Castro, "A comparison of heartbeat detectors for the seismocardiogram," in *Computing in Cardiology 2013*, Sept 2013, pp. 461–464.

[28] H. Nguyen, J. Zhang, and Y. H. Nam, "Timing detection and seismocardiography waveform extraction," in *2012 Annual International Conference of the IEEE Engineering in Medicine and Biology Society*, Aug 2012, pp. 3553–3556.

[29] F. Khosrow-khavar, K. Tavakolian, and C. Menon, "Moving toward automatic and standalone delineation of seismocardiogram signal," in *2015 37th Annual International Conference of the IEEE Engineering in Medicine and Biology Society (EMBC)*, Aug 2015, pp. 7163–7166.

[30] W. Sandham, D. Hamilton, A. Fisher, W. Xu, and M. Conway, "Multiresolution wavelet decomposition of the seismocardiogram," *IEEE Transactions on Signal Processing*, vol. 46, no. 9, pp. 2541–2543, Sep 1998.

[31] A. Laurin, F. Khosrow, A. Blaber, and K. Tavakolian, "Accurate and consistent automatic seismocardiogram annotation without concurrent ecg," in *2015 Computing in Cardiology Conference (CinC)*, Sept 2015, pp. 25–28.

[32] Y. Li, X. Tang, and Z. Xu, "An approach of heartbeat segmentation in seismocardiogram by matched-filtering," in *Intelligent Human-Machine Systems and Cybernetics (IHMSC), 2015 7th International Conference on*, vol. 2, Aug 2015, pp. 47–51.

[33] A. K. Verma, R. Fazel-Rezai, A. Blaber, and K. Tavakolian, "Pulse transit time extraction from seismocardiogram and its relationship with pulse pressure," in *2015 Computing in Cardiology Conference (CinC)*, Sept 2015, pp. 37–40.

[34] P. Castiglioni, P. Meriggi, F. Rizzo, E. Vaini, A. Faini, G. Parati, G. Merati, and M. D. Rienzo, "Cardiac sounds from a wearable device for sternal seismocardiography," in *2011 Annual International Conference of the IEEE Engineering in Medicine and Biology Society*, Aug 2011, pp. 4283–4286.

[35] C. A. Wick, J. J. Su, J. H. McClellan, O. Brand, P. T. Bhatti, A. L. Buice, A. E. Stillman, X. Tang, and S. Tridandapani, "A system for seismocardiography-based identification of quiescent heart phases: Implications for cardiac imaging," *IEEE Transactions on Information Technology in Biomedicine*, vol. 16, no. 5, pp. 869–877, Sept 2012.

[36] M. Jerosch-Herold, J. Zanetti, H. Merkle, L. Poliac, H. Huang, A. Mansoor, F. Zhao, and N. Wilke, "The seismocardiogram as magnetic-field-compatible alternative to the electrocardiogram for cardiac stress monitoring," *The International Journal of Cardiac Imaging*, vol. 15, no. 6, pp. 523–531, 1999.

[37] T. Koivisto, M. Pänkäälä, T. Hurnanen, T. Vasankari, T. Kiviniemi, A. Saraste, and J. Airaksinen, "Automatic detection of atrial fibrillation using mems accelerometer," in *2015 Computing in Cardiology Conference (CinC)*, Sept 2015, pp. 829–832.

[38] R. A. Wilson, V. S. Bamrah, J. Lindsay, M. Schwaiger, and J. Morganroth, "Diagnostic accuracy of seismocardiography compared with electrocardiography for the anatomic and physiologic diagnosis of coronary artery disease during exercise testing," *The American Journal of Cardiology*, vol. 71, no. 7, pp. 536 – 545, 1993.

[39] K. Tavakolian, G. A. Dumont, and A. P. Blaber, "Analysis of seismocardiogram capability for prediction of mild to moderate haemorrhage; preliminary results," in *Computing in Cardiology 2013 (CinC)*, Sept 2013, pp. 1107–1110.

[40] M. Paukkunen, P. Parkkila, T. Hurnanen, M. Pänkäälä, T. Koivisto, T. Nieminen, R. Kettunen, and R. Sepponen, "Beat-by-beat quantification of cardiac cycle events detected from three-dimensional precordial acceleration signals," *IEEE Journal of Biomedical and Health Informatics*, vol. 20, no. 2, pp. 435–439, March 2016.

[41] V. Zakeri and K. Tavakolian, "Identification of respiratory phases using seismocardiogram: A machine learning approach," in *2015 Computing in Cardiology Conference (CinC)*, Sept 2015, pp. 305–308.

[42] K. Pandia, O. T. Inan, and G. T. A. Kovacs, "A frequency domain analysis of respiratory variations in the seismocardiogram signal," in *2013 35th Annual International Conference of the IEEE Engineering in Medicine and Biology Society (EMBC)*, July 2013, pp. 6881–6884.

[43] K. Tavakolian, A. P. Blaber, B. Ngai, and B. Kaminska, "Estimation of hemodynamic parameters from seismocardiogram," in *2010 Computing in Cardiology*, Sept 2010, pp. 1055–1058.

[44] M. S. Imtiaz, R. Shrestha, T. Dhillon, K. A. Yousuf, B. Saeed, A. Dinh, and K. Wahid, "Correlation between seismocardiogram and systolic blood pressure," in *Electrical and Computer Engineering (CCECE), 2013 26th Annual IEEE Canadian Conference on*, May 2013, pp. 1–4.

[45] M. D. Rienzo, E. Vaini, P. Castiglioni, P. Lombardi, G. Parati, C. Lombardi, P. Meriggi, and F. Rizzo, "Wearable seismocardiography for the beat-to-beat assessment of cardiac intervals during sleep," in *2014 36th Annual International Conference of the IEEE Engineering in Medicine and Biology Society*, Aug 2014, pp. 6089–6091.

[46] M. D. Rienzo, E. Vaini, B. Bruno, P. Castiglioni, P. Lombardi, G. Parati, C. Lombardi, P. Meriggi, and F. Rizzo, "Wearable seismocardiography: Towards the beat-to-beat assessment of cardiac mechanics during sleep in microgravity," in *Cardiovascular Oscillations (ESGCO), 2014 8th Conference of the European Study Group on*, May 2014, pp. 239–240.

[47] M. D. Rienzo, P. Meriggi, F. Rizzo, E. Vaini, A. Faini, G. Merati, G. Parati, and P. Castiglioni, "A wearable system for the seismocardiogram assessment in daily life conditions," in *2011 Annual International Conference of the IEEE Engineering in Medicine and Biology Society*, Aug 2011, pp. 4263–4266.

[48] M. D. Rienzo, E. Vaini, P. Castiglioni, P. Lombardi, P. Meriggi, and F. Rizzo, "A textile-based wearable system for the prolonged assessment of cardiac mechanics in daily life," in *2014 36th Annual International Conference of the IEEE Engineering in Medicine and Biology Society*, Aug 2014, pp. 6896–6898.

[49] M. D. Rienzo, P. Meriggi, E. Vaini, P. Castiglioni, and F. Rizzo, "24h seismocardiogram monitoring in ambulant subjects," in *2012 Annual International Conference of the IEEE Engineering in Medicine and Biology Society*, Aug 2012, pp. 5050–5053.

[50] M. Etemadi, O. T. Inan, J. A. Heller, S. Hersek, L. Klein, and S. Roy, "A wearable patch to enable long-term monitoring of environmental, activity and hemodynamics variables," *IEEE Transactions on Biomedical Circuits and Systems*, vol. 10, no. 2, pp. 280–288, April 2016.

[51] B. Bozhenko, "Seismocardiography-a new method in the study of functional conditions of the heart," *Terapevticheskii arkhiv*, vol. 33, pp. 55–64, 1961.

[52] R. M. Baevskii, A. D. Egorov, and L. A. Kazarian, "The method of seismocardiography," *Kardiologiia*, vol. 18, pp. 87–89, 1964.

[53] P. F. Migeotte, S. D. Ridder, J. Tank, N. Pattyn, I. Funtova, R. Baevsky, X. Neyt, and G. K. Prisk, "Three dimensional ballisto- and seismo-cardiography: Hij wave amplitudes are poorly correlated to maximal systolic force vector," in *2012 Annual International Conference of the IEEE Engineering in Medicine and Biology Society*, Aug 2012, pp. 5046–5049.

[54] D. Salerno and J. Zanetti, "Seismocardiography: A new technique for recording cardiac vibrations. concept, method, and initial observations," *Journal of cardiovascular technology*, vol. 9, no. 2, pp. 111–118, 1990.

[55] M. Di Rienzo, F. Rizzo, G. Parati, G. Brambilla, M. Ferratini, and P. Castiglioni, "Magic system: a new textile-based wearable device for biological signal monitoring. applicability in daily life and clinical setting," in *2005 IEEE Engineering in Medicine and Biology 27th Annual Conference*, Jan 2005, pp. 7167–7169.

[56] A. M. Carek, J. Conant, A. Joshi, H. Kang, and O. T. Inan, "Seismowatch: Wearable cuffless blood pressure monitoring using pulse transit time," *Proc. ACM Interact. Mob. Wearable Ubiquitous Technol.*, vol. 1, no. 3, pp. 40:1–40:16, Sep. 2017.

[57] T. Ha, J. Tran, S. Liu, H. Jang, H. Jeong, R. Mitbander, H. Huh, Y. Qiu, J. Duong, R. L. Wang *et al.*, "A chest-laminated ultrathin and stretchable e-tattoo for the measurement of electrocardiogram, seismocardiogram, and cardiac time intervals," *Advanced Science*, vol. 6, no. 14, p. 1900290, 2019.

[58] M. Di Rienzo, G. Rizzo, Z. M. IÅŸilay, and P. Lombardi, "Seismote: A multi-sensor wireless platform for cardiovascular monitoring in laboratory, daily life, and telemedicine," *Sensors*, vol. 20, no. 3, 2020.

[59] F. Khosrow-Khavar, "Automatic and non-invasive delineation of the seismocardiogram signal for the estimation of cardiac time intervals with applications in diastolic timed vibration and early stage hemorrhage detection," Ph.D. dissertation, Applied Sciences: School of Engineering Science, 2016.

[60] F. Khosrow-Khavar, K. Tavakolian, A. Blaber, and C. Menon, "Automatic and robust delineation of the fiducial points of the seismocardiogram signal for noninvasive estimation of cardiac time intervals," *IEEE Transactions on Biomedical Engineering*, vol. 64, no. 8, pp. 1701–1710, Aug 2017.

[61] G. Shafiq, S. Tatinati, and K. C. Veluvolu, "Automatic annotation of peaks in seismocardiogram for systolic time intervals," in *2016 38th Annual International Conference of the IEEE Engineering in Medicine and Biology Society (EMBC)*, Aug 2016, pp. 2672–2675.

[62] G. Shafiq, S. Tatinati, W. T. Ang, and K. C. Veluvolu, "Automatic identification of systolic time intervals in seismocardiogram," *Scientific reports, Nature*, vol. 6, p. 37524, 2016.

[63] P. K. Sahoo, H. K. Thakkar, W.-Y. Lin, P.-C. Chang, and M.-Y. Lee, "On the design of an efficient cardiac health monitoring system through combined analysis of ecg and scg signals," *Sensors*, vol. 18, no. 2, p. 379, 2018.

[64] J. Yao, S. Tridandapani, C. A. Wick, and P. T. Bhatti, "Seismocardiography-based cardiac computed tomography gating using patient-specific template identification and detection," *IEEE Journal of Translational Engineering in Health and Medicine*, vol. 5, pp. 1–14, 2017.

[65] M. Pänkäälä, T. Koivisto, O. Lahdenoja, T. Kiviniemi, A. Saraste, T. Vasankari, and J. Airaksinen, "Detection of atrial fibrillation with seismocardiography," in *2016 38th Annual International Conference of the IEEE Engineering in Medicine and Biology Society (EMBC)*, Aug 2016, pp. 4369–4374.

[66] N. K. Canino, R. R. Wang, and C. J. Robinson, "Using multiple placements of accelerometers to measure cardiovascular pulse transit times," in *2016 38th Annual International Conference of the IEEE Engineering in Medicine and Biology Society (EMBC)*, Aug 2016, pp. 4248–4251.

[67] N. T. Alamdari, "A morphological approach to identify respiratory phases of seismocardiogram," Ph.D. dissertation, The University of North Dakota, 2016.

[68] V. Zakeri, A. Akhbardeh, N. Alamdari, R. Fazel-Rezai, M. Paukkunen, and K. Tavakolian, "Analyzing seismocardiogram cycles to identify the respiratory phases," *IEEE Transactions on Biomedical Engineering*, vol. 64, no. 8, pp. 1786–1792, Aug 2017.

[69] G. Zhang, A. C. Cottrell, I. C. Henry, and D. B. McCombie, "Assessment of pre-ejection period in ambulatory subjects using seismocardiogram in a wearable blood pressure monitor," in *2016 38th Annual International Conference of the IEEE Engineering in Medicine and Biology Society (EMBC)*, Aug 2016, pp. 3386–3389.

[70] P. K. Jain and A. K. Tiwari, "An algorithm for automatic segmentation of heart sound signal acquired using seismocardiography," in *2016 International Conference on Systems in Medicine and Biology (ICSMB)*, Jan 2016, pp. 157–161.

[71] A. Taebi, B. E. Solar, and H. A. Mansy, "An adaptive feature extraction algorithm for classification of seismocardiographic signals," in *IEEE Conference SoutheastCon 2018*, April 2018, pp. 1–5.

[72] A. Taebi and H. A. Mansy, "Grouping similar seismocardiographic signals using respiratory information," in *2017 IEEE Signal Processing in Medicine and Biology Symposium (SPMB)*, Dec 2017, pp. 1–6.

[73] A. Taebi and H. A. Mansy, "Time-frequency distribution of seismocardiographic signals: A comparative study," *Bioengineering*, vol. 4, no. 2, p. 32, 2017.

[74] H. Ashouri and O. T. Inan, "Automatic detection of seismocardiogram sensor misplacement for robust pre-ejection period estimation in unsupervised settings," *IEEE Sensors Journal*, vol. 17, no. 12, pp. 3805–3813, June 2017.

[75] O. T. Inan, M. Baran Pouyan, A. Q. Javaid, S. Dowling, M. Etemadi, A. Dorier, J. A. Heller, A. O. Bicen, S. Roy, T. De Marco *et al.*, "Novel wearable seismocardiography and machine learning algorithms can assess clinical status of heart failure patients," *Circulation: Heart Failure*, vol. 11, no. 1, p. e004313, 2018.

[76] H. Ashouri, S. Hersek, and O. T. Inan, "Universal pre-ejection period estimation using seismocardiography: Quantifying the effects of sensor placement and regression algorithms," *IEEE Sensors Journal*, vol. 18, no. 4, pp. 1665–1674, Feb 2018.

[77] F. Landreani, A. Martin-Yebra, C. Casellato, C. Frigo, E. Pavan, P. Migeotte, and E. G. Caiani, "Beat-to-beat heart rate detection by smartphone's accelerometers: Validation with ecg," in *2016 38th Annual International Conference of the IEEE Engineering in Medicine and Biology Society (EMBC)*, Aug 2016, pp. 525–528.

[78] O. Lahdenoja, T. Hurnanen, Z. Iftikhar, S. Nieminen, T. Knuutila, A. Saraste, T. Kiviniemi, T. Vasankari, J. Airaksinen, M. Pänkäälä, and T. Koivisto, "Atrial fibrillation detection via accelerometer and gyroscope of a smartphone," *IEEE Journal of Biomedical and Health Informatics*, vol. 22, no. 1, pp. 108–118, Jan 2018.

[79] Z. Iftikhar, O. Lahdenoja, M. J. Tadi, T. Hurnanen, T. Vasankari, T. Kiviniemi, J. Airaksinen, T. Koivisto, and M. Pänkäälä, "Multiclass classifier based cardiovascular condition detection using smartphone mechanocardiography," *Scientific reports, Nature*, vol. 8, no. 1, pp. 1–14, 2018.

[80] P. K. Jain and A. K. Tiwari, "A novel method for suppression of motion artifacts from the seismocardiogram signal," in *2016 IEEE International Conference on Digital Signal Processing (DSP)*, Oct 2016, pp. 6–10.

[81] P. K. Jain, A. K. Tiwari, and V. S. Chourasia, "Performance analysis of seismocardiography for heart sound signal recording in noisy scenarios," *Journal of Medical Engineering & Technology*, pp. 1–13, 2016.

[82] P. K. Jain, A. K. Tiwari, and O. L. Bhagat, "Seismocardiography: An alternate method to estimate electro-mechanical window," in *2016 International Conference on Systems in Medicine and Biology (ICSMB)*, Jan 2016, pp. 136–139.

[83] A. Dinh, F. M. Bui, and T. Nguyen, "An accelerometer based system to measure myocardial performance index during stress testing," in *2016 38th Annual International Conference of the IEEE Engineering in Medicine and Biology Society (EMBC)*, Aug 2016, pp. 4877–4880.

[84] C. Yang, S. Tang, and N. Tavassolian, "Utilizing gyroscopes towards the automatic annotation of seismocardiograms," *IEEE Sensors Journal*, vol. 17, no. 7, pp. 2129–2136, April 2017.

[85] C. Yang and N. Tavassolian, "Combined seismo- and gyro-cardiography: A more comprehensive evaluation of heart-induced chest vibrations," *IEEE Journal of Biomedical and Health Informatics*, vol. 22, no. 5, pp. 1466–1475, Sep. 2018.

[86] C. Yang, S. Tang, and N. Tavassolian, "Annotation of seismocardiogram using gyroscopic recordings," in *2016 IEEE Biomedical Circuits and Systems Conference (BioCAS)*, Oct 2016, pp. 204–207.

[87] M. J. Tadi, E. Lehtonen, O. Lahdenoja, M. Pankaala, and T. Koivisto, "An adaptive approach for heartbeat detection based on s-transform in seismocardiograms," in *2016 38th Annual International Conference of the IEEE Engineering in Medicine and Biology Society (EMBC)*, Aug 2016, pp. 2370–2373.

[88] T. Hurnanen, E. Lehtonen, M. J. Tadi, T. Kuusela, T. Kiviniemi, A. Saraste, T. Vasankari, J. Airaksinen, T. Koivisto, and M. Pänkäälä, "Automated detection of atrial fibrillation based on time–frequency analysis of seismocardiograms," *IEEE Journal of Biomedical and Health Informatics*, vol. 21, no. 5, pp. 1233–1241, Sep. 2017.

[89] C. Yang and N. Tavassolian, "Motion artifact cancellation of seismocardiographic recording from moving subjects," *IEEE Sensors Journal*, vol. 16, no. 14, pp. 5702–5708, July 2016.

[90] M. Di Rienzo, P. Lombardi, D. Scurati, and E. Vaini, "A new technological platform for the multisite assessment of 3d seismocardiogram and pulse transit time in cardiac patients," in *2016 Computing in Cardiology Conference (CinC)*, Sep. 2016, pp. 781–784.

[91] P.-F. Migeotte, V. Mucci, Q. Delière, L. Lejeune, and P. Van De Borne, "Multi-dimensional kineticardiography a new approach for wearable cardiac monitoring through body acceleration recordings," in *XIV Mediterranean Conference on Medical and Biological Engineering and Computing 2016*. Springer, 2016, pp. 1125–1130.

[92] H. Lee, H. Lee, and M. Whang, "An enhanced method to estimate heart rate from seismocardiography via ensemble averaging of body movements at six degrees of freedom," *Sensors*, vol. 18, no. 1, p. 238, 2018.

[93] Z. XIA, M. M. H. SHANDHI, O. T. INAN, and Y. ZHANG, "Interference and removal of respiration harmonics on noncontact seismo-cardiogram signals," *Structural Health Monitoring 2017*, no. shm, 2017.

[94] M. M. H. SHANDHI, Z. XIA, O. T. INAN, and Y. ZHANG, "Clutter effect on the noncontact seismocardiogram signals measured using microwave radars," *Structural Health Monitoring 2017*, no. shm, 2017.

[95] J. Metzler, K. Kroschel, and D. Willersinn, "Automatic detection of measurement points for non-contact vibrometer-based diagnosis of cardiac arrhythmias," in *Medical Imaging 2017: Image-Guided Procedures, Robotic Interventions, and Modeling*, vol. 10135. International Society for Optics and Photonics, 2017, p. 101351S.

[96] M. J. Tadi, E. Lehtonen, A. Saraste, J. Tuominen, J. Koskinen, M. Teräs, J. Airaksinen, M. Pänkäälä, and T. Koivisto, "Gyrocardiography: A new non-invasive monitoring method for the assessment of cardiac mechanics and the estimation of hemodynamic variables," *Scientific reports*, vol. 7, no. 1, pp. 1–11, 2017.

[97] P. Shirkovskiy, A. Laurin, N. Jeger-Madiot, D. Chapelle, M. Fink, and R. Ing, "Airborne ultrasound surface motion camera: application to seismocardiography," *Applied Physics Letters*, vol. 112, no. 21, p. 213702, 2018.

[98] C. Yang and N. Tavassolian, "Motion noise cancellation in seismocardiogram of ambulant subjects with dual sensors," in *2016 38th Annual International Conference of the IEEE Engineering in Medicine and Biology Society (EMBC)*, Aug 2016, pp. 5881–5884.

[99] G. Cosoli, L. Casacanditella, E. Tomasini, and L. Scalise, "Heart rate assessment by means of a novel approach applied to signals of different nature," in *Journal of Physics: Conference Series*, vol. 778, no. 1. IOP Publishing, 2017, p. 012001.

[100] C. Yang and N. Tavassolian, "Combined seismo-and gyro-cardiography: A more comprehensive evaluation of heart-induced chest vibrations," *IEEE journal of biomedical and health informatics*, vol. 22, no. 5, pp. 1466–1475, 2017.

[101] A. Q. Javaid, S. Dowling, M. Etemadi, J. A. Heller, S. Roy, L. Klein, and O. T. Inan, "Quantification of posture induced changes in wearable seismocardiogram signals for heart failure patients," in *2016 Computing in Cardiology Conference (CinC)*, Sep. 2016, pp. 777–780.

[102] R. Abbasi-Kesbi, A. Valipour, and K. Imani, "Cardiorespiratory system monitoring using a developed acoustic sensor," *Healthcare Technology Letters*, vol. 5, no. 1, pp. 7–12, 2018.

[103] A. Sundar and V. Pahwa, "Evaluating the performance of state of the art algorithms for enhancement of seismocardiogram signals," in *Proceedings of the First International Conference on Intelligent Computing and Communication*. Springer, 2017, pp. 37–45.

[104] C. Yang and N. Tavassolian, "Motion noise cancellation in seismocardiographic monitoring of moving subjects," in *2015 IEEE Biomedical Circuits and Systems Conference (BioCAS)*, Oct 2015, pp. 1–4.

[105] A. Taebi and H. Mansy, "Noise cancellation from vibrocardiographic signals based on the ensemble empirical mode decomposition," *J. Biotechnol. Bioeng*, vol. 2, no. 2, p. 00024, 2017.

[106] C. Yang and N. Tavassolian, "An independent component analysis approach to motion noise cancelation of cardio-mechanical signals," *IEEE Transactions on Biomedical Engineering*, vol. 66, no. 3, pp. 784–793, March 2019.

[107] T. Choudhary, L. N. Sharma, and M. K. Bhuyan, "Heart sound extraction from sternal seismocardiographic signal," *IEEE Signal Processing Letters*, vol. 25, no. 4, pp. 482–486, 2018.

[108] T. Choudhary, L. N. Sharma, and M. K. Bhuyan, "Suppression of artifacts from seismocardiogram signal using two-stage kalman filtering model," in *2018 International Conference on Signal Processing and Communications (SPCOM)*, July 2018, pp. 417–421.

[109] M. Malcangi, H. Quan, E. Vaini, P. Lombardi, and M. Di Rienzo, "Applying the efunn evolving paradigm to the recognition of artefactual beats in continuous seismocardiogram recordings," in *International Conference on Engineering Applications of Neural Networks*. Springer, 2017, pp. 256–264.

[110] A. Laurin, F. Khosrow-Khavar, A. P. Blaber, and K. Tavakolian, "Accurate and consistent automatic seismocardiogram annotation without concurrent ecg," *Physiological Measurement*, vol. 37, no. 9, pp. 1588–1604, 2016. [Online]. Available: http://stacks.iop.org/0967-3334/37/i=9/a=1588

[111] J. Wahlström, I. Skog, P. Händel, F. Khosrow-khavar, K. Tavakolian, P. K. Stein, and A. Nehorai, "A hidden markov model for seismocardiography," *IEEE Transactions on Biomedical Engineering*, vol. 64, no. 10, pp. 2361–2372, Oct 2017.

[112] W. Xu, W. A. Sandham, A. C. Fisher, and M. Conway, "Detection of the seismocardiogram w complex based on multiscale edges," in *Engineering in Medicine and Biology Society, 1996. Bridging Disciplines for Biomedicine. Proceedings of the 18th Annual International Conference of the IEEE*, vol. 3, Oct 1996, pp. 1023–1024 vol.3.

[113] N. Mora, F. Cocconcelli, G. Matrella, and P. Ciampolini, "Fully automated annotation of seismocardiogram for noninvasive vital sign measurements," *IEEE Transactions on Instrumentation and Measurement*, pp. 1–1, 2019.

[114] P. H. Charlton, D. A. Birrenkott, T. Bonnici, M. A. F. Pimentel, A. E. W. Johnson, J. Alastruey, L. Tarassenko, P. J. Watkinson, R. Beale, and D. A. Clifton, "Breathing rate estimation from the electrocardiogram and photoplethysmogram: A review," *IEEE Reviews in Biomedical Engineering*, vol. 11, pp. 2–20, 2018.

[115] T. Choudhary, M. Bhuyan, and L. Sharma, "Effect of respiratory effort levels on scg signals," in *The IEEE Region 10 Symposium (TENSYMP)*, 2019.

[116] (Accessed: 2019.08.01) What is dyspnea? [Online]. Available: https://www.medicalnewstoday.com/articles/314963.php.

[117] N. Alamdari, K. Tavakolian, V. Zakeri, R. Fazel-Rezai, and A. Akhbardeh, "A morphological approach to detect respiratory phases of seismocardiogram," in *2016 38th Annual International Conference of the IEEE Engineering in Medicine and Biology Society (EMBC)*, Aug 2016, pp. 4272–4275.

[118] N. Alamdari, K. Tavakolian, V. Zakeri, R. Fazel-Rezai, M. Paukkunen, R. Sepponen, and A. Akhbardeh, "Using electromechanical signals recorded from the body for respiratory phase detection and respiratory time estimation: A comparative study," in *2015 Computing in Cardiology Conference (CinC)*, Sep. 2015, pp. 65–68.

[119] (Accessed: Mar. 2019) Accelerometer data-sheet (adxl335). [Online]. Available: https://www.analog.com/media/en/technical-documentation/data-sheets/ADXL335.pdf.

[120] J. S. Walker, *A primer on wavelets and their scientific applications*. CRC Press LLC, Chapman and Hall/CRC, 1999.

[121] L. Sharma, S. Dandapat, and A. Mahanta, "Ecg signal denoising using higher order statistics in wavelet subbands," *Biomedical Signal Processing and Control*, vol. 5, no. 3, pp. 214 – 222, 2010.

[122] K. Dragomiretskiy and D. Zosso, "Variational mode decomposition," *IEEE Transactions on Signal Processing*, vol. 62, no. 3, pp. 531–544, Feb 2014.

[123] S. Choi and Z. Jiang, "Comparison of envelope extraction algorithms for cardiac sound signal segmentation," *Expert Systems with Applications*, vol. 34, no. 2, pp. 1056–1069, 2008.

[124] T. Choudhary and M. S. Manikandan, "Robust photoplethysmographic (ppg) based biometric authentication for wireless body area networks and m-health applications," in *2016 Twenty Second National Conference on Communication (NCC)*, March 2016, pp. 1–6.

[125] A. L. Goldberger, L. A. Amaral, L. Glass, J. M. Hausdorff, P. C. Ivanov, R. G. Mark, J. E. Mietus, G. B. Moody, C.-K. Peng, and H. E. Stanley, "Physiobank, physiotoolkit, and physionet components of a new research resource for complex physiologic signals," *Circulation*, vol. 101, no. 23, pp. e215–e220, 2000.

[126] F. J. Harris, "On the use of windows for harmonic analysis with the discrete fourier transform," *Proceedings of the IEEE*, vol. 66, no. 1, pp. 51–83, 1978.

[127] M. Mishra, S. Banerjee, D. C. Thomas, S. Dutta, and A. Mukherjee, "Detection of third heart sound using variational mode decomposition," *IEEE Transactions on Instrumentation and Measurement*, vol. 67, no. 7, pp. 1713–1721, July 2018.

[128] Y. Wang, C. J. Deepu, and Y. Lian, "A computationally efficient qrs detection algorithm for wearable ecg sensors," in *2011 Annual International Conference of the IEEE Engineering in Medicine and Biology Society*, Aug 2011, pp. 5641–5644.

[129] G. Strang, *Linear algebra and its applications*. Belmont, CA: Thomson, Brooks/Cole, 2006.

[130] J. Pan and W. J. Tompkins, "A real-time QRS detection algorithm," *IEEE Transactions on Biomedical Engineering*, no. 3, pp. 230–236, 1985.

[131] A. B. Hertzman, "The blood supply of various skin areas as estimated by the photoelectric plethysmograph," *American Journal of Physiology-Legacy Content*, vol. 124, no. 2, pp. 328–340, 1938.

[132] T. Choudhary, M. K. Bhuyan, and L. N. Sharma, "A novel method for aortic valve opening phase detection using scg signal," *IEEE Sensors Journal*, pp. 1–1, 2019.

[133] J. T. Bialasiewicz, D. González, J. Balcells, and J. Gago, "Wavelet-based approach to evaluation of signal integrity," *IEEE Transactions on Industrial Electronics*, vol. 60, no. 10, pp. 4590–4598, Oct 2013.

[134] R. Hussein, K. B. Shaban, and A. H. El-Hag, "Wavelet transform with histogram-based threshold estimation for online partial discharge signal denoising," *IEEE Transactions on Instrumentation and Measurement*, vol. 64, no. 12, pp. 3601–3614, Dec 2015.

[135] D. Li, H. Zhao, and S. Dou, "A new signal decomposition to estimate breathing rate and heart rate from photoplethysmography signal," *Biomedical Signal Processing and Control*, vol. 19, pp. 89–95, 2015.

[136] M. Finžgar and P. Podržaj, "A wavelet-based decomposition method for a robust extraction of pulse rate from video recordings," *PeerJ*, vol. 6, p. e5859, 2018.

[137] P. S. Addison, "Wavelet transforms and the ecg: a review," *Physiological measurement*, vol. 26, no. 5, p. R155, 2005.

[138] C. Varon, A. Caicedo, D. Testelmans, B. Buyse, and S. V. Huffel, "A novel algorithm for the automatic detection of sleep apnea from single-lead ECG," *IEEE Transactions on Biomedical Engineering*, vol. 62, no. 9, pp. 2269–2278, Sep. 2015.

[139] C. Ye, B. V. K. Vijaya Kumar, and M. T. Coimbra, "Heartbeat classification using morphological and dynamic features of ECG signals," *IEEE Transactions on Biomedical Engineering*, vol. 59, no. 10, pp. 2930–2941, Oct 2012.

[140] A. Tharwat, "Classification assessment methods," *Applied Computing and Informatics*, 2018.

[141] L. N. Sharma, "Multiscale analysis of heart sound for segmentation using multiscale hilbert envelope," in *2015 13th International Conference on ICT and Knowledge Engineering (ICT Knowledge Engineering 2015)*, Nov 2015, pp. 33–37.

[142] V. N. Varghees and K. Ramachandran, "A novel heart sound activity detection framework for automated heart sound analysis," *Biomedical Signal Processing and Control*, vol. 13, pp. 174 – 188, 2014.

[143] Ying-Wen Bai, Cheng-Lung Tsai, and Siao-Cian Wu, "Design of a breath detection system with remotely enhanced hand-computer interaction device," in *2012 IEEE International Conference on Consumer Electronics (ICCE)*, Jan 2012, pp. 333–334.

[144] T. Choudhary, M. Bhuyan, and L. Sharma, "Orthogonal subspace projection based framework to extract heart cycles from scg signal," *Biomedical Signal Processing and Control*, vol. 50, pp. 45 – 51, 2019.

[145] D. Ravì, C. Wong, F. Deligianni, M. Berthelot, J. Andreu-Perez, B. Lo, and G. Yang, "Deep learning for health informatics," *IEEE Journal of Biomedical and Health Informatics*, vol. 21, no. 1, pp. 4–21, Jan 2017.

[146] A. Gogna, A. Majumdar, and R. Ward, "Semi-supervised stacked label consistent autoencoder for reconstruction and analysis of biomedical signals," *IEEE Transactions on Biomedical Engineering*, vol. 64, no. 9, pp. 2196–2205, Sep. 2017.

[147] Q. Niyaz, W. Sun, and A. Y. Javaid, "A deep learning based ddos detection system in software-defined networking (sdn)," *EAI Endorsed Transactions on Security and Safety*, vol. 4, no. 12, 12 2017.

[148] T. Hastie, R. Tibshirani, J. Friedman, and J. Franklin, "The elements of statistical learning: data mining, inference and prediction," *The Mathematical Intelligencer*, vol. 27, no. 2, pp. 83–85, 2005.

[149] M. Vollmer, "HRVTool - an open-source matlab toolbox for analyzing heart rate variability," in *2019 Computing in Cardiology Conference (CinC)*, Dec. 2019.